Structural Geology of the Andes of Central Chile: Controls on Magmatism and the Emplacement of Giant Ore Deposits

by

José Meulén Piquer Romo

Submitted in fulfilment of the requirements for the degree of Doctor of Philosophy at the ARC Centre of Excellence in Ore Deposits (CODES), School of Physical Sciences, University of Tasmania, Australia

May, 2015

Declaration

This thesis contains no material which has been accepted for the award of any other degree or diploma in any tertiary institution, and to the best of my knowledge and belief, contains no material previously published or written by another person, except where due reference is made in the text of the thesis.

Jose Piquer

Date 30/10/2014

Confidentiality statement

This thesis is not to be made available for loan and copying until 31/12/2015. Following that time, this thesis may be made available for loan and limited copying in accordance with the Copyright Act 1968.

Statement of Co-authorship

The following people and institutions contributed to the publication of work undertaken as part of this thesis:

Jose Piquer, CODES, University of Tasmania (Candidate)

Jorge Skarmeta, Codelco-Chile (Author 1)

David R. Cooke, CODES, University of Tasmania (Author 2)

Paper: Structural Evolution of the Rio Blanco-Los Bronces District, Andes of Central Chile: Controls on Stratigraphy, Magmatism and Mineralization

Submitted to the journal Economic Geology

Corresponds to Chapter 3 of the thesis

Candidate was the primary author (65%), author 1 contributed to cross-section construction and structural interpretation and to the preparation of the manuscript (25%), author 2 contributed to the formalisation, refinement and presentation of the idea (10%)

We the undersigned agree with the above stated proportion of work undertaken for each of the published (or submitted) peer-reviewed manuscripts contributing to this thesis:

Signed:

David R. Cooke	*John Dickey*
Supervisor	*Head of School*
School Of Physical Sciences	*School of Physical Sciences*
University of Tasmania	University of Tasmania

Date: 28/10/14

Abstract

The Andes of central Chile contain the world's largest concentrations of Cu and Mo in two porphyry-type deposits of late Miocene to early Pliocene age: Rio Blanco-Los Bronces and El Teniente. The mineral deposits are hosted by a belt of Tertiary volcanic and intrusive rocks. The geologic evolution of this late Eocene to early Pliocene magmatic arc is characterized by the opening and subsequent inversion of the intra-arc volcano-tectonic Abanico Basin; mineralisation was coeval with the last pulses of tectonic inversion. Individual segments of the inverted basin-margin faults have been documented by previous works, but the internal architecture of the Abanico Basin remains poorly understood. Most of the syn-inversion plutonic bodies and in particular the mineral deposits and their associated sub-volcanic complexes were emplaced in the central part of the inverted basin; consequently, relationships between magmatism, hydrothermal activity and upper-crustal structures in this porphyry Cu-Mo belt have remained obscure. Based on a combination of new structural and stratigraphic mapping, cross-section interpretation, dynamic and kinematic analysis of fault-slip data, regional geophysical datasets, U-Pb and $^{40}Ar/^{39}Ar$ geochronology, (U-Th)/He thermochronology and whole-rock geochemistry, this study describes the structural architecture and evolution of the Abanico Basin and its relationship with magmatism and the emplacement of porphyry Cu-Mo deposits.

The evolution of the Andes of central Chile, and in particular the emplacement of Miocene plutonic bodies and late Miocene-early Pliocene porphyry Cu-Mo deposits, was strongly controlled by NW- and NE-striking fault systems, oblique to the N-striking basin-margin faults and to the general trend of the magmatic arc and the Andean orogen. They correspond to deep, long-lived, translithospheric weakness zones which have been recognized in the basement of the Andes to the east and west of the study area. These structures remain active under the current stress regime, as shown by the distribution of upper-crustal earthquakes which form clusters and alignments along them.

Arc-oblique fault systems were active as normal ± strike-slip faults during the opening of the Abanico Basin in the late Eocene-Oligocene, as shown by

stratigraphic correlations and syn-extensional pyroclastic deposits. These faults controlled the compartmentalization of the basin into individual sub-basins with characteristic volcano-sedimentary facies and thicknesses. Fault plane kinematics and $^{40}Ar/^{39}Ar$ dating of syn-tectonic hydrothermal minerals, in turn, demonstrates that arc-oblique faults were reactivated during Mio-Pliocene tectonic inversion as strike-slip ± reverse faults. Syn-inversion magmatic and hydrothermal activity was channelled and focused by both sets of pre-existing arc-oblique structures, and in turn fault rupture was promoted by high fluid pressures.

The kinematic and dynamic analysis of fault-slip data shows that structural reactivation during tectonic inversion was concentrated in the mining districts and around major plutons. This suggests feedback between magmatic and hydrothermal activity, fluid pressure, and the reactivation under compression of the structural architecture inherited from the extensional period. In the Rio Blanco-Los Bronces segment, fault-slip kinematics is consistent with fault reactivation under E- directed compression, while in the El Teniente segment the compression direction was ENE. In the inverted margins of the Abanico Basin, compression was accommodated by reverse faulting (sub-vertical σ_3), while in the central part of the basin, where the rock column is considerably thicker and the topography higher, a strike-slip regime (sub-vertical σ_2) was predominant during Miocene-early Pliocene tectonic inversion.

Based on the results of geological mapping, U-Pb and $^{40}Ar/^{39}Ar$ geochronology and whole-rock geochemistry, the Abanico Basin can be divided into two main segments, separated by the NW-trending Piuquencillo fault and conjugate, NE-trending structures. The northern segment contains the Rio Blanco-Los Bronces cluster, while El Teniente is located in the southern segment. Volcanic and sedimentary rocks of the northern segment can be grouped into the syn-extensional Abanico Formation (late Eocene-Oligocene) and the syn-inversion Farellones Formation (early to middle Miocene). In the southern segment, syn-extensional rocks are grouped into the Coya-Machali Formation (late Oligocene-middle Miocene) which is overlain by the syn-inversion Teniente Volcanic Complex (middle to late Miocene). Stratigraphic units defined in the northern segment cannot be correlated with the rocks of the southern segment in terms of lithofacies, depositional ages and geochemistry. The northern and southern segments show temporal differences in their tectonic evolution. An

early deformation event beginning at ~22 Ma affected only the northern segment and is associated with the formation of progressive unconformities between the Abanico and Farellones formations and with crustal thickening, reflected in the geochemistry of the Farellones Formation. A second stage of crustal thickening and exhumation began at ~12 Ma, resulting in a sharp increase of the La/Yb ratios in the northern segment, whereas in the southern segment it is reflected by a moderate increase of La/Yb ratios and the transition from the strongly folded Coya-Machali Formation to the flat-lying to gently folded Teniente Volcanic Complex. Finally, a third stage of exhumation and crustal thickening beginning at ~7 Ma affected both the northern and southern segments. According to (U-Th)/He thermochronology in zircons and apatites, this last stage was the main exhumation event affecting the rocks of the Andes of central Chile. It is recorded in the geochemistry of igneous rocks by a sharp increase in the La/Yb ratios in the southern segment. As the crust thickened and the tectonic regime changed from extensional to transpressional, the rates of volcanic output diminished and magmas began to pool in the upper crust. This is reflected by the crystallization ages of Tertiary plutons, which are coeval with tectonic inversion of the Abanico Basin. The oldest Tertiary plutons were emplaced during the early Miocene. They occur only in the northern segment and are coeval with the transition between the Abanico and Farellones formations. The oldest plutonic rocks of the southern segment were emplaced in the middle Miocene, coeval with the transition between the Coya-Machali Formation and the Teniente Volcanic Complex.

Intersections of conjugate, arc-oblique strike-slip faults are a favourable geometric location for the emplacement of magmatic bodies and hydrothermal breccias related with porphyry Cu-Mo systems. Both porphyry Cu-Mo deposits (Rio Blanco-Los Bronces and El Teniente) are located at the intersection of regional-scale, conjugate strike-slip fault systems. Favourable areas for exploration can be defined based on the criteria that they must be located at the intersections of major arc-oblique conjugate fault systems and that the area contains evidence of Miocene-early Pliocene intrusive activity. The new knowledge generated by this work about the structural architecture of the Andes of central Chile can also be applied to problems such as the location of active hydrothermal systems (economically important as geothermal energy reservoirs), the position and alignment of active volcanic centres, and the geological hazards associated with active, upper-crustal faults.

Acknowledgments

First of all, I would like to thank my wife Loreto and my children Victor and Rayen. They had to settle down in a different country and learn a new language, and their presence and continuous input of love, happiness and joy was invaluable and also the main motivation behind this work.

I would like to sincerely acknowledge my main supervisor David Cooke. His scientific rigour and extraordinarily broad geological knowledge was a continuous source of learning during the course of my PhD, not only when he was supervising my research but also during the numerous field trips in which he gave me the opportunity to participate. I would also like to thank my two co-supervisors, Ron Berry and Rob Scott. Their continuous support and guidance, both in the field and in the office, was fundamental and is greatly appreciated. Pete Hollings (Lakehead University), Mike Baker (CODES), Jorge Skarmeta (Codelco), Orlando Rivera (EMSA) and Gonzalo Yañez (Universidad Catolica) are thanked for invaluable scientific discussions which helped to improve this thesis.

The sponsor companies of the AMIRA P1060 project are acknowledged for providing the funding for this research project. Part of the analytical costs was also covered by a student research grant from the Society of Economic Geologists. Codelco, one of the sponsors of the P1060 project, is acknowledged for providing all the necessary logistical support for fieldwork and also access to internal reports and geological maps. Specifically, I would like to thank Erwin Wettke, Ruben Pardo, Jorge Camacho, Carlos Huete and Alvaro Puig for their collaboration and good disposition towards my research project. Conicyt and its Becas Chile program are thanked for providing me the scholarship which allowed me to study at CODES.

Thanks to all CODES academic and general staff and post-graduate students. They are a group of wonderful people which made my time here enjoyable and also gave me so many learning opportunities during these years.

To all the friends that we made in Hobart, thank you very much for your presence, for your support with so many little and big things and for all the good moments we enjoyed together. It would have been impossible without you.

Table of Contents

Digital appendices

Appendix I Zircon U-Pb geochronology

Appendix IA Analytical procedures

Appendix IB LA-ICPMS U-Pb zircon results

Appendix II $^{40}Ar/^{39}Ar$ geochronology

Appendix IIA Analytical procedures

Appendix IIB $^{40}Ar/^{39}Ar$ incremental heating results

Appendix III (U-Th)/He zircon and apatite thermochronology

Appendix IIIA Analytical procedures

Appendix IIIB (U-Th)/He zircon and apatite results

Appendix IV Thin section descriptions

Appendix V Whole rock chemical analysis

Appendix VA Analytical procedures

Appendix VB ICP-MS whole rock results

Appendix VI Maps and cross-sections

Geological map

Cross-section 6194000N

Cross-section 6213000N

Cross-section 6228000N

Cross-section 6260000N

Cross-section 6295000N

List of Figures

List of Tables

Chapter 1 Introduction

1.1 Preamble and statement of the problem

Understanding the complex relationships between fault systems, magmatism and hydrothermal fluid flow is a major challenge in Earth Sciences, with a wide array of practical applications. Adding to the natural complexity of the problem, conclusions can differ markedly depending on the scales of observation (mine or geothermal field, regional scale or continental scale). Resolving this complexity is of fundamental importance, because if the structures that act as pathways for magmas and hydrothermal fluids are identified properly, they can be used as guides in the exploration for new resources, particularly mineral deposits that are totally or partially concealed, without any clear evidence of their existence recognizable at the present-day surface.

Porphyry Cu-Mo deposits are one of the most important type of mineral resources worldwide. They are the source of nearly three quarters of the world's Cu production and half of the Mo production (Sillitoe, 2010). Some porphyry Cu-Mo provinces show strong relationships between major structural systems and mineral deposits, particularly when major arc-parallel faults are present. A good example of this situation is the late Eocene-Oligocene porphyry Cu-Mo province of northern Chile, where magmatism and the location of mineral deposits has long been recognized as controlled by the intra-arc, strike-slip Domeyko fault system (Mpodozis and Cornejo, 2012, and references therein; Fig. 1.1). But in other metallogenic belts, the structural architecture is not well understood and the structural controls on magma and hydrothermal fluid circulation are poorly constrained. This is the case of the Andes of central Chile, a major metallogenic province containing two giant ore deposits (Rio Blanco-Los Bronces and El Teniente) which have no evident structural control (Fig. 1.2). It is well established that the two deposits were emplaced within an inverted intra-arc volcano-tectonic basin of Tertiary age, the Abanico Basin (Charrier et al., 2002, 2007). However, even the most recently published works (e.g. Mpodozis and Cornejo, 2012) do not clearly recognize the structural systems associated with the deposits. In general, the knowledge of the structural geology of the Andes of central Chile remains relatively obscure, particularly its relationships with

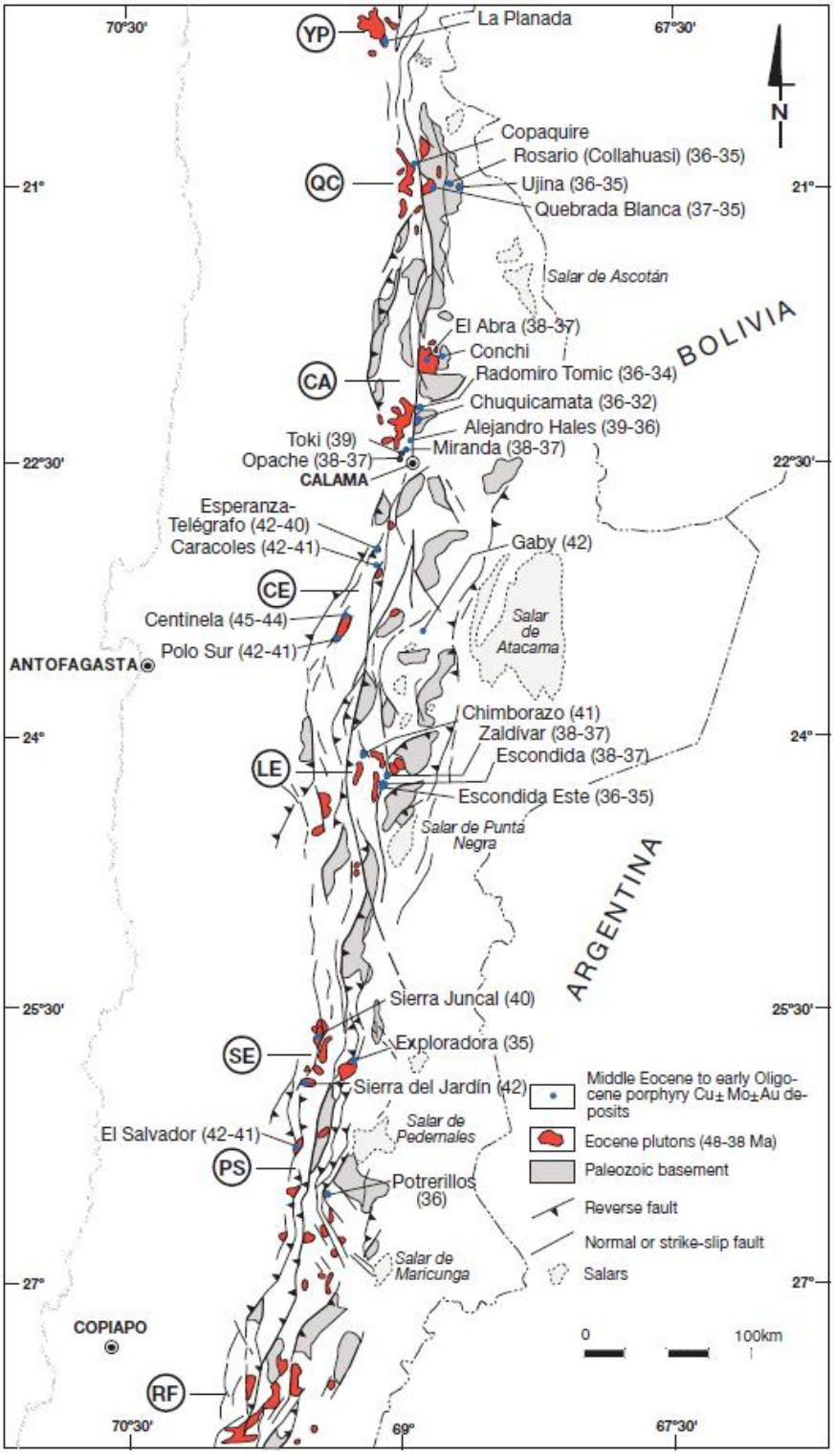

Figure 1.1. Map of the Eocene to early Oligocene porphyry Cu-Mo belt of northern Chile and the N-striking Domeyko Fault System, an example of a magmatic-metallogenic belt with a strong structural control given by an arc-parallel fault system. YP = Yabricoya-La Planada intrusive cluster; QBC = Quebrada Blanca-Collahuasi; CA = Chuquicamata-El Abra; CE = Centinela; LE = La Escondida; SE = Sierra Exploradora-Juncal; PS = Potrerillos-El Salvador; RF = Río Figueroa.

magmatism and mineralization. With the exception of two specific studies of intrusions emplaced along the eastern inverted basin-margin faults (Godoy, 1998; Piquer et al., 2010) there have been no previous studies about the relationships between magmas, hydrothermal fluids and faults in this part of the Andes.

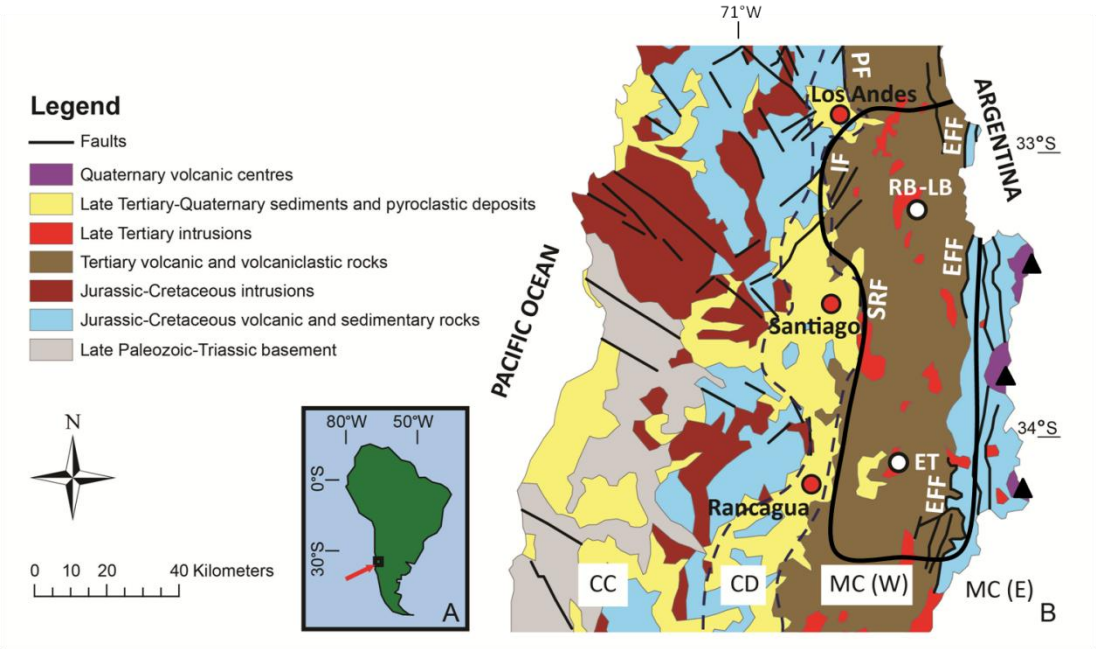

Figure 1.2. A. Location of the study area in South America. B. Simplified geology of central Chile modified from SERNAGEOMIN (2002), showing the location of the two giant porphyry copper systems (RB-LB=Rio Blanco-Los Bronces, ET=El Teniente) and the main morphological units of central Chile (CC = Coastal Cordillera, CD = Central Depression, MC (W) = Western Main Cordillera, MC (E) = Eastern Main Cordillera). The Western Main Cordillera corresponds to the inverted Abanico Basin; the main inverted basin-margin faults are labelled: PF = Pocuro fault, IF = Infiernillo fault, SRF = San Ramon fault, EFF = El Fierro fault. Black triangles highlight the location of active volcanic centres; from north to south, they correspond to the Tupungatito, San Jose and Maipo volcanoes. The study area is outlined in black.

Apart from segments of the inverted basin-margin faults and their splays, there are no major faults recognized within the Tertiary volcanic sequences of the Andes of central Chile in public geology (SERNAGEOMIN, 2002; Fig. 1.2B) or in maps and cross-sections published in the geological literature. Intrusive bodies and mineral deposits, particularly the two largest, Rio Blanco-Los Bronces and El Teniente, occur in the central part of the inverted basin, tens of kilometres away of the basin-margin faults (Fig. 1.2B). In any of the available maps and cross-sections the ore deposits seem to have no relation with fault systems. The main hypothesis of the current study

is that major internal faults do exist, and can be recognized and studied in the field. Their presence is obscured close to the mineral deposits because they controlled the emplacement of multi-stage intrusions, breccias and veins, but in more distal positions they can be recognized as brittle faults cutting the Tertiary volcanic rocks. Mapping programs carried out by Codelco (Chilean copper mining company) around the mineral deposits (El Teniente – Rivera and Falcon, 1998; Rio Blanco-Los Bronces – Piquer, 2010) have recognized some of these faults in the field, but there have been no detailed studies about their characteristics, kinematic history and relationships with magmatic emplacement and hydrothermal fluid flow.

Another limiting factor for understanding the structural geometry of the central Chile region is the lack of knowledge of stratigraphic variations in the Tertiary volcanic sequences. Many geologists who have worked in the area (e.g., Rivera and Falcon, 1998; Charrier et al., 2002; Piquer, 2010; Piquer et al., 2010) have noted huge lateral variations in stratigraphic facies and thicknesses in the Tertiary units, but there have been no detailed studies regarding their distribution or the location of major sub-basins and depocentres. The current study hypothesises that there are major internal faults which controlled magmatism and mineralization. Furthermore, these are long-lived fault systems which were also active during the extensional period, bounding sub-basins where the Tertiary volcanic and sedimentary units accumulated.

The contemporary published literature regarding the geology of central Chile typically shows schematic sections of the upper 1-2 kilometres or sections at the subduction-scale (Charrier et al., 2002; Farías et al., 2010). There are no interpretations available for the geometry of the upper crust nor are there models for the distribution of the different Tertiary sub-basins or the geometry and modes of emplacement of late Tertiary intrusive bodies. Solving these problems and acquiring a detailed understanding of the structural architecture of the Andean segment containing the giant Cu-Mo deposits of central Chile is essential for the improvement of geodynamic models of arc magmatism and porphyry mineralisation and have the potential for providing a very powerful exploration tool for companies exploring in the region and in similar environments elsewhere.

1.2 Project aims

The main objective of the research project is to understand the internal structural architecture of the inverted Abanico Basin, and its relationship with magmatism and the emplacement of mineral deposits. This area contains the two largest Cu and Mo deposits in the world (El Teniente and Rio Blanco-Los Bronces). The structures that controlled mineralisation remain an unresolved geological problem.

This research formed part of the AMIRA International P1060 project "Enhanced Geochemical Targeting in Magmatic-Hydrothermal Systems" led by CODES at the University of Tasmania, Lakehead University in Canada and the Imperial College of London. This project was sponsored by Anglo American Exploration, Australia Pty Limited, AngloGold Ashanti Australia Limited, Barrick Limited, BHP Billiton, Codelco, Compania de Minas Buenaventura, Eldorado Gold, First Quantum, Freeport-McMoRan Exploration Corporation, Glencore, Gold Fields, G-Resources, Intrepid Mines, Lundin Mining, MMG, Newcrest Mining Limited, Newmont USA Limited, Rio Tinto Exploration Pty Limited and Teck Resources Limited. Codelco provided all the necessary logistical support to complete the fieldwork.

Specific aims of the research project are as follows:

- Understand the spatial orientation and the kinematic history of faults affecting the Tertiary rocks of the central Chilean Andes.
- Identify evidence for syn-tectonic hydrothermal and/or magmatic activity.
- Investigate fault-controlled depositional changes in Tertiary volcano-sedimentary facies and thicknesses
- Establish the relative and absolute chronology of events in the area, from deposition of volcanic and sedimentary rocks to intrusion, hydrothermal activity, faulting and exhumation
- Understand the 3D geometry of intrusions, stratigraphic units and structures in the study area.

1.3 Thesis organization

The main body of the thesis comprises four chapters (chapters 3 to 6) which are prepared for submission to scientific journals. They are preceded by two introductory chapters and followed by one concluding chapter.

Chapter 1 gives a general introduction to the thesis topic and the characteristic of the study area, while **Chapter 2** reviews the geological understanding of the Andes of central Chile before the initiation of the current study.

Chapter 3 presents a detailed description of the geology and structural evolution of the Main Cordillera around the Rio Blanco-Los Bronces porphyry Cu-Mo cluster, located in the northern part of the study area (Fig. 1.2B). The structural geology of this region is poorly understood, and is of crucial importance as this area contains the world's largest concentration of Cu and Mo. A new geological map is presented, accompanied by a set of four regional-scale cross-sections.

Chapter 4 discusses the regional-scale architecture of the Andes in the study area, integrating the new structural observations and interpretations with the spatial patterns observed in regional-scale geophysical datasets. A new geological map of the central Chilean Andes is presented.

Chapter 5 focuses on the U-Pb geochronology, (U-Th)/He thermochronology and whole-rock geochemistry analysis of Tertiary rock units and their implications for the geologic evolution of the area. Traditional stratigraphic definitions are questioned and the new chronological data are interpreted within the regional structural framework presented in chapter 4.

Chapter 6 deals with the analysis of new structural data from the study area. This chapter presents the results of the statistical, kinematic and dynamic analysis of the fault plane database, including the calculations of paleostress tensors from the inversion of fault plane data.

Finally, **Chapter 7** concludes the thesis integrating chapters 3 to 6 in a comprehensive discussion of the geological and structural evolution of the study area, its implications for mineral exploration and additional applications.

1.4 Location

The study area is located in south-western South America (Fig. 1.2A), specifically within the Andes of central Chile, to the east of the cities of Los Andes, Santiago and Rancagua (Fig. 1.3). It covers the Andean or eastern segment of three of the Chilean administrative regions: Valparaiso, Metropolitan and O'Higgins (Fig. 1.3). The topography is steep, varying from 500 m a.s.l. (meters above mean sea level) in the western foothills of the Andes to summits reaching above 6,000 m. During the winter months (April/May to September/October) thick snow covers most of the area above 2,000 m, mostly precluding fieldwork activities outside the summer period.

Access is provided by roads which in most cases follow the main river valleys. Some roads provide access to mountain ranges as well, in the vicinity of ski resorts or mining operations. The main valleys which provide access to the high Andes are the Aconcagua, Mapocho, Maipo and Cachapoal rivers and their tributaries (Fig. 1.3).

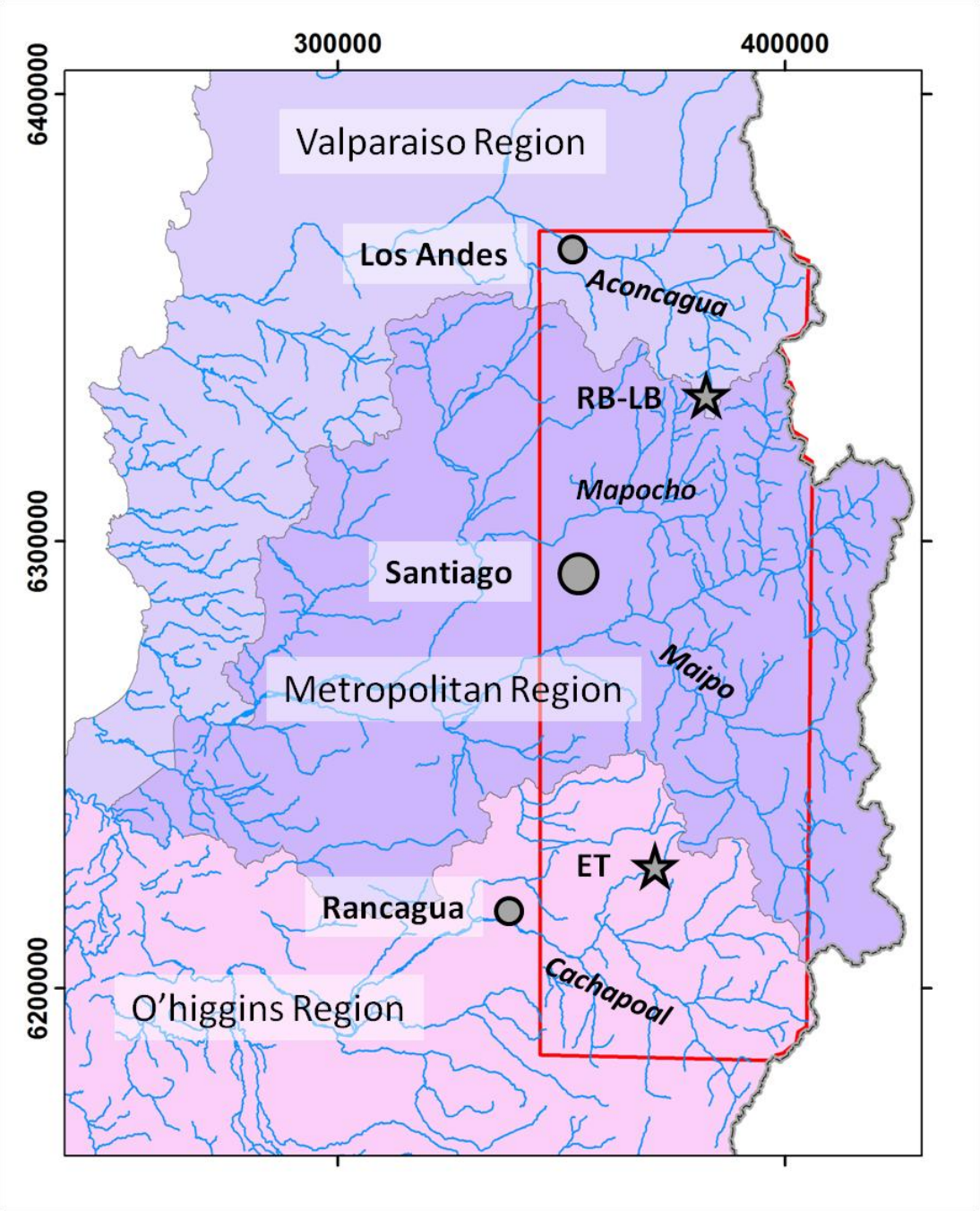

Figure 1.3. Location map. The study area is outlined in red. RB-LB = Rio Blanco-Los Bronces, ET = El Teniente. Colour shading corresponds to the administrative regions of Valparaiso (grey), Metropolitan (purple-grey) and O'higgins (pink).

1.5 Previous studies

The first recorded geological observations of the Main Andean Cordillera in central Chile were made by Darwin (1846), who completed two traverses of the Andes. He rode eastwards along the Maipo valley (Fig. 1.3) through Chile and crossing to

Argentina. He then rode back from Argentina and entered Chile following the Aconcagua river valley (Fig. 1.3). Darwin documented a thick sequence of volcanic rocks of andesitic composition in the Andes of central Chile, which he grouped in the Porphyritic Formation. The next major geological studies were made by Thomas (1953), Aguirre (1960) and Klohn (1960). They separated the Porphyritic Formation of Darwin into three different, formally-defined stratigraphic units: the Abanico, Farellones and Coya-Machali formations. The Abanico Formation is overlain by the Farellones Formation, and both units have their type localities immediately to the east of the city of Santiago (Fig. 1.3). The type locality of the Coya-Machali Formation is located further south, to the east of the city of Rancagua (Fig. 1.3), and according to Klohn (1960) is also overlain by Farellones Formation rocks. The age of volcanic rocks in the Andes of central Chile was poorly constrained initially; no fossils were found and there were no radiometric ages available. They were younger than fossiliferous, Early Cretaceous limestones, and were therefore estimated to be Late Cretaceous-early Tertiary in age (Aguirre, 1960; Klohn, 1960). The first radiometric ages were reported by Drake et al. (1976). The results suggested that Abanico and Farellones formation volcanism was much younger than previously thought, occurring between the Oligocene and the upper early Miocene (31-17 Ma). Much younger, early Pliocene ages were obtained from a rhyolitic diatreme of the La Copa complex, at the Rio Blanco-Los Bronces porphyry Cu-Mo deposit (Fig. 1.2B).

The understanding of the tectonic history of the Main Cordillera of central Chile experienced a revolution after 1990 thanks to the application of new geochronological and thermochronological techniques ($^{40}Ar/^{39}Ar$, U-Pb, Re-Os, fission tracks in apatite; e.g., Charrier et al., 2002; Maksaev et al., 2004; Deckart et al., 2005; Fock et al., 2006; Maksaev et al., 2009), the discovery of abundant fossil mammals in the Tertiary volcanic rocks (e.g., Charrier et al., 1990; Flynn et al., 1995, 2003) and the acquisition of large datasets of geophysical information (detailed magnetometry, AMT, natural seismicity, gravimetry; e.g., Yañez et al., 2002; Caceres et al., 2006; Farías et al., 2006). These new studies confirmed the late Eocene-middle Miocene age range of the Abanico, Farellones and Coya-Machali formations. It was also proposed that the Tertiary volcanic rocks of central Chile were erupted during the opening and subsequent inversion of an intra-arc volcano-tectonic basin (Godoy et al., 1999; Charrier et al., 2002), which has since been called

the Abanico Basin (Charrier et al., 2007). The basin is bounded by oppositely-dipping, high-angle, inverted basin-margin faults. However, the internal architecture of this basin and its relationship with the emplacement of magmas and porphyry Cu deposits during basin inversion has received little attention. The pioneer works of Rivera and Cembrano (2000) and Rivera and Falcon (2000) proposed that the internal architecture of the Abanico Basin around the El Teniente porphyry Cu-Mo deposit (Figs. 1.2B, 1.3) was controlled by NW-striking faults, oblique to the basin-margin faults. They suggested that these arc-oblique structures controlled the distribution of depocenters within the basin, the position of Miocene volcanic centres during tectonic inversion, the emplacement of intrusive bodies and in particular, the location of the El Teniente deposit. They also reported a series of K-Ar ages of volcanic and intrusive rocks which, together with K-Ar ages reported previously by Kay and Kurtz (1995) showed that the volcanic rocks traditionally assigned to the Farellones Formation in the El Teniente area were younger than the rocks of Farellones Formation at its type locality. Kay and Kurtz (1995) grouped these rocks in the Teniente Volcanic Complex, but still considered them an equivalent of the Farellones Formation. The age range inferred from K-Ar ages is 14-9 Ma (middle to late Miocene).

1.6 Methodology

This study can be divided into three main lines of research: the analysis of structural data, the geochronological and thermochronological studies, and the study of the 3D geometry of the upper crust through the construction of a new geological map and regional-scale cross-sections. Structural and stratigraphic data and samples for radiometric dating were collected during two field campaigns, totalling four months of field work. The first field campaign was completed between 05/02/2012 and 15/04/2012; the second was carried out between 14/01/2013 and 12/03/2013.

1.6.1 Structural analysis

In the first stage of the research project, Codelco and public (SERNAGEOMIN) geological maps, together with satellite images, were used to infer the location and orientation of regional-scale fault systems. This interpretation, in turn, was used to orient the first field campaign towards recognized or inferred major faults. The

second field campaign was oriented towards areas not accessed during the first campaign, and to acquire measurements systematically along transects following the main river valleys which cross-cut this Andean segment with an ~E-W orientation. Every observed outcrop-scale fault plane was characterized by its strike and dip. Information about the width of the fault and its damage zone was also collected. When present, the rake of fault plane striation was measured. The sense of movement was established where possible, by the use of kinematic criteria for brittle faults (e.g., Petit, 1987). The type of kinematic indicator used was always registered. The most common was the presence of steps in slickenfibres, followed by an array of different criteria such as syn-tectonic minerals precipitating in pressure shadows, dilational jogs filled by hydrothermal minerals or magma, displacement of a stratigraphic or structural marker and P-only surfaces (Petit, 1987). A total of 651 fault planes were measured; a subset of 391 provided reliable kinematic information.

Stratigraphic studies were performed in fault-bounded volcanic sequences, with the aim of identifying evidence of syn-tectonic deposition and fault-related variations on stratigraphic facies and thicknesses. Evidence of syn-tectonic intrusion of porphyries and plutons, such as magmatic foliation or emplacement on dilational jogs, were also registered.

The predominant orientation of fault planes was established using the Stereonet^{TM} software (Allmendinger et al., 2012). Kinematic and dynamic analyses were performed for different subgroups of the total fault-slip database. For the kinematic analysis, FaultKin^{TM} software (Marrett and Allmendinger, 1990; Allmendinger et al., 2012) was used to calculate the orientation of the pressure and tension axes for each individual fault plane and the average kinematic axes (shortening, stretching and intermediate axes) for different fault populations. For the dynamic analysis, the Multiple Inverse Method (Yamaji, 2000) was used to calculate the orientation of paleo-stress tensors from the inversion of fault-slip data. This method allows the identification of separate stress states from heterogeneous data sets.

1.6.2 Geochronology and thermochronology

A set of sixteen new U-Pb ICP-MS zircon ages and two groundmass $^{40}Ar/^{39}Ar$ ages were obtained to establish the crystallization age of Tertiary volcanic and intrusive

rocks, with a focus on rock units in which geochronological information was non-existent or of low accuracy. Nine of the samples dated by the U-Pb method correspond to volcanic rocks, four to subvolcanic intrusions and three to granodioritic and dioritic plutons. The $^{40}Ar/^{39}Ar$ analyses were completed in volcanic rock samples where no suitable zircons for U-Pb dating were found. Additionally, one $^{40}Ar/^{39}Ar$ age was obtained from syn-tectonic actinolite, with the aim of directly dating the last reactivation event of the selected fault plane. The U-Pb ICP-MS analyses were done at the geochronology laboratory of the University of Tasmania, Australia, while the $^{40}Ar/^{39}Ar$ analyses were completed at the Argon Geochronology Laboratory of the Oregon State University.

Eight of the rocks analysed by the U-Pb system in zircons were also analysed by the (U-Th)/He method in zircons and apatites. The analyses were done at the Arizona Geochronology Centre of the University of Arizona. The new (U-Th)/He ages were compared with new and existing geochronological data obtained from samples collected in the same localities but in which different methods were used (fission tracks in zircons and apatites, K-Ar in biotite, U-Pb in zircon). This sets of ages obtained from systems with different closure temperatures allowed us to investigate the thermal history of these rocks.

The analytical procedures and results for each of the three radiometric dating methods are detailed in Appendix I (U-Pb), II ($^{40}Ar/^{39}Ar$) and III ((U-Th)/He).

1.6.3 Geological map and cross-sections

A new geological map of the study area was prepared (Appendix VI). The map is based on fieldwork completed for this study, and incorporates published data from Wall et al. (1999), Rivera and Cembrano (2000), SERNAGEOMIN (2002), Fuentes et al. (2004), Fock (2005) and Armijo et al. (2010). It shows the distribution of the four main volcanic units of the study area: the Abanico, Farellones and Coya-Machali formations and the Teniente Volcanic Complex. Each of these four units is divided into three facies: pyroclastic, volcano-sedimentary and lava flows. The regional-scale structural architecture deduced from the new geological map was compared with the geometry and patterns of available gravimetric, magnetic and seismic datasets.

Based on the new geological map, a set of nine E-W cross-sections was prepared, with the aim of interpreting the 3D geometry of intrusives, stratigraphic units and structures in the upper ~15 kilometres of the crust.

The geological map and the cross-sections were prepared in the software ArcMap. Attached to this thesis (Appendix VI) is a complete set of digital maps and cross-sections presented at 1:100,000 scale.

Chapter 2 Geologic Evolution and Metallogeny of the Andes of Central Chile

This chapter reviews the geologic evolution of central Chile and its main metallogenic events, based on previously published data and Codelco internal reports. Particular emphasis is made on what is currently understood about the structural geology of this Andean segment, both at the regional and deposit scales.

2.1 Introduction

The geological record of central Chile begins with late Palaeozoic meta-greywackes and intrusive rocks and finishes with active volcanism and sedimentation. The oldest rocks are exposed near the coastline to the west, and progressively younger rocks crop out to the east, culminating in the active volcanoes that partly define the border between Chile and Argentina (Fig. 1.2B). This is associated with a progressive migration of the magmatic arc to the east during the Mesozoic and Cenozoic (Mpodozis and Ramos, 1989; Charrier et al., 2007).

Morphologically, central Chile can be divided in three main N-trending physiographic units. They are, from west to east, the Coastal Cordillera, the Central Depression and the Main Cordillera (Fig. 1.2B). The Coastal Cordillera is a low elevation mountain range, with altitudes up to ~2,000 m. It is composed of late Paleozoic to Triassic intrusive and metamorphic rocks (commonly referred to as the "basement" of the Andes), and Jurassic to Lower Cretaceous volcanic, intrusive and sedimentary rocks. The Central Depression is a longitudinal valley bounded by the two Cordilleras. Early hypotheses regarding the origin of this depression favoured a graben bounded by normal faults (Aubouin et al., 1973). Currently, its boundary with the Main Cordillera to the east is thought to be defined by west-vergent reverse faults (such as the San Ramon and Infiernillo faults, Fig. 1.2B; Cembrano et al., 2007). The Central Depression in central Chile is filled by up to 500 m of Oligocene to Holocene sedimentary and pyroclastic deposits (Araneda et al., 2000). There are, however, isolated ridges and mountains which are not covered by these upper Cenozoic deposits, and they are composed mainly of upper Early Cretaceous coarse-grained sedimentary rocks and Late Cretaceous volcanic rocks (SERNAGEOMIN, 2002).

The Main Cordillera can be divided into two major geological domains (Fig. 1.2B). The Eastern Main Cordillera is exposed close to the international border with Argentina. It is composed of marine and continental sedimentary rocks with minor volcanic intercalations. They were deposited east of the Andean arc in an ensialic marginal basin during the Jurassic-Early Cretaceous, and are now strongly deformed, forming part of the thin-skinned Aconcagua fold and thrust belt (Ramos, 1996). The Mesozoic rocks are covered by the products of the Pleistocene to Holocene volcanic arc (Fig. 1.2B), which constitutes the northern end of the South Volcanic Zone of the Andes. North of the city of Los Andes (Fig. 1.2B) lies the Chilean flat-slab segment, characterized by a widening of the orogenic belt, the disappearance of the Central Depression and the absence of Quaternary volcanic activity (Kay et al., 1999). There are three active volcanoes in the study area, from north to south, Tupungato-Tupungatito, San Jose and Maipo (Fig. 1.2B), plus five eroded Pleistocene volcanic edifices (Stern et al., 2007). Volcanic activity in this area commenced after cessation of magmatic activity in the Pliocene at the western Main Cordillera and subsequent migration of the magmatic arc to the east, associated with a combination of subduction erosion and a decrease in the subduction angle (Stern, 1989).

The Western Main Cordillera (Fig. 1.2B) is the focus of this study. This western domain constitutes the bulk of the Main Cordillera in central Chile (Fig. 1.2B), and is represented by the products of the Eocene to Pliocene volcanic arc. It is composed of volcanic, sedimentary and intrusive rocks which are associated with the opening and inversion of an intra-arc volcano-tectonic extensional basin, the Abanico Basin (Charrier et al., 2002, 2007). The last magmatic pulses of this volcanic arc are related with the formation of the world's two largest concentrations of copper and molybdenum, the Rio Blanco-Los Bronces cluster and the El Teniente porphyry copper deposit (Fig. 1.2B).

2.2 Pre-Andean rocks: the Palaeozoic-Triassic basement

The southern part of the Coastal Cordillera of central Chile exposes a wide belt of Carboniferous to Triassic metamorphic and intrusive rocks (Fig. 1.2B; SERNAGEOMIN, 2002). This is the northern termination of a belt of basement

rocks which crop out continuously through southern Chile to the Strait of Magellan (Herve et al., 2007).

The metamorphic component of the basement has been described as a paired metamorphic belt, divided into a western and an eastern series. The western series represents the highest P-T conditions, and includes accreted blocks of oceanic crust among highly deformed continental-derived greywackes (Herve et al., 2007). Metamorphism peaked during the late Carboniferous (Herve et al., 2007). The eastern series is composed mainly of meta-greywackes of turbiditic origin with minor calc-silicate lenses (Herve et al., 2007). The metamorphic rocks were intruded by the Coastal Batholith of central Chile between the late Carboniferous and the Permian, with some isolated plutons emplaced during the Triassic (SERNAGEOMIN, 2002).

The basement rocks are thought to comprise a magmatic arc to the east and a fore-arc with an accretionary complex to the west, associated with active subduction on the western margin of Gondwana (Charrier et al., 2007). During the Triassic, subduction at the Gondwanan margin is thought to have been interrupted, or at least greatly diminished, possibly due to a pause in the continental drift of Gondwana (Charrier et al., 2007). This favoured the accumulation of heat in the upper mantle, melting of the lower crust, the generation of large volumes of silicic magma, and the onset of extensional tectonics in the upper crust. Palaeo-geography was dominated by NNW to NW-trending extensional basins (Mpodozis and Ramos, 1989; Giambiagi et al., 2003a; Charrier et al., 2007; Fig. 2.1). According to Ramos (1994), this orientation reflects the existence of NW-trending weakness zones in the crust represented by suture zones bounding allochthonous terranes accreted during the Proterozoic and the Palaeozoic. Silicic magmatism associated with this Triassic event is represented in central Chile only by sparse isolated plutons cropping out in the Coastal Cordillera. At the same latitude in Argentina, there is a much larger volume of Triassic silicic plutonic and volcanic rocks (Perez and Ramos, 1996a). The Triassic volcanic rocks of the Choiyoi Group consist mainly of rhyolitic to rhyodacitic lavas, domes, pyroclastic and volcaniclastic rocks (Perez and Ramos, 1996a).

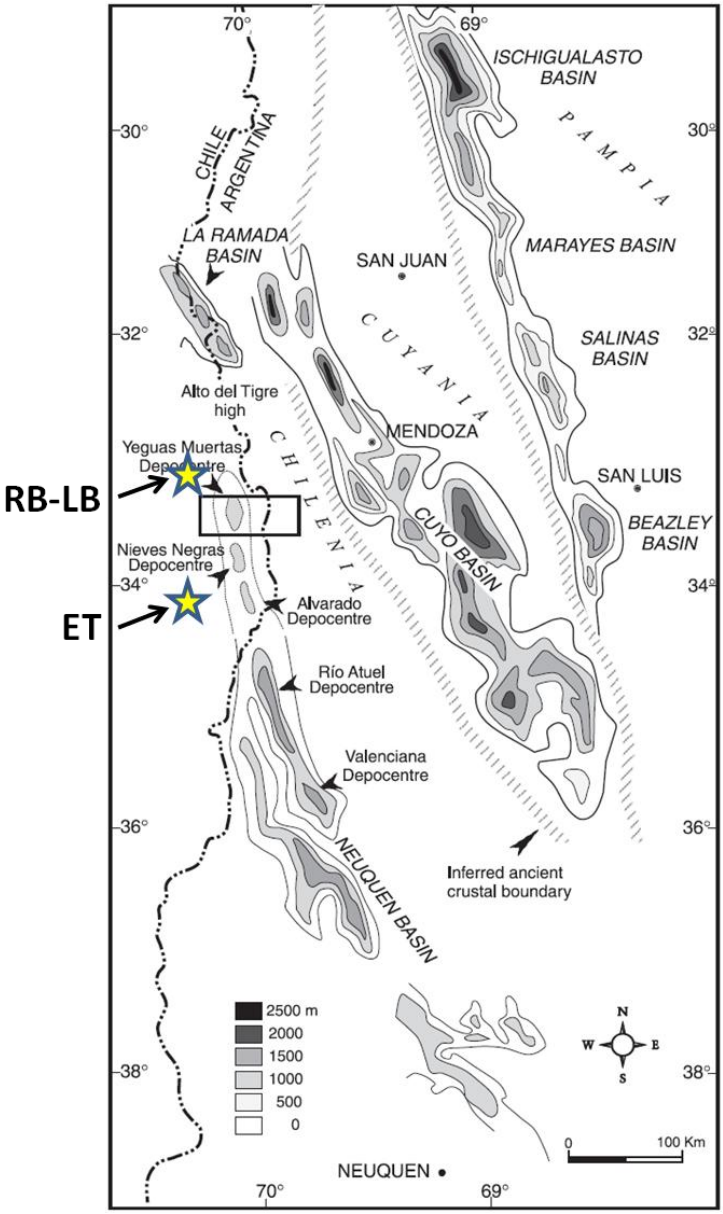

Figure 2.1. Distribution of syn-rift Triassic depocentres in central Argentina, according to Giambiagi et al. (2003a). The Rio Blanco-Los Bronces (RB-LB) and El Teniente (ET) porphyry deposits are shown for reference.

2.3 Mesozoic Andean evolution

2.3.1 Jurassic to Early Cretaceous marine transgression-regression cycles

Subduction processes have been active continuously at the western margin of Gondwana (later South America) since the Middle Jurassic. This period is referred to as the Andean tectonic cycle (Charrier et al., 2007), and its main stages are summarized in Table 2.1. The Middle Jurassic to Early Cretaceous is characterized by the development of a magmatic arc along the western margin of Gondwana, with an ensialic back-arc basin located to the east. The products of the Mesozoic

magmatic arc in central Chile constitute a large part of the Coastal Cordillera, while outcrops of mainly sedimentary rocks that were deposited in the back-arc basins are located in the Eastern Main Cordillera (Fig. 1.2B, SERNAGEOMIN, 2002).

Table 2.1. Summary of the Meso-Cenozoic tectono-stratigraphic evolution of central Chile, based on Mpodozis and Ramos (1989) and Charrier et al. (2007).

Age	Stratigraphic units	Depositional environment	Position of volcanic arc	Tectonic regime
Quaternary	Volcanic deposits and unconsolidated sediments	Continental	Eastern Main Cordillera	Compressional
Neogene	Farellones Fm.	Continental	Western Main Cordillera	Compressional
Paleogene	Abanico Fm.	Continental	Western Main Cordillera	Extensional
Late Cretaceous	Lo Valle Fm.	Continental	Central Depression	Compressional
Upper Early Cretaceous	Las Chilcas Fm. in the Coastal Cordillera, Colimapu Fm. in the Eastern Main Cordillera	Continental	Eastern Coastal Cordillera-Central Depression	Compressional
Lower Early Cretaceous	Lo Prado Fm. in the Coastal Cordillera, San Jose, Lo Valdes and Baños del Flaco fms. in the Eastern Main Cordillera	Marine	Coastal Cordillera	Extensional
Late Jurassic	Horqueta Fm. in the Coastal Cordillera, Rio Damas Fm. in the Eastern Main Cordillera	Continental	Coastal Cordillera	Compressional
Middle Jurassic	Ajial Fm. in the Coastal Cordillera, Rio Colina and Nacientes del Teno fms. in the Eastern Main Cordillera	Marine	Coastal Cordillera	Extensional

The Middle Jurassic is represented by volcanic rocks intercalated with marine sedimentary rocks in the arc region (Coastal Cordillera) and by calcareous, fossiliferous, shallow-marine sedimentary rocks in the back-arc region (Main Cordillera). The rocks at the Coastal Cordillera have been grouped in the Ajial Formation (Thomas, 1958), while those at the Main Cordillera are grouped in the Rio Colina and Nacientes del Teno Formations (Klohn, 1960; Thiele, 1978). They are interpreted to be part of an island arc with a marine back-arc sedimentary basin. The lower Late Jurassic was characterized by a marine regression, which ended with the deposition of thick evaporitic sequences during the Oxfordian grouped in the Santa

Elena member of the Nacientes del Teno Formation, and sometimes referred to as the "Oxfordian Gypsum" (Klohn, 1960).

The Kimmeridgian sediments and volcanic rocks that overlie the Santa Elena member were deposited in a sub-aerial environment. They are grouped in the Horqueta Formation at the arc region and the Rio Damas Formation in the back-arc. The Horqueta Formation is a sub-aerial sequence of 1,600-1,700 m of andesitic and volcaniclastic rocks (Thomas, 1958), while the Rio Damas Formation (Klohn, 1960) consists of 3,000 m of continental, detrital red sedimentary rocks, with an upper member comprising up to 1,000 m of andesitic lavas and volcanic breccias.

The Tithonian to Early Cretaceous was characterized by a new transgression-regression cycle, with the re-establishment of marine conditions both in the arc and the back-arc regions. The arc sequence is grouped in the Lo Prado Formation (Thomas, 1958) and in its northern equivalent, the Los Pelambres Formation (Rivano et al., 1995). These formations contain more than 3,000 m of stratigraphy, composed of marine sandstones, breccias and calcareous deposits intercalated with volcanic rocks of bimodal geochemistry. The back-arc rocks consist of shallow calcareous marine deposits referred to as the San Jose, Lo Valdes and Baños del Flaco formations (Aguirre, 1960; Klohn, 1960; Gonzalez, 1963). Similar to the situation in the Middle Jurassic, the palaeo-geography of the Tithonian-Early Cretaceous was characterized by an island arc and a shallow marine ensialic back-arc basin towards the east (Mpodozis and Ramos, 1989; Charrier et al., 2007).

2.3.2 Upper Early Cretaceous to Late Cretaceous continental rocks

The upper Early Cretaceous registered the final marine regression in central Chile, with sub-aerial conditions dominant in the region from then until the present. This period was associated with contractional deformation, uplift and erosion of the pre-existing units, initiating the Peruvian tectonic phase (Charrier and Vicente, 1972). This phase has been correlated with the transition from Mariana-type to Chilean-type subduction in the western margin of South America, during the opening of the South Atlantic Ocean (Charrier et al., 2007).

The upper Early Cretaceous marine regression is marked by a second evaporitic layer, the "Barremian Gypsum", on top of which thick sequences of continental, syn-orogenic red conglomerates and sandstones were deposited during the Aptian-Albian. These sedimentary rocks crop out in both the eastern part of the Coastal Cordillera (being partially covered by the unconsolidated sediments of the Central Depression) and in the eastern Main Cordillera. In the Coastal Cordillera rocks of this age form the 3,500-m-thick Las Chilcas Formation (Thomas, 1958), while in the Main Cordillera they constitute the 1,500-m-thick Colimapu Formation (Klohn, 1960).

In the northern part of central Chile, the Las Chilcas Formation is covered by the Upper Cretaceous volcanic, mainly pyroclastic rocks of the Lo Valle Formation, which erupted during the Campanian and Maastrichtian (Gana and Wall, 1997).

2.3.3 Early Cretaceous manto-type deposits of central Chile

The Early Cretaceous volcanic rocks of the Coastal Cordillera of central Chile contain six recognized manto-type copper deposits (Maksaev et al., 2007). The largest is El Soldado (200 Mt @ 1.4% Cu), followed by Lo Aguirre (19 Mt @ 1.66% Cu) and the minor deposits of Guayacan, Cerro Negro, Mantos de Catemu and El Salado. Although they were initially defined as manto-type deposits because of the presence of strong mineralization in favourable, permeable lithologies, it is now recognized that many of the orebodies are distinctly discordant, displaying a strong structural control associated mainly with NW to NNW-striking structures (Boric, 1997; Infanta et al., 2006; Maksaev et al., 2007). These structures control the emplacement of mineralized veins, breccias and fracture zones, around which numerous mantos formed where copper sulphides have precipitated in the most porous units of the volcanic host rocks. $^{40}Ar/^{39}Ar$ radiometric dating of hydrothermal K-feldspar and albite (Boric, 1997) provide a well-defined age range of 106 ± 1.1 to 100.5 ± 1.5 Ma for El Soldado. Hydrothermal activity was synchronous with the emplacement of the Cretaceous batholiths that intruded the Early Cretaceous volcanic rocks of the Lo Prado Formation (Rivano et al., 1995).

2.4 Late Eocene to early Miocene: the extensional Abanico Basin

The oldest Tertiary rocks exposed in the Andes of central Chile correspond to a 2,500 m thick package of andesitic and basaltic-andesitic lava flows, with intercalated pyroclastic and volcanogenic sedimentary deposits up to 500 m thick (Charrier et al., 2002). These rocks have been grouped into the Abanico (Thomas, 1953; Aguirre, 1960) and Coya-Machali (Klohn, 1960) formations, which have been considered equivalents by later studies (Charrier et al., 2002). These units contain numerous subvolcanic intrusions that were emplaced coeval with volcanism (Vergara et al., 2004) and present a well developed paragenesis of low grade burial metamorphic minerals, characteristic of upper zeolite to lower prehnite-pumpellyite facies (Bevins et al., 2003).

The first studies of the Abanico Formation estimated a Cretaceous-early Tertiary age for this unit (Aguirre, 1960; Klohn, 1960). Later authors, based on K-Ar ages, concluded that at least the upper part of this unit was of mid-Tertiary age (Drake et al., 1976; Thiele, 1978), but the reliability of K-Ar ages was questioned because the studied rocks are affected by pervasive low-grade metamorphism and in some cases by hydrothermal alteration. The determination of $^{40}Ar/^{39}Ar$ ages and the discovery of mammal fossils in the pyroclastic and volcanogenic sedimentary intercalations, have confirmed the mid-Tertiary age of these rocks (Charrier et al., 1990, 1994, 1996, 2002, 2005). The currently accepted age range is 37 to 16 Ma (late Eocene to early Miocene; Charrier et al., 2002).

Several independent lines of research suggest that the rocks of Abanico Formation were deposited in an intra-arc extensional basin (Charrier et al., 2002; Piquer et al., 2010). Evidence includes the presence of extensional growth-strata in the sedimentary rocks associated with major high-angle inverted normal faults (Charrier et al., 2002; Piquer et al., 2010) and high heat flow suggested by the thermal maturity of organic matter based on vitrinite reflectance (Zurita et al., 2000). Furthermore, geochemical and isotopic signatures show a tholeiitic differentiation trend and primitive, mantle-like isotopic signatures (Nystrom et al., 1993) with a low-pressure residual assemblage of plagioclase, olivine and pyroxene suggesting a relatively thin

(30-35 km) continental crust (Kurtz et al., 1995). Extensional tectonics in the intra-arc region was a common feature during the Oligocene and early Miocene not only in central Chile, but also along the entire Southern Andes and at least in parts of the Central Andes (Jordan et al., 2001).

Three main N-striking fault systems have been identified in the Western Main Cordillera, which are interpreted as inverted normal faults forming the margins of the former Abanico Basin. In the proposed western margin of the basin, two major fault systems are associated with the contact between the Abanico Formation and Mesozoic rocks further west: the Infiernillo and the Pocuro-San Ramon faults (Fig. 1.2B; Farías et al., 2010). Both fault systems have associated folds which suggest reverse west-vergent movement, but the uplifted (eastern) block contains Tertiary rocks, while the footwall block contains Mesozoic units. This has been interpreted as evidence of partial inversion of a previous basin-margin normal fault. The same situation occurs in the eastern margin of the Abanico Basin, where the El Fierro fault (Fig. 1.2B), currently an east-vergent high angle reverse fault associated with the contact between Abanico Formation and the Mesozoic units, is interpreted to be the inverted eastern margin of the basin (Farias et al., 2010).

Apart from these inverted basin-margin, N-striking faults, geological mapping carried out by Codelco around the El Teniente and Rio Blanco porphyry Cu deposits (Rivera and Cembrano, 2000; Rivera and Falcon, 2000; Piquer, 2010) have identified arc-oblique, NE- and NW-striking fault systems (Fig. 2.2) which are associated with dramatic changes of thicknesses and volcano-sedimentary facies of the Abanico and Coya-Machali formations. This suggests the existence of several sub-basins and depocenters bounded by these orogen-oblique fault systems.

In some localities close to the inverted basin-margin faults, the depositional contact between the Mesozoic units and Abanico Formation lava flows is exposed. The contact is unconformable, and represents a hiatus of at least 37 m.y. The unconformity has been recognized on both the western and eastern margins of the basin (Gana and Wall, 1997; Charrier et al., 2002).

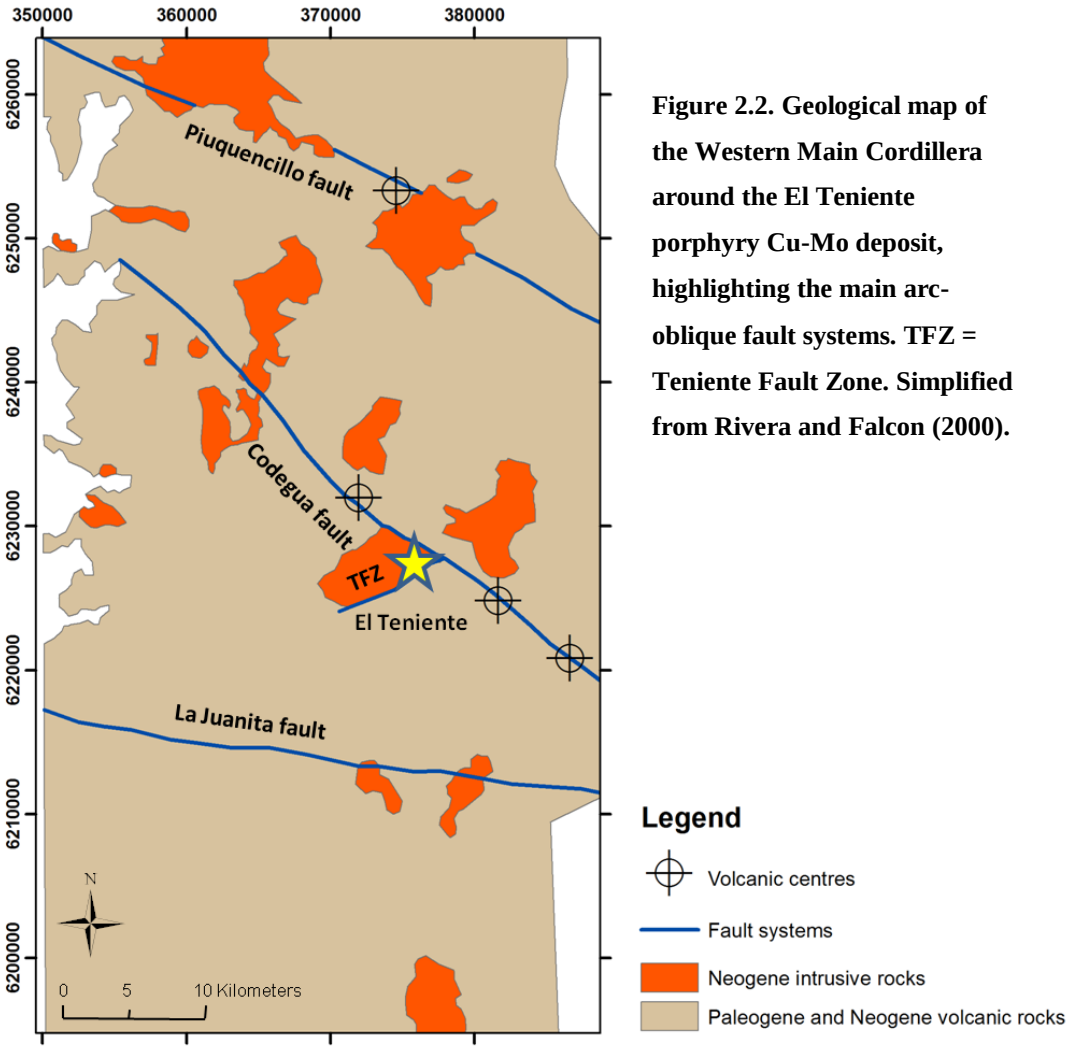

Figure 2.2. Geological map of the Western Main Cordillera around the El Teniente porphyry Cu-Mo deposit, highlighting the main arc-oblique fault systems. TFZ = Teniente Fault Zone. Simplified from Rivera and Falcon (2000).

2.5 Early Miocene to early Pliocene: basin inversion and associated volcanism and plutonism

This period is represented in the stratigraphy of the study area by up to 2,400 metres of almost exclusively volcanic rocks of the Farellones Formation (Thomas, 1953; Aguirre, 1960; Klohn, 1960; Thiele, 1978; Vergara et al., 1988). It is composed of basaltic-andesitic to rhyolitic lava flows, pyroclastic and volcaniclastic deposits and very limited clastic sedimentary rocks. The lower part of this unit has been affected by zeolite-facies burial metamorphism (Bevins et al., 2003). While the Abanico Formation forms a continuous blanket, which covers (with variable thickness) the entire area between the basin-margin faults, the Farellones Formation is volumetrically smaller and restricted to specific volcanic centres. Another difference between these two units is the intensity of deformation; Abanico Formation rocks are

often tightly folded, whereas Farellones Formation rocks are subhorizontal to gently folded. Some authors (Charrier et al., 2002; Fock et al., 2006) have reported the presence of progressive unconformities and syn-tectonic deposits in the transition between the Abanico and Farellones formations. Consequently, the Farellones Formation has been interpreted as a syn-inversion unit, deposited during folding of the Abanico Formation rocks and inversion of the Abanico Basin (Charrier et al., 2002).

The oldest age obtained from rocks of Farellones Formation is 22.7 ± 0.4 Ma (U-Pb SHRIMP in zircons; Piquer, 2010). The sample was obtained in the northern part of the study area, from a crystal- and lithic-rich andesitic pyroclastic flow which covers progressive unconformities developed in volcaniclastic deposits of the upper Abanico Formation. In the central part of the study area, Aguirre et al. (2000) reported $^{40}Ar/^{39}Ar$ ages of 21.6 ± 0.2 and 20.1 ± 0.3 in lower Farellones Formation rocks, while in the southern sector, to the southeast of the El Teniente deposit, folded andesitic lava flows intercalated with syn-tectonic sedimentary rocks were dated at 16.1 Ma ($^{40}Ar/^{39}Ar$; Kay and Kurtz, 1995). The sedimentary rocks sit on top of a mammal-bearing volcaniclastic layer dated at 20.09 ± 0.27 Ma (Flynn et al., 1995). This situation has led to Charrier et al. (2002, 2005) suggesting that the contact between the Abanico and Farellones formations is diachronous and that Miocene basin inversion and deformation progressed from north to south. Deformation of the Abanico Formation rocks was associated with the reactivation as reverse faults of the western and eastern basin-margin faults (Charrier et al., 2002). The youngest rocks of the Farellones Formation are lava flows erupted around 6 Ma in the southernmost part of the study area (Kay and Kurtz, 1995; Vergara et al., 1988).

Syn-orogenic deposits associated with Miocene deformation are also recorded in foreland basins in the Argentinean (eastern) flank of the Andes (Perez and Ramos, 1996b). Based on K-Ar ages of ash layers intercalated with the sediments and on its contact relationships, it has been established that the onset of syn-orogenic sedimentation in this eastern domain occurred at ~20 Ma (Perez and Ramos, 1996b). This age is coincident with the transition between the Abanico and Farellones formations.

The tectonic shift from an extensional to compressive tectonic regime in the intra-arc region has also been recognized in the geochemistry of the volcanic rocks (Kay and Kurtz, 1995; Kay et al., 1999). Farellones Formation lavas, at similar SiO_2 concentrations, show increasing $^{87}Sr/^{86}Sr$ ratios, decreasing εNd values and an increase in REE slopes with decreasing age. This is accompanied by a decrease in the absolute volume of lavas erupted and an increase in the relative percentages of high-silica magmas. All of these observations are consistent with an increase in crustal contamination, as magmas had to ascend through an increasingly thicker crust. Crustal thickening, in turn, is thought to be associated with shortening during inversion of the Abanico Basin (Kay and Kurtz, 1995; Kay et al., 1999).

Under the compressive regime prevailing since the early Miocene, magmas began to pool in the upper crust to form plutonic bodies, which in some areas coalesced to form batholiths (Fig. 1.2B). The oldest Tertiary plutonic rocks identified in the study area were emplaced at 22-20 Ma (Warnaars et al., 1985; Kurtz et al., 1997), which is the age range of the Farellones Formation basal units (Aguirre et al., 2000; Fock, 2005; Piquer, 2010). Pluton emplacement was episodic throughout the Miocene and broadly coeval with Farellones Formation volcanism, with plutons emplaced between 21.6 Ma and 3.85 Ma (early Miocene to early Pliocene; Kurtz et al., 1997; Maksaev et al., 2004; Deckart et al., 2005, 2010). This is in a marked contrast with the record of the late Eocene-early Miocene extension where the volcanic sequences have no coeval plutonic activity.

A Miocene tectonic event involving compression, deformation, shortening, uplift, high exhumation rates and crustal thickening is recognized in central Chile and throughout most of the Central and Southern Andes. It is sometimes referred to as the Quechua tectonic phase (Mpodozis and Ramos, 1989; Jordan et al., 2001). In central Chile and Argentina, this shortening event can be divided in four main stages (Giambiagi et al., 2003b; Farías et al., 2010):

- **First stage: 22 - 15 Ma.** Deformation was concentrated in the Abanico Basin, inverting the normal faults at both basin margins and generating the progressive angular unconformities which separate the Abanico and

Farellones formations. To a lesser extent, the Mesozoic rocks to the east were also deformed.

- **Second stage: 15 - 8.5 Ma.** Deformation was almost entirely concentrated in the Mesozoic rocks of the Argentinean flank of the Andes, forming the Aconcagua fold and thrust belt.

- **Third stage: 8.5 - 4 Ma.** Uplift of basement blocks forming the Frontal Cordillera in the Argentinean flank of the Andes, and out-of-sequence reactivation of the east-vergence faults at the eastern boundary of the Abanico Basin (El Fierro fault). This period is associated with very rapid uplift and exhumation in the Chilean Main Cordillera, and was coeval with the formation of both the Rio Blanco-Los Bronces cluster and the El Teniente porphyry Cu-Mo deposit.

- **Fourth stage: 4 - 0 Ma.** Deformation migrated to the east, and is now almost entirely concentrated in the Argentinean foreland, to the east of the Frontal Cordillera.

2.5.1 The Mio-Pliocene metallogenic belt of central Chile

The early Miocene to early Pliocene magmatic arc of central Chile is associated with a metallogenic belt characterized by three world-class porphyry Cu-Mo ± Au deposits. They are, form north to south, Los Pelambres-El Pachon, Rio Blanco-Los Bronces and El Teniente. The belt can be divided in a northern and a southern sub-belt (Fig. 2.3), with different formation ages of the hydrothermal systems, different tectonic settings and also different mineralization styles. The study area of this work covers the southern sub-belt.

Northern sub-belt: includes the Los Pelambres-Frontera-El Pachon cluster of porphyry Cu-Mo and Cu-Au deposits and several porphyry Cu-Mo-Au and epithermal Au exploration projects, including the San Felipe cluster in Chile (Toro et al., 2006) and the Altar and Los Azules projects located in Argentina to the NE of Los Pelambres-El Pachon (Maydagan et al., 2014). Deposits in this sub-belt are of smaller size than in the southern sub-belt, but are richer in Au (Toro et al., 2006, 2009; Perello et al., 2009, 2012; Maydagan et al., 2014). They were formed between

12 and 8 Ma, and mineralization is contained mainly in vein systems genetically related to porphyritic intrusions of quartz diorite composition. Hydrothermal breccias are volumetrically small and their economic importance is minor. At the latitude of this sub-belt there is currently no active volcanism in the Andes, as a consequence of flat subduction of the Nazca plate below South America since the late Miocene, and there is also no Central Depression, a morphological effect of the anomalously low subduction angle (Charrier et al., 2007).

Los Pelambres-Frontera-El Pachon is a giant porphyry cluster formed between 12 and 8 Ma. It is located close to the international border of Chile and Argentina. The cluster contains both Cu-Mo and Cu-Au mineralized centres (Perello et al., 2009, 2012),

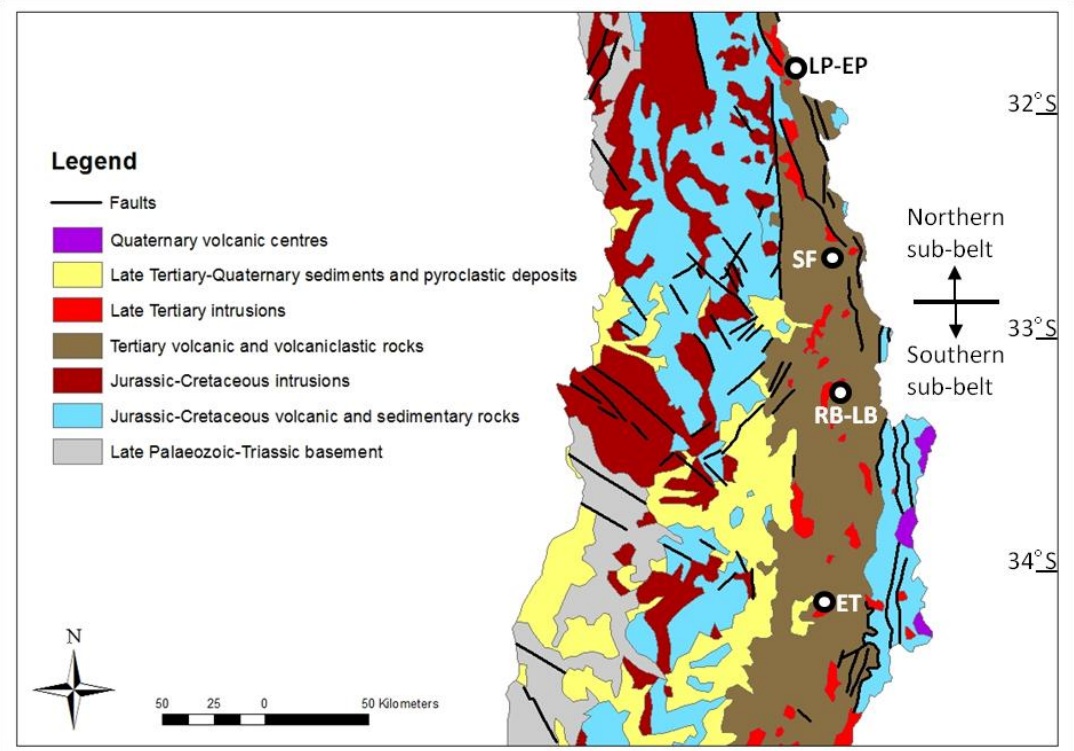

Figure 2.3. Geological map of central Chile (based on SERNAGEOMIN, 2002), showing the main deposits and clusters of the Mio-Pliocene belt and the approximate boundary between the two sub-belts. LP-EP=Los Pelambres-El Pachon, SF=San Felipe cluster, RB-LB=Rio Blanco-Los Bronces, ET=El Teniente.

including the main Cu-Mo deposit of Los Pelambres, currently owned and operated by Antofagasta Minerals, and the more recently discovered Cu-Mo-Au centres of Frontera and El Pachon. They define a NW-oriented mineralised trend, with Los

Pelambres in the NW, El Pachon in the SE and Frontera between them. El Pachon is located on the Argentinean side of the border. The resource estimated for Los Pelambres is 4,550 Mt @ 0.59% Cu and 0.012% Mo (26.8 Mt Cu and 0.5 Mt Mo), while a preliminary estimate for Frontera is 700 Mt @ 0.52% Cu and 0.1 g/t Au (3.6 Mt Cu; Perello et al., 2009). Resources at El Pachon are estimated at 860 Mt @ 0.63% Cu (5.4 Mt Cu; Almandoz et al., 2005). Adding the resources of the three mineralized centres, the entire Cu content of the cluster would be 35.8 Mt. Perello et al. (2012) gave a total resource for the entire cluster of 6,165 Mt @ 0.56% Cu and 0.011% Mo, which result in a slightly different figure of 34.5 Mt Cu plus 0.7 Mt Mo. The cluster is associated with a quartz-dioritic intrusive body, which is cut by porphyry dikes of similar composition. The host rocks of this intrusive complex are volcanic and volcaniclastic rocks which are equivalent in age to the Abanico Formation (Perello et al., 2012). Porphyry-style mineralization and veining was coeval with the emplacement of porphyry dikes and minor magmatic-hydrothermal breccias (Perello et al., 2012). The intrusive rocks and the main Los Pelambres orebody were emplaced along the Los Pelambres fault, a west-dipping, N-striking structure (Perello et al., 2012) which is part of the east-vergent reverse fault system associated with the eastern boundary of the inverted Abanico Basin. This system is a northern equivalent to the El Fierro fault system.

The *San Felipe cluster* (Toro et al., 2006) is a group of hydrothermal systems, with at least five individual mineralized centres (Toro et al., 2009): Novicio, Vizcachitas, Pimenton, West Wall and Amos-Andres. None of them are currently being exploited, with the exception of Au-rich epithermal veins at Pimenton. The prospects are at different stages of exploration. Advanced argillic alteration and epithermal mineralized veins containing precious metals are commonplace in the cluster, suggesting a smaller amount of exhumation in comparison with other clusters of the Mio-Pliocene belt. The timing of alteration and mineralization is 11-9 Ma, coeval with the mineralising events at Los Pelambres. The only exception is the Novicio system which was formed between 15 and 13 Ma (Toro et al., 2009). This cluster is located in the central part of the Abanico Basin (Fig. 2.3). The hydrothermal systems are genetically related to equigranular and porphyritic polyphase intrusions (predominantly of dioritic and quartz-dioritic composition) and minor hydrothermal breccias (Toro et al., 2006). They are hosted by both the Abanico and Farellones

formations. Piquer et al. (2009) suggested that hydrothermal activity in the cluster was preceded by a caldera-forming volcanic eruptive event. The intra- and extra-caldera pyroclastic deposits form the basal part of the Farellones Formation in the area, covering progressive unconformities developed on the upper Abanico Formation.

Southern sub-belt: this sub-belt is defined by the two largest known Cu and Mo concentrations on the planet: the Rio Blanco-Los Bronces cluster and the El Teniente deposit. They formed between 7 and 4 Ma (Maksaev et al., 2004; Cannell et al., 2005; Deckart et al., 2005, 2013, 2014), although in the Los Bronces sector of the Rio Blanco-Los Bronces cluster there is local evidence of older pulses of hydrothermal activity (Deckart et al., 2013, 2014). Mineralization is contained in vein systems related to episodic intrusion of dacitic porphyry dikes, and in the matrix and clasts of large hydrothermal breccia complexes. The relative proportion of ore contained in veins versus breccias has been a matter of debate (Serrano et al., 1996; Skewes et al., 2002; Frikken et al., 2005; Cannell et al., 2005, 2007; Skewes and Stern, 2007).

Rio Blanco-Los Bronces cluster: consists of seven recognizable mineralized centres which form an almost continuous 12 km long and 1-2 km wide belt along a NW-NNW trend (Fig. 2.4). Codelco owns the Rio Blanco and Sur Sur deposits, currently in production, and the recently discovered La Americana and Cerro Negro orebodies. Anglo American exploits the Los Bronces deposit and is currently in advanced stages of exploration on the Los Sulfatos and San Enrique-Monolito orebodies. Los Bronces is where mineralisation in the cluster was first discovered and mined, during the second half of the 19th century (Irarrazaval et al., 2010). With ~205 Mt of contained copper, this cluster is the largest known Cu concentration in the world (Irarrazaval et al., 2010; Sillitoe, 2010; Toro et al., 2012). An updated Mo resource has not been published. The last Mo resource estimate dates from 2003 (Camus, 2003), when the resource of the cluster was estimated to be 6.99 Gt @ 0.75% Cu and 0.018% Mo, which equates to 52.4 Mt of copper and 1.26 Mt of Mo. Since that time the Cu resource has been expanded to more than 200 Mt of Cu, almost four times the 2003 figure. This is the result of exploration and expansion work done in the last decade by both Codelco and Anglo American (Irarrazaval et al., 2010). All the newly

discovered mineralized centres are molybdenum-rich, so it is likely that an updated Mo content will be as much as four times larger than the 2003 figure, making this cluster the largest Mo concentration on the planet.

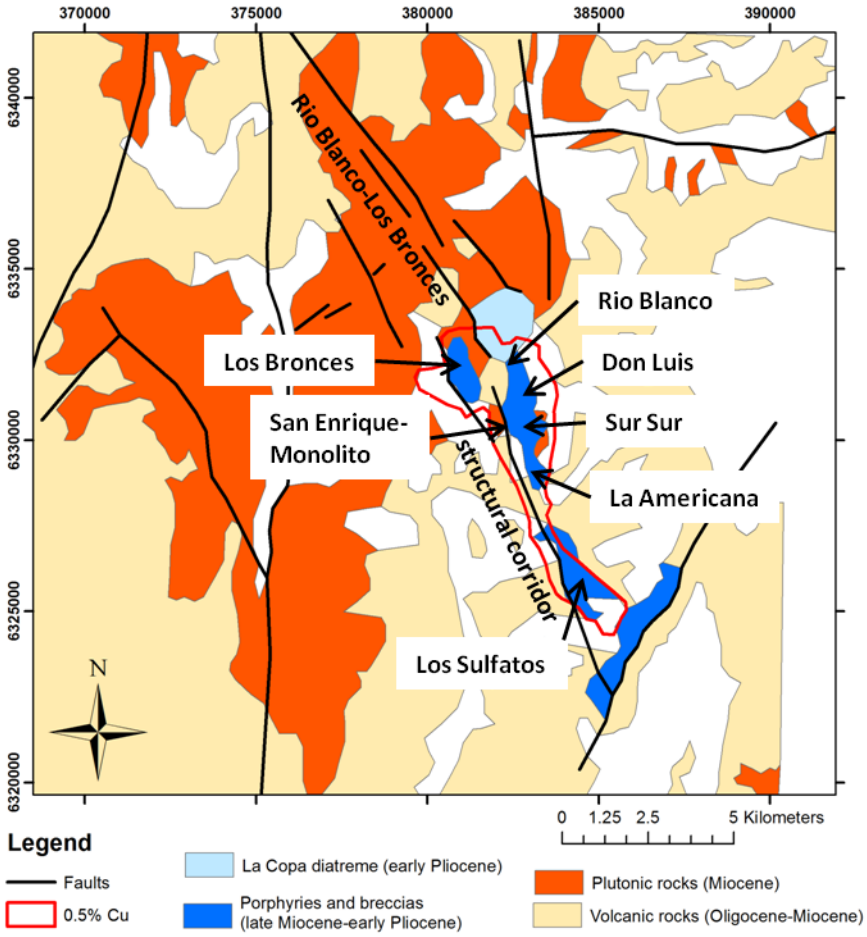

Figure 2.4. Geology of the Rio Blanco-Los Bronces district, simplified from Toro et al. (2012). This figure shows the NNW alignment of the seven mineralised centres of the cluster, which are surrounded by the 0.5% Cu isograd.

The oldest host rocks in the cluster are andesitic lava flows of the Farellones Formation. U-Pb dating show that the volcanic rocks were erupted and deposited during a very narrow time window, between 16.7 and 17.2 Ma (Deckart et al., 2005; Piquer, 2010). The lavas are intruded by a polyphase intrusive complex, the Rio Blanco-San Francisco batholith, which in the area of the cluster can be divided into three main units, according to cross-cutting relationships and U-Pb ages (Deckart et al., 2005): the Rio Blanco granodiorite (11.96 ± 0.40 Ma), the Cascada granodiorite (8.40 ± 0.23 Ma) and a diorite (8.16 ± 0.45 Ma). Mineralization in the cluster is

associated with the intrusion of dacitic porphyries and hydrothermal breccias, which were emplaced in both the Farellones Formation lavas and the plutonic units. At least three distinct mineralized or partly mineralized dacitic porphyries can be recognized, based on textural differences, cross-cutting relationships and U-Pb ages (Deckart et al., 2005). They are, from oldest to youngest, the Quartz Monzonite porphyry (6.32 ± 0.09 Ma), the Feldspar porphyry (5.84 ± 0.03 Ma) and the Don Luis porphyry (5.23 ± 0.07 Ma). Based on cross-cutting relations, it is inferred that hydrothermal breccias cover a similar time range, beginning with biotite breccias that pre-date the Quartz Monzonite porphyry and ending with the mostly post-mineral La Copa diatreme and breccia complex at 4.69 ± 0.23 Ma (Deckart et al., 2013). The breccias contain variable amounts of rock flour, biotite and tourmaline in the matrix. In general, the older breccias contain less matrix and their formation is associated with less clast movement and rotation. The hydrothermal matrix is predominantly composed of biotite-magnetite in the deeper part of the breccias (associated with potassic alteration) and of tourmaline-specularite in shallower levels (associated with phyllic alteration; Frikken et al., 2005). The younger breccias have abundant rock-flour matrix and are polymictic, with rounded clasts showing evidence of major transport and attrition. These younger breccias are in general associated with lower Cu grades than the older ones, and have lower temperature alteration assemblages (chlorite-sericite).

The deposit scale structural geology for the Rio Blanco and Sur Sur sectors of the cluster was documented by Skarmeta et al. (2004). They concluded that these mineralized centers have markedly different fault patterns: in the Rio Blanco underground mine they identified a major N30°W trend whilst fault systems in the Sur Sur open pit have a N60°E strike with dextral strike-slip sense of movement. Both the NW- and NE-striking faults were active during intrusion and mineralization, as they control the geometry of intrusive bodies and Cu isograds, but only the NE faults show evidence of post-mineral reactivation. Silva and Toro (2009) reported that mineralization and potassic alteration in the Los Bronces sector was syn-tectonic, based on the geometry and alignment of hydrothermal minerals. According to these authors, fluids were channeled by a NNW-striking structural corridor which they defined as the “Rio Blanco-San Francisco Fault Zone”. Based on

$^{40}Ar/^{39}Ar$ ages from syn-tectonic biotite crystals, they concluded that this fault zone was active at 7-6 Ma.

El Teniente deposit: this orebody was previously thought to be the largest Cu and Mo resource on the planet (Camus, 2003) until the recent dramatic increase in the resources of the Rio Blanco-Los Bronces cluster. It is owned and exploited by Codelco, and contains 12.4 Gt @ 0.62% Cu and 7.8 Gt @ 0.018% Mo. Adding past production, the total metal content of the deposit is 94.4 Mt of copper and 2.5 Mt of molybdenum (Camus, 2003).

Like the Rio Blanco-Los Bronces cluster, the oldest host rocks of El Teniente are andesitic lava flows correlated with the Farellones Formation. They were defined by Kay and Kurtz (1995) as the Teniente Volcanic Complex. Their age range (K-Ar) is 14 to 6 Ma (Kay and Kurtz, 1995; Rivera and Falcon, 2000). These lavas are broadly coeval with the Teniente Plutonic Complex (Kay and Kurtz, 1995), which is a polyphase intrusive complex with ages between 12 and 7 Ma (Kay and Kurtz, 1995).

Both the lavas and the plutonic complex have been intruded by stocks and dikes of quartz-diorite, tonalite and dacitic porphyry, genetically related with the mineralization (Maksaev et al., 2004). These include the Sewell Diorite and the Teniente Porphyry. U-Pb ages of these intrusive rocks are bracketed between 6.46 and 4.58 Ma, coeval with Re-Os ages of molybdenite from several different vein generations which have ages between 6.30 and 4.42 Ma (Maksaev et al., 2004; Cannell et al., 2005; Baker et al., 2011). Mineralization is also contained in the matrix and clasts of hydrothermal breccias. The deposit contains tourmaline, anhydrite, biotite and rock-flour breccias (Skewes et al., 2002; Maksaev et al., 2004; Cannell et al., 2005; Vry et al., 2010). The Braden breccia pipe is a giant diatreme complex which cuts all the volcanic and intrusive rocks mentioned before. It is a polymictic, high-energy breccia with rounded clasts and rock flour matrix. It is not entirely post-mineral as some segments of the diatreme contain economic mineralization in the matrix, and it is also related to a ring-shaped marginal tourmaline breccia which also contains high Cu grades (Maksaev et al., 2004). Post-mineral intrusion in the deposit is represented by amphibole-rich lamprophyre dikes with an $^{40}Ar/^{39}Ar$ age of 3.85 ± 0.18 Ma (Maksaev et al., 2004).

Garrido (1995) prepared a detailed report for Codelco about the structural geology of the El Teniente deposit, concluding that the main structure controlling the location of the deposit was the Teniente Fault Zone (Fig. 2.2). This mainly dextral strike-slip, N46°E striking, anastomosing fault focused volcanic activity during Farellones Formation volcanism, controlled the emplacement of the Sewell Diorite and also focused the hydrothermal activity related to the mineral deposit (Garrido, 1995). The stress state during formation of the deposit and movement of the Teniente Fault Zone involved E-W compression, with σ_1 subhorizontal and trending N86° ± 9° W (Garrido, 1995). Cannell et al. (2005) concluded that during the formation of El Teniente, local stresses around high-level intrusions in the central part of the deposit were more important than far-field stresses, explaining the formation of concentric and radial veins and fractures.

Post-mineral and post-lamprophyre dikes movement was recognized in some of the fault planes of the Teniente Fault Zone. Kinematic indicators associated with these late movements of the Teniente Fault Zone allowed Garrido (1995) to establish that σ_1 during this period was oriented between N21°E and N19°W. This broadly N-S compression during the late Pliocene-Quaternary is in agreement with the conclusions of Lavenu and Cembrano (1999, 2008) for the entire central Chile region. In addition to the Teniente Fault Zone, Garrido (1995) also defined a secondary fault system striking N64°W. This structural system is in broad agreement with the NW-striking Codegua fault system identified at a regional-scale by Rivera and Cembrano (2000).

Garrido (1995) also reported structural measurements acquired in selected localities across central Chile and concluded that the compression was broadly E-W, with a slight change in orientation at the latitude of the El Teniente deposit: to the south, σ_1 was N70°E, while to the north, σ_1 was N75°W. A few specific structural stations showed an orogen-oblique NE and NW direction for σ_1. Garrido (1995) associated this with local perturbations on the stress tensors in the vicinity of major NE and NW strike-slip fault systems. A N-S direction for σ_1 was only recorded in the stations at El Teniente deposit mentioned before. Based on these findings, Garrido (1995) proposed the existence of major arc-oblique structures affecting the entire central Chile region (Fig. 2.5).

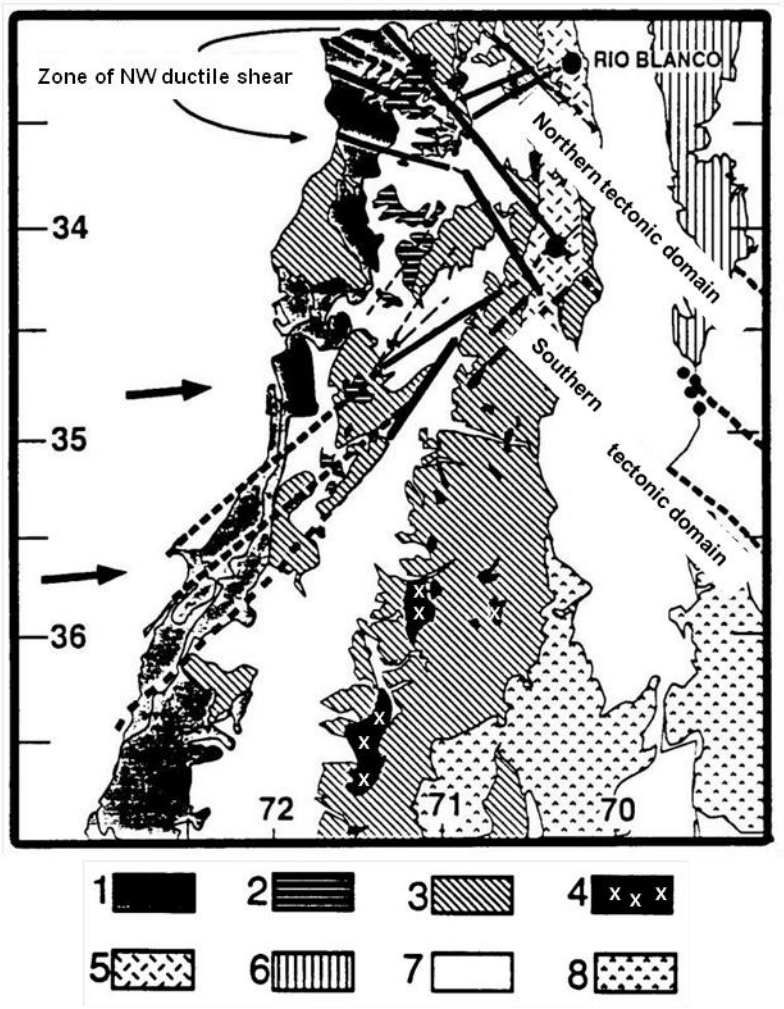

Figure 2.5. Main structures proposed by Garrido (1995) for central Chile. Black arrows show the plate convergence direction. 1: coastal batholith; 2: Jurassic intrusives; 3: Cretaceous and Lower Tertiary rocks; 4: Tertiary intrusives; 5: Miocene volcanism; 6: Frontal Cordillera; 7: Principal Cordillera; 8: basaltic Quaternary volcanism.

2.6 Quaternary geology of central Chile

The Quaternary of central Chile is characterized by relatively slow uplift rates in the Chilean Andes as deformation migrated to the eastern foreland in Argentina (Farías et al., 2010) and by the establishment of a weak N-S compressional regime associated with strike-slip movements in seismically-active segments of the El Fierro fault, at the eastern margin of the Abanico Basin (Garrido, 1995; Lavenu and Cembrano, 1999, 2008; Farías et al., 2006, 2010). Farías et al (2008) suggested that the migration of shortening to the foreland was caused by the high elevations reached by the Main Cordillera during the Pliocene. Vertical stress would have been large

enough to inhibit horizontal contraction and reverse faulting, resulting in the present-day strike-slip kinematics of the N-striking faults like the El Fierro fault demonstrated by the focal mechanisms reported for shallow earthquakes.

During the Quaternary a new volcanic arc was established in the Eastern Main Cordillera (Fig. 1.2B). In central Chile there are eight recognized composite stratovolcanoes. Three of them are active; they are, from north to south, the Tupungato-Tupungatito, San Jose and Maipo volcanoes (Fig. 1.2B). These late Pleistocene to Holocene volcanoes are built on top of an older chain of mid-Pleistocene volcanic edifices, which are named, from north to south, the Nevados de Piuquenes, Marmolejo, Castillo, Diamante Caldera, Listado and Picos del Barroso centres (Stern et al., 2007). All of these older volcanic centres are glacially-eroded and partially collapsed stratovolcanoes, with the exception of the Diamante Caldera. The formation of this giant (15 x 20 km) middle Pleistocene caldera was associated with the evacuation of 450 km^3 of rhyolitic pyroclastic material, which covered the entire Central Depression with the >30-m-thick Pudahuel Ignimbrite (Stern et al., 1984).

2.7 Summary

- The oldest rocks in central Chile crop out in the Coastal Cordillera, and are metamorphosed late Paleozoic fore-arc sediments and intrusive rocks associated with active subduction on the western margin of Gondwana.

- During the Triassic subduction was interrupted. This period is associated with lower crust melting, formation of large volumes of silicic magmas and subsidence along NW to NNW-trending basins. This basin orientation probably reflects the trend of Proterozoic and Paleozoic suture zones formed after collision of continental blocks with the western margin of Gondwana.

- In the Middle Jurassic subduction was active again in the western margin of Gondwana. Two marine transgression-regression cycles have been recognized between the Middle Jurassic and the Early Cretaceous. This period is characterized by Mariana-type subduction, with an island arc

located in the present day Coastal Cordillera, and an ensialic back-arc sedimentary basin in the present location of the Main Cordillera. The magmatic arc of this period is related to the formation of manto-type Cu deposits located along NW-NNW structures, which were probably inherited Triassic basin-margin faults.

- During the late Early Cretaceous the Atlantic Ocean began to open. This period is associated with compression and deformation in the western margin of South America, related with a transition from Mariana-type to Chile-type subduction. The magmatic arc was located in the present-day Central Depression.

- The late Eocene to early Miocene was characterized by the formation of the Abanico Extensional Basin, an intra-arc, N-trending volcano-tectonic basin filled with up to 3 km of volcanic and sedimentary rocks. During this period the volcanic axis was located in the western Main Cordillera.

- The early Miocene to early Pliocene period was characterized by inversion and deformation of the Abanico Extensional Basin. Magmas were trapped in the upper crust to form plutons and batholiths, and there was a marked decrease in the amounts of magma erupted at the surface.

- The final pulses of the Tertiary magmatic arc during the late Miocene-early Pliocene were associated with the formation of the porphyry Cu-Mo belt of central Chile, which includes the two largest concentrations of Cu and Mo in the world. Regional-scale geological mapping and deposit-scale structural studies suggest that arc-oblique, NW-NNW- and NE-striking structures are dominant in the porphyry Cu-Mo districts.

- After the formation of the porphyry Cu-Mo deposits, magmatic activity stopped in the Western Main Cordillera. A new volcanic arc was established during the Pleistocene in the Eastern Main Cordillera. It has remained active until the present day, forming the northern end of the South Volcanic Zone of the Andes.

Chapter 3 Structural Evolution of the Rio Blanco-Los Bronces District, Andes of Central Chile: Controls on Stratigraphy, Magmatism and Mineralization

3.1 Introduction

The Andes of central Chile host a belt of late Miocene to early Pliocene porphyry deposits, which includes three giant Cu and Mo ore bodies: from north to south, Los Pelambres-El Pachon, Rio Blanco-Los Bronces and El Teniente (Fig. 2.3; Sillitoe and Perello, 2005; Maksaev et al., 2007). With 206.7 Mt of contained copper, the Rio Blanco-Los Bronces cluster is the largest known concentration of this metal in the world (Irarrazaval et al., 2010; Sillitoe, 2010; Toro et al., 2012), and consists of several mineralized centers aligned in a NNW orientation (Irarrazaval et al., 2010; Toro et al., 2012).

The late Miocene to early Pliocene deposits of central Chile are contained within the inverted Abanico Basin, an intra-arc volcano-tectonic basin of Tertiary age (Fig. 1.2B). Segments of the main basin-margin fault systems have been identified and described previously (e.g., Charrier et al., 2002; Farias et al., 2010; Fig. 1.2B), but the structures controlling the internal basin geometry and its relationship with magma and hydrothermal fluid flow still remain enigmatic. Intra-basin fault systems are of crucial importance for the Rio Blanco-Los Bronces and the El Teniente deposits, as they are localized close to the centre of the basin, tens of kilometers away from the inverted basin-margin faults (Fig. 1.2B). In this chapter the problem of the structural controls on the emplacement of the Rio Blanco-Los Bronces cluster is addressed, proposing a model that relates the internal architecture of the inverted Abanico Basin with Mio-Pliocene magmatic and hydrothermal activity. This study is based on the results of new 1:10,000 and 1:25,000 geological and structural mapping and the construction of four E-W cross-sections across the entire Rio Blanco-Los Bronces district (Figs. 3.1, 3.2).

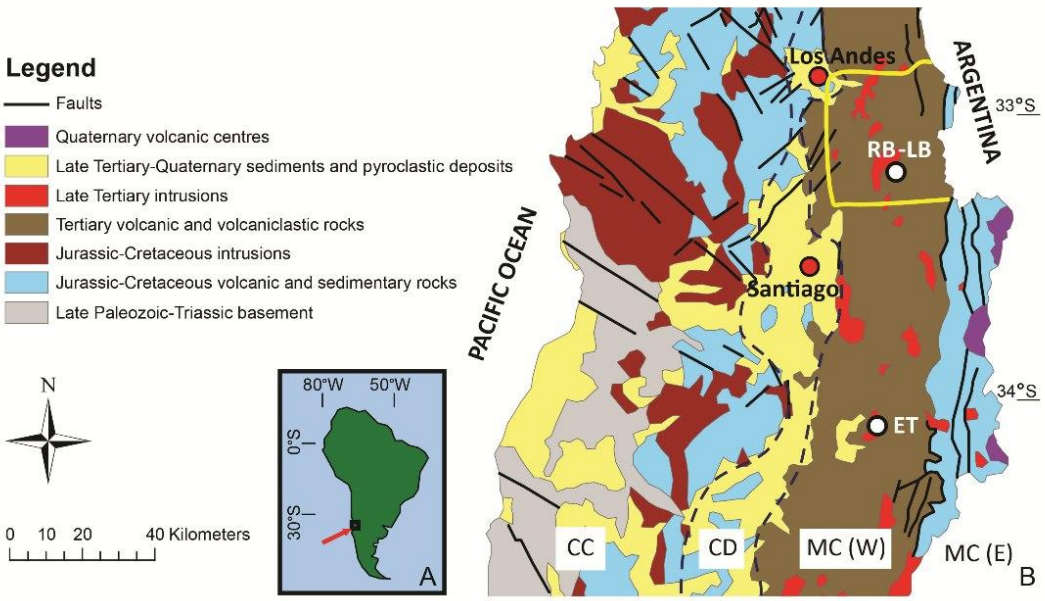

Figure 3.1. A. Location of the Rio Blanco-Los Bronces district in South America. B. Simplified geology of Central Chile, showing the location of the porphyry copper deposits (RB-LB = Rio Blanco-Los Bronces, ET = El Teniente) and the main geomorphological units (CC = Coastal Cordillera, CD = Central Depression, MC (W) = Western Main Cordillera, MC (E) = Eastern Main Cordillera). The Rio Blanco-Los Bronces district is outlined in yellow. Modified from SERNAGEOMIN (2002).

3.2 Tectonic setting: the South American margin of central Chile

The Rio Blanco-Los Bronces district is located in a major transition zone between two different segments of the Andean subduction system (Mpodozis and Ramos, 1989). To the south of the district is the Southern Volcanic Zone, associated with a normal subduction angle and active volcanism. To the north lies the Chilean flat-slab, characterized by a widening of the orogenic system and the absence of active volcanism (Kay et al., 1999). This transition zone coincides broadly with the subduction of the aseismic Juan Fernandez ridge, a buoyant feature in the subducting plate which some authors have proposed is directly related to establishment of flat subduction to the north and with generation of the appropriate conditions for the formation of giant porphyry Cu-Mo deposits (Yañez et al., 2002; Hollings et al., 2005).

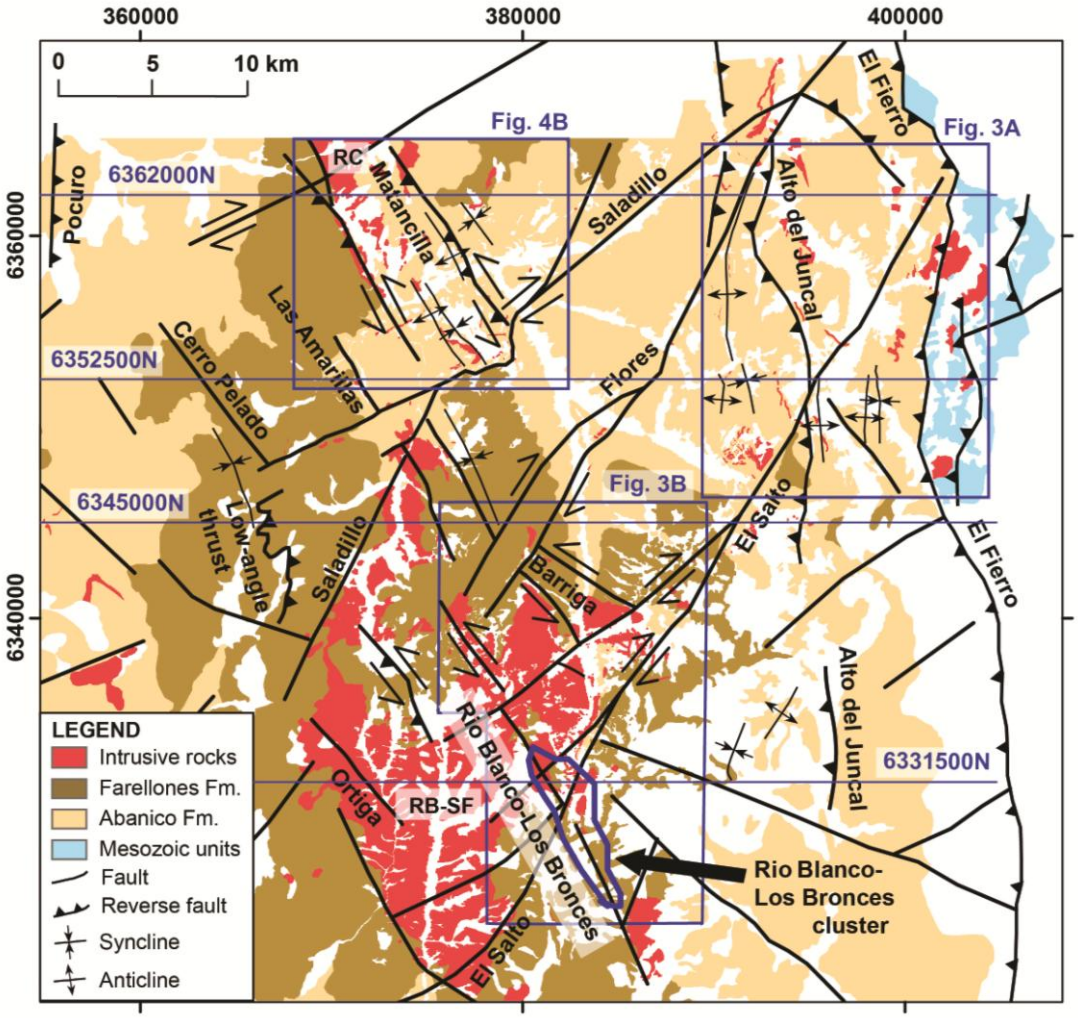

Figure 3.2. Simplified geological map of the Rio Blanco-Los Bronces district, showing the main fault systems and fold trends. The areas covered by the detailed maps of Figures 3.4 and 3.5 are shown, and the traces of the cross-sections presented in Figure 3.10 are also indicated. RC = Rio Colorado plutonic complex, RB-SF = Rio Blanco-San Francisco batholith.

The Rio Blanco-Los Bronces district is located within the Western Main Cordillera (Fig. 3.1), a N-trending morpho-tectonic domain composed of Eocene to Pliocene volcanic rocks and Miocene to Pliocene intrusive rocks. This Mio-Pliocene magmatism is genetically related to the formation of the porphyry Cu-Mo deposits of central Chile. The volcanic rocks of this domain were deposited during the opening and subsequent inversion of the intra-arc Abanico Basin. They have been grouped into the syn-extensional Abanico Formation (late Eocene to early Miocene) and the syn-inversion Farellones Formation (early to late Miocene; Charrier et al., 2002 and references therein).

Gana and Wall (1997) and Fuentes et al. (2002, 2004) reported several $^{40}Ar/^{39}Ar$ whole rock and plagioclase ages for Abanico Formation rocks in the western part of the Rio Blanco-Los Bronces district, all ranging between 34 and 21 Ma. The Tertiary volcanic rocks cover in unconformity Late Cretaceous volcanic deposits of the Lo Valle Formation (Gana and Wall, 1997). For the basal part of the Farellones Formation, Aguirre et al. (2000) reported $^{40}Ar/^{39}Ar$ biotite and hornblende ages of 21.6 ± 0.2 and 20.1 ± 0.3 Ma from samples collected 12 km to the south of the Rio Blanco-Los Bronces district. Fuentes et al. (2002) obtained an age range of 21 – 18 Ma for this unit in the western part of the Rio Blanco-Los Bronces district based on $^{40}Ar/^{39}Ar$ ages (biotite and hornblende). The andesitic lava flows that host the intrusive units at the Rio Blanco-Los Bronces cluster were dated by Deckart et al (2005), obtaining an age range of 17 to 16 Ma (U-Pb in zircon).

Existing K-Ar and U-Pb ages show that plutonic activity in the Rio Blanco-Los Bronces district was continuous throughout the early to middle Miocene and broadly coeval with Farellones Formation volcanism (Warnaars et al., 1985; Deckart et al., 2005; Deckart et al., 2010).

The Miocene volcanic and plutonic units have been cut by subvolcanic porphyries and hydrothermal breccias of late Miocene-early Pliocene age, which are genetically and spatially related to the formation of the Rio Blanco-Los Bronces porphyry Cu-Mo cluster (Warnaars et al., 1985; Serrano et al., 1996; Vargas et al., 1999; Deckart et al., 2013). Available U-Pb zircon ages show that the emplacement of this subvolcanic magmatic-hydrothermal complex occurred between 7 and 4 Ma (Deckart et al., 2013).

3.3 Methodology

The structural model presented in this chapter is based on recently acquired stratigraphic, structural and geochronological data. Part of this information was collected during a long term, multi-scale geological mapping program carried out by Codelco between 2004 and 2010. The new data were integrated with previous mine geology information. The program involved mapping over 1,000 km^2 at 1:10.000 and 1:25.000 scale covering most of the Rio Blanco-Los Bronces district (Piquer, 2010). The characterization of lithological units in the field was complemented by

petrographic studies in thin sections. A simplified and updated version of the map produced by this program is shown in Figure 3.2. A more detailed version of this map is included within the map of the Andes of central Chile presented at 1:100,000 scale in Appendix VI.

Structural information was collected both during the mapping programs carried out by Codelco and during additional structural mapping campaigns completed for this work in 2012 and 2013. Structural data collected included strike and dip of fault planes, rake of striation and width of damage zone. Kinematic information was registered when present; the main kinematic indicators correspond to steps in syn-tectonic hydrothermal mineral fibers, P-only surfaces (Petit, 1987), displaced markers (stratigraphic horizons, fold axis, older fault planes) and drag folds. The total database for the Rio Blanco-Los Bronces district consists of 284 fault planes, 186 of which have reliable kinematic information associated.

Nine new U-Pb zircon ages are summarized in Table 3.1. They were obtained from surface samples of both volcanic and intrusives rocks outcropping in the Rio Blanco-Los Bronces district, in areas where no reliable crystallization ages were available. Three of the samples (135375, 135376 and 153119) were collected during the Codelco mapping programs and reported internally in Piquer (2010). The remaining six samples were collected during this study. They were analyzed by the LA-ICPMS method at the University of Tasmania, and their inverse concordia plots are presented in Figure 3.3. All geochronology sample locations are shown on Figures 3.4 and 3.5. The analytical procedures for the samples analysed during this study are described in Appendix IA, and the complete analytical results are presented in Appendix IB.

Table 3.1. U-Pb zircon age data for nine surface samples from the Rio Blanco – Los Bronces district.

Sample	N (UTM)	E (UTM)	Elevation	Geological unit	Method	Age (Ma) (±2σ)
135375	6334910	384871	3956	Farellones Fm., middle member	U-Pb CA-TIMS	16.879 ± 0.045
135376	6352317	378509	3187	Farellones Fm., lower member	U-Pb SHRIMP	22.7 ± 0.4
153119	6338366	376928	3187	Syenogranite	U-Pb SHRIMP	16.39 ± 0.15
AN12JP008	6336679	380467	3248	Rio Blanco Granodiorite	U-Pb LA-ICPMS	11.68 ± 0.26
AN12JP010	6361560	369510	1110	Farellones Fm., lower member	U-Pb LA-ICPMS	21.73 ± 0.27
AN12JP011	6360516	370859	1084	Rio Colorado granodiorite	U-Pb LA-ICPMS	21.76 ± 0.53
AN12JP014	6357436	377110	1444	Abanico Fm.	U-Pb LA-ICPMS	25.06 ± 0.18
AN13JP013	6339076	385604	3122	Rhyolitic breccia	U-Pb LA-ICPMS	4.69 ± 0.22
AN13JP014	6336371	379886	3337	Andesitic porphyry	U-Pb LA-ICPMS	9.23 ± 0.33

3.4 Results

3.4.1 Stratigraphy

The new geological map of the district (Figs. 3.4, 3.5) presents the Abanico and Farellones formations subdivided into three different facies: lava flows, pyroclastic deposits and volcano-sedimentary deposits. In the Abanico Formation, these facies are highly discontinuous and commonly fault-bounded, although it is notable that both the pyroclastic and the volcano-sedimentary intercalations are more common and thicker towards the upper parts of the unit (Fig. 3.6). From our geological map and cross-sections, we estimate a minimum thickness of 5 km for the entire Abanico

Formation, which is almost twice the thickness previously estimated for this unit (Charrier et al., 2002). The pyroclastic and volcano-sedimentary intercalations reach a combined thickness of up to 800 meters (Fig. 3.6). One pyroclastic flow belonging to the thickest and most continuous of these intercalations was dated at 25.06 ± 0.18 (U-Pb in zircon, this study; Table 3.1, Figs. 3.3, 3.5, sample AN12JP014).

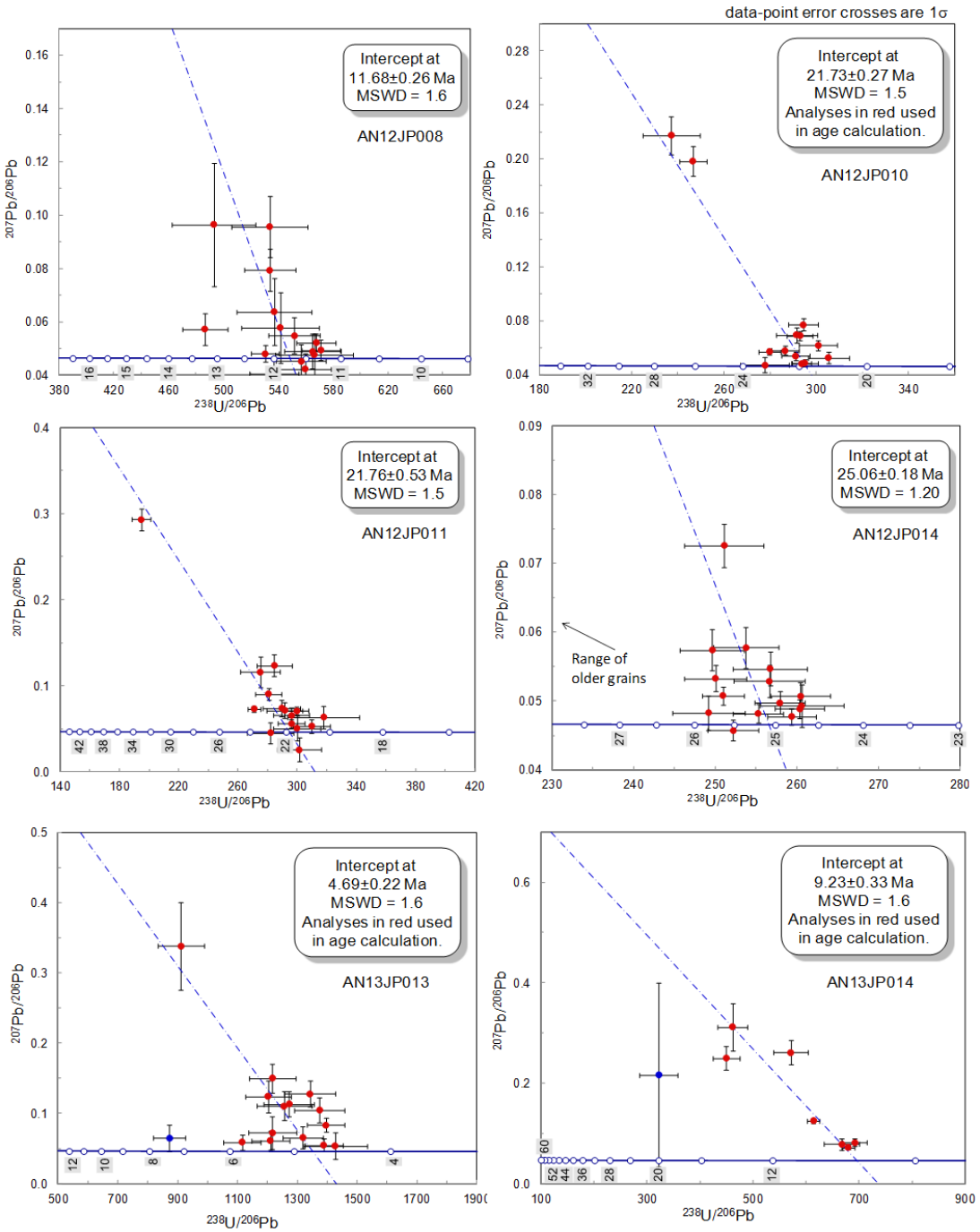

Figure 3.3. Inverse concordia plots for six U-Pb analyses from the Rio Blanco-Los Bronces district. Numbers on the reference concordia traces are millions of years.

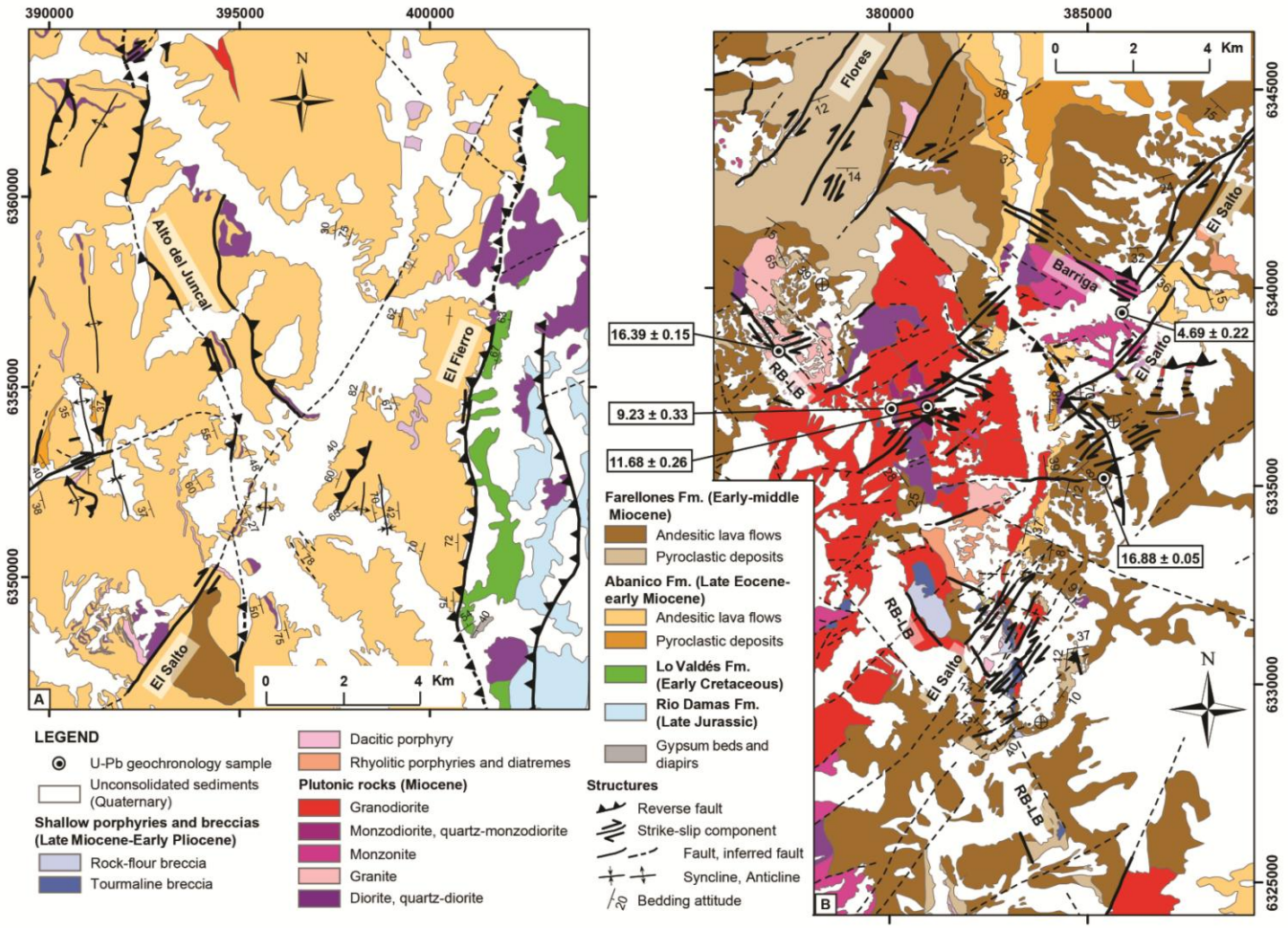

Figure 3.4. Geological maps of two sectors of the Rio Blanco-Los Bronces district. The main high-angle fault systems are labeled. A. Geology of the easternmost part of the district, where the contact between Mesozoic and Cenozoic units is exposed. B. Geology of the eastern margin of the Rio Blanco-San Francisco batholith, where the hydrothermal breccia complexes associated with the Rio Blanco-Los Bronces cluster were emplaced. RB-LB = Rio Blanco-Los Bronces fault system.

In the commonly subhorizontal Farellones Formation, it is possible to distinguish three well defined members (Figs. 3.4B, 3.5B, 3.6): a lower pyroclastic sequence deposited in progressive unconformities over Abanico Formation rocks; a middle member composed of andesitic lava flows with minor, lenticular volcano-sedimentary intercalations; and an upper pyroclastic sequence intercalated with andesitic lava flows.

The lower pyroclastic member of the Farellones Formation reaches a maximum thickness of 600 meters in the northern and western parts of the study area, diminishing in thickness to the south and east until it finally disappears a few kilometers north of the Rio Blanco-Los Bronces cluster (Figs. 3.4B, 3.6). Here we report the first two U-Pb zircon ages obtained from this pyroclastic member, yielding 22.7 ± 0.4 and 21.73 ± 0.27 Ma (Table 3.1, Figs. 3.3, 3.5B, 3.6, samples 135376 and AN12JP010). The first one is the oldest age obtained so far from rocks of the Farellones Formation. Because of its distinctive lithology and angular discordance with the underlying Abanico Formation, this member, when present, is an unmistakable stratigraphic marker.

The middle andesitic member of the Farellones Formation is the stratigraphic level at which the Rio Blanco-Los Bronces porphyry cluster was emplaced (Fig. 3.4B). The thickness of this member is up to 800 meters (Fig. 3.6), and it lies conformably over the lower pyroclastic sequence. A ~17 Ma age was reported for this member at the Rio Blanco deposit (Deckart et al., 2005). This age has been confirmed from a more distal location by a new U-Pb age of 16.88 ± 0.05 Ma (Table 3.1, Figs. 3.4B, 3.6, sample 135375).

The upper pyroclastic member of Farellones Formation has a minimum thickness of 600 meters (Fig. 3.6). It lies conformably over the intermediate member. Its minimum age is given by andesitic dykes which cut the upper pyroclastic member, and which have been dated at 10.7 ± 0.6 Ma (K/Ar in whole rock; Rivera and Navarro, 1996). This implies a middle Miocene age for this unit.

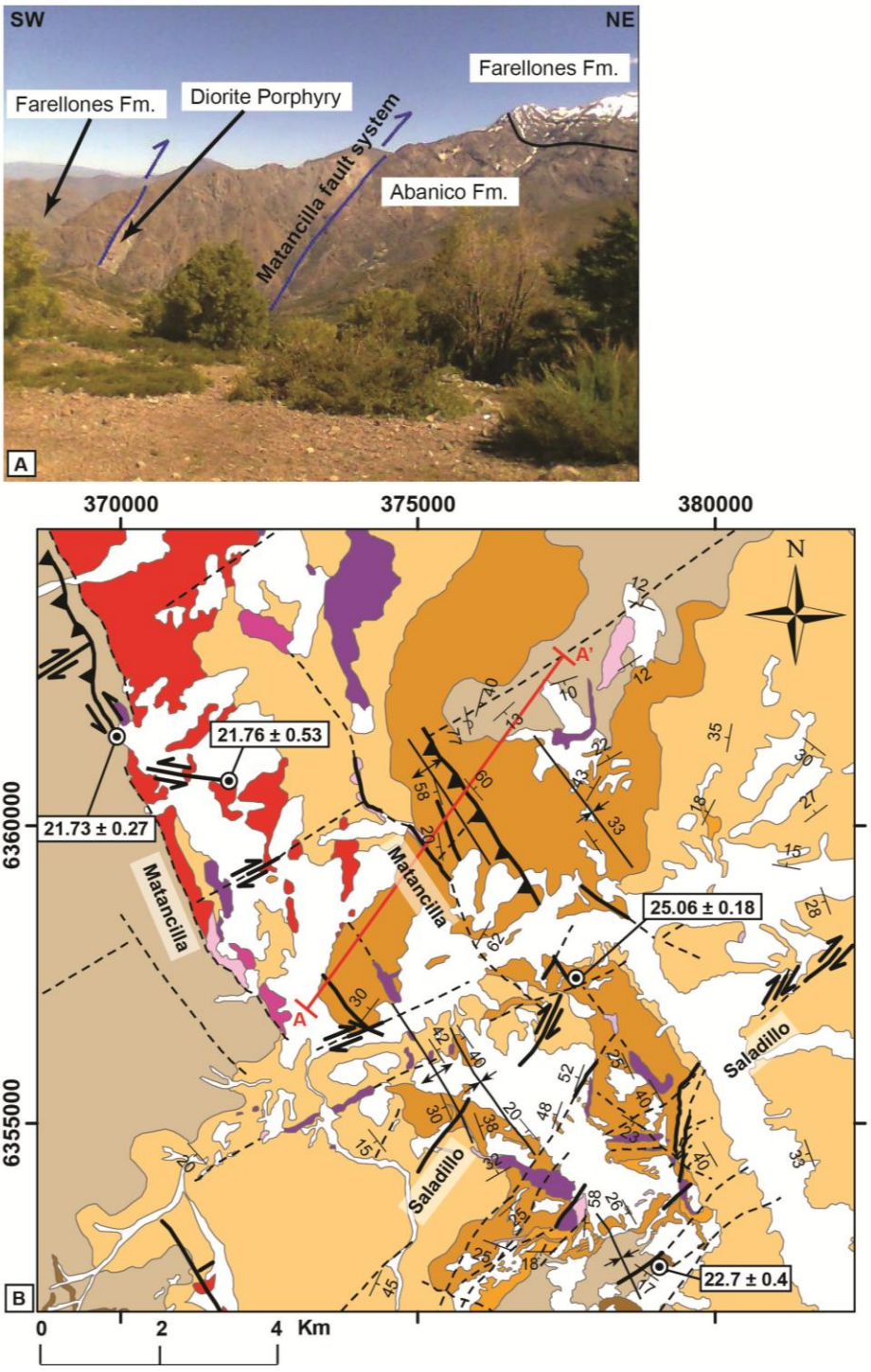

Figure 3.5. A. Branches of the E-vergent, NNW-striking Matancilla fault system that controlled the emplacement of dioritic porphyries of the Rio Colorado plutonic complex and folded both the Abanico and Farellones formations. The black line shows the folded unconformity separating the two volcanic units. The transition between the Abanico and Farellones formations is found at considerably lower elevations in the hanging wall, suggesting an earlier normal movement. View NW from 377317mE, 6354761mN. B. Geological map of the Rio Colorado plutonic complex and the area of intersection between the Matancilla and Saladillo fault systems. A-A' shows the field of view of (A).

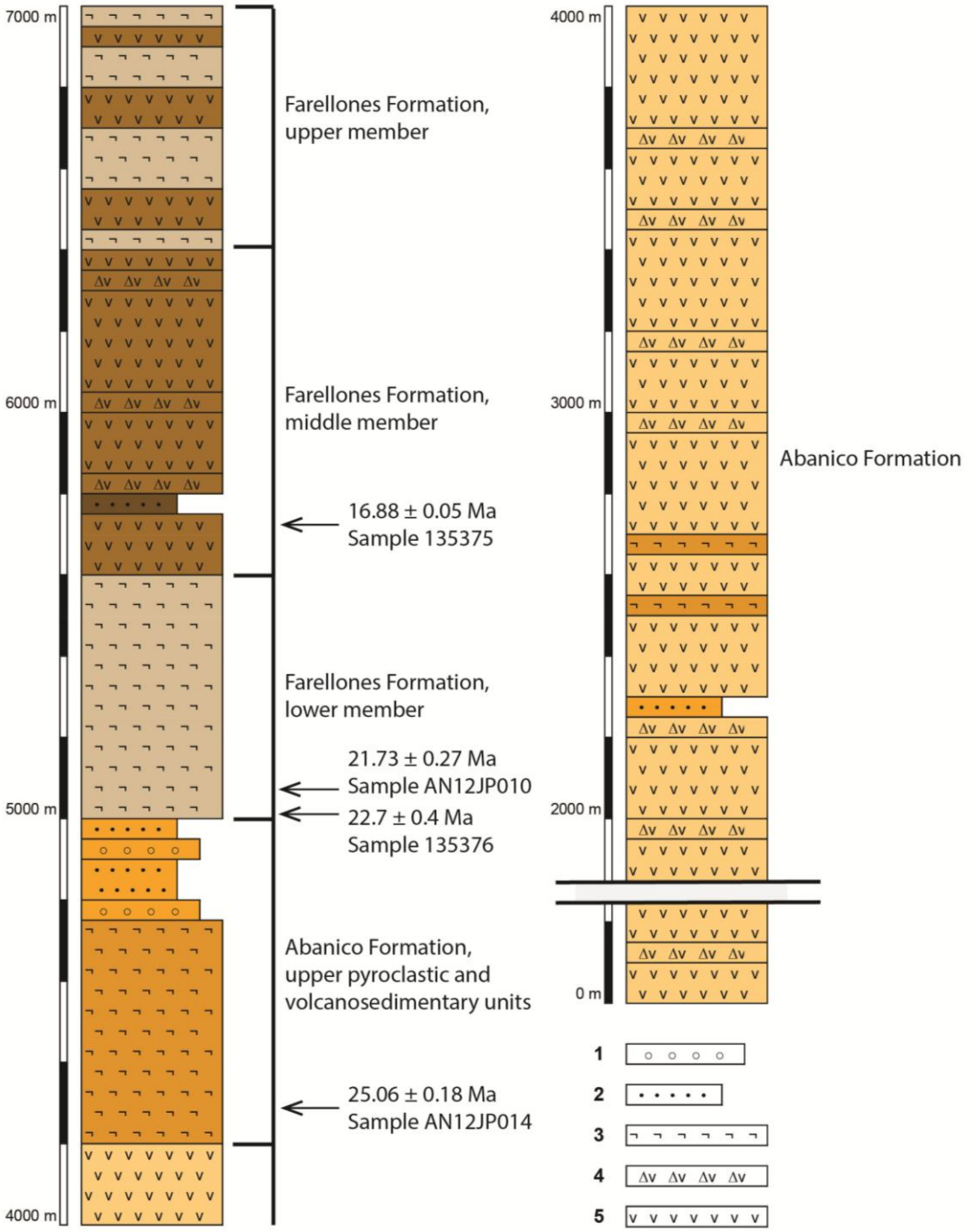

Figure 3.6. Generalized stratigraphic column of the Tertiary volcanic sequences in the Rio Blanco-Los Bronces district. Thicknesses shown in the figure correspond to maximum values. Key to rock types: 1 = volcaniclastic conglomerates, 2 = volcaniclastic sandstones, 3 = pyroclastic deposits, 4 = poorly sorted, angular debris-flow deposits; 5 = andesitic and basaltic-andesitic lava flows.

The basement of the Tertiary volcanic package is exposed in the easternmost part of the district, in the footwall of the N-striking, west-dipping El Fierro fault (Figs. 3.2,

3.4A). Two different Mesozoic units crop out: the older Rio Damas Formation, which is composed of continental sedimentary rocks of Late Jurassic age, and the younger Lo Valdes or its equivalent San Jose Formation, which is made up of fossiliferous marine limestones and calcareous sandstones of Early Cretaceous age (Fig. 3.4A).

Mesozoic rocks are also exposed about 10 km to the west of the study area (Figs. 1.2B, 3.1), in the footwall of the N-striking, east-dipping Infiernillo fault. These outcrops correspond to the Lo Valle Formation, a Late Cretaceous volcanic, mainly pyroclastic, continental unit (Gana and Wall, 1997; Fuentes et al., 2002).

3.4.2 Plutons and porphyries

Figure 3.2 shows that outcropping Miocene intrusions are concentrated along two belts. The main one is located in the central part of the inverted Abanico Basin, and has a strong spatial association with NNW-striking, W-dipping high-angle faults with composite reverse and sinistral strike-slip movements. A second, minor belt is located at the eastern part of the district and is spatially related with the El Fierro fault and other parallel, N-striking reverse faults. Between these two major intrusive belts, only minor subvolcanic bodies occur. They were emplaced along NE-striking faults, and their compositions range from basaltic-andesitic to rhyodacitic. The plutons of the westernmost intrusive belt can be grouped in two batholiths: the Rio Blanco – San Francisco batholith in the central and southern parts of the district and the Rio Colorado plutonic complex in its northern area (Fig. 3.2).

Rio Blanco-San Francisco batholith: this is the largest intrusive complex in the Rio Blanco-Los Bronces district. In plan view it has a rhombic shape, with its margins trending NW-NNW and NE-NNE (Fig. 3.2). Its N-S axis is nearly 30 km long, while its E-W axis is about 20 km. It is hosted by the Abanico Formation volcanic rocks and the lower and middle members of the Farellones Formation.

The roof of the batholith is preserved in several localities as a subhorizontal intrusive contact with the overlying Farellones Formation, which covers parts of the batholith obscuring its complete extent in map view (Fig. 3.2). The western and eastern contacts of the batholith show local steps and variations in orientation, but on

average they dip moderately (~30°) away from the central part of the intrusive complex.

Based on lithology, petrography and geochronology, fourteen different facies have been recognized within the batholith. The oldest units are early Miocene coarse grained, equigranular granodiorites, quartz-monzonites (minimum age 20.1 Ma, K-Ar in hornblende; Warnaars et al., 1985), diorites and syenogranites (16.39 ± 0.15, U-Pb in zircon, this study; Table 3.1, Fig. 3.4B, sample 153119). Existing geochronological data shows that emplacement of these phases was coeval with the deposition of the lower and middle members of the Farellones Formation (Table 3.1).

The oldest intrusive units are cut by a set of younger, middle Miocene equigranular to coarse- porphyritic plutons of dioritic, monzonitic, quartz-monzonitic and granodioritic composition. The ages of these intrusive units range from 14.7 ± 0.1 (U-Pb in zircon, Deckart et al., 2010) to 8.16 ± 0.45 Ma (U-Pb in zircon, Deckart et al., 2005) and they are coeval with early, non-economic phases of hydrothermal alteration and mineralization in the district (15-8 Ma, $^{40}Ar/^{39}Ar$ ages in sericite, biotite and hypogene alunite, Toro et al., 2012). Some of these plutons, such as the Rio Blanco and Cascada granodiorites (11.96 ± 0.40 and 8.40 ± 0.23 Ma respectively; U-Pb in zircon, Deckart et al., 2005), host part of the Cu and Mo mineralization in the Rio Blanco – Los Bronces cluster. The Cascada granodiorite is restricted to the mine area, but the Rio Blanco granodiorite extends at least 6-7 km to the NNW of the cluster, as demonstrated by a new U-Pb zircon age of 11.68 ± 0.26 Ma (this study; Table 3.1, Figs. 3.3, 3.4B, sample AN12JP008), identical within error to the ages obtained in the mineral deposits (11.96 ± 0.40 Ma; Deckart et al., 2005).

The middle Miocene plutons are coeval with a family of subvertical andesitic dikes, which display both NE and NW preferred orientations. Rivera and Navarro (1996) obtained a K-Ar age range of 11-10 Ma for these dikes. Sample AN13JP014, also coming from an andesitic dike, gave an U-Pb LA-ICPMS zircon age of 9.23 ± 0.33 Ma (Table 3.1, Figs. 3.3, 3.4B). This dike is of particular interest as it intruded the Rio Blanco granodiorite after an event of sericitic alteration associated with the emplacement of tourmaline, specular hematite, quartz and sulfide veins, constraining the age of alteration and mineralization in the area to the 11-9 Ma range, about 3 m.y.

older than the Rio Blanco-Los Bronces cluster, but probably coeval with some of the unproductive hydrothermal centers of the district such as San Manuel and El Plomo (Toro et al., 2012).

The youngest intrusions in the batholith are late Miocene to early Pliocene dacitic to rhyolitic subvolcanic porphyries, diatremes and coeval hydrothermal breccias. The emplacement time range established for this subvolcanic complex is between 7.12 ± 0.19 and 4.69 ± 0.23 Ma (U-Pb in zircon; Deckart et al., 2013). Porphyries and breccias of this age range are temporally and genetically related with the mineralization at the Rio Blanco – Los Bronces cluster (Serrano et al., 1996; Vargas et al., 1999; Deckart et al., 2005). However, isolated early Pliocene rhyolitic porphyries have been identified emplaced along major fault systems as far as 11 km away from the mineral deposits. Sample AN13JP013 comes from one such porphyry, and gave a U-Pb LA-ICPMS zircon age of 4.69 ± 0.22 Ma (Table 3.1, Figs. 3.3, 3.4B), identical to the published ages for the La Copa rhyolitic complex in the Rio Blanco-Los Bronces cluster (4.69 ± 0.23 Ma, U-Pb in zircon; Deckart et al., 2013). The porphyry where this sample was collected is located more than 7 km to the NE of the La Copa complex, emplaced along the same NE-trending fault system (Fig. 3.4B).

Rio Colorado plutonic complex: this polyphase intrusive complex is located in the northern part of the study area (Fig. 3.2). Seven different intrusive facies have been recognized, all with a distinctive NNW-elongation, suggesting a structural control on their emplacement. This was most likely provided by the NNW-striking Matancilla fault system which extends between this plutonic complex and the Rio Blanco –San Francisco batholith to the SSE (Fig. 3.2). The first U-Pb age for the Rio Colorado plutonic complex was obtained for this study, and it indicates that an early, coarse-grained, equigranular granodiorite was emplaced at 21.76 ± 0.53 Ma (Table 3.1, Fig. 3.3, 3.5B, sample AN12JP011). This is the oldest age ever obtained in Tertiary plutonic rocks of central Chile, and is coeval with the lowermost pyroclastic flows of the Farellones Formation. This equigranular unit is cut by younger, amphibole and biotite-bearing dacitic and rhyolitic porphyries. A dacitic breccia from this suite of porphyries was dated by Munizaga and Vicente (1982) at 18.4 ± 1.4 (K-Ar in whole rock), providing a minimum age for this unit.

Eastern intrusive belt: is defined by several stocks, dikes and sills that show a strong spatial relationship with the El Fierro and Alto del Juncal faults (Figs. 3.2, 3.4A). They are composed of a series of equigranular to coarse porphyritic plutons of dioritic and granodioritic compositions, which are in turn cut by andesitic, dacitic and rhyodacitic subvolcanic porphyries. Montecinos et al. (2008) published two U-Pb zircon ages from intrusive rocks that crop out in the northernmost part of this belt. They obtained an 11.53 ± 0.19 Ma age for a granodiorite and 12.28 ± 0.15 Ma for a diorite (middle to late Miocene).

3.4.3 District-scale fault systems

High-angle fault systems recognized in the district can be grouped in three main sets, according to their orientation: NW-, NE- and N-striking. The first two sets are predominant in most of the study area, while the N-striking faults are restricted to the western and eastern inverted margins of the Abanico Basin (Fig. 3.2). Apart from these three sets of high-angle fault systems, locally there are low-angle detachments and ramp-flat thrust faults rooted in stratigraphic boundaries between contrasting packages of Tertiary volcanic rocks. All the individual faults mentioned in this section are labeled in Figure 3.2.

NW-striking fault systems: they occur in the central part of the district (Fig. 3.2). The general strike is N35°W, dipping 60-70°W. The strike of individual fault planes varies between N20°W and N60°W. Fault activity generated major drag folds, which indicate east-vergent reverse movements (Fig. 3.5A). Drag folds affected the Abanico Formation and the lower and middle members of the Farellones Formation (Fig. 3.5A), showing that their last reverse-reactivation increment was post-early Miocene. Steps in syn-tectonic hydrothermal mineral fibers coating fault planes indicate that the reverse movement was coupled with a sinistral strike-slip component. However, stratigraphic correlations indicating normal movements (Fig. 3.5A), together with the high dip angle of the fault planes, provide evidence that these structures correspond to reactivated normal faults.

It is possible to distinguish three main parallel NW-striking fault systems in both the northern and the southern parts of the district. The correlation along strike between these two groups of faults is not evident as their trace is obscured by syn-tectonic

magmatic and hydrothermal activity and by displacements of up to 400 meters along cross-cutting NE-striking faults (Fig. 3.2).

In the northern part of the district, three main faults can be distinguished, from west to east: the Cerro Pelado, Las Amarillas and Matancilla faults (Fig. 3.2). These faults are spatially associated with the emplacement of dikes and elongated stocks of both the northernmost Rio Blanco – San Francisco batholith and the Rio Colorado plutonic complex (Figs. 3.2, 3.5). The contacts between the plutons and their volcanic host rocks are rectilinear and located on strike of major faults (Figs. 3.2, 3.5) but they are of intrusive nature, without evidence of significant post-magmatic fault reactivations. The Matancilla fault is also related to major drag folds that affect strata of the Abanico Formation and the lower member of the Farellones Formation, indicative of reverse movement (Fig. 3.5A). However, stratigraphic correlations across the fault indicate an earlier normal movement (Fig. 3.5A). In the southern area, from west to east the Ortiga, Rio Blanco – Los Bronces and Barriga fault systems are recognized (Fig. 3.2). Rhyolitic domes were emplaced along the Ortiga fault in the south-western margin of the Rio Blanco – San Francisco batholith. The Rio Blanco – Los Bronces fault system (Castelli and Lara, 1999; Silva and Toro, 2009) extends both to the NNW and to the SSE of the Rio Blanco – Los Bronces cluster (Figs. 3.2, 3.4B). Steps in syn-tectonic tourmaline and actinolite fibers systematically indicate sinistral strike-slip movements, occasionally with a reduced reverse component. Subvolcanic porphyries and hydrothermal breccias of the cluster were emplaced along the central part of the fault system (Fig. 3.4B). Individual branches of the Rio Blanco – Los Bronces fault system controlled the emplacement of syn-tectonic hydrothermal biotite veins in late Miocene times (Silva and Toro, 2009) and have been recognized by mine geologists as the most prominent fault system in the Rio Blanco sector of the cluster (Skarmeta et al., unpub. report for CODELCO, 2004). The Barriga fault system forms the north-eastern margin of the Rio Blanco – San Francisco batholith (Fig. 3.2, 3.4B), and shows evidence of sinistral strike-slip movement with a smaller reverse component, according to steps in syn-tectonic actinolite fibers.

NE-striking fault systems: these fault systems have a general strike of N40°E, although the strikes of individual fault planes vary from N30° to N70°E. They generally dip at high angles to the NW, varying from 60° to 90°. These faults show a dextral strike-slip movement, with minor reverse dip-slip components (Fig. 3.7). They commonly displace NW- and N-trending faults and fold axis, such as the Matancilla and Alto del Juncal faults and their related fold trends (Figs. 3.2, 3.4A). The observed offsets are of up to 400 meters. As with the NW fault systems, the stratigraphic correlations across these faults generally indicate normal movements, showing they also correspond to reactivated normal faults. In the core of these faults, there are abundant zones rich in fault gouge and tectonic breccia, while in the damage zone there are abundant E-W vertical extensional structures filled mainly by quartz and calcite, which commonly occur in the transition to undamaged rock. The main faults are commonly surrounded by several individual fault planes displaying syn-tectonic hydrothermal minerals fibers of quartz, chlorite, epidote, calcite or tourmaline (Fig. 3.7D, E).

At least three individual major fault systems with NE strikes can be recognized across the Rio Blanco – Los Bronces district. Magmatic bodies and syn-tectonic hydrothermal veins have been emplaced along all of them (Fig. 3.7B, C, D, E). From north to south, they are the Saladillo, Flores and El Salto fault systems (Fig. 3.2). The Escondida fault, identified in the Los Bronces sector of the cluster by previous workers (Warnaars et al., 1985), is considered here as part of the El Salto fault system. Several individual faults belonging to this system have been recognized by mine geologists in the Rio Blanco and Sur Sur areas as well (Skarmeta et al., 2004). The average strike of fault planes within the El Salto fault system is N40°E, while the average dip is 70-80°NW. Across the district, several plutonic bodies and subvolcanic porphyries occur at the intersection of this fault system with the NW- and N-striking faults. Quartz and tourmaline veins with sericitic haloes, hydrothermal breccia dikes and dacitic and rhyolitic dikes were emplaced along different branches of the El Salto fault system (Fig. 3.7B, C). Some of these branches are the only faults that record evidence of post-mineral reactivation in the Rio Blanco – Los Bronces cluster, as they cross-cut the tourmaline-cemented mineralized hydrothermal breccias with displacements in the order of meters to tens of meters (Fig. 3.4B).

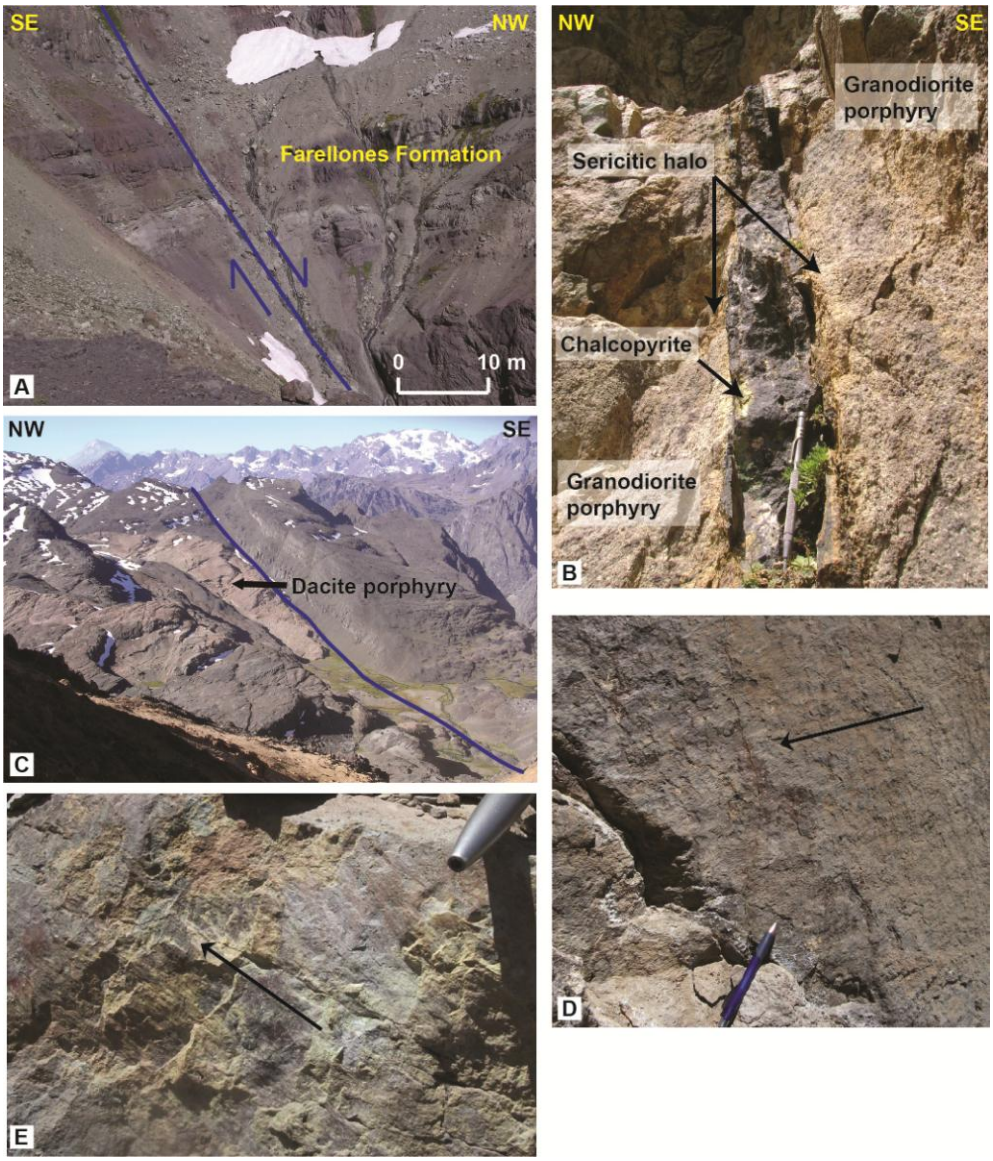

Figure 3.7. NE-striking fault systems in the Rio Blanco-Los Bronces district. A. Pyroclastic layers of the lower member of Farellones Formation displaced by strike-slip dextral movement along a N45°E fault, part of the Flores fault system at 380687mE, 6348584mN. The offset is approximately seven meters. B. Tourmaline-quartz-pyrite-chalcopyrite vein with sericitic halo and clasts of granodiorite porphyry emplaced along a N60°E-striking, subvertical fault. View NE at 383262mE, 6339743mN. C. Dacite porphyry emplaced along a N35°E structure, part of the Flores fault system. All the contacts of the porphyritic intrusion are of intrusive nature. View NE from 379198mE, 6342426mN. D. Main fault of the El Salto fault system at 386364mE, 6339053mN. The orientation of the fault plane is N40°E/80°NW and it displays syn-tectonic quartz and chlorite fibers indicating dextral strike-slip movement with a reduced normal component. Black arrow indicates sense of movement of the missing block. E. Fault plane belonging to the Saladillo fault system at 381485mE, 6357206mN. Orientation of the fault plane is N55°E/80°N. Steps in syn-tectonic epidote fibers indicate a dextral strike-slip movement with a minor reverse component. Black arrow indicates sense of movement of the missing block.

N-striking fault systems: in the eastern part of the study area, there is a system of east-vergent reverse faults striking N-S and dipping 55°-70°W, with some local, west-vergent back-thrusts (Figs. 3.2, 3.4A). The main faults of this system are the El Fierro and Alto del Juncal faults (Figs. 3.2, 3.4A). Miocene intrusive bodies have been emplaced along the trace of both of these faults (Figs. 3.2, 3.4A), without evidences of post-magmatic faulting. Between these two structures, the lava flows of Abanico Formation have been tightly folded in a series of east-vergent, overturned folds (Fig. 3.8A).

The El Fierro fault juxtaposes the Tertiary Abanico Formation hanging wall rocks to the west against the Mesozoic San Jose or Lo Valdes Formation footwall sedimentary rocks to the east (Fig. 3.8B). Bedding in the hanging wall is parallel to the fault. This structure was originally defined by Davidson (1971) in southern central Chile as a high angle reverse fault which juxtaposes Tertiary volcanic rocks (Piquer et al., 2010) on top of older Mesozoic sedimentary rocks. This structure has been correlated with equivalent faults exposed to the north of Davidson's (1971) original locality, where they have been given different names (Las Leñas and El Diablo faults, Charrier et al., 2002; Fock et al., 2006; Farias et al., 2010). Here we retain the original nomenclature, as the structure observed in our study area fits with the original definition given by Davidson (1971).

The faults associated with the western margin of the inverted Abanico Basin are almost entirely located outside the study area, with the exception of some outcrops in the north-west (Fig. 3.2) where the Pocuro fault can be observed. This structure strikes N-S and dips 60-80°E, and juxtaposes different andesitic packages of the Abanico Formation. The fault is associated with a trend of parallel folds in the Tertiary volcanic rocks and, outside of the study area, has controlled the emplacement of several intrusive bodies of small dimensions and variable textures and compositions (Castelli and Lara, 1999). The contact with the Late Cretaceous rocks of the Lo Valle Formation is located further west, associated with the Infiernillo fault (Fig. 1.2B; Fuentes et al., 2002; Farias et al., 2010).

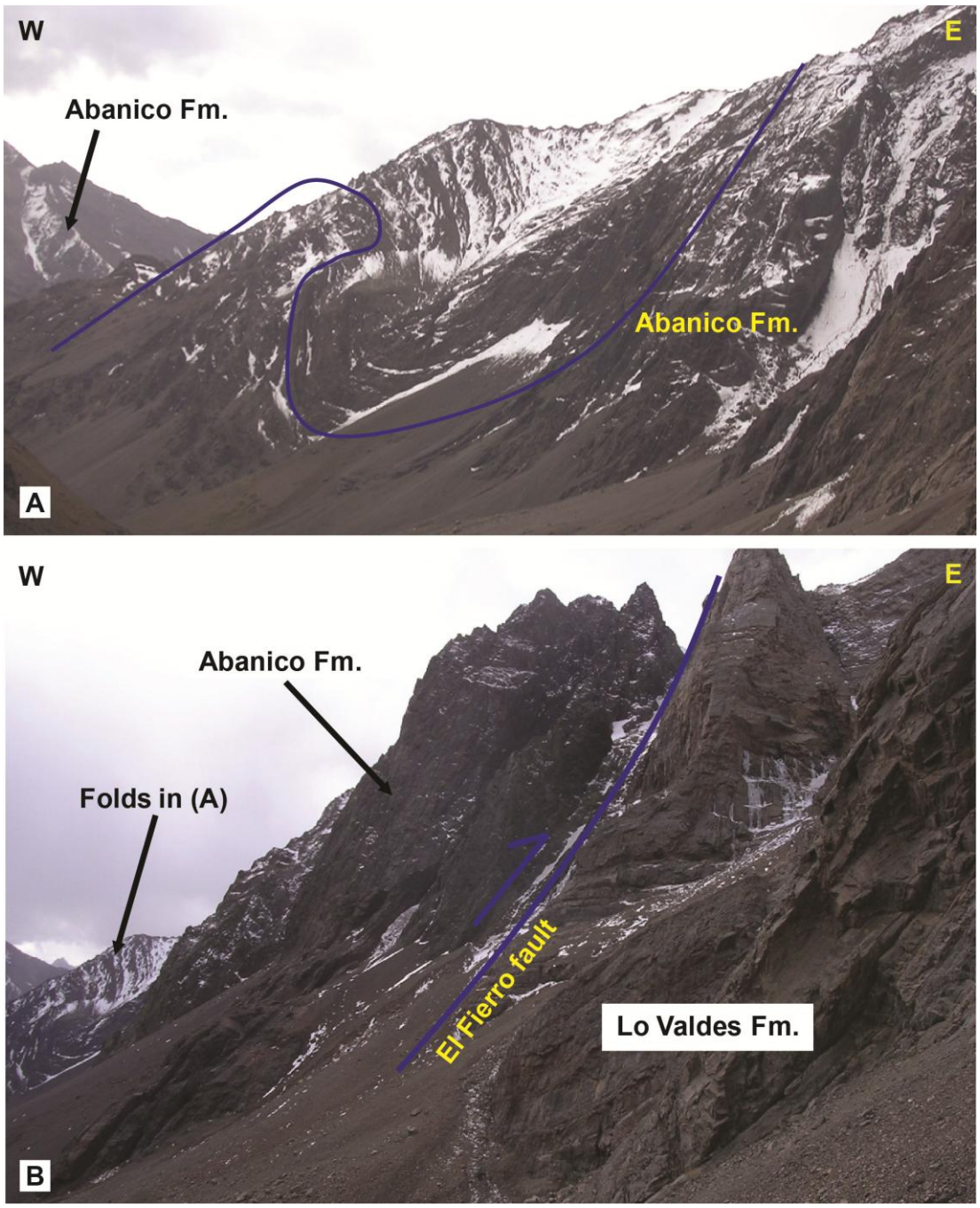

Figure 3.8. Deformation style at the inverted eastern margin of the Abanico Basin. A. East-vergent anticline-syncline pair affecting Abanico Formation lava flows. View N from 399397mE, 6349379mN. B. Immediately to the east of (A), the Tertiary volcanic rocks are in fault contact with Mesozoic limestones of the Lo Valdes Formation along the El Fierro fault. View N from 400682mE, 6348304mN.

Detachments and ramp-flat thrusts: local low-angle thrusts detachments are developed in stratigraphic contacts within the Tertiary volcanic sequence. The most continuous of these faults occurs in the western part of the district (Fig. 3.2), where

the middle andesitic member of Farellones Formation is detached from the lower pyroclastic member by a west-vergent thrust, which propagates upwards forming a ramp which repeats the middle member (Fig. 3.9).

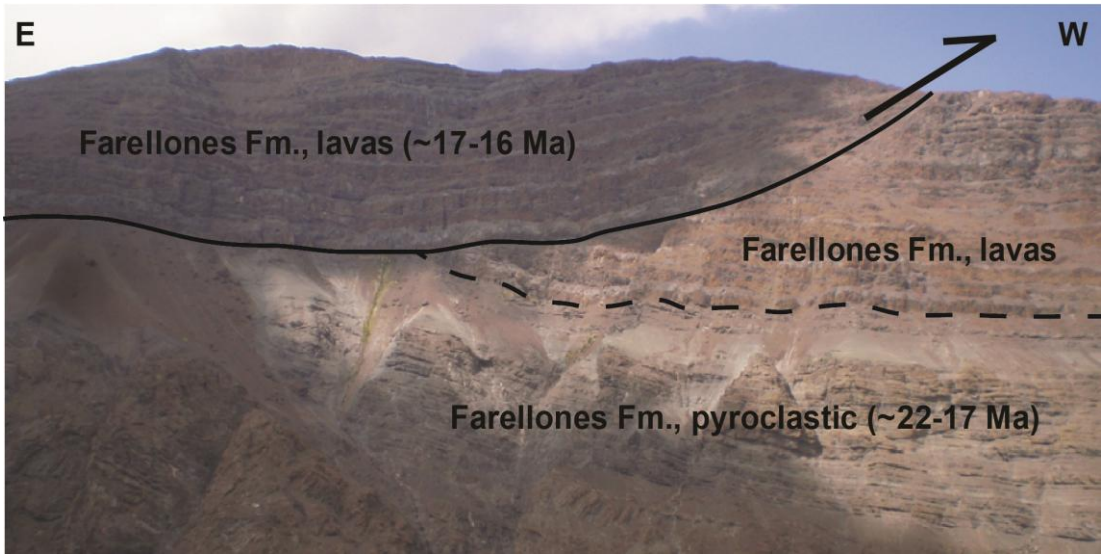

Figure 3.9. Ramp-flat fault in the Farellones Formation (solid black line). Andesitic lavas of the middle member are detached from the lower pyroclastic member, and are repeated by a west-vergent ramp. Dashed line represents the contact between the two members. Aerial view S from 366600mE, 6346600mN.

3.4.4 Cross-sections

Based on the new geological map of the Rio Blanco-Los Bronces district a set of four E-W structural cross-sections across the area were prepared, with the southernmost one passing through the porphyry deposits (Fig. 3.10; 1:100,000 scale cross-sections are included in Appendix VI). Interpretation of the deep geometry of these cross-sections was aided by unpublished Codelco geophysical information (aeromagnetic, seismic and gravimetric data) and correlation with published cross-sections of the Argentinean flank of the Andes (Ramos, 1996; Giambiagi et al., 2003b, 2012), where the different detachment levels that are inferred to be present in the Chilean side, below the Rio Blanco-Los Bronces district, are well exposed. Three main Miocene detachment levels are proposed here. The lowermost is an intra-basement detachment, while the two upper ones coincide with the inferred stratigraphic location of Mesozoic evaporites (Fig. 3.10). The thicknesses of the different Mesozoic units below the Abanico Basin were estimated from their observed

thicknesses both to the east and to the west of the basin, based on our own observations and on the published descriptions of the Mesozoic stratigraphy (Thiele, 1978; Rivano et al., 1995; Wall et al., 1999).

The cross-sections show a very consistent pattern of deformation in the inverted Abanico Basin. The maximum thickness of the Abanico Formation is preserved along the axis of two broad synclines where it reaches up to 5 km. The synclines are located to the west and east of the Matancilla – Barriga and Las Amarillas – Rio Blanco – Los Bronces fault systems, which cut through the central part of the inverted basin (Fig. 3.10). The folds affecting the Abanico Formation between the Pocuro and Alto del Juncal faults are open, with wavelengths of several kilometers, with the exception of the localized tight east-vergent, fault-propagation folds in the vicinity of the aforementioned NW fault systems. This deformation style changes abruptly to the east of the Alto del Juncal fault, as from this structure to the El Fierro fault, the Abanico Formation is affected by an east-verging sequence of tight, locally isoclinal, N-trending folds (Fig. 3.8). The inferred thickness of the Abanico Formation within this block is less than 2 km. We propose that the main basin-margin fault in this area is the Alto del Juncal fault. The El Fierro fault is interpreted as a reverse fault which detaches the base of the Tertiary volcanic column from the underlying Mesozoic rocks and is linked at depth with the Alto del Juncal fault (Fig. 3.10). This is consistent with the fact that the El Fierro fault is always parallel to bedding in the overlying Abanico Formation rocks (Fig. 3.8B).

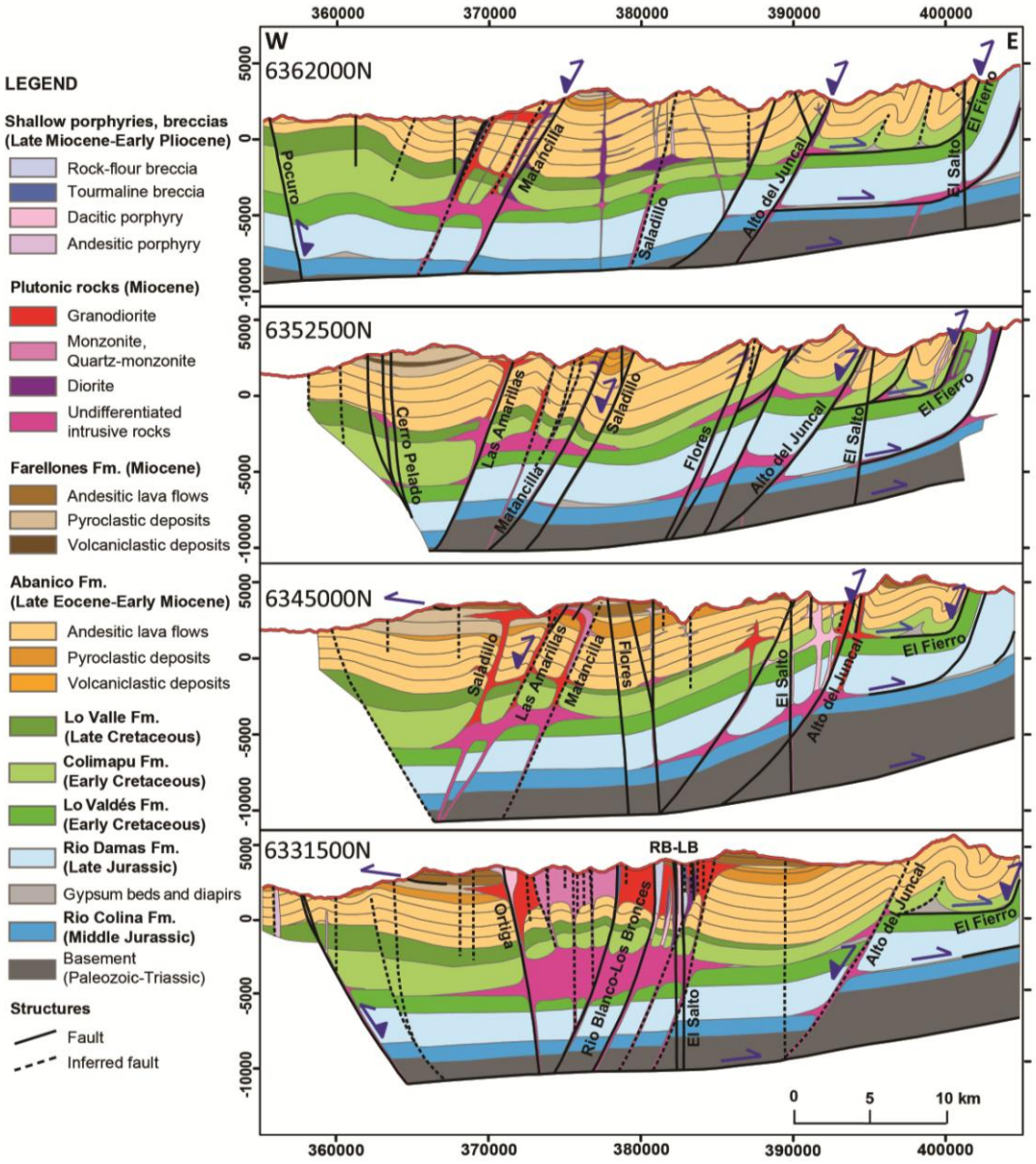

Figure 3.10. East-west cross-sections, looking north, across the Rio Blanco-Los Bronces district. The southernmost section (6331500N) contains the porphyry deposits of the Rio Blanco-Los Bronces cluster (RB-LB).

3.5 District-scale structural model

3.5.1 Structural controls on deposition and deformation of stratigraphic sequences

Structurally-controlled facies and thickness changes within the Tertiary stratigraphic units are common in the Rio Blanco-Los Bronces district. In the central and western parts of the district, the structures that bound contrasting volcanic and sedimentary

sequences are always orogen-oblique, NE and NW-striking fault systems (Figs. 3.2, 3.4B, 3.5B, 3.10). In the eastern part of the district, there are major thickness changes associated with the N-striking Alto del Juncal fault (Fig. 3.10). Fold axis orientations follow this same pattern, with a major NW-NNW fold trend and minor NE trending folds in the central and western parts of the district (Figs. 3.2, 3.5B), and N-trending folds in the eastern sector (Fig. 3.2, 3.4A).

The northern part of the district, where the Matancilla fault is interrupted by the Saladillo fault (Fig. 3.2, 3.5B), provides a good example of structurally-controlled facies and thickness changes and fault-related folds. The Matancilla fault system is NW-striking and dips 60-70° to the SW, while the Saladillo fault system strikes to the NE and dips 60-70° to the NW. The oldest rocks in the area are andesitic and basaltic-andesitic lava flows of the Abanico Formation. Lava flows of identical composition have been dated in the western part of the district. They have an $^{40}Ar/^{39}Ar$ (whole rock and plagioclase) age range of 34 to 28 Ma (late Eocene to Oligocene; Gana and Wall, 1997; Fuentes et al., 2004). In the hanging wall of the Saladillo fault system, these andesitic flows are covered by up to 800 meters of pyroclastic rocks dated at 25.06 ± 0.18 (this study, LA-ICPMS U-Pb in zircons; Fig. 3.2, Table 3.1, sample AN12JP014). The pyroclastic rocks are not present in the footwall, to the SE of the fault (Fig. 3.11). In the hanging wall these pyroclastic deposits are affected by an incipient syncline (Fig. 3.11). This structural geometry provides evidence that they were deposited syn-tectonically in a fault-bounded depocenter, with space being created by normal subsidence accommodated by the Saladillo fault. Because of its syn-extensional deposition and its age we assign these pyroclastic rocks to the Abanico Formation.

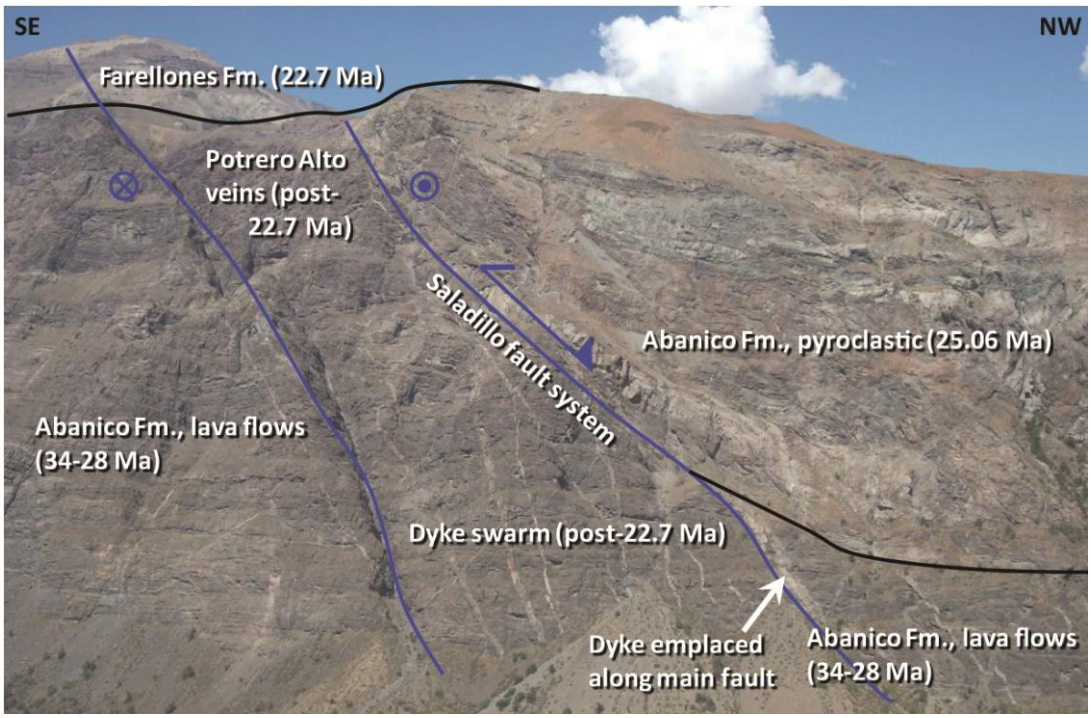

Figure 3.11. View of the NE-striking Saladillo fault system. About 800 metres of Abanico Fm. pyroclastic rocks were accumulated in a tectonic basin to the NW of the fault system. The same structures were later reactivated as dextral-reverse faults, and controlled the emplacement of andesitic and dacitic dikes and the Potrero Alto veins. Blue lines represent faults and black lines show stratigraphic contacts. View SW from 380995mE, 6357149mN.

The pyroclastic rocks are covered by volcano-sedimentary deposits that were not affected by normal faulting. Instead, they were accumulated syn-tectonically along the axis of a NNW-trending syncline developed in the pyroclastic sequence of the Abanico Formation at the footwall of the E-vergent Matancilla reverse fault (Fig. 3.12). This reflects a change in tectonic regime, from extension during deposition of the Abanico Formation pyroclastic rocks, to compression during deposition of the volcano-sedimentary deposits. This volcano-sedimentary sequence is then interpreted to represent a transitional unit between the Abanico and Farellones formations, marking the first pulse of compressive deformation affecting this part of the Andes. All of the previously described rocks are covered by sub-horizontal pyroclastic flows of the lower Farellones Formation (Figs. 3.11, 3.12), which were dated in this locality at 22.7 ± 0.4 Ma (early Miocene; Fig. 3.5B, Table 3.1, sample 135376).

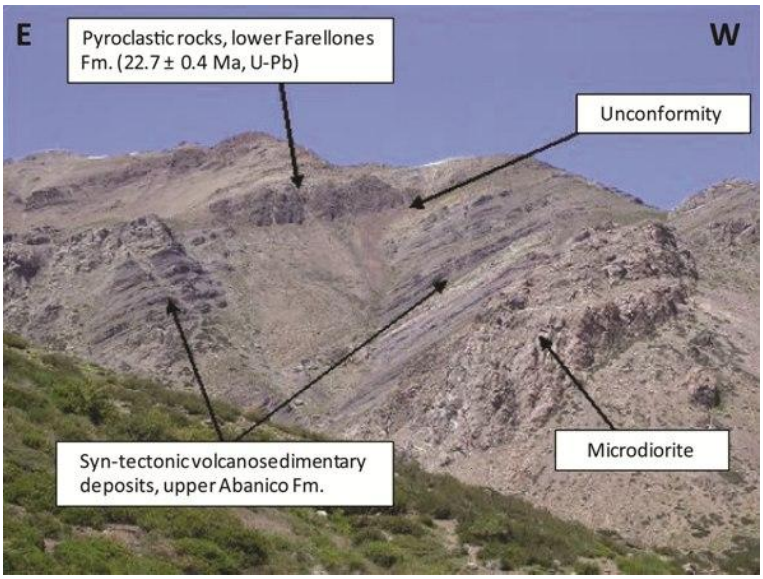

Figure 3.12. Growth strata in volcano-sedimentary deposits at the transition between the Abanico and Farellones formations. The thickness of the deposits increases to the E, towards the axis of a NNW-trending syncline. They are covered unconformably by the lower member of the Farellones Formation. View SSW from 378123mE, 6354269mN.

3.5.2 Interplay between structures, magmatism and hydrothermal fluids

The abundance of syn-tectonic hydrothermal minerals, with epidote, chlorite, tourmaline, biotite, quartz and calcite fibers coating various fault planes (Fig. 3.7D, E), provide evidence that Miocene fault reactivation occurred during hydrothermal fluid flow. There is also evidence of syn-tectonic Miocene magmatic activity. Figure 3.13A shows a syn-tectonic gabbro-diorite emplaced in a dilational jog associated with a NW-striking, sinistral strike-slip fault. This sense of movement is consistent with an E-W compression direction. The age of similar gabbro-dioritic dikes from the same locality was determined by Montecinos et al. (2008) to be 22.2 ± 0.15 Ma (early Miocene, U-Pb in zircon), coinciding within error range with the age for the base of the Farellones Formation and the onset of compression. Figure 3.13B shows a set of syn-tectonic rhyodacitic sills first described by Godoy (1998). They were emplaced on subhorizontal dilational lenses formed during eastward transport of Abanico Formation rocks in the core of a tight, E-vergent anticline developed in the hanging wall of the Alto del Juncal fault. Sills of similar composition outcropping 2.5 km to the NE were dated by Montecinos et al. (2008) at 11.53 ± 0.19 Ma (Lower

late Miocene, U-Pb zircon age). Several other Miocene intrusive units, although they do not present evidence of syn-tectonic intrusion, are spatially controlled by fault systems which acted as pathways for magma ascent and emplacement. The contacts of several plutons and dikes are rectilinear and they are on-strike of major fault systems (Fig. 3.2, 3.4B, 3.5, 3.7C), but they are of intrusive nature, without evidence of post-magmatic reactivation as a fault. This indicates that magmas were emplaced along the faults, and the geometry of the intrusions is not due to large-scale post-magmatic faulting. Examples of structurally-controlled intrusions include the NNW-trending facies of the Rio Colorado plutonic complex related to the Matancilla fault (Figs. 3.2, 3.5), the dacitic porphyries emplaced along the Flores fault (Figs. 3.2, 3.4B, 3.7C) and the early Pliocene rhyolitic porphyries emplaced around the intersection of the El Salto and Barriga fault systems (Figs. 3.2, 3.4B, 3.14).

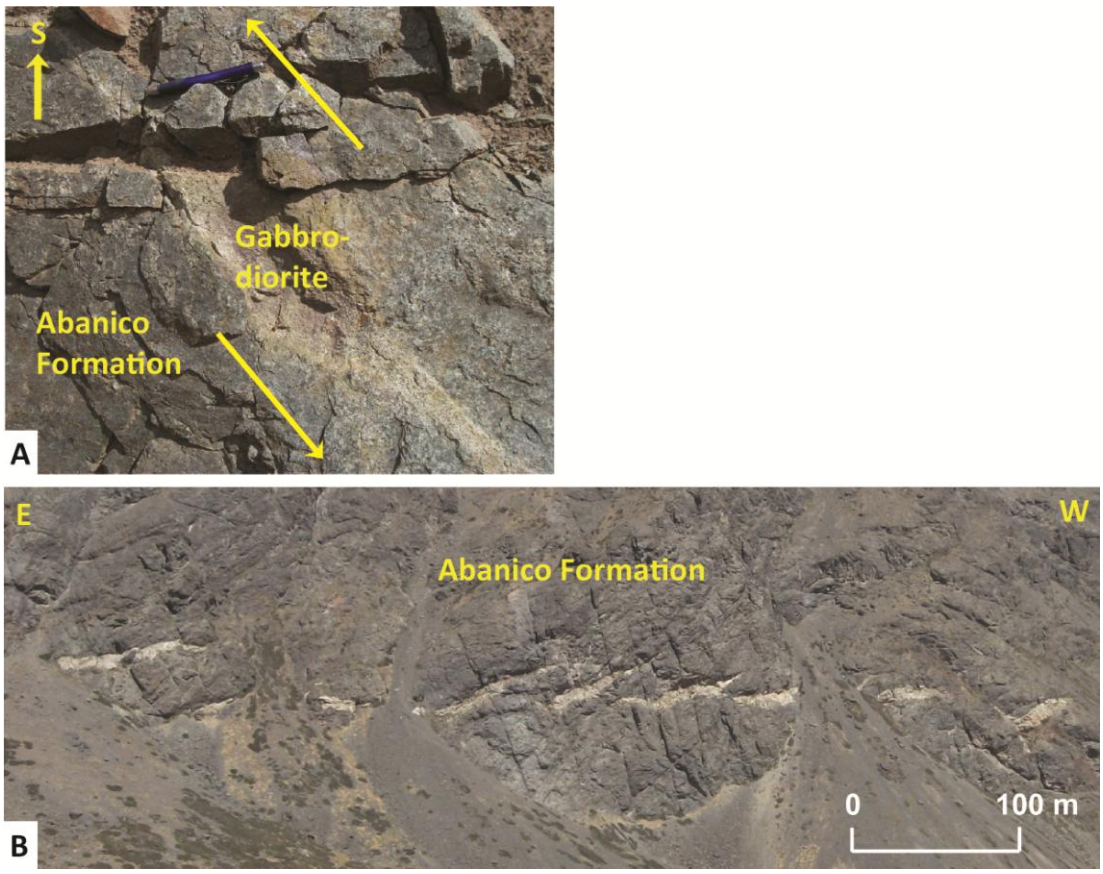

Figure 3.13. Examples of syn-tectonic intrusions emplaced during E-W compression. In both cases the host rocks are basaltic-andesitic lava flows of the Abanico Formation. A. Gabbro-diorite dike emplaced in a dilational jog within a sinistral, NW-striking fault, at 383791mE, 6349678mN. B. Rhyodacitic sills emplaced on slightly rotated dilational lenses, developed in the core of an E-vergent anticline. View SSW from 392885mE, 6363419mN.

Figure 3.14. El Salto fault system. The main fault branches are shown in yellow. The northernmost branch juxtaposes contrasting volcanic sequences of Farellones Formation: thinly bedded andesitic lava flows to the NW, and thick pyroclastic deposits to the SE. This fault system controlled the emplacement of several intrusive bodies, including the rhyolitic porphyries shown here. View ENE from 380728mE, 6335549mN.

The Saladillo fault system (Figs. 3.2, 3.5B, 3.7E, 3.10, 3.11) provides a good example of syn-tectonic emplacement of magma and hydrothermal fluids in a reactivated orogen-oblique fault. This structure, which was active as a normal fault during deposition of the Oligocene Abanico Formation pyroclastic rocks, subsequently localized the emplacement of andesitic and dacitic dikes, and also the Potrero Alto vein system, a set of parallel, NE-striking Cu-Ag hydrothermal veins filled with epidote, quartz, calcite, hypogene chalcocite and stromeyerite (Fig. 3.7E, 3.11). The dikes and the veins cut the basal layers of the Farellones Formation, indicating that their emplacement was post-early Miocene. Dikes and veins show mutual cross-cutting relationships, suggesting they are broadly coeval. The epidote contained in the veins forms well-developed syn-tectonic mineral fibers (Fig. 3.7E), which together with displaced stratigraphic markers, consistently show dextral strike-slip movement with a smaller reverse component. These relationships indicate that the Saladillo fault system was active as a normal fault during the Oligocene, controlling the syn-tectonic deposition of the Abanico Formation pyroclastic rocks, and it was subsequently reactivated as a composite dextral-reverse fault during the Miocene, controlling the syn-tectonic emplacement of both magmas and hydrothermal fluids. A similar evolution has been traced for other fault systems across the district, such as the Matancilla or El Salto faults (Figs. 3.2, 3.4, 3.5, 3.10,

3.14), which also show evidence of an earlier normal movement and subsequent strike slip ± reverse reactivation with syn-tectonic emplacement of hydrothermal veins.

3.6 Tectonic evolution

3.6.1 Late Eocene to early Miocene: extension and intra-arc basins

This period was characterized by the opening and infill of the Abanico intra-arc volcano-tectonic basin. The main basin-margin normal faults (Pocuro-Infiernillo and Alto del Juncal faults) were N-striking, and the area within them was completely covered by the products of the Abanico Formation (Figs. 3.2, 3.10). However, strong changes in thickness and volcano-sedimentary facies in this unit indicate the presence of various sub-basins and depocenters. These internal sub-basins were bounded by NW- and NE-striking normal faults (e.g., Figs. 3.5A, 3.11). The tectonic regime during this period was characterized by broadly E-W extension, and the ascent of magma to the surface was favored by a thinned continental crust (Kurtz et al., 1995) and several deep-tapping, high-angle normal faults. From 34 to 22 Ma as much as 5 km of volcanic rocks were deposited in the basin (Figs. 3.6, 3.10), with no coeval plutonic bodies recognized (Table 3.2).

3.6.2 Early Miocene to early Pliocene: Tectonic inversion, plutonism and porphyries

During this period the high angle, ~N35°W and ~N40°E, intra-basin extensional faults of the Abanico Basin were reactivated in strike-slip sinistral and dextral mode, respectively. Some reverse dip-slip movement occurred, locally associated with intense folding of the nearby Abanico and Farellones formations (Fig. 3.5A). The mainly N-striking basin-margin faults were reactivated as reverse faults.

Table 3.2. Summary of the tectonic, stratigraphic and magmatic evolution of the Rio Blanco-Los Bronces district

Age	**Tectonic regime**	**Stratigraphic units**	**Plutonic units**	**Porphyries and breccias**	**Active structures**
Pliocene-Quaternary (4-0 Ma)	Post-compression relaxation	Moraines, colluvial and alluvial unconsolidated deposits			NE faults are reactivated as post-mineral normal faults
Late Miocene-early Pliocene (7-4 Ma)	Compression	Rhyolitic pyroclastic deposits within the diatreme of the La Copa subvolcanic complex		Dacitic, rhyolitic and andesitic porphyries, tourmaline and rock-flour breccias, dacitic and rhyolitic diatremes; porphyry-style mineralization	NW faults control the emplacement of early syn-tectonic veins and breccias, but late veins were emplaced along dextral NE faults; uplift is controlled by reverse faults located in the eastern part of the district and in Argentina
Middle to late Miocene (15-8 Ma)	Compression	Farellones Formation, upper member	Monzonite, monzodiorite, granodiorite, diorite, tonalite	Andesitic dikes, early tourmaline and actinolite-magnetite breccias	Strike-slip dextral NE faults, reverse-sinistral NW faults, reverse N-S faults
Upper early Miocene-middle Miocene (17-16 Ma)	Compression	Farellones Formation, middle member	Syenogranite	Andesitic dikes	Strike-slip dextral NE faults, reverse-sinistral NW faults, reverse N-S faults
Early Miocene (23-17 Ma)	Compression	Farellones Formation, lower member	Granodiorite, diorite, gabbro	Andesitic dikes, dacitic and rhyolitic porphyries	N-S faults are reactivated as reverse faults; NW faults reactivated as composite sinistral-reverse faults; NE faults reactivated as dextral strike-slip faults
Late Eocene-late Oligocene (34-25 Ma)	Extension	Abanico Formation		Andesitic dikes	Normal N-S, NW and NE faults

This selective reactivation of pre-existing normal faults with different orientations generated the present-day structural architecture, whereby sub-basins are bounded by high-angle faults, each with its own thickness of local volcano-sedimentary facies, intensity of folding and exhumation level (Fig. 3.10). None of the pre-existing fault systems was ideally oriented for reactivation under E-W compression (e.g., Sibson, 2000). After the early Miocene supra-lithostatic fluid pressures were achieved in the study area, as evidenced by the presence of abundant dilational, sub-horizontal sills of Miocene age (Fig. 3.13B). This, together with the abundance of syn-tectonic hydrothermal minerals, demonstrates that conditions were appropriate for the reactivation of non-ideally oriented faults (Sibson, 1985, 2000). Tectonic inversion was coeval with the deposition of the Farellones Formation, which differs markedly from the Abanico Formation in that it covers a considerably smaller surface area and it reaches a maximum thickness of only 1.5 km (Figs. 3.6, 3.10). The basal layers of Farellones Formation cover the Abanico Formation in progressive unconformity. The 22.7 Ma age obtained in the basal pyroclastic flow (Table 3.1) marks the inception of the compressive regime in this segment of the Tertiary Andean magmatic arc (see Table 3.2). This is in good agreement with field evidence showing that NW-striking, subvertical dikes dated at ~22 Ma were emplaced syn-tectonically under an E-W compression direction (Fig. 3.13A).

Initiation of plutonic activity was coeval with Farellones Formation volcanism and tectonic inversion of the Abanico Basin. The earliest plutons in the district correspond to granodioritic bodies currently exposed at the Colorado (21.76 ± 0.53 Ma; U-Pb in zircon, this study, Table 3.1, sample AN12JP011) and San Francisco river valleys (20.1 ± 2.0 Ma; K-Ar in hornblende, Warnaars et al., 1985). Magmatism culminated with the emplacement of structurally-controlled rhyolitic porphyries and diatremes (~4.69 Ma, U-Pb zircon ages; Deckart et al., 2013; this study, Table 3.1, sample AN13JP013). The units dated between 20.1 and 8.16 Ma, are equigranular plutonic rocks, while those with ages between 7.12 and 4.69 Ma are subvolcanic rocks directly associated with hydrothermal activity and mineralization (Table 3.2; Deckart et al., 2005, 2013). The host rocks of these subvolcanic complexes include the older equigranular plutons. This implies that in a 1 m.y. period between 8.16 and 7.12 Ma, this area was subject to high exhumation rates, unroofing of the older plutonic rocks and exposure to the subvolcanic environment, with porphyry dikes

and diatremes being fed by a deeper, unexposed magma chamber. Given the characteristics and erosion level of the Rio Blanco-Los Bronces cluster (e.g., Proffett, 2009; Sillitoe, 2010), this magma chamber is inferred to have been located at 5-7 km below the present-day surface. This depth coincides well with the uppermost of the three detachment levels interpreted in our cross-sections, and also with a notable area of low Vp/Vs ratios in seismic tomography (Fig. 3.15), which we speculate correlates with the very young (<4 Ma) crystalline rocks of the deep magma chamber that solidified after volatile exsolution and formation of the deposits of the Rio Blanco-Los Bronces cluster. Isotopic data from anhydrite in the Rio Blanco and Sur Sur sectors (Frikken, 2004; Frikken et al., 2005), suggest an interaction of the mineralizing fluids with Mesozoic evaporites, indicating their source must be located below the base of the Tertiary volcanic rocks.

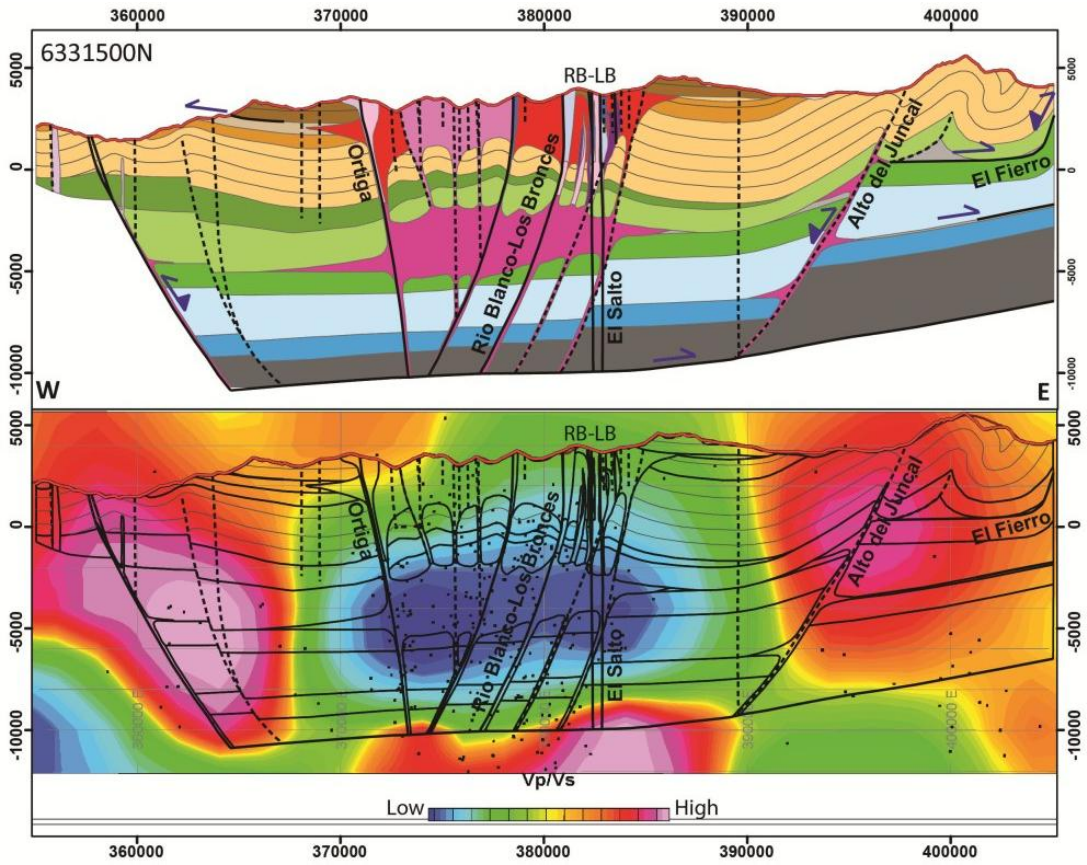

Figure 3.15. Upper panel: geological cross-section through the porphyry deposits of the Rio Blanco-Los Bronces cluster (legend in Fig. 3.10). Lower panel: bedding planes and intrusive contacts, faults, Vp/Vs tomography and distribution of hypocentres in the same cross-section. RB-LB = Rio Blanco-Los Bronces cluster.

Intrusive contacts, porphyry dikes, hydrothermal breccias and veins, all show strong NW and NE preferred orientations (Fig. 3.2, 3.4, 3.5, 3.7B, C), indicating that reactivated faults channeled the ascent and emplacement of magma and hydrothermal fluids during the compressive stage, acting as feeders both to the batholiths and the mineralized systems. In the Rio Blanco – Los Bronces cluster in particular, the main breccia bodies are aligned and elongated parallel to the N35°W Rio Blanco-Los Bronces fault system (Fig. 3.4B), while most of the late veins (quartz – tourmaline – sulfide veins with sericitic haloes and carbonate – sulfide – sulfosalts veins) are emplaced along the ~N40°E faults (Fig. 3.7B).

3.7 Discussion

Stratigraphic correlation shows that the main district-scale high-angle fault systems had early normal movements, and controlled the location of depocenters of Tertiary volcanic and sedimentary rocks. In particular, the three main NE fault systems (Saladillo, Flores and El Salto faults, Fig. 3.2) dip to the NW, and their normal movements seem to have produced progressively deeper sub-basins towards the NW, which were only partly filled by volcanic and sedimentary rocks of the Abanico Formation, producing a NW-dipping paleo-topography. This paleosurface was covered by the volcanic products of the Farellones Formation, explaining why the Abanico-Farellones unconformity is found at ~3100 meters a.s.l. (above sea level) close to the Rio Blanco – Los Bronces cluster, while in the northern part of the district is located at ~2600 meters a.s.l. A paleo-topography controlled by normal faults can also explain why the Abanico-Farellones transition is found at considerably lower elevations in the hanging wall of the Matancilla fault compared with the foot wall (Fig. 3.5).

Kinematic indicators demonstrate that during tectonic inversion, after the deposition of the Farellones Formation, the NE-striking structures were reactivated as dextral strike-slip faults, whereas NW-NNW faults typically show a combination of sinistral and reverse movements (Figs. 3.2, 3.4, 3.5, 3.7). This suggests that the bulk of the measured fault planes were reactivated under E-W contraction, and that compressive stresses were accommodated in the central part of the inverted Abanico Basin by a combination of strike-slip movement along arc-oblique, high-angle fault systems and

local ramp-flat reverse faults (Fig. 3.9). Structural style is different in the easternmost part of the inverted basin (to the east of the Alto del Juncal fault) and in the Mesozoic rocks of the Eastern Main Cordillera, where compressive deformation was accommodated by widespread thrusting and folding (Fig. 3.8, Aconcagua fold and thrust belt), not by strike-slip faults.

The Abanico and Farellones formations and the Miocene plutons are all cut by fault planes with kinematic indicators consistent with E-W contraction, suggesting that deformation associated with tectonic inversion was active at least throughout the Miocene.

3.7.1 The emplacement of subvolcanic porphyries and hydrothermal breccias

The Rio Blanco-Los Bronces cluster is defined by a NW-NNW-trend of subvolcanic porphyries and hydrothermal breccias, which were emplaced along the Rio Blanco-Los Bronces fault (Fig. 3.4B). As noted by Mpodozis and Cornejo (2012), the orientation of this fault is, in theory, not favorable for dilation under an E-W compressive regime. They suggested that a possible answer to this paradox is the sudden release of magmas and hydrothermal fluids triggered by major earthquakes, allowing their ascent through non-ideally oriented faults, decompressing a magma chamber which under normal conditions would remain sealed.

The geometry of the deposit can also be explained by the interaction of two conjugate fault systems, the NE-striking dextral El Salto fault and the NW-NNW-striking sinistral Rio Blanco-Los Bronces fault (Fig. 3.4B). Incremental movement of the El Salto fault system can produce dilation in the NW-NNW-striking structures, creating space for the emplacement of porphyries and hydrothermal breccias even under E-W compression, as shown in Figure 3.16. A similar mechanism was proposed by Hodgson (1989) for the emplacement of gold-rich veins in one of two sets of intersecting conjugate faults. This could be considered an analog to the fluid-pump behavior of faults suggested by Sibson (1986). The original model was proposed for the epithermal environment under hydrostatic fluid pressures, but the same geometric arrangement could promote even more catastrophic fluid suction and

hydrothermal brecciation in the deeper porphyry environment, which under stable conditions (inter-seismic periods) is under quasi-lithostatic pressures.

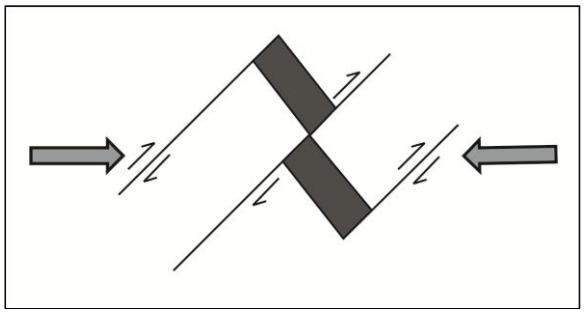

Figure 3.16. Diagram illustrating how space (represented by dark gray rectangles) can be created along NW-NNW-striking faults under E-W compression, through incremental slip along an active, NE-striking, dextral fault system.

3.7.2 The role of structures oblique to the magmatic axis

This study shows that NE- and NW-striking faults controlled the compartmentalization of the Abanico Basin during the late Eocene-Oligocene, absorbed most of the internal deformation of the basin during inversion in the Mio-Pliocene and also controlled the emplacement of magma and hydrothermal veins. This has not been suggested previously for the Rio Blanco-Los Bronces district, but Rivera and Cembrano (2000) and Rivera and Falcon (2000) presented similar conclusions from regional mapping around the El Teniente deposit, located about 100 km to the south in the same metallogenic belt (Figs. 1.2B, 3.1).

The origin of these arc-oblique structural systems may be found in the basement of the Main Cordillera. The main faults identified in published geological maps at the Coastal Cordillera of central Chile, where Paleozoic and Mesozoic rocks are exposed without the Tertiary cover, also have a NW- and NE orientation, with a complete absence of major faults parallel to the continental margin (Fig. 1.2B, 3.1; SERNAGEOMIN, 2002). These orogen-oblique faults controlled the location of Mesozoic plutons and also seem to be responsible for the interruption of the late Paleozoic-Triassic belt, which gets interrupted to the north of Santiago by a major NW-striking structural system (Fig. 1.2B, 3.1). This regional-scale structural architecture of the Coastal Cordillera is remarkably similar to the structural pattern observed at the Rio Blanco-Los Bronces district (Fig. 3.2).

During the Triassic, subduction at the Gondwanan margin is thought to have been interrupted, or at least greatly diminished, signaling a pause in the continental drift of

Gondwana (Charrier et al., 2007). This pause favored the accumulation of heat in the upper mantle, melting of the lower crust, the generation of large volumes of silicic magma, and the onset of extensional tectonics in the upper crust (Charrier et al., 2007). Palaeo-geography was dominated by fault-bounded NNW to NW-trending extensional basins and NE-striking transfer faults (Mpodozis and Ramos, 1989; Niemeyer et al., 2004; Charrier et al., 2007; Ramos, 1996; Giambiagi et al., 2003a). According to Ramos (1994), the orientation of the Triassic rifts reflects the existence of even older, NW-trending weakness zones in the crust associated with suture zones bounding allochthonous terranes accreted during the Proterozoic and the Paleozoic to the western margin of Gondwana. Other authors (e.g., Salfity, 1985; Jacques, 2003) have shown that these NW and NE structures are major features of the entire South American continent, acting as weakness zones which are repeatedly reactivated, playing a major role in the tectono-stratigraphic evolution of the continent. These arc-oblique fault systems are interpreted to have played an important role controlling the emplacement of plutonic bodies and the location of volcanic centers and mineral deposits in different segments of the Andes of Chile and Argentina, sometimes at their intersections with arc-parallel strike-slip faults (Richards et al., 2001; Chernicoff et al., 2002; Cembrano and Lara, 2009; Acocella et al., 2011).

Considering all of the evidence outlined above, we suggest that both the NW- and NE-trending fault systems observed in the Rio Blanco-Los Bronces district correspond to pre-Andean structures which characterize the structural architecture of the Paleozoic-Triassic basement. These structures have been reactivated several times throughout the Mesozoic and Cenozoic, with different kinematics depending on the prevailing tectonic regime. The middle to late Tertiary movements described in this paper corresponds to the last part of this reactivation history. The fact that they are deep, penetrative basement structures explains their effectiveness in channeling and focusing magmatism through the crust.

3.8 Conclusions

The evidence presented in this chapter shows that the structural history of the Rio Blanco-Los Bronces district is consistent with the Tertiary tectonic evolution of the Andes of Central Chile established by previous workers for the region to the south of

the study area, specifically with regards to the development and subsequent inversion of an intra-arc volcano-tectonic basin. The change from an extensional to compressive regime must have occurred after the deposition of 25.06 ± 0.18 Ma syn-extensional pyroclastic flows of Abanico Formation and before the deposition of 22.7 ± 0.4 Ma pyroclastic flows of the basal member of Farellones Formation, which cover syn-inversion volcano-sedimentary deposits.

Based on geometric constraints given by the folding style and thickness changes in the Abanico Formation, it is suggested that at the eastern margin of the inverted basin the main basin-margin fault was the Alto del Juncal fault, and not the El Fierro fault.

N-striking faults are strongly restricted to the eastern margin of the inverted Abanico Basin; in the internal part of the inverted basin, the structural data shows a strong predominance of arc-oblique faults. Those NE- and NW-striking structures are associated with major stratigraphic changes in both facies and thicknesses in the Abanico Formation, indicating they were active as normal faults during the late Eocene-Oligocene extensional period. They were reactivated in dextral (NE) and sinistral (NW) mode during the Miocene, with varying degrees of reverse components, producing fold trends parallel to the main fault systems. These orogen-oblique faults accommodated most of the internal deformation of the Abanico Basin, in combination with the activity of low-angle detachments and ramp-flat thrusts developed at different stratigraphic levels. Major detachments were also activated within the Paleozoic and Mesozoic basement; it is postulated that one of these detachments, associated with the Barremian gypsum layers, controlled the emplacement of the magma chamber which sustained the hydrothermal systems of the Rio Blanco-Los Bronces cluster.

Intrusive contacts, dykes, hydrothermal breccias and veins show strong NE and NW preferred orientations, and both hydrothermal minerals and magmas display evidence of syn-tectonic crystallization during E-W contraction. This indicates that hydrothermal fluids and magmas were channeled during tectonic inversion by the pre-existing NW and NE fault systems. Intersections of pairs of conjugate strike-slip faults seem to have been particularly favorable for the localization of Mio-Pliocene magmatic and hydrothermal activity. The Rio Blanco – Los Bronces cluster in

particular, was emplaced at the intersection of the Rio Blanco – Los Bronces (NW-NNW) and the El Salto (NE) faults. The presence of abundant hydrothermal fluids and magmas promoted fault rupture and propagation across the district, and in particular, allowed the reactivation of non-ideally oriented faults inherited from the extensional period.

The presence of pre-existing, regional-scale arc-oblique fault systems such as the ones described in this chapter, might be the key to understand the structural controls on magmatism and mineralization in other metallogenic belts, in particular in those which, like the Mio-Pliocene belt of central Chile, lack major arc-parallel fault systems. Examples of such belts include the Jurassic porphyry belt of Ecuador, the middle Eocene-early Oligocene porphyry belt of southern Peru (the Andahuaylas-Yauri belt), or both the Paleocene and the Miocene porphyry and epithermal belts of northern Chile.

Chapter 4 Orogen-oblique Fault Systems and their role in the Tertiary Evolution and Metallogenesis of the Andes of Central Chile

4.1 Introduction

Major high-angle fault systems, under favourable conditions, can act as pathways for both magmas and hydrothermal fluids to ascend through the crust, enabling them to control the location of different types of mineral deposits (e.g., Grocott and Taylor, 2002; Sillitoe, 2003; Amilibia et al., 2008). There are several mineral districts or belts, however, where the emplacement of magmatic-hydrothermal centres is not related to any obvious fault system, posing an important challenge for the development of conceptual exploration models. The Mio-Pliocene metallogenic belt of the Andes of central Chile is one such example. It contains the world's largest exploitable concentrations of Cu and Mo in two giant porphyry copper deposits: Rio Blanco-Los Bronces and El Teniente (Sillitoe, 2010; Fig. 1.2B). The ore deposits are hosted by Tertiary volcanic and intrusive rocks, which define a late Eocene to early Pliocene magmatic arc characterized by the opening and subsequent inversion of the Abanico Basin, an intra-arc volcano-tectonic basin (Charrier et al., 2002; Fig. 1.2B). The volcanic stratigraphy has traditionally been divided in two main successions: the syn-extensional Abanico Formation and equivalent units (late Eocene to early Miocene), and the syn-inversion Farellones Formation (early to late Miocene; Aguirre, 1960; Klohn, 1960; Charrier et al., 2002). Segments of the inverted basin-margin faults have been documented (Charrier et al., 2002; Fuentes et al., 2002; Fock, 2005; Farías et al., 2010; Fig. 1.2B), but the internal architecture of the Abanico Basin remains poorly understood. Most of the syn-inversion plutonic bodies (early to late Miocene) and in particular the mineral deposits and their associated subvolcanic complexes (late Miocene-early Pliocene) were emplaced in the central part of the inverted basin (Fig. 1.2B); consequently, relationships between magmatism, hydrothermal activity and upper-crustal structures in this belt have remained obscure (e.g., Mpodozis and Cornejo, 2012). This chapter attempts to clarify the regional-scale internal structural architecture of the inverted Abanico Basin between the two porphyry Cu-Mo deposits. This effort is based on new

structural and stratigraphic information collected during four months of field work, incorporating the results of Codelco mapping programs and complementing this geological information with recently acquired regional geophysical datasets. The structural model proposed for this area has implications for the interpretation of structural controls on magmatism in other segments of the Andes, as well as in other active or fossil orogenic belts globally.

4.2 Structural geology of the Andes of central Chile

Structural mapping of this Andean segment shows that within the inverted Abanico Basin, faults show preferred NW and NE strikes (Fig. 4.1B, C). Stratigraphic correlation across major faults indicates up to several hundred meters of normal displacement (Fig. 3.11), with evidence of syn-tectonic deposition of the volcanic sequences. Normal faulting has affected late Eocene-Oligocene rocks of the Abanico Formation (Fig. 4.2E) and locally early Miocene rocks of the lower part of Farellones Formation (e.g., Fig. 4.2D), suggesting that the first pulse of deformation, responsible for widespread progressive unconformities found between the Abanico and Farellones formations, was followed by a period of renewed extension, at least locally. However, kinematic indicators in individual fault planes commonly show strike-slip movements with variable amounts of reverse component (Fig. 4.2C), indicating that the normal faults were subsequently reactivated under a different stress regime. The strike-slip displacement is small, usually on the order of meters to tens of meters for an individual fault, based on the displacement of stratigraphic markers (Fig. 3.7A). Sense of movement is preferably dextral in NE faults and sinistral in NW faults (Fig. 4.1C), consistent with broadly E-directed compression. Most of the kinematic indicators are given by syn-tectonic hydrothermal minerals (mainly epidote, tourmaline, quartz, calcite, chlorite, biotite and muscovite; e.g., Fig. 4.2C). The ages of barren and productive hydrothermal systems in the study area is well constrained to the middle Miocene – early Pliocene (~14 – 4 Ma; Maksaev et al., 2004; Toro et al., 2012; Deckart et al., 2013), coeval with the period of tectonic inversion and E-directed compression (Charrier et al., 2002). Some of the orogen-oblique faults, in particular those with a larger reverse dip-slip component, produced localized folding of the Abanico and Farellones Formation rocks during tectonic inversion (Fig. 3.5A).

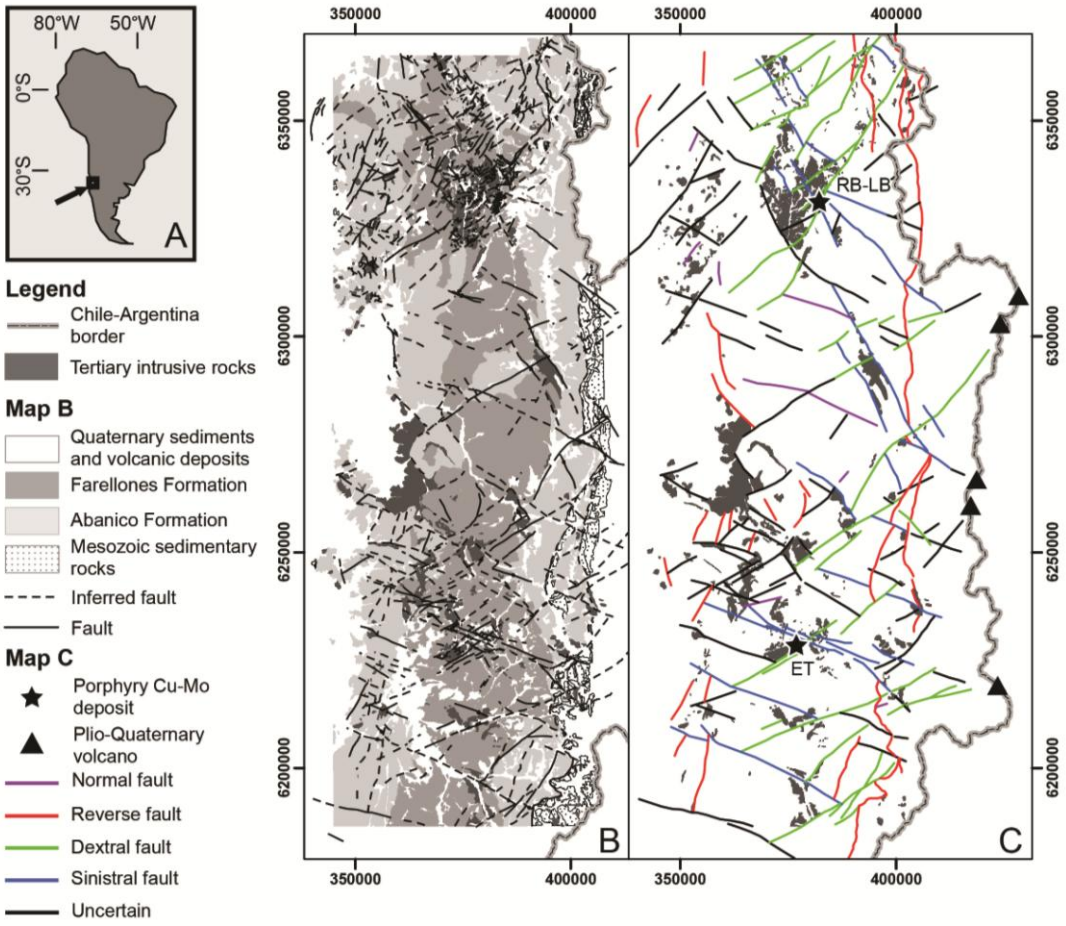

Figure 4.1. A. Location of the study area in South America. B. Geology of the Andes of central Chile, based on Rivera and Cembrano (2000), SERNAGEOMIN (2002), Fuentes et al. (2004), Fock (2005), Piquer (2010) and this work. C. Main arc-oblique and arc-parallel fault systems, interpreted from mapped faults shown in B. Each fault system is coloured according to its predominant sense of movement during its last reactivation event. The figure also illustrates the correlation between the structural architecture of the inverted Abanico Basin, the emplacement of Mio-Pliocene plutons and mineral deposits and the location of active volcanoes. RB-LB = Rio Blanco-Los Bronces; ET = El Teniente.

Not all of the pre-existing high-angle normal faults in the Abanico Basin were reactivated during tectonic inversion (Fig. 4.1C, 4.2E). Kinematic indicators showing normal movements, without any evidence of a superimposed strike-slip or reverse displacement, are commonly found away from major mineral deposits or intrusive centers (Fig. 4.1C).

At the inverted eastern margin of the Abanico Basin, NW- and SW-dipping oblique faults commonly bound structural blocks with contrasting deformation styles (Fig. 4.2A, B, D). Towards the central part of the former basin, the hanging wall blocks

contain younger, mostly flat-lying rocks that have been affected by local ramp-flat thrusts (Fig. 3.9). Towards the east, in turn, the footwall Tertiary volcanic rocks are older and tightly folded. They have been affected by the thin-skinned deformation which characterizes the Aconcagua fold and thrust belt on the eastern flank of the Andes in Argentina (e.g. Giambiagi et al., 2003b).

Major oblique structures are intimately related with the location and geometry of Miocene-early Pliocene intrusive bodies (Fig. 4.1C). Plutons are spatially related with major fault systems, and the individual plutonic facies are either strongly elongated with their major axis following the fault trend, or have rhombic shapes with their margins defined by intersecting NW- and NE-trending faults. In particular, the two porphyry copper deposits contained in this segment were emplaced at the intersections of conjugate NW- and NE-trending fault systems (Fig. 4.1C).

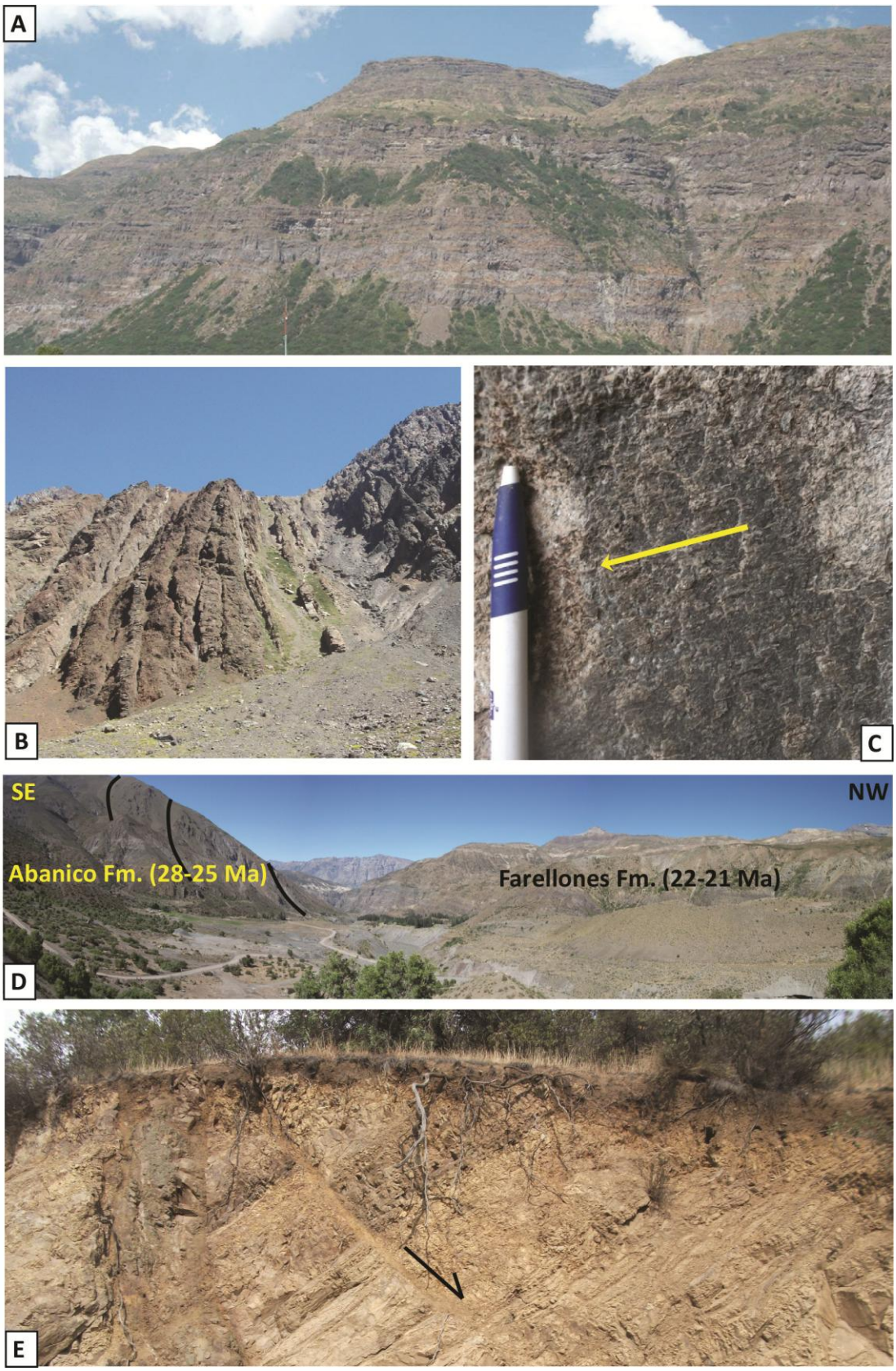
A
B
C
SE
NW
Abanico Fm. (28-25 Ma)
Farellones Fm. (22-21 Ma)
D
E

Figure 4.2. Field photographs illustrating different aspects of the oblique fault systems which affect Tertiary volcanic rocks in the Andes of central Chile. A. Flat-lying middle Miocene rocks, typical of the central part of the Abanico Basin. View SSW from 370500mE, 6201900mN. B. To the east of A., early to middle Miocene volcanic and sedimentary rocks are strongly folded within wedges formed between the N-striking thrust faults at the eastern margin of the Abanico Basin and conjugate, NW- and NE-striking strike-slip fault systems. View S from 387050mE, 6192200mN. C. Syn-tectonic crystallization of tourmaline in a NE-striking, NW-dipping fault plane, with steps in mineral fibers indicating dextral strike-slip movement. Yellow arrow indicates the sense of movement of the missing block. Picture taken at 387888mE, 6255000mN. D. View SW from 393700mE, 6266260mN, looking along strike of the NE-striking, NW-dipping fault system to which the fault plane of C belongs. The structure juxtaposes strongly folded, Oligocene Abanico Formation rocks in the footwall with flat-lying, early Miocene Farellones Formation rocks in the hanging wall. Black lines highlight bedding surfaces. Ages from Baeza (1999), Charrier et al. (2002) and Fock (2005). E. WNW-striking, S-dipping normal fault affecting pyroclastic and sedimentary deposits of Abanico Formation at 373809mE, 6310183mN. The fault is part of a WNW system of normal faults without evidence of subsequent reverse or strike-slip reactivation.

4.3 Geophysics

Regional geophysical information has been gathered in the study area from different sources, qualities and resolution over the last 30 years. Relevant to this study are the crustal seismicity, gravity and magnetic data. Crustal seismicity is a key parameter given the fact that deformation inside the inverted Abanico Basin remains active today, representing part of the permanent deformation associated with the Andean subduction cycle. Gravity and magnetic signals are complementary tools that can be used to define major lithological and structural domains.

4.3.1 Seismicity

Within the last 20 Ma, the Andes of central Chile and Argentina have experienced ~ 100 km of shortening (Farías et al., 2010), corresponding to a deformation rate on the order of 5 mm/year. This permanent deformation is about 5-7% of the convergence rate between the Nazca and South American plates, and produces active crustal seismicity and sporadically some large earthquakes, such as the Las Melosas 1958 Mw 6.9 earthquake (Sepulveda et al., 2008; Alvarado et al., 2009; Fig. 4.3A). Instrumental information at teleseismic distance is available for the study area for the

last 50 years (National Earthquake Information Centre), with error envelops in the range of 10/20 km in the horizontal and vertical dimension and magnitudes over 3 Mw. In addition, two local networks (CHASE 2005, Pardo et al., 2008; ANILLO 2006-2008, Farías et al., 2010), provide a representative data set that characterizes the active deformation of the crust in the study area. Databases considered in this study provide a good representation for magnitudes over 2.5 Mw with errors in the range of 5-10 km in horizontal coordinates and 8-15 km in depth. On the other hand, the time window of 40 years for the regional network and 4 years for the local networks ensures that enough small seismic events are recorded to characterize crustal deformation, given the fact that the mean deformation rate is about 5 mm/yr and relatively large earthquakes (~ 6.5 Mw) occur every ~ 25 years.

Figure 4.3A shows the total crustal seismicity over the structural network of the study area. A depth filter was applied, so that only the events with depths above 20 km are shown. The seismic events associated with the mining operations (Rio Blanco-Los Bronces and El Teniente) were also eliminated. Seismicity is mostly concentrated in the N-striking eastern border of the former Abanico basin, in particular in the southern segment. However, clustering of seismic events and NE - NW trends are observed in the central and western parts of the Abanico Basin, some of them spatially correlated with the location of the Rio Blanco-Los Bronces and El Teniente deposits. These seismic clusters and alignments are strongly concentrated along regional-scale oblique structures (Fig. 4.3A).

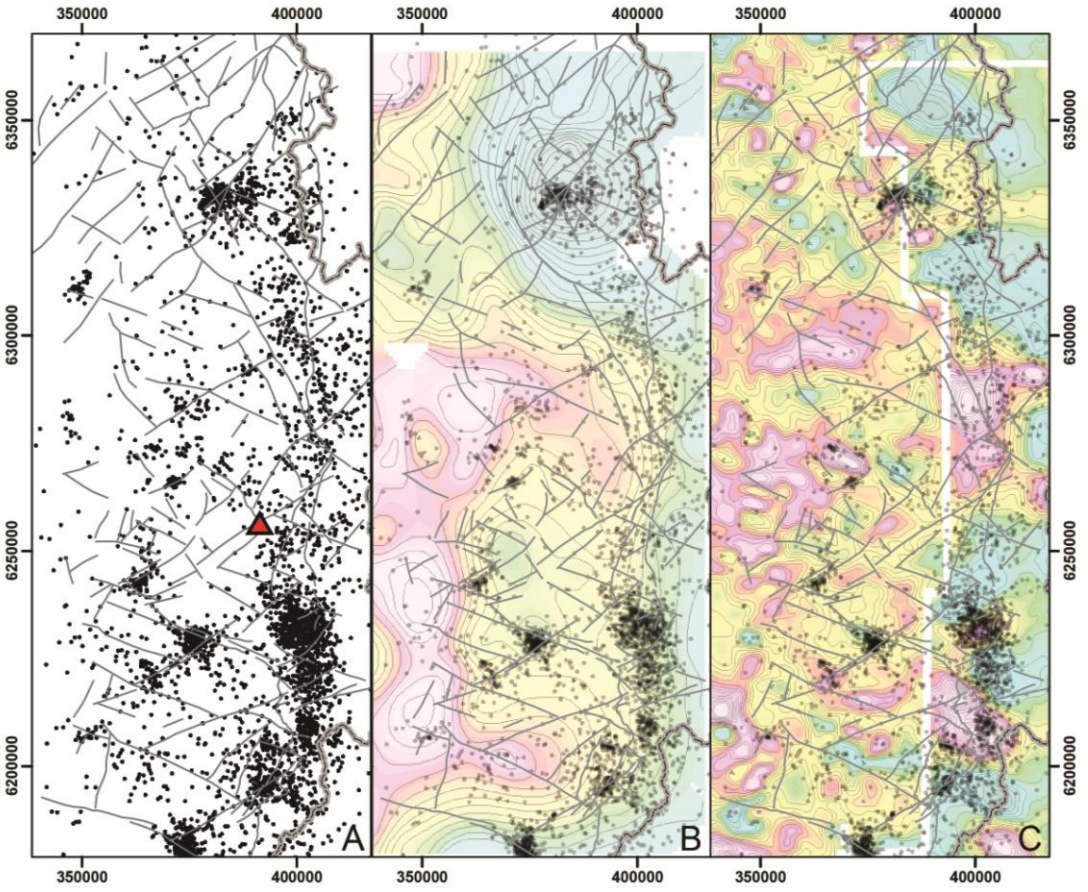

Figure 4.3. Main arc-oblique and arc-parallel fault systems (from Fig. 4.1C) plotted against different regional geophysical data: A. Shallow hypocenters. Red triangle marks the location of the Las Melosas 1958 Mw 6.9 earthquake. B. Shallow hypocenters and gravity field. C. Shallow hypocenters and the reduced to pole magnetic field. The two different surveys mentioned in the text are delimitated by a narrow mask zone in order to clarify which domain belongs to each survey.

4.3.2 Gravimetry

Gravity data have being gathered within the framework of the Ring Project ACT N°18 (Yañez et al., 2008). This is a regional data set with stations at an average sampling distance of 5 km, with differential GPS height control and errors on the order of 0.3 mGal. The residual gravity field for the study area is shown in Figure 4.3B, along with the structural network and crustal seismicity. A simple interpretation of this data set shows that the strongest deformation of the Tertiary volcanic rocks, observed in the structural geology and seismicity record, is spatially correlated with a gradient between medium and low density domains on the eastern flank of the area. In the southern part, this gradient is N-trending and follows the

eastern margin of the Abanico Basin. Towards the north, this transition zone acquires a NW trend, parallel to the NW-striking structures which traverse the Rio Blanco-Los Bronces district (Fig. 4.3B). In the western part of the area, long wavelength positive anomalies are associated with dense and deep crustal blocks. Previous studies (Yañez and Rivera, 2009; Rivera and Cerda, 2012) have suggested a relationship between these dense blocks and the emplacement of giant copper deposits. More precise correlation with structures is hampered by the low resolution of this regional data set.

4.3.3 Magnetometry

The regional magnetic field of the western part of the study area was surveyed in the early 1980s by the Chilean Geological Survey. The eastern part was surveyed in the early 1990s by Codelco. Even though technical conditions at the time of the two surveys were limited (pre GPS era for the western survey and without the appropriate aircraft for high altitude surveys on the eastern side), data quality is good enough for the purposes of the present study. The western survey was flown with NS lines every 2.5 km and nominal clearance of 600-1000m. The eastern survey specifications were NS lines every 1 km and a clearance of 1000m, however in practice the mean altitude above the topography was 1500m. With cross-checking calibration between both surveys, we estimate errors below 500m in plan view. Figure 4.3C shows the reduced to the pole magnetic field of the study area, overlapped by the structural network and crustal seismicity. The magnetic data highlights the major oblique structural trends much better than the gravity data, due to better resolution and line orientations (N-S) at high angles with respect to the structural pattern.

4.4 Relevance and role of arc-oblique fault systems

The internal architecture of the inverted Abanico Basin is dominated by regional-scale faults oblique to the continental margin of South America and to the axis of the magmatic arc. These orogen-oblique faults were active both during the extensional period and during tectonic inversion (Fig. 4.1, 4.2). Miocene contraction also activated low-angle thrusts rooted in stratigraphic contacts within the Tertiary volcanic packages (Fig. 3.9). These NW- and NE-striking fault systems controlled the ascent and emplacement of magma and the location of the two giant porphyry

Cu-Mo deposits contained in this area (Fig. 4.1C). The fact that fault reactivation during tectonic inversion was concentrated around hydrothermal centers and mineral deposits, suggests a close relationship between fault reactivation and fluid pressure, associated with magmatic-derived hydrothermal fluid flow.

This proposition has strong implications for mineral exploration in the area and for the understanding of structural controls on active volcanism, geothermal systems and intra-plate earthquakes occurring in this Andean segment. As shown by Figure 4.1C, Plio-Quaternary volcanic centers of this region are located along strike of major oblique fault systems. We interpret these oblique faults to be reactivated basement structures, inherited from pre-Andean tectonic cycles: suture zones formed during accretion of continental blocks to the western margin of Gondwana in the Palaeozoic, and basin-margin and transfer faults active during Triassic rifting events. These orogen-oblique fault systems are well developed in the Paleozoic-Triassic basement of the Andes, and have been recognized both in basement blocks cropping out in the Chilean Andes (e.g., Niemeyer et al., 2004) and in the Argentinean basement to the east (Salfity, 1985; Chernicoff et al., 2002; Acocella et al., 2011; Sagripanti et al., 2014). These high-angle, long-lived basement structures are major weakness zones which can focalize the ascent of magma through the brittle upper crust (Fig. 4.4). We suggest that they were active as composite normal – strike slip faults accommodating the opening of the Abanico basin during the late Eocene – early Miocene. They were then reactivated as composite strike slip – reverse faults during Miocene – early Pliocene E-W compression and basin inversion (Fig. 4.4).

Field evidence for these long-lived, arc-oblique structures can be subtle when covered by Cenozoic rocks and overprinted by more evident, arc-parallel faulting. In the Andes of central Chile, with its continuous deposition of Tertiary volcanic and sedimentary products, they are often represented as small-displacement, discontinuous fault systems. But they can still be traced across the orogenic belt by a combination of structural, stratigraphic and geophysical methods.

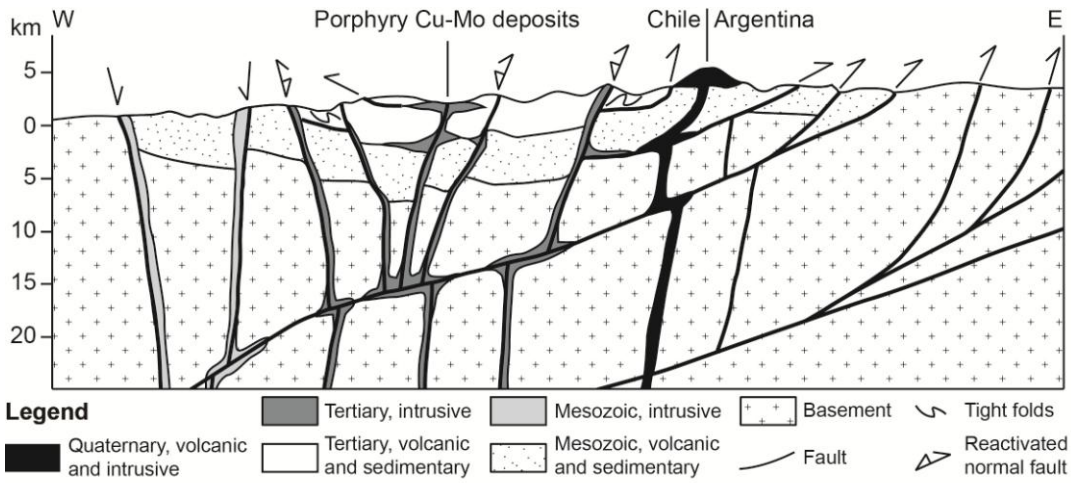

Figure 4.4. Schematic cross-section of the upper crust across the Andes of central Chile and Argentina. It illustrates the complex interaction between high-angle, arc-oblique, basement-inherited faults and low-angle, arc-parallel thrusts formed during Andean orogenesis. High-angle oblique faults have played a prominent role channelling magmatism through the upper crust in the Mesozoic, Tertiary and Quaternary magmatic arcs. Geology of the eastern (Argentinean) flank of the Andes and geometry of the main Andean thrusts based on Giambiagi et al. (2003b).

4.5 Conclusions

Geological mapping and geophysical analysis allowed the identification of the main regional-scale fault systems which controlled the along-strike segmentation of the Abanico Basin. These NE- and NW-striking structures correspond to reactivated weakness zones inherited from the pre-existing structural architecture of the Andean basement (Fig. 4.4). They were active as normal faults during the late Eocene to early Miocene, and controlled dramatic changes of facies, thicknesses and age of the volcanic rocks deposited during this period. The same structures were reactivated as strike-slip faults with minor reverse components during tectonic inversion in the early Miocene to early Pliocene. During this period, they localized syn-tectonic magmatic and hydrothermal activity and controlled the strike of fold trends developed in volcanic rocks. These oblique fault systems control the location of active crustal seismicity within the Abanico Basin (Fig. 4.3A), showing that they are still active under the current stress regime. Some of the faults bound gravimetric domains (Fig. 4.3B), suggesting that they define the deep architecture of the crust beneath the Andes. A first-order role of arc-oblique fault systems in the geologic

evolution of this Andean segment has never been suggested before, but there is compelling geological and geophysical evidence to support this hypothesis.

By combining field-based structural geology with regional-scale geophysics, major oblique fault systems can be identified even in magmatic arcs where they have been obscured by young volcanic and sedimentary deposits and/or arc-parallel structures. This approach can be applied to other Andean segments and to orogenic belts elsewhere, leading to improved exploration models for subduction-related mineral deposits and also to a better understanding of the structural controls on volcanism, geothermal activity and crustal seismicity.

Chapter 5 Evolution of the Abanico Basin, Central Chile: new Chronological, Geochemical and Structural Constrains

5.1 Introduction

Most of the Main Andean Cordillera of central Chile is composed of arc-related volcanic and intrusive rocks (Fig. 1.2B; Charrier et al., 2002, 2007; SERNAGEOMIN, 2002). Due to the lack of appropriate chronostratigraphical data, this sequence was originally interpreted to be Late Cretaceous-early Paleogene in age (Aguirre, 1960; Klohn, 1960), but more recent studies have demonstrated a late Paleogene-Neogene age based on mammal fossils, K-Ar and $^{40}Ar/^{39}Ar$ geochronology (late Eocene to early Pliocene; Charrier et al., 1990, 2002; Flynn et al., 1995, 2003; Fock et al., 2005). The lower part of this Tertiary volcanic sequence was deposited under extensional conditions within the Abanico intra-arc volcano-tectonic basin (Charrier et al., 2002, 2007). Syn-extensional rocks have been grouped into the Abanico Formation (Thomas, 1953; Aguirre, 1960) in the area in front of the cities of Santiago and Los Andes, and into the Coya-Machali Formation (Klohn, 1960) in the Main Cordillera to the east of Rancagua (Fig. 1.2B). More recent studies have considered these two units as stratigraphic equivalents, and the name Abanico Formation has been preferred (e.g., Charrier, 2002). The younger part of the Tertiary sequence was deposited during tectonic inversion of the basin, which resulted in strong folding of the syn-extensional units and reactivation in reverse mode of the basin-margin faults (Charrier et al., 2002). Syn-inversion volcanic rocks have been grouped into the Farellones Formation, first defined by Klohn (1960) in the Main Cordillera to the east of the city of Santiago (Fig. 1.2B). Flat-lying or gently folded Tertiary volcanic rocks have been correlated with the Farellones Formation both to the south and to the north of its original type locality, in the Andes to the east of Los Andes and Rancagua (Fig. 1.2B), and also further to the south and north (e.g., Godoy et al., 1999; Charrier et al., 2002; Jara and Charrier, 2014).

Different segments of the inverted basin-margin faults of the Abanico Basin have been recognized (e.g., Charrier et al., 2002; Fock, 2005; Armijo et al., 2010; Farias et

al., 2010; Piquer et al., 2010). They define the boundaries of the Western Main Cordillera with the Central Depression to the west and the Eastern Main Cordillera to the east. However, few studies (Rivera and Falcon, 2000; Rivera and Cembrano, 2000) have focused on the internal architecture of the inverted basin. They concluded that the main internal fault systems are oblique to the N-striking inverted basin-margin faults, presenting mainly NW strikes.

This chapter presents new geochronological, thermochronological and geochemical data from Tertiary volcanic and intrusive rocks of central Chile. This new data is interpreted within the structural context provided by new interpretations of the internal architecture of the inverted Abanico Basin (Chapter 4). We discuss the similarities and differences in the tectonic evolution of different segments of the Western Main Cordillera, as well as the implications of this segmentation for the stratigraphic definitions currently in use.

5.2 Methodology

A set of sixteen new U-Pb LA-ICP-MS zircon ages and two whole rock $^{40}Ar/^{39}Ar$ ages are reported in this chapter. They were obtained to establish the crystallization age of Tertiary volcanic and intrusive rocks, with a focus on rock units in which geochronological information was non-existent or of low accuracy. The $^{40}Ar/^{39}Ar$ analyses were obtained from volcanic rock samples where no zircons suitable for U-Pb dating were found. The U-Pb LA-ICP-MS analyses were undertaken at the geochronology laboratory of the University of Tasmania, Australia. $^{40}Ar/^{39}Ar$ analyses were completed at the Argon Geochronology Laboratory of the Oregon State University. Ten of the sixteen U-Pb analyses reported here were completed as part of this PhD study. The remaining six analyses are the product of unpublished research conducted by P. Hollings and M. Baker for the AMIRA P1060 project.

Eight of the U-Pb zircon dated samples were also analysed by applying the (U-Th)/He method to zircons and apatites. The analyses were completed at the Arizona Geochronology Centre, University of Arizona. The new (U-Th)/He ages were compared with new and existing geochronological data obtained from samples collected in the same localities but in which different methods were used (fission tracks in zircons and apatites, K-Ar in biotite, U-Pb in zircon). The collection of age

data obtained from isotopic systems with different closure temperatures allowed us to investigate the thermal history of these rocks.

Major and trace element data were generated for 38 samples (Appendix V) using ICP-MS whole-rock geochemical analyses undertaken at Acme Analytical Laboratories Ltd. in Santiago, Chile. These data were integrated with the whole-rock geochemistry database of the AMIRA P1060 project. The final geochemical database used in this PhD thesis contains a total of 447 analysed samples from central Chile. An age was assigned to each of these samples, using both new and published U-Pb and $^{40}Ar/^{39}Ar$ geochronology and the structural architecture of the area. From this, the temporal and spatial geochemical variations of Tertiary igneous rocks were investigated.

Analytical procedures for the different geochronological and thermochronological methods are presented in Appendices I (U-Pb), II ($^{40}Ar/^{39}Ar$) and III ((U-Th)/He). For the whole-rock geochemical analyses, analytical procedures are detailed in Appendix V.

5.3 Geochronology and thermochronology

The locations of all the samples discussed herein are illustrated in Figure 5.1B.

5.3.1 U-Pb geochronology

The results of the new U-Pb LA-ICPMS zircon analyses are summarized in Table 5.1. Inverse concordia plots for the ten samples analysed during this study are shown in Fig. 5.2. Complete analytical results are presented in Appendix IB.

Abanico Formation: Sample AN12JP005 is from a crystal-rich pyroclastic deposit which crops out close to the core of an anticline in the lower part of the Olivares river valley (Fig. 5.1B). Four inherited zircon grains yielded a range of Proterozoic ages, whereas a group of six grains yielded an U-Pb age of 31.57 ± 0.45 Ma (MSWD = 1.2; Fig. 5.2). This result confirms that this volcanic deposit belongs to the lowermost part of the Abanico Formation, according to the age range established for this unit regionally (late Eocene-early Miocene, Charrier et al., 2002).

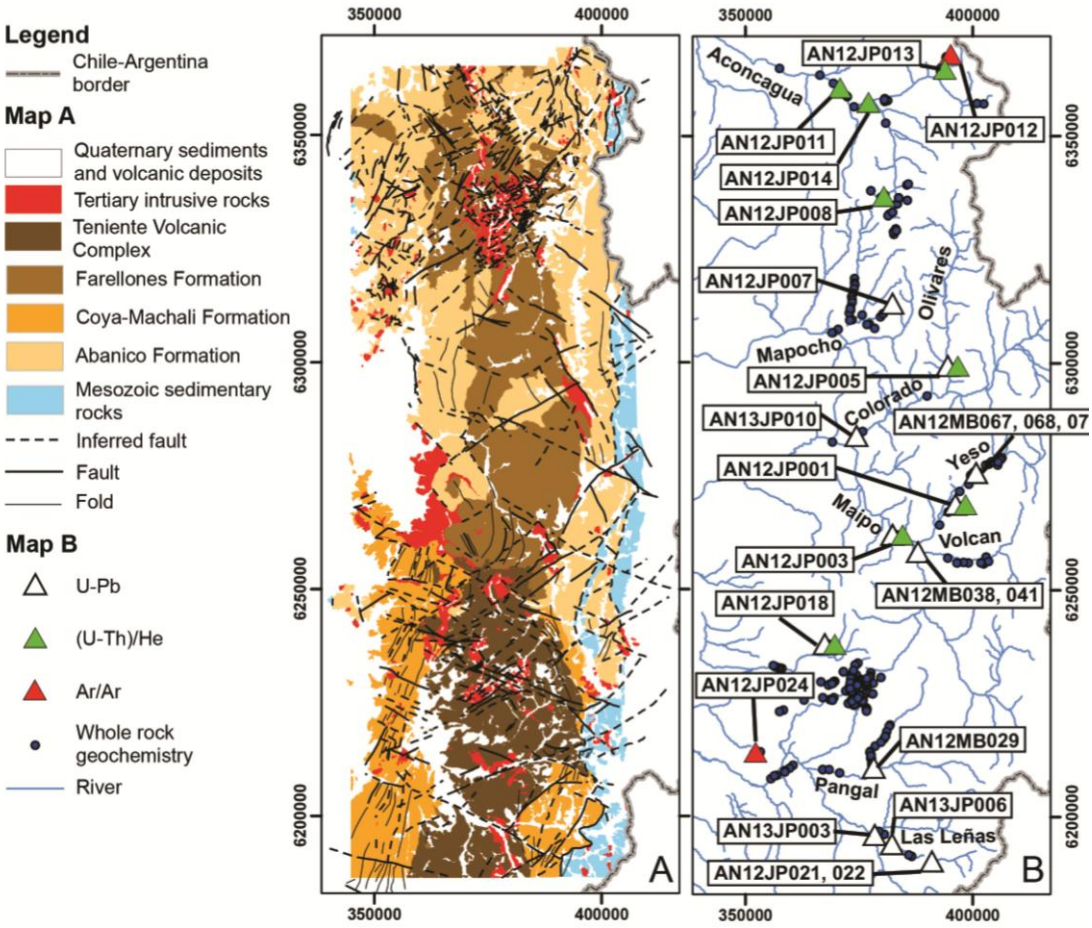

Figure 5.1. A. Simplified geological map of the study area, based on Rivera and Cembrano (2000), SERNAGEOMIN (2002), Fuentes et al. (2004), Fock et al. (2005) and this work. B. Map of the study area showing the distribution of all the analysed samples. Main river valleys mentioned in the text are labelled.

Sample AN12JP003 was collected in the Maipo valley, from a sequence of crystal-rich pyroclastic deposits commonly assigned to the uppermost part of the Abanico Formation (e.g., SERNAGEOMIN, 2002). In the sample locality beds dip 20° to the NE, and are covered in progressive unconformity by younger, sub-horizontal pyroclastic deposits and lava flows. Similar progressive unconformities have been documented both to the east and west of this locality (Fock, 2005; Fock et al., 2005), and also in the Rio Blanco district to the north (Fig. 3.12). They have been interpreted as reflecting the transition between Abanico and Farellones formations, having been formed by syn-tectonic deposition of pyroclastic units during folding of the older Abanico Formation rocks. The age of this transition has been constrained to

Table 5.1. Summary of new U-Pb and $^{40}Ar/^{39}Ar$ results reported in this chapter

Sample	N (UTM)	E (UTM)	Elevation (m a.s.l.)	Geological unit	Lithology	Method	Material	Age (Ma) (±2σ)
AN12JP001	6268758	396176	2330	Miocene dikes and sills	Dacitic dike	U-Pb	Zircon	8.86 ± 0.15
AN12JP003	6262100	383212	1220	Transition Abanico-Farellones Formations	Crystal rich ignimbrite	U-Pb	Zircon	21.41 ± 0.47
AN12JP005	6299269	394472	1878	Abanico Formation	Crystal rich tuff	U-Pb	Zircon	31.57 ± 0.45
AN12JP007	6313081	382369	3673	Farellones Formation	Rhyolitic lava	U-Pb	Zircon	17.91 ± 0.45
AN12JP018	6238036	368287	2345	Teniente Volcanic Complex	Crystal rich tuff	U-Pb	Zircon	12.73 ± 0.35
AN12JP021	6190184	390975	2344	Coya-Machali Formation	Andesitic lava	U-Pb	Zircon	15.48 ± 0.29

AN12JP022	6190172	391024	2322	Miocene dikes and sills	Rhyolitic breccia	U-Pb	Zircon	12.87 ± 0.32
AN13JP003	6196055	378490	1259	Cortaderal Intrusive Complex	Granodiorite	U-Pb	Zircon	11.33 ± 0.16
AN13JP006	6194007	382275	1602	Coya-Machali Formation	Andesitic lava	U-Pb	Zircon	12.62 ± 0.36
AN13JP010	6283891	374470	986	Farellones Formation	Crystal rich lapilli tuff	U-Pb	Zircon	19.23 ± 0.26
AN12MB029	6210779	378211	1509	Pangal Intrusive Complex	Granodiorite	U-Pb	Zircon	9.87 ± 0.17
AN12MB038	6258303	387999	1319	San Gabriel pluton	Granodiorite	U-Pb	Zircon	12.11 ± 0.27
AN12MB041	6258303	387999	1319	San Gabriel pluton	Diorite	U-Pb	Zircon	12.01 ± 0.26
AN12MB067	6275775	400864	2596	Meson Alto pluton	Gabbro	U-Pb	Zircon	11.55 ± 0.20

Table 5.1. (Cont.)

AN12MB068	6275737	400768	2591	Meson Alto pluton	Diorite	U-Pb	Zircon	11.22 ± 0.18
AN12MB077	6275228	399774	2582	Miocene dikes and sills	Andesitic dike	U-Pb	Zircon	11.17 ± 0.22
AN12JP012	6367081	394279	2900	Abanico Formation	Andesitic lava flow	$^{40}Ar/^{39}Ar$	Groundmass	14.28 ± 0.12
AN12JP024	6213996	352009	914	Abanico Formation	Crystal rich andesitic tuff	$^{40}Ar/^{39}Ar$	Groundmass	22.16 ± 0.09

Table 5.1. (Cont.)

22-21 Ma (Fock, 2005; Fock et al., 2005; Chapter 3). Two different zircon populations yielded slightly different ages. From a group of six zircon grains a U-Pb age of 21.41 ± 0.47 Ma was obtained (MSWD = 0.3; Fig. 5.2), while an older age of 24.07 ± 0.75 Ma was calculated from another group of six zircon grains (MSWD = 3.2). Considering the pyroclastic nature of the sample, it is likely that the older age represent grains inherited from older volcanic deposits, probably mixed with older zircon cores. The younger age obtained for sample AN12JP003 and its position at the base of progressive unconformities suggests that these rocks belong to a transitional sequence between the Abanico and Farellones formations.

Farellones Formation: Sample AN13JP010 was obtained from a massive, coarse-grained pyroclastic breccia which crops out in the lower part of the Colorado River valley and on the ridges to the west of it (Fig. 5.1B). The thickness of these very coarse-grained pyroclastic deposits is at least 900 m. They have been assigned to the Abanico Formation by all previous workers (e.g. Thiele, 1978; SERNAGEOMIN, 2002; Fock, 2005). However, the analysis of fifteen zircon fractions yielded a single U-Pb age of 19.23 ± 0.26 Ma (MSWD = 0.78; Fig. 5.2), which demonstrates that these deposits are 2 m.y. younger than the Abanico-Farellones transition, making them part of the lower, pyroclastic member of the Farellones Formation.

Sample AN12JP007 comes from a sequence of flow-banded rhyolitic lava flows intercalated with andesitic and basaltic-andesitic lavas of the Farellones Formation. Ten zircon fractions yielded a single U-Pb age of 17.91 ± 0.45 Ma (MSWD = 3.1), slightly older than the andesitic lava flows which host the Rio Blanco-Los Bronces porphyry Cu-Mo cluster to the north (17.2-16.7 Ma; Deckart et al., 2005; Chapter 3).

Coya-Machali Formation: Two U-Pb ages were obtained from samples collected in andesitic lava flows at the eastern Coya-Machali Formation in the Las Leñas river valley (Fig. 5.1B). The lava flows show well-developed autobreccias and abundant vesicles towards the top of individual flows. Rocks in this area are strongly deformed, forming a series of tight anticlines and synclines (Fig. 5.3A).

Sample AN12JP021 was obtained from andesitic flows that crop out immediately to the west of the El Fierro thrust, an E-vergent reverse fault which juxtaposes the

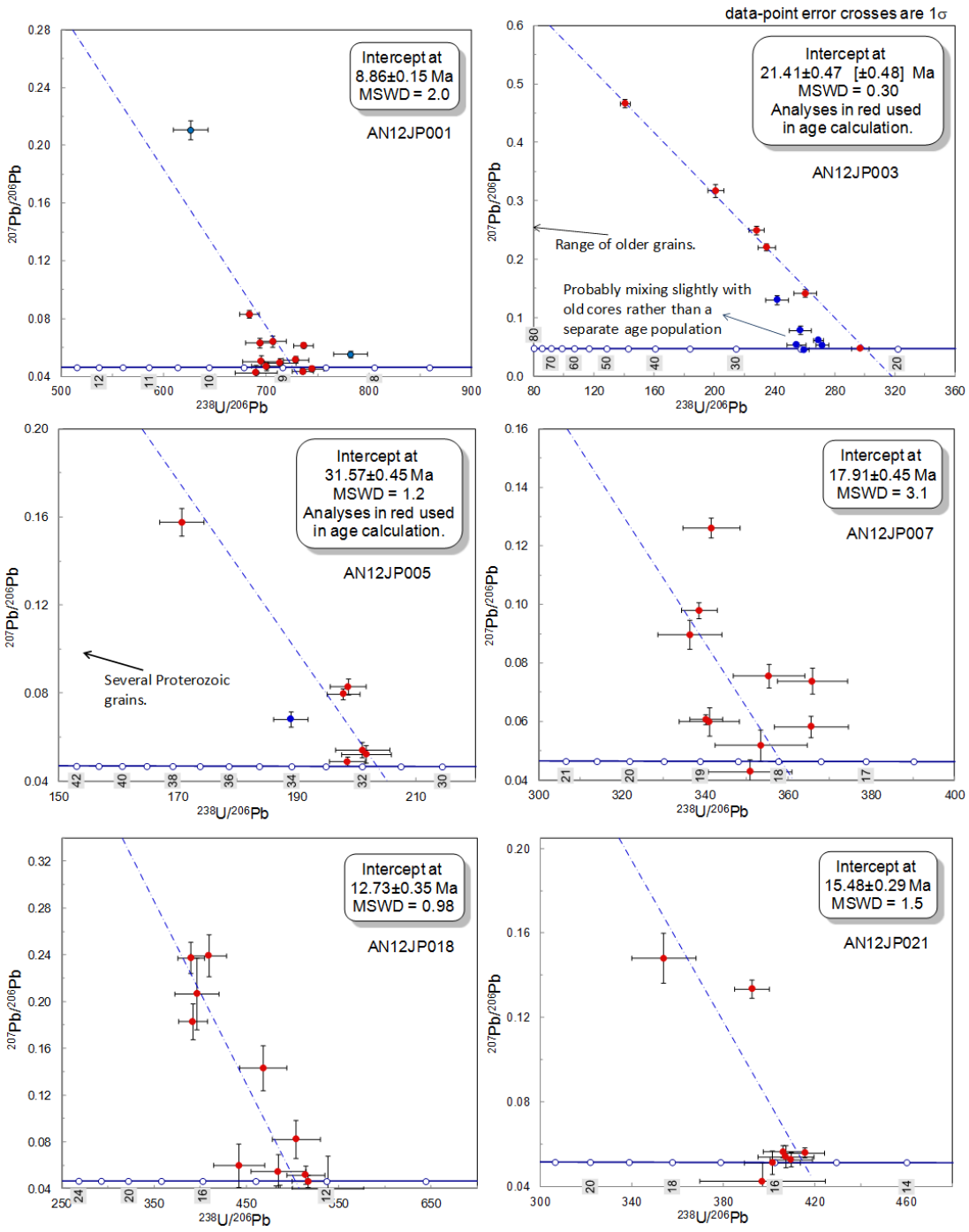

Figure 5.2. Inverse concordia plots for ten U-Pb analyses completed during this study. Numbers on the reference concordia traces are millions of years.

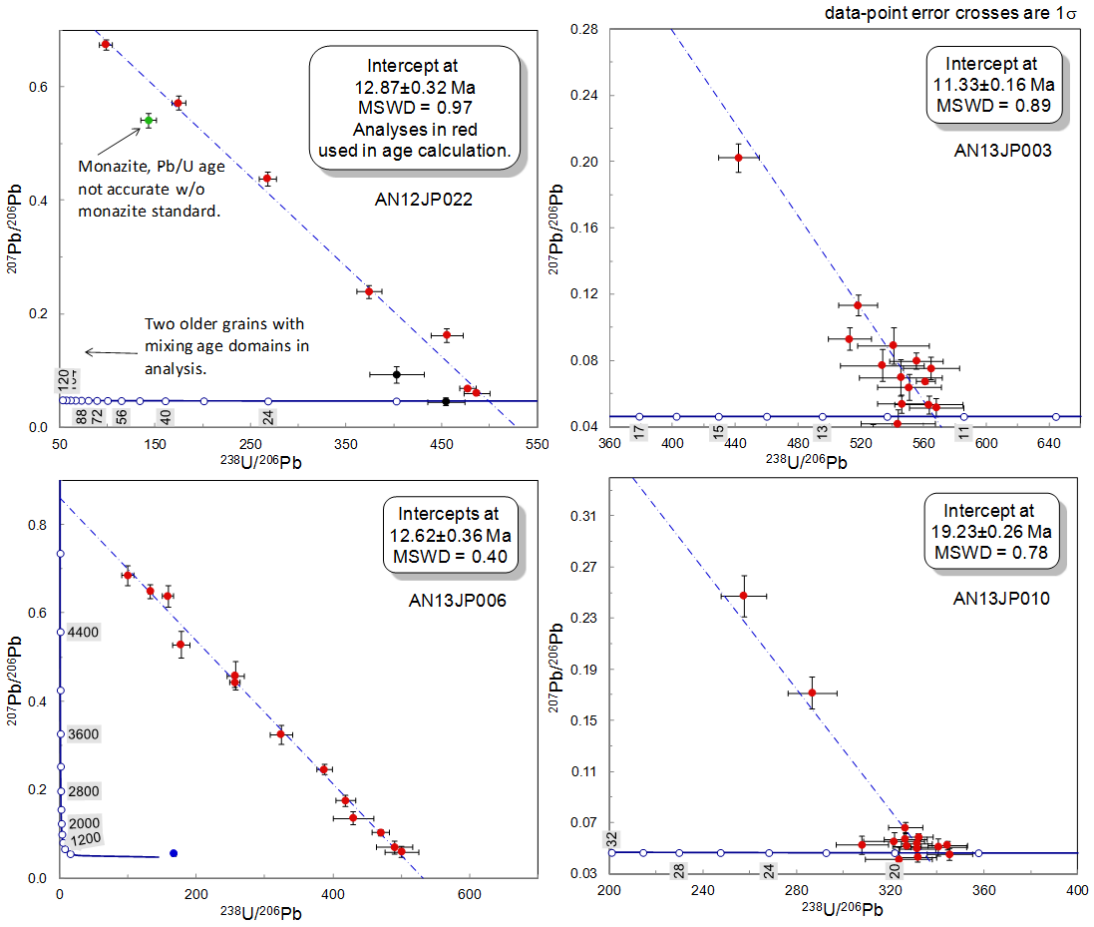

Figure 5.2. (Cont.)

Coya-Machali rocks on top of Early Cretaceous limestones (Figs. 5.3A, 5.4). As has been noted by previous authors (e.g. Charrier et al., 2002) this geometric relationship suggests El Fierro corresponds to an inverted normal fault, forming part of the structural system that defines the eastern margin of the inverted Abanico Basin. Three inherited zircon grains yielded Proterozoic to Cretaceous ages, but the remaining eight zircon grains yielded a U-Pb age of 15.48 ± 0.29 Ma (MSWD = 1.5; Fig. 5.2). This confirms that these rocks were erupted during the early to middle Miocene, as previously suggested by two $^{40}Ar/^{39}Ar$ minimum ages of 20.1 and 16.1 Ma (Kay and Kurtz, 1995; Flynn et al., 1995).

Sample AN13JP006 was collected from the youngest andesitic lavas affected by the strong thin-skinned deformation characteristic of the Coya-Machali Formation in this area (Fig. 5.3A). Two inherited zircons yielded Cretaceous and Eocene ages, but a population of thirteen grains yielded an age of 12.62 ± 0.36 Ma (MSWD = 0.40; Fig. 5.2). This is the youngest age obtained to date for the strongly deformed rocks in

central Chile (Charrier et al., 2002) and overlaps, within error, the oldest ages obtained from the overlying Teniente Volcanic Complex (described below).

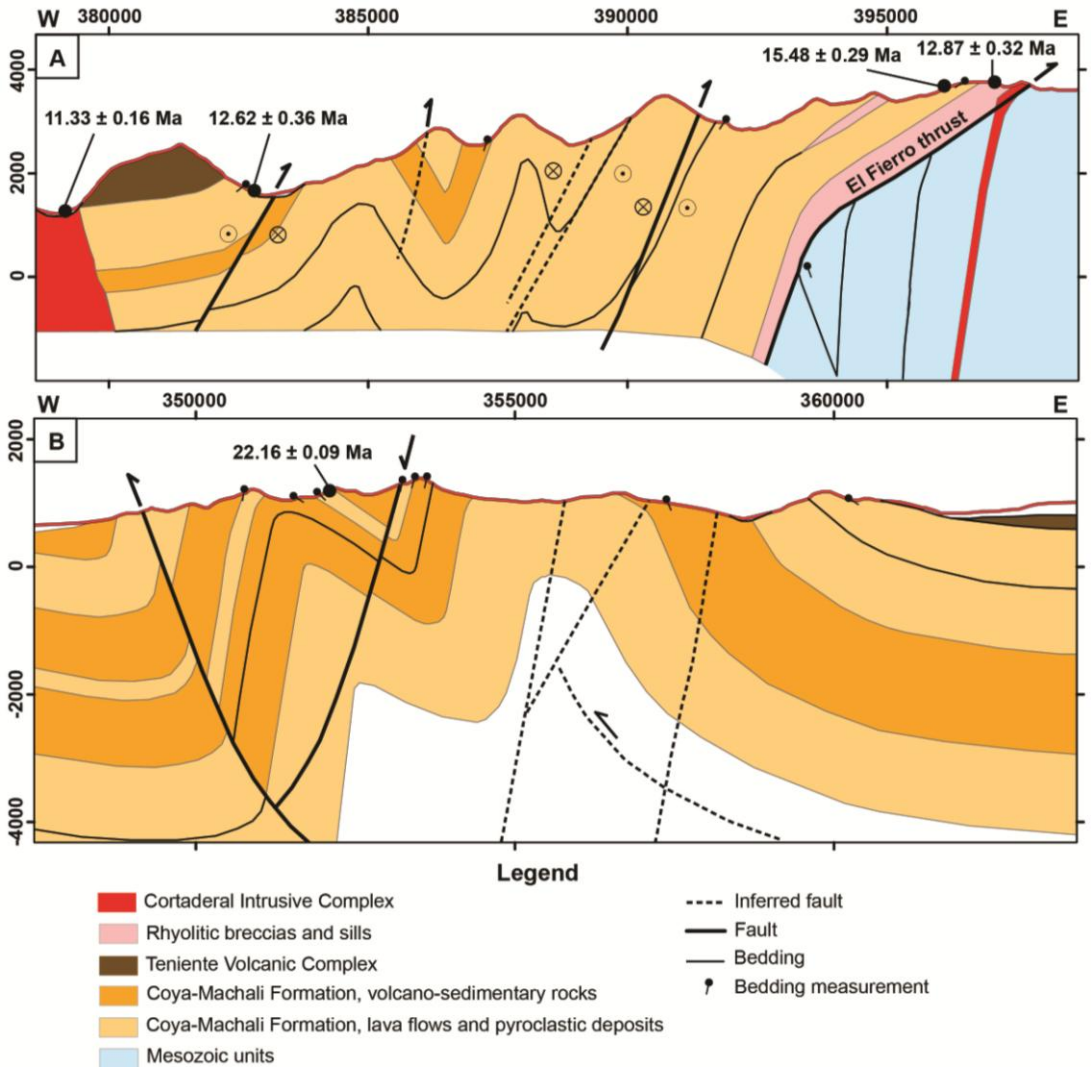

Figure 5.3. A. Cross-section of the Las Leñas river valley, showing the position where samples for U-Pb dating were collected. B. Cross-section at the type locality of Coya-Machali Formation, showing the position where sample AN12JP024 was collected for $^{40}Ar/^{39}Ar$ dating.

Teniente Volcanic Complex: Sample AN12JP018 was obtained from a horizontal to shallowly dipping, crystal- and lithic-rich pyroclastic deposit underlying the andesitic-basaltic lava flows which host the El Teniente porphyry Cu-Mo deposit. These rocks overlie strongly deformed volcano-sedimentary and pyroclastic deposits of the western Coya-Machali Formation. Fourteen zircon fractions yielded a single age of 12.73 ± 0.35 Ma (MSWD = 0.98; Fig. 5.2), which overlaps with the youngest age obtained from the Coya-Machali Formation (sample AN13JP006). This suggests

that, as with the Abanico-Farellones transition, there is no temporal hiatus between the Coya-Machali Formation and the Teniente Volcanic Complex.

Figure 5.4. El Fierro thrust in the Las Leñas river valley. Tertiary volcanic rocks of the Coya-Machali Formation are thrust over the Early Cretaceous marine sedimentary rocks of the Lo Valdes Formation. The shallow dip of the fault in the image is apparent; the true dip of the thrust is 40°, as shown in Figure 5.3A.

Middle to late Miocene Intrusions: Nine U-Pb zircon ages were obtained from samples of plutons, sills and dikes (Table 5.1). These new ages, together with those previously published from other plutons within the same Andean segment (Deckart et al., 2005, 2010; Muñoz et al., 2009), define a continuous belt of middle to late Miocene intrusions with ages concentrated between 12 and 10 Ma. Magmatic activity of this age is present throughout the study area, with most of the plutons emplaced in the central part of the Abanico Basin (Fig. 5.1A). Intrusive bodies with ages of 12-10 Ma are the oldest intrusive rocks identified to date in the southernmost segment of the study area, around the El Teniente porphyry Cu-Mo deposit (Kay and Kurtz, 1995; Kurtz et al., 1997; this work), and they are coeval with the transition between the Coya-Machali Formation and the Teniente Volcanic Complex. In the central and northern segments (Maipo and Aconcagua river valleys, Fig. 5.1B) there is also a belt of early Miocene intrusions, with plutonic emplacement beginning at ~22-21 Ma (Chapter 3), coeval with the transition between the Abanico and Farellones formations.

Sample AN12JP022 comes from the rhyolitic groundmass of a polymictic, bedding-parallel igneous breccia emplaced next to the El Fierro thrust in the Las Leñas river valley (Figs. 5.1A, 5.3A). Five inherited zircon grains yielded ages from the Carboniferous to the early Miocene, while a group of seven grains yielded a U-Pb age of 12.87 ± 0.32 Ma (MSWD = 1.01; Fig. 5.2). This age confirms the intrusive character of the breccia, as it is 3 m.y. younger than the andesitic host rocks of the Coya-Machali Formation, dated from the same locality at 15.48 ± 0.29 Ma (this work, sample AN12JP021). The age of the rhyolitic breccia is identical to the age of leucocratic dikes also emplaced along the El Fierro thrust to the north of the Las Leñas river valley, dated by Muñoz et al. (2009) at 12.87 ± 0.14 Ma (U-Pb zircon age).

Sample AN13JP003 comes from the Cortaderal Intrusive Complex, in the lower part of the Las Leñas river valley (Figs. 5.1B, 5.3A). There are no previously published radiometric ages for this pluton. The fifteen zircon grains analysed yielded a single U-Pb age of 11.33 ± 0.16 Ma (MSWD = 0.89; Fig. 5.2).

Samples AN12MB038 and AN12MB041 from two different facies, one granodioritic and one dioritic, of the San Gabriel pluton in the Maipo river valley (Fig. 5.1B). Although the contact relationships indicate that the dioritic phase was emplaced later, the two U-Pb ages are undistinguishable within error: 14 zircon grains yielded a single U-Pb age of 12.11 ± 0.27 Ma for the granodiorite (MSWD = 0.46), while a single U-Pb age of 12.01 ± 0.26 Ma was obtained from 15 grains for the diorite (MSWD = 0.62). The U-Pb zircon ages are at least 0.3 m.y. older than previously published $^{40}Ar/^{39}Ar$ biotite ages (11.4 - 11.3 Ma; Kurtz et al., 1997).

Samples AN12MB067 and AN12MB068 were collected from outcrops of the Meson Alto pluton in the Yeso River valley (Fig. 5.1B). The main granodioritic phase of this pluton has been previously dated by $^{40}Ar/^{39}Ar$ in hornblende with a result of 12.4 ± 2.5 Ma (Kurtz et al., 1997) and by U-Pb in zircon with a calculated age of 11.29 ± 0.1 Ma (Deckart et al., 2010). Sample AN12MB067 is a gabbroic xenolith contained in the granodiorite, and yielded a single U-Pb age of 11.55 ± 0.2 Ma from fifteen zircon grains (MSWD = 0.37), slightly older but within error of the age of the main pluton. Sample AN12MB068 was obtained from a dioritic enclave, and from a

population of fifteen zircon grains a single U-Pb age of 11.22 ± 0.18 Ma was obtained (MSWD = 1.30), identical to the age of the main pluton.

Samples AN12MB077 and AN12JP001 were collected from dikes emplaced into Abanico Formation rocks in the Yeso river valley (Fig. 5.1B). AN12MB077 comes from an andesitic dike, and has a calculated age of 11.17 ± 0.22 Ma obtained from eight sphene and zircon grains (MSWD = 1.20). Both the sphene and zircon grains returned similar individual isotopic ages. The calculated age is within error of the age of the nearby Meson Alto pluton. Sample AN12JP001, collected from a dacitic dike which forms part of a set of parallel, sub-vertical, E-trending dikes, yielded a clearly younger age of 8.86 ± 0.15 Ma, calculated from eleven zircon grains (MSWD = 2.0; Fig. 5.2).

Sample AN12MB029 comes from a granodioritic phase of the Pangal Intrusive Complex, from the river valley of the same name (Fig. 5.1B). The only existing radiometric age from this pluton is an unpublished K-Ar age in biotite reported by Rivera and Falcon (1998) of 10.8 ± 0.6 Ma. A single U-Pb zircon age of 9.87 ± 0.17 Ma was obtained from fifteen grains (MSWD = 0.82), almost identical within error to the K-Ar age.

5.3.2 $^{40}Ar/^{39}Ar$ geochronology

Two $^{40}Ar/^{39}Ar$ analyses were completed in the groundmass of andesitic volcanic rocks that did not contain zircons suitable for U-Pb dating. The results are summarized in Table 5.1. Laser-heated $^{40}Ar/^{39}Ar$ age spectra are presented in Figure 5.5. Complete analytical results are presented in Appendix IIB.

Sample AN12JP012 was obtained from strongly folded lava flows commonly assigned to the Abanico Formation (e.g., SERNAGEOMIN, 2002) in the north-eastern corner of the study area (Fig. 5.1B). The sampling locality lies within the Alto del Juncal and El Fierro east-vergent reverse faults (Chapter 3, Fig. 3.5), which define the eastern margin of the Abanico Basin in the area (Fig. 5.1A). The $^{40}Ar/^{39}Ar$ analysis yielded a plateau age of 14.28 ± 0.12 Ma (Fig. 5.5). This age is unexpectedly young, considering its location about 20 km to the east of the main axis of Miocene volcanism, the intense folding (more characteristic of the Abanico

Formation) and the existence of nearby dikes cross-cutting Abanico Formation rocks dated at 28.1 ± 1.5 Ma (Montecinos et al., 2008). However, the presence of isolated

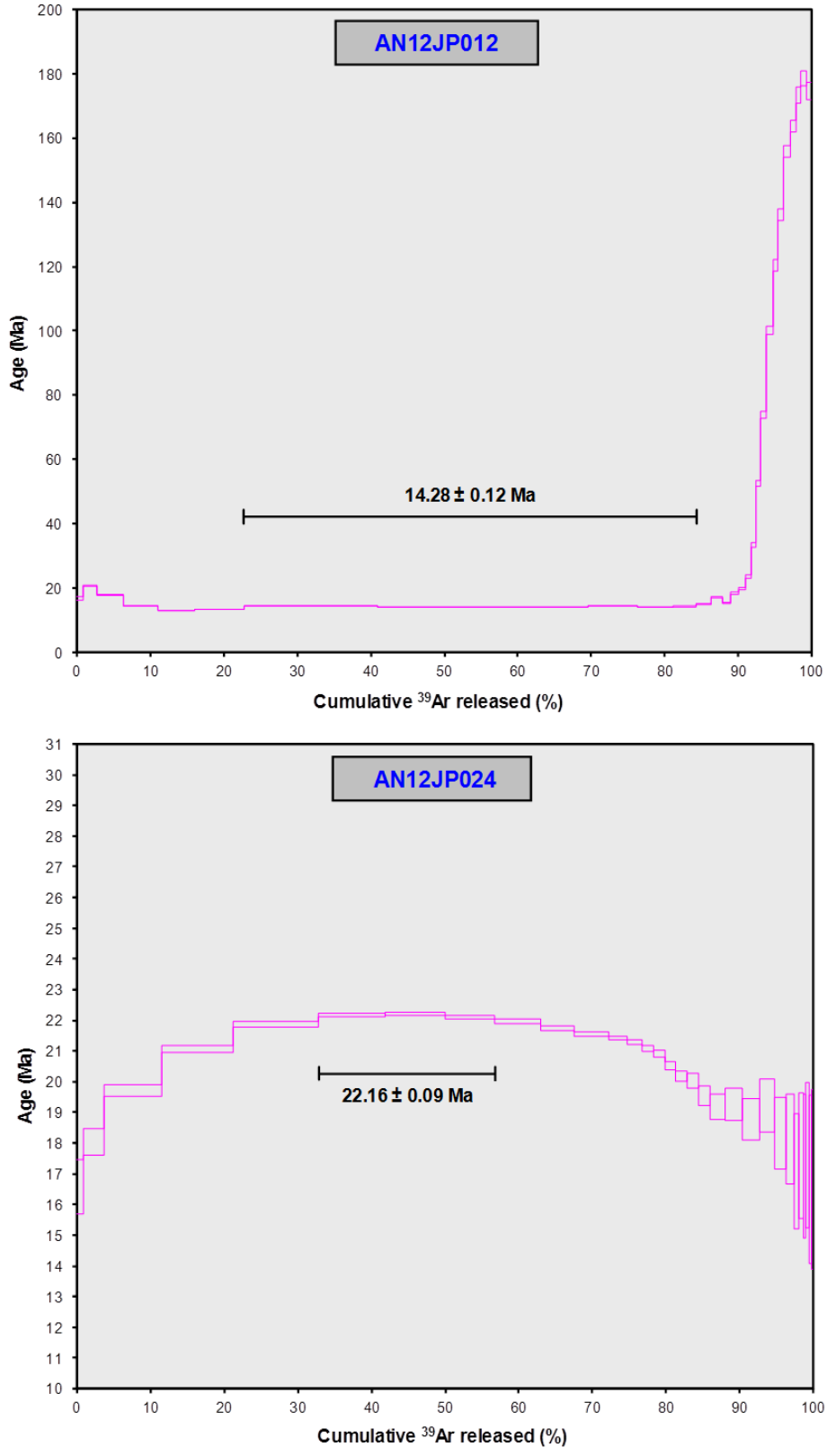

Figure 5.5. Laser-heated ^{40}Ar/^{39}Ar age spectra for the groundmass of andesitic volcanic rocks.

Miocene volcanic centres in this area cannot be ruled out. About 20 km to the northeast of the sampling locality lies the Miocene Aconcagua Volcanic Complex, with ages between 16 and 8 Ma (Ramos et al., 1996). Furthermore, the Oligocene dikes dated by Montecinos et al. (2008) are located to the west of the Alto del Juncal fault, in a different structural block. Strongly deformed Miocene andesitic rocks with Farellones Formation ages (19-16 Ma, $^{40}Ar/^{39}Ar$ in plagioclase and U-Pb in zircon) have also been documented by Aguirre et al. (2009) in the Volcan river valley (Fig. 5.1B). Their samples came from a similar structural position to sample AN12JP012, within two major faults at the eastern margin of the Abanico Basin. However, E. Godoy (pers. comm., 2012) argues that the samples dated by Aguirre et al. (2009) were collected from a sill with chilled margins. Although the lava flow where sample AN12JP012 was collected is fresh, the surrounding area is affected by epidote veining of variable intensity, and in general the El Fierro fault in central Chile channelled abundant Miocene-Pliocene magmatic and hydrothermal activity. It is therefore possible that the $^{40}Ar/^{39}Ar$ system was partially or totally reset. U-Pb dating with good geological control is needed to test the possible existence of fault-bounded, strongly folded slices of Farellones Formation rocks irregularly distributed along the eastern margin of the Abanico Basin in both the Aconcagua and Volcan river valleys.

The second groundmass sample analysed by $^{40}Ar/^{39}Ar$ (AN12JP024) was collected in the south-western part of the study area (Fig. 5.1B) at the type locality of the Coya-Machali Formation (Klohn, 1960), from a sequence of pyroclastic and volcano-sedimentary deposits affected by tight, west-vergent folds (Fig. 5.3B). The sampled pyroclastic deposit crops out close to the core of the westernmost west-verging anticline (Fig. 5.3B). The groundmass yielded a disturbed age spectrum, with a plateau from which an age of 22.16 ± 0.09 Ma was calculated (Table 5.1; Fig. 5.5). This is interpreted as a minimum age for the sample. The result is in agreement with previously published K-Ar ages for the lower part of the Coya-Machali Formation (Charrier and Munizaga, 1979). Together with the new U-Pb ages in the eastern Coya-Machali Formation, it is possible to estimate a total age range of 23 to 12 Ma for this unit.

5.3.3 (U-Th)/He thermochronology

Eight samples were analysed by the (U-Th)/He system to investigate the exhumation history of Tertiary igneous rocks. The results are presented in Table 5.2 and the complete analytical results are detailed in Appendix IIIB. Sample distribution is shown in Figure 5.1B. The volcanic origin of most samples collected meant that many apatite and zircon crystals were small and broken, making them unusable for the purposes of (U-Th)/He dating.

Six of the new (U-Th)/He ages were obtained from samples with U-Pb ages reported in this work (samples AN12JP001, AN12JP003, AN12JP005 and AN12JP018 in this chapter; samples AN12JP008, AN12JP011 and AN12JP014 in Chapter 3). Sample AN12JP013 was collected from a granodioritic sill which crops out close to the Portillo ski resort in the northeast of the study area (Fig. 5.1B). The sill was emplaced in strongly deformed volcanic rocks of Abanico Formation. This intrusion was dated by Montecinos et al. (2008), who reported a U-Pb zircon age of 11.53 ± 0.19 Ma.

The calculated (U-Th)/He ages have relatively high errors (Appendix IIIB); however, even considering the error ranges, all zircon and apatite ages fall within a very restricted time range, between 6 and 2 Ma. The early Miocene Rio Colorado Granodiorite, located in the northernmost part of the study area, is the only sampled rock unit which was exhumed before 6 Ma, with an (U-Th)/He zircon age of 9.71 ± 0.23 Ma (Table 5.2, sample AN12JP011).

Table 5.2. Summary of new (U-Th)/He thermochronology in zircons and apatites.

Sample	N (UTM)	E (UTM)	Elevation (m a.s.l.)	Geological unit	Lithology	Material	Age (Ma) (±1σ)
AN12JP001	6268758	396176	2330	Miocene dikes and sills	Dacitic dike	Apatite	2.72 ± 0.13
AN12JP003	6262100	383212	1220	Farellones Formation	Crystal rich ignimbrite	Apatite	3.23 ± 0.17
AN12JP005	6299269	394472	1878	Abanico Formation	Crystal rich tuff	Apatite	2.13 ± 0.1
AN12JP008	6336679	380467	3248	Rio Blanco Granodiorite	Granodiorite	Zircon	2.76 ± 0.23
AN12JP011	6360516	370859	1084	Rio Colorado Granodiorite	Granodiorite	Zircon	9.71 ± 0.23
AN12JP013	6364667	393882	2608	Miocene dikes and sills	Granodioritic sill	Zircon	5.17 ± 0.09
AN12JP013	6364667	393882	2608	Miocene dikes and sills	Granodioritic sill	Apatite	2.11 ± 0.2
AN12JP014	6357436	377110	1444	Abanico Formation	Crystal rich tuff	Apatite	4.04 ± 0.27
AN12JP018	6238036	368287	2345	Teniente Volcanic Complex	Crystal rich tuff	Zircon	5.01 ± 0.32

5.4 Geochemical evolution

The 447 ICP-MS geochemical analyses contained in the AMIRA P1060 project database have been grouped according to their lithology and age into the main rock units present in this Andean segment: Abanico Formation, Farellones Formation, Coya-Machali Formation, Teniente Volcanic Complex, early and middle Miocene plutons and late Miocene-early Pliocene shallow intrusions. Table 5.3 presents a summary of the chemical characteristics for each of these units.

The samples from all four volcanic units are predominantly basaltic andesites and andesites but overall range from basalt through to rhyolite in composition (SiO_2 = 39.8 to 77.2 wt %), similar to those described by Hollings et al. (2005). The average SiO_2 content is remarkably constant across the volcanic units (56.5 wt % for the Abanico Formation, 57.9 wt % for the Coya-Machali Formation, 55.3 wt % for the Farellones Formation and 54.2 wt % for the Teniente Volcanic Complex), and in general their major element chemistry is similar (Table 5.3).

Important differences appear when the rare earth element chemistry of the volcanic units is considered (Table 5.3). The Abanico and Coya-Machali formations show similar La/Sm and Sm/Yb ratios, despite their differences in age (Table 5.3, Fig. 5.6). On average, both show a moderate LREE enrichment (La/Sm = 3.4 for Abanico Formation and 3.3 for Coya-Machali Formation) and relatively flat HREE slopes (Sm/Yb = 1.9 for Abanico Formation and 1.80 for Coya-Machali Formation). The Farellones Formation, which overlies the Abanico Formation and according to new and existing data, is broadly coeval with the Coya-Machali Formation, has a different REE chemistry (Fig. 5.6). Its LREE enrichment is stronger (average La/Sm = 4.5) and it has more fractionated HREE (Sm/Yb = 2.6). The chemistry of the youngest volcanic unit of the study area, the Teniente Volcanic Complex, indicates a moderate LREE enrichment similar to the Abanico and Coya-Machali formations (La/Sm = 2.9) but a strong HREE fractionation similar to Farellones Formation (Sm/Yb = 2.4; Fig. 5.6).

The oldest plutonic rocks of the study area are early Miocene intrusions, which crop out only in the northern segment, between the Aconcagua and Maipo river valleys (Fig. 5.1B), where the Abanico and Farellones formations are found. They have a

Table 5.3. Whole-rock geochemistry summary for volcanic and intrusive units of central Chile.

Unit	N	SiO_2	Al_2O_3	Fe_2O_3	MgO	CaO	Na_2O	K_2O	TiO_2	P_2O_5	MnO	Sc	Y
						wt %						ppm	
Late Miocene-early Pliocene intrusions	27	64.94	16.11	4.21	1.59	2.63	3.93	3.55	0.50	0.15	0.07	6.86	10.30
Middle Miocene intrusions, northern segment	100	60.63	15.53	7.51	2.07	3.03	3.66	3.01	0.59	0.17	0.09	8.76	9.15
Middle Miocene intrusions, southern segment	60	58.92	17.02	6.30	2.63	4.90	3.91	4.69	0.75	0.19	0.11	13.31	15.74
Teniente Volcanic Complex	129	54.24	17.82	8.68	3.49	5.96	3.71	4.18	0.95	0.23	0.20	19.70	19.49
Farellones Fm	43	55.34	16.75	9.50	3.29	4.52	3.42	2.51	0.90	0.23	0.17	16.90	17.00
Coya-Machali Fm	19	57.91	16.17	8.43	2.48	5.17	4.23	1.44	1.05	0.29	0.17	23.41	31.51
Early Miocene intrusions	10	59.67	15.80	6.87	2.14	4.66	4.48	2.01	0.89	0.28	0.26	17.60	28.19
Abanico Fm	59	56.47	16.75	8.17	2.52	5.72	4.12	1.51	0.98	0.28	0.17	20.95	26.09

Unit	La	Ce	Pr	Nd	Sm	Eu	Gd	Tb	Dy	Ho	Er	Yb	Lu	La/Sm	Sm/Yb	La/Yb
							ppm									
Late Miocene-early Pliocene intrusions	16.21	34.57	4.19	16.29	3.04	0.74	2.41	0.34	1.86	0.34	1.00	0.99	0.14	5.85	3.47	21.02
Middle Miocene intrusions, northern segment	16.74	33.48	4.06	15.69	2.90	0.76	2.34	0.31	1.73	0.32	0.91	0.94	0.14	5.80	3.48	21.25
Middle Miocene intrusions, southern segment	14.89	35.44	4.68	19.49	3.96	1.02	3.38	0.52	2.76	0.55	1.55	1.50	0.23	3.93	2.94	12.22
Teniente Volcanic Complex	12.29	32.04	4.40	19.44	4.27	1.19	3.98	0.64	3.51	0.69	1.95	1.83	0.28	2.86	2.43	7.00
Farellones Fm	18.07	38.09	4.87	19.96	4.13	1.09	3.69	0.55	3.18	0.62	1.78	1.73	0.26	4.48	2.55	11.60
Coya-Machali Fm	17.41	40.25	5.37	23.62	5.64	1.55	5.85	0.95	5.64	1.22	3.42	3.31	0.51	3.00	1.80	5.60
Early Miocene intrusions	20.80	47.97	6.13	25.11	5.69	1.30	5.28	0.89	4.86	1.07	3.01	3.05	0.47	3.76	1.89	7.08
Abanico Fm	16.38	36.69	4.86	21.52	4.87	1.40	4.88	0.81	4.73	0.99	2.86	2.69	0.43	3.38	1.89	6.44

Table 5.3. (Cont.)

higher SiO_2 content than the coeval Farellones Formation (average 59.7 vs. 55.3 wt %), but are less LREE-enriched and have a flatter HREE slope (Fig. 5.6; average La/Sm = 3.8 and Sm/Yb = 1.9). The middle Miocene plutons have an average of 60.0 wt % SiO_2, similar to early Miocene plutons and higher than coeval volcanic rocks of the Teniente Volcanic Complex (54.2 wt %). Plutons of this age emplaced in the southern part of the study area, around the El Teniente porphyry Cu-Mo deposit (Fig. 1.2B), have REE chemistry similar to the Farellones Formation (Fig. 5.6; average La/Sm = 3.9 and Sm/Yb = 2.9), while those emplaced further north show distinctive more enriched LREE and more fractionated HREE (Fig. 5.6; average La/Sm = 5.8 and Sm/Yb = 3.5). Late Miocene-early Pliocene intrusions, which do not have a volcanic equivalent, have an average of 64.9 wt % SiO_2, higher than any of the older Tertiary rocks. Their REE chemistry shows minimal variation across the study area and is similar to the northern middle Miocene plutons (Fig. 5.6), characterized by strong LREE enrichment (average La/Sm = 5.9) and HREE fractionation (average Sm/Yb = 3.5).

As illustrated by Figures 5.6 and 5.7, the northern and southern segments of the study area show different patterns of evolution of La/Yb ratios over time. In the northern segment, the first increase of La/Yb is observed in the early Miocene volcanic rocks of the Farellones Formation, which show higher ratios than the older rocks of the Abanico Formation. A second change in REE ratios is observed in middle Miocene plutons, which show higher La/Yb compared with the Farellones Formation (Figs. 5.6, 5.7). La/Yb ratios in late Miocene-early Pliocene intrusions remained high, with values similar to the middle Miocene plutons (Figs. 5.6, 5.7). In the southern segment, around the El Teniente deposit, the volcanic rocks of the Coya-Machali Formation and the Teniente Volcanic Complex show little difference in La/Yb ratios. The first increase in REE slope in rocks from the southern segment is observed in middle Miocene plutons, which show La/Yb ratios similar to the early Miocene Farellones Formation and distinctively lower than coeval middle Miocene plutons emplaced in the northern segment (Figs. 5.6, 5.7). A second increase in La/Yb ratios is observed in late Miocene-early Pliocene intrusions, which show similar REE ratios to those observed in coeval rocks from the northern segment (Figs. 5.6, 5.7).

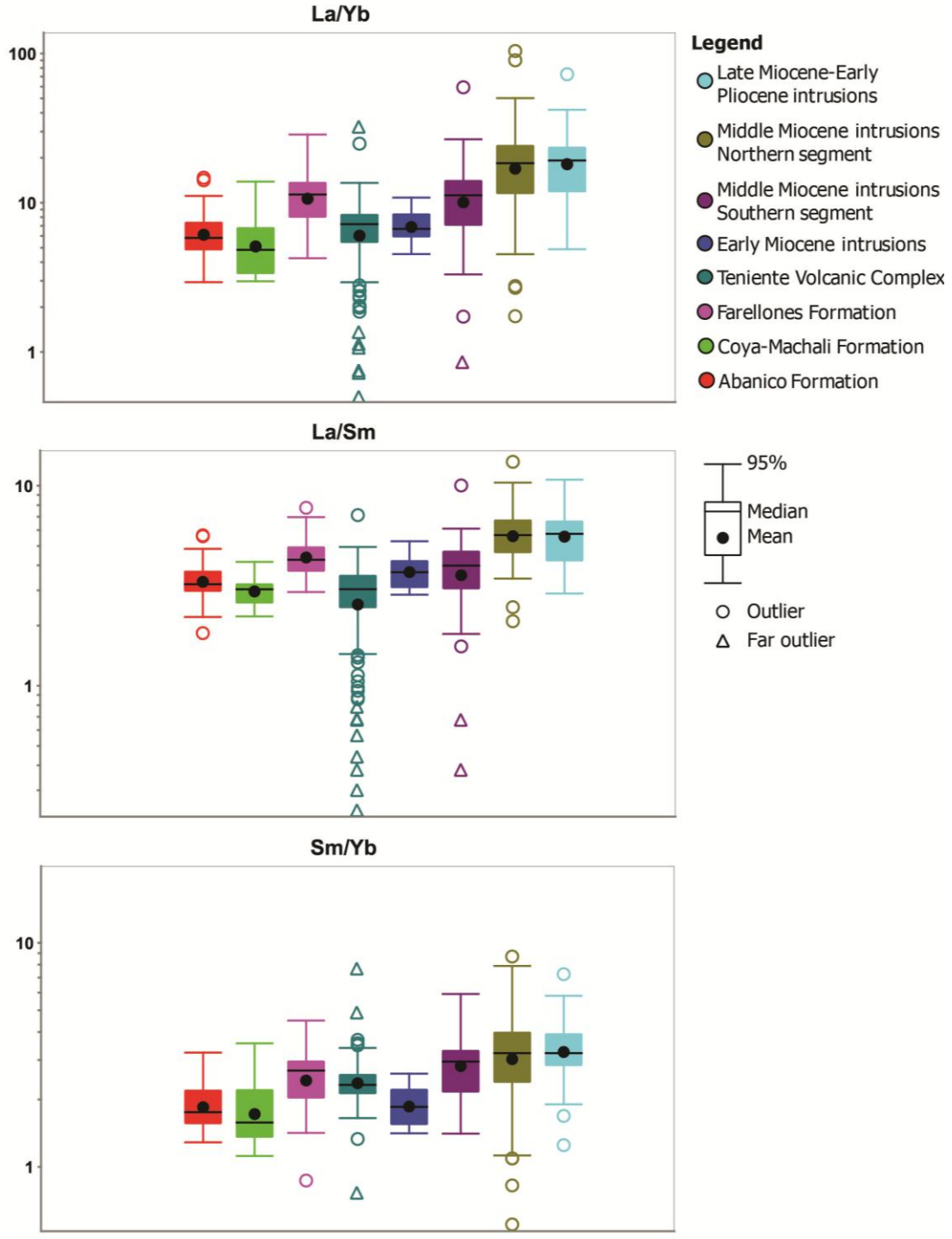

Figure 5.6. ***Box and whisker*** **plots showing the range of La/Yb, La/Sm and Sm/Yb ratios for different groups of Tertiary igneous rocks.**

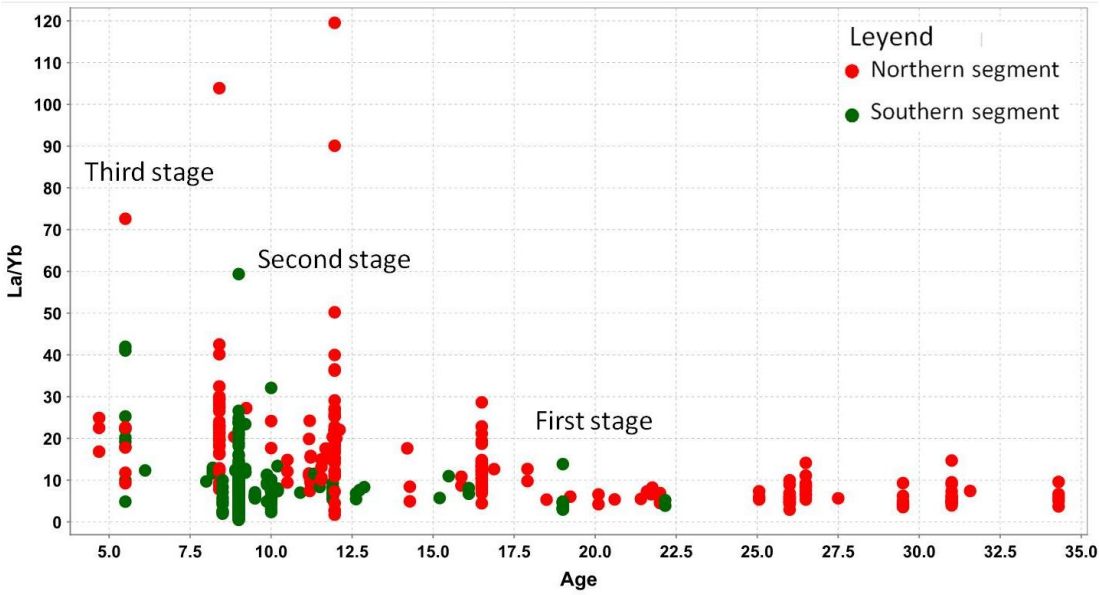

Figure 5.7. La/Yb versus time plot for all the igneous rocks of the study area. The three main stages of crustal thickening and exhumation are labelled.

5.5 Discussion

5.5.1 Deposition of volcano-sedimentary units and stratigraphic subdivisions

The compilation of new and existing geochronological data for the Tertiary volcanic units allows for the division of the Abanico Basin into two distinctive segments. The northern segment (from the Maipo to the Aconcagua river valleys; Fig. 5.1B) displays a very consistent geologic history involving older rocks of the Abanico Formation, deposited under extensional conditions between 34 and 23 Ma, overlain in progressive unconformity by the Farellones Formation that was deposited during tectonic inversion between 22 and 14 Ma. In the southern segment of the Abanico Basin, the ages of the strongly folded volcanic and volcano-sedimentary rocks of the Coya-Machali Formation range in age between 22 and 12 Ma, and the overlying, flat-lying rocks exposed in the central part of the Tertiary magmatic arc (Teniente Volcanic Complex) have ages of 13 to 6 Ma (Godoy, 1993; Rivera and Falcon, 1998; this work).

The boundary between these two segments is abrupt (Fig. 5.8), and is likely to have been controlled by regional-scale, arc-oblique fault systems. These fault systems

dominated the internal architecture of the Abanico Basin and control its segmentation into individual sub-basins, each with its own array of volcano-sedimentary facies and thicknesses (Rivera and Falcon, 2000; Chapters 3 and 4). The transition between the two segments occurs at the NW-striking, SW-dipping Piuquencillo fault system (defined by Rivera and Falcon, 2000; Fig. 5.8). This fault has an average strike of N60°W and dips 70-80°S. In some sectors is more than 10 m wide, and several dikes of different composition have been emplaced parallel to the fault. Syn-tectonic hydrothermal mineral fibers indicate sinistral strike-skip movements, which probably correspond to the sense of slip of the fault during Miocene tectonic inversion of the Abanico Basin. The transition between the two segments may also be related to NE-striking faults, conjugate to the Piuquencillo fault system (Fig. 5.8).

The coarse grained pyroclastic breccias of the Farellones Formation from where sample AN13JP010 was collected are bounded to the north by a WNW-striking, arc-oblique fault system (Fig. 5.9), parallel to the Piuquencillo fault zone but located ~35 km to the north. This structure corresponds to a south-dipping normal fault, based on stratigraphic correlations across the fault and kinematic indicators in fault planes (steps in syn-tectonic chlorite fibres). This explains why these rocks, being ~3-2 m.y. younger than the flat-lying pyroclastic deposits dated by Fock (2005) at the base of Farellones Formation 9 km to the north (Fig. 5.9), crop out at an elevation 1.4 km lower. Other contacts of these pyroclastic breccias are linear and possibly fault-related (Fig. 5.9), but they have not been checked in the field. The fact that these ~900 m thick, massive, coarse-grained pyroclastic breccias are at least partially bounded by normal faults suggests they may correspond to an intra-caldera sequence, formed during the early stages of Farellones Formation volcanism, with the northern margin of the caldera being controlled by a WNW-striking fault system (Fig. 5.9).

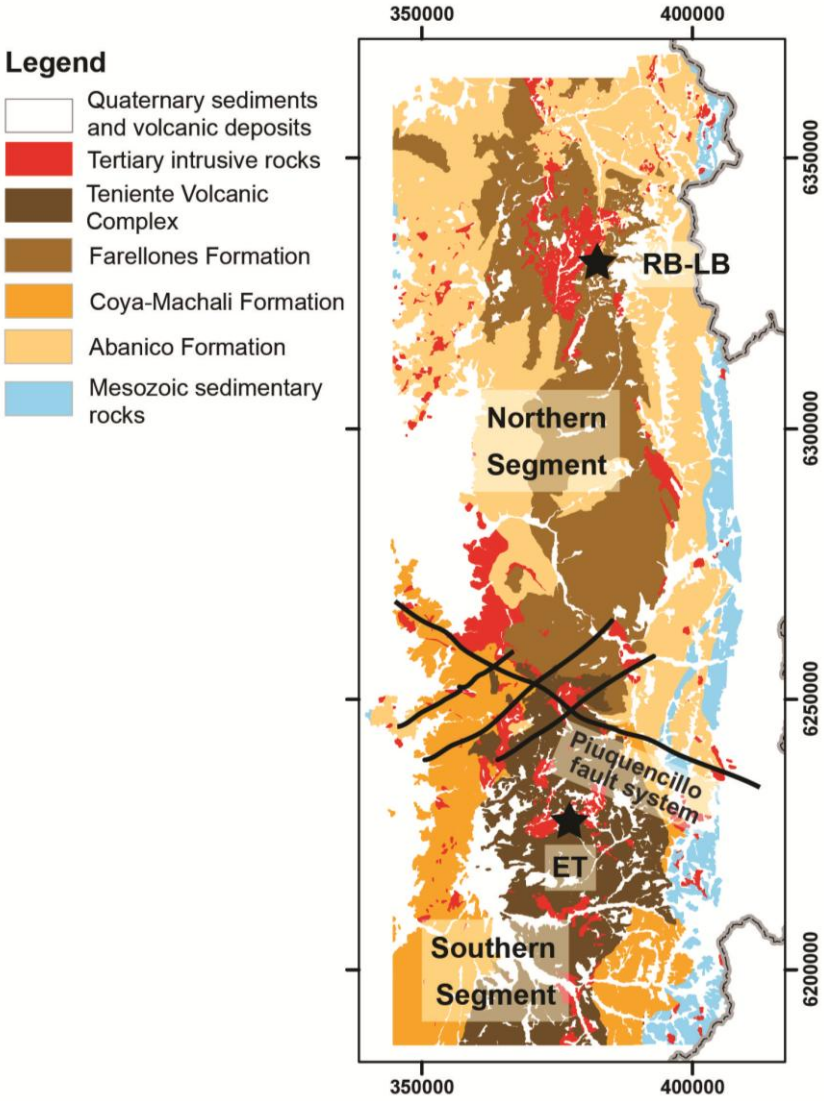

Figure 5.8. Map of the Andes of central Chile showing the subdivision of the Abanico Basin into two segments, separated by the NW-trending Piuquencillo fault zone and NE-trending conjugate faults. RB-LB = Rio Blanco-Los Bronces, ET = El Teniente.

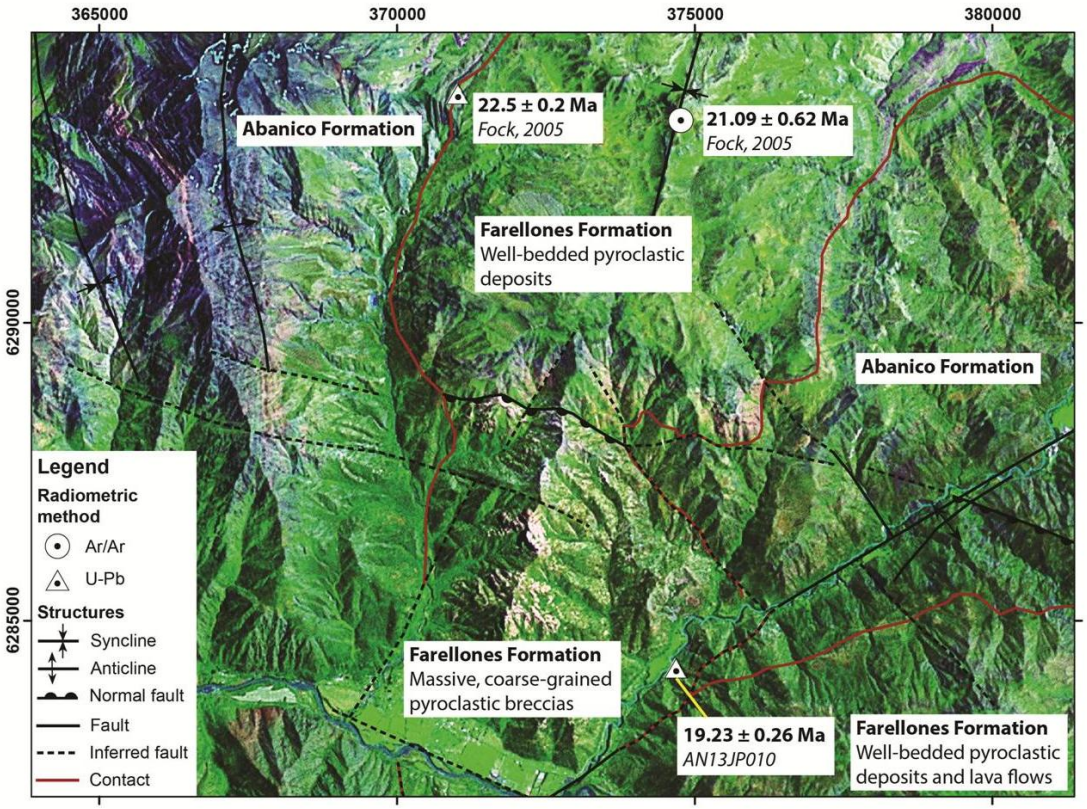

Figure 5.9. Satellite image from the area where sample AN13JP010 was collected (Fig. 5.1B), showing the main structural features and the boundaries between stratigraphic units.

The age ranges of the four main volcano-sedimentary units make it difficult to correlate the strongly folded rocks of the southern segment with the Abanico Formation, as well as the flat-lying rocks of the same area with the Farellones Formation. The Abanico Formation at its original type locality is composed of basaltic and andesitic lava flows, pyroclastic deposits and continental lacustrine intercalations (Nyström et al., 2003) with an age range of 31-25 Ma (Vergara et al., 1999). Volcanic and volcano-sedimentary rocks with a similar lithology and age range are found throughout the northern segment in two parallel belts that are separated by the Farellones Formation (Figs. 5.1A, 5.8). The Farellones Formation, in turn, can be divided at its type locality into a lower member composed of pyroclastic and volcano-sedimentary rocks and an upper member composed of well-bedded andesitic, basaltic and locally rhyolitic lava flows (Vergara et al., 1988). The total age range for the Farellones Formation at its type locality is 22-17 Ma (Drake et al., 1976; Aguirre et al., 2000; this work). The two members of the Farellones Formation can be followed throughout the northern segment of the study area; within

this segment they are consistent in terms of lithology and age, although with strong variations in thickness, particularly for the lower pyroclastic member (Rivera and Navarro, 1996; this work). To the south of the Piuquencillo fault system, the rocks of the Teniente Volcanic Complex are flat-lying to gently folded and occupy a central position within the inverted Abanico Basin, similar to the Farellones Formation (Fig. 5.8), but they are much younger in age. In a similar way, the Coya-Machali Formation is structurally similar to the Abanico Formation as it is strongly folded and crops out in two parallel belts separated by the Teniente Volcanic Complex (Fig. 5.8), but it has a larger volcano-sedimentary component and it is also considerably younger. The transition between the Coya-Machali Formation and the Teniente Volcanic Complex occurs at 13-12 Ma, ~10 m.y. later than the Abanico-Farellones transition in the northern segment. Previous authors (Charrier et al., 2002, 2005; Godoy, 2012) have already noted that the transition between strongly folded and flat-lying rocks in central Chile gets younger to the south, and have explained this as a diachronic contact. However, the new geochronological, geochemical and structural evidence presented in this study is more consistent with a sharp, fault-controlled boundary between two different segments of the basin, rather than progressive diachronism. In particular, the Coya-Machali Formation, both at its type locality and in the eastern portion in the Las Leñas river valley, is in fact coeval with the Farellones Formation, having no temporal overlap with the Abanico Formation.

It is proposed that the Coya-Machali Formation and the Teniente Volcanic Complex should be considered as separate stratigraphic units. They cannot be correlated in terms of lithology and age with the Abanico or Farellones formations. The term Farellones Formation should be restricted to the Miocene volcanic rocks of the northern segment. However, volcanic rocks coeval with the Abanico Formation (late Eocene-Oligocene), are not entirely restricted to the northern segment. They have been documented in the westernmost part of the southern segment next to the Central Depression (Fock, 2005; see Figs. 5.1A and 5.8) and also further to the south in the Tinguiririca River valley, next to the El Fierro thrust (Charrier et al., 1996). The contact relationship between these older rocks and the overlying Miocene rocks of the Coya-Machali Formation sensu stricto remains unclear. More specific work is needed to establish their proper stratigraphic assignation, either as a lower segment of the Coya-Machali Formation, in which case this unit would temporally overlap

both the Abanico and the Farellones formations, or as a separate stratigraphic unit which may be correlated with the Abanico Formation.

5.5.2 Exhumation and geochemical trends of igneous rocks

Figure 5.10 shows the current dataset of radiometric ages, from this work and previous publications, for rocks at the eight localities where new (U-Th)/He ages have been obtained. Also included in Figure 5.10 are two samples (AN12MB029 and AN12MB038) from middle to late Miocene intrusives rocks from which we obtained new U-Pb zircon ages, and for which previous workers obtained K-Ar and $^{40}Ar/^{39}Ar$ ages in biotite and fission track ages in zircons and apatites (Kurtz et al., 1997; Rivera and Falcon, 1998; Maksaev et al., 2009). Figure 5.10 shows that for middle-late Miocene plutons, U-Pb zircon, K-Ar biotite ages and zircon fission track ages are indistinguishable and probably reflect rapid magmatic cooling after emplacement. On the other hand, apatite fission track ages and (U-Th)/He ages in zircons and apatites are distinctly younger, suggesting they reflect exhumation-related cooling. The ten samples illustrated in Figure 5.10 include Oligocene-early Miocene Abanico Formation rocks, early Miocene plutons, middle Miocene Teniente Volcanic Complex rocks and middle to late Miocene intrusions, collected from across the study area (Fig. 5.1B). Despite the large variability in crystallization ages and geographic positions, the analysed samples clearly show a major exhumation event affecting the entire study area between 6 and 2 Ma (Fig. 5.10).

The new thermochronological and geochronological data can be combined with our expanded geochemical database to make inferences about the tectonic evolution of the Andes of central Chile. Various researchers have argued that the geochemistry of igneous rocks, in particular their REE ratios, can be used to infer the tectonic evolution of a region, as the ratio changes in response to changes in the nature of the magmatic source and REE are immobile under most types of hydrothermal alteration (Kay and Mpodozis, 2002; Haschke and Siebel, 2002; Haschke and Gunther, 2003; Hollings et al., 2005). Van Dongen et al. (2010) showed that high-temperature (>400°C) and high-salinity fluids can modify the REE signatures of magmatic rocks; however, these types of fluids are restricted to the potassic cores of porphyry

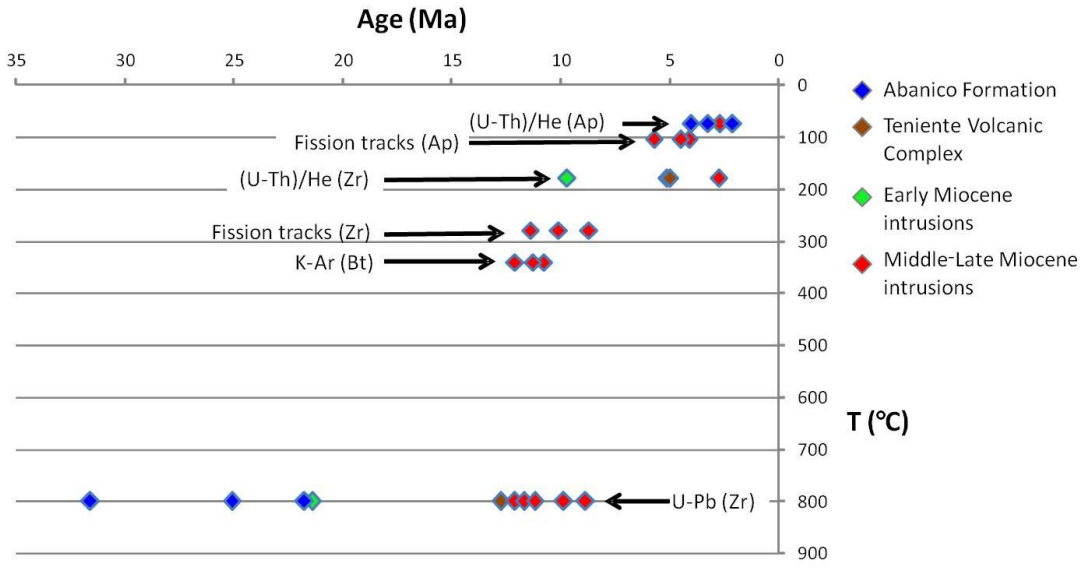

Figure 5.10. Temperature versus age plot for different radiometric methods applied to the eight samples dated in this work by (U-Th)/He in zircons and/or apatites. Closure temperatures used are 800°C for U-Pb in zircon, 340°C for K-Ar in biotite, 280°C for fission tracks in zircon, 180°C for (U-Th)/He in zircon, 105°C for fission tracks in apatite, and 75°C for (U-Th)/He in apatite. K-Ar ages from Rivera and Navarro (1996), Kurtz et al. (1997) and Rivera and Falcon (1998). Fission track ages from Maksaev et al. (2009).

systems, and none of the analysed samples was collected from rocks affected by that type of high-temperature alteration.

Kay and Kurtz (1995) and Kay and Mpodozis (2002) documented a gradual trend to increasing LREE abundances and HREE fractionation with decreasing age for the ~25 to ~5 Ma rocks in the vicinity of El Teniente. This was interpreted to be the result of increasing crustal thicknesses during tectonic inversion of the Abanico Basin, as well as a change from a pyroxene-dominated to amphibole-dominated and finally garnet-dominated lower crustal mineral assemblages. However, Hollings et al. (2005) proposed that regional data from central Chile showed very little difference in the LREE (La/Sm_n) or HREE (Sm/Yb_n) ratios between the Cretaceous Las Chilcas and the Tertiary Abanico and Farellones Formations and that the range of La/Yb ratios were broadly constant until the Pliocene. They interpreted this to indicate that rather than gradual thickening, the geochemical data preserved evidence of abrupt changes in the geochemistry coeval with the arrival to central Chile of the point of

subduction of the aseismic Juan Fernandez Ridge, according to the reconstruction of Yáñez et al. (2001).

The combined analysis of the new geochemical, structural, stratigraphic and chronological datasets allows for a more comprehensive evaluation of the tectonic evolution of central Chile. This integrated approach suggests the existence of three stages of crustal thickening and exhumation affecting this Andean segment during tectonic inversion of the Abanico Basin.

The first stage affected only the northern segment of the study area, and is reflected in our data by consistently higher REE ratios in the Farellones Formation compared with the other three volcano-sedimentary units (Fig. 5.6), suggesting it was extruded through a moderately thickened crust. This geochemical change occurred at ~22 Ma, after the formation of the progressive unconformities which separate the Abanico and Farellones formations, and after the initiation of plutonic activity in the northern segment. Regionally, this time period coincides with the first major shortening event affecting this Andean segment, evidence for which is recognized in both the Chilean and Argentinean flanks of the Cordillera (Giambiagi et al., 2003b; Farias et al., 2010). Compression caused tectonic inversion of the pre-existing extensional architecture of the Abanico Basin. This shortening event was temporally associated with late Oligocene-early Miocene initiation of a period of progressive increase in the absolute westward velocity of the South American plate (Silver et al., 1998).

The second stage is marked by a sharp increase in La/Yb ratios occurring at 12-9 Ma (Fig. 5.7), more pronounced in the northern segment but still recognizable in middle Miocene plutons from the southern segment, and also by the exhumation of the early Miocene Rio Colorado plutonic complex at 10-9 Ma, as suggested by (U-Th)/He ages (Fig. 5.10). Temporally, this event coincides with the transition in the southern segment between the strongly deformed Coya-Machali Formation and the shallowly-dipping Teniente Volcanic Complex. It is also coeval with the extension of plutonic activity to the southern segment, reflected by the emplacement in the central part of the Abanico Basin of a continuous plutonic belt with ages between 12 and 9 Ma. In both the northern and southern segments, the transition between strongly deformed and flat-lying units coincides with the initiation of plutonic activity, suggesting a

relationship between shortening, thickening of the crust and the emplacement of magmas at upper-crustal levels. In the Rio Blanco-Los Bronces district, the 12-9 Ma time range is associated with the development of non-economic hydrothermal systems (Toro et al., 2012; Chapter 3). To the north of the study area, this time period coincides with the termination of arc-related andesitic volcanism and the establishment of flat subduction (Kay et al., 1999). It is the period when the giant Los Pelambres porphyry Cu-Mo deposit (Perello et al., 2012) and the San Felipe cluster of porphyry Cu-Mo prospects (Toro et al., 2009) formed. This second stage of crustal thickening, deformation and exhumation coincides temporally with the arrival of the point of subduction of the Juan Fernandez ridge to the northern part of the study area (Yañez et al., 2001), consistent with a causal relationship between these two events as suggested by Hollings et al. (2005).

The third stage occurred between 7 and 2 Ma (Fig. 5.7) and corresponds to the main exhumation event affecting this part of the Andes, as shown by our (U-Th)/He data and by previous works based on (U-Th)/He and fission track analyses (McInnes et al., 2005; Maksaev et al., 2009; Fig. 5.10). It is also reflected in whole rock geochemistry by an extension to the south of the extremely high REE ratios (Fig. 5.6), similar to the ones observed in the northern segment after the second stage. Based on the study of Hf and Nd isotopic data, Muñoz et al. (2013) also observed a major change in the composition of igneous rocks of the Western Main Cordillera at ~5 Ma. They followed the interpretation of Farias et al. (2010), associating this geochemical change and the sudden thickening of the crust with westward underthrusting of basement rocks. The basement was detached from the upper part of the crust by a west-dipping, east-vergent detachment level associated with active seismicity and linked to the subduction zone. In contrast, Kay et al. (1999) and Hollings et al. (2005) interpreted radiogenic isotope data from central Chile to indicate localized assimilation of crustal material within the mantle wedge as a result of subduction erosion adjacent to a zone of ridge subduction. However, the simultaneous generation of more enriched magmas in the Eastern Main Cordillera and more primitive magmas in the Western Main Cordillera before ~5 Ma, and the westward expansion of enriched signatures after ~5 Ma (Muñoz et al., 2013), are better explained by the hypothesis of Muñoz et al. (2013). This suggests that the influence of the subducted material and mantle wedge processes in the isotopic

characteristics of the magmas is overwhelmed by the imprint given by the different lithospheric compositions through which the magmas have to ascend.

After the third stage of crustal thickening and exhumation, magmatic activity within the Abanico Basin terminated and the magmatic axis migrated ~50 km eastwards to its current position at the Eastern Main Cordillera (Fig. 1.2B).

5.6 Conclusions

Based on a combination of U-Pb geochronology, (U-Th)/He thermochronology, whole rock geochemistry and structural data, it is proposed that the Abanico Basin in central Chile can be divided into two main segments (Fig. 5.8). The boundary between them lies to the south of the Maipo-Volcan river valleys, and is controlled by the NW-striking Piuquencillo fault and probably by conjugate, NE-striking faults (Fig. 5.8). Correlation of stratigraphic units between both segments based on deformation style is not appropriate. This is well illustrated by the Coya-Machali Formation, which is similar to the Abanico Formation in terms of intensity of folding and outcrop pattern (Fig. 5.1A), but its depositional age is equivalent to the younger Farellones Formation. We propose that, while in the northern segment all the Tertiary volcanic and sedimentary rocks can be correlated with either the Abanico or the Farellones formations, this is not possible in the southern segment. The Abanico Formation may still be present, but it is overlain by the Coya-Machali Formation, which is early to middle Miocene in age and has a much larger volcano-sedimentary component. This unit is in turn covered by the Teniente Volcanic Complex, which is several m.y. younger than the youngest volcanic units of the northern segment.

The northern and southern segments also differ in their exhumation history and geochemical variations over time (Figs. 5.6, 5.7). The northern segment was affected by an early deformation event beginning at ~22 Ma, associated with the formation of progressive unconformities between the Abanico and Farellones formations. This was the time of initiation of plutonic activity in this segment and coincided with the onset of crustal thickening as reflected in the geochemistry of the Farellones Formation. There is no evidence for this event having affected the southern segment (Figs. 5.6, 5.7). A second stage of crustal thickening and exhumation began at ~12 Ma. This event is reflected by a sharp increase of La/Yb ratios in the already

thickened crust of the northern segment (Figs. 5.6, 5.7). In the southern segment is characterized by a moderate increase of La/Yb ratios (Figs. 5.6, 5.7), the initiation of plutonic activity and the transition between the Coya-Machali Formation and the Teniente Volcanic Complex. Finally, a third stage of exhumation and crustal thickening, beginning at ~6 Ma, affected both the northern and southern segment. This last stage was the main exhumation event affecting the rocks of the Andes of central Chile (Fig. 5.10), and is coeval with the formation of large hydrothermal breccia complexes associated with the porphyry Cu-Mo deposits of the area. Geochemically, this event is reflected by a sharp increase in La/Yb ratios at the southern segment.

Chapter 6 Structural Evolution of the Andean Main Cordillera of Central Chile

6.1 Introduction

Segments of the Andean orogenic system have, during specific time periods, accommodated part of the plate convergence obliquity by arc-parallel strike-slip faulting. Examples of this type of faulting in the Chilean Andes can be found in the Atacama fault system (Jurassic-Cretaceous arc of northern Chile; Arabasz, 1971; Scheuber and Andriessen, 1990), the Domeyko or Precordilleran fault system (Eocene-Oligocene arc of northern Chile, Fig. 1.1; Reutter et al., 1991, 1996; Tomlinson et al., 1994) and the Liquiñe-Ofqui fault system (Jurassic-Quaternary arc of southern Chile; Herve, 1976, 1994; Cembrano et al., 1996). These trans-lithospheric structures have exerted strong controls on magmatism, including the emplacement of porphyry copper deposits and the location of active volcanoes (Maksaev and Zentilli, 1988; Reutter et al., 1991; Herve, 1994; Cembrano et al., 1996; Grocott and Taylor, 2002).

On the other hand, some segments of the Andean orogen have not developed major arc-parallel strike-slip fault systems. One such segment is the Central Chilean Andes (Fig. 6.1), an area of particular economic significance as it contains the world's largest exploitable concentrations of Cu and Mo in two giant porphyry deposits of late Tertiary age, Rio Blanco-Los Bronces and El Teniente (Sillitoe, 2010). In the absence of obvious arc-parallel fault systems, the structural controls on Tertiary magmatism and hydrothermal fluid flow have remained enigmatic (e.g., Mpodozis and Cornejo, 2012). However, regional-scale geological mapping and geophysical studies (Chapters 3 and 4) have shown that fault systems oblique to the continental margin and to the magmatic axis played an important role in the tectonic evolution of the Andes of Central Chile, and in particular, are relevant for understanding the structural controls on magmatism and hydrothermal activity in this segment.

This chapter presents the first systematic study of fault orientation, kinematics and paleo-stress calculations for the Andes of Central Chile. It is based on a structural database of 650 fault planes, 391 with kinematic information. Structural data come

from across the entire Main Cordillera of central Chile to the east of the city of Santiago, from the Aconcagua to the Cachapoal river valleys (Fig. 6.1). The study area contains the Rio Blanco-Los Bronces and El Teniente porphyry Cu-Mo deposits (Fig. 6.1B).

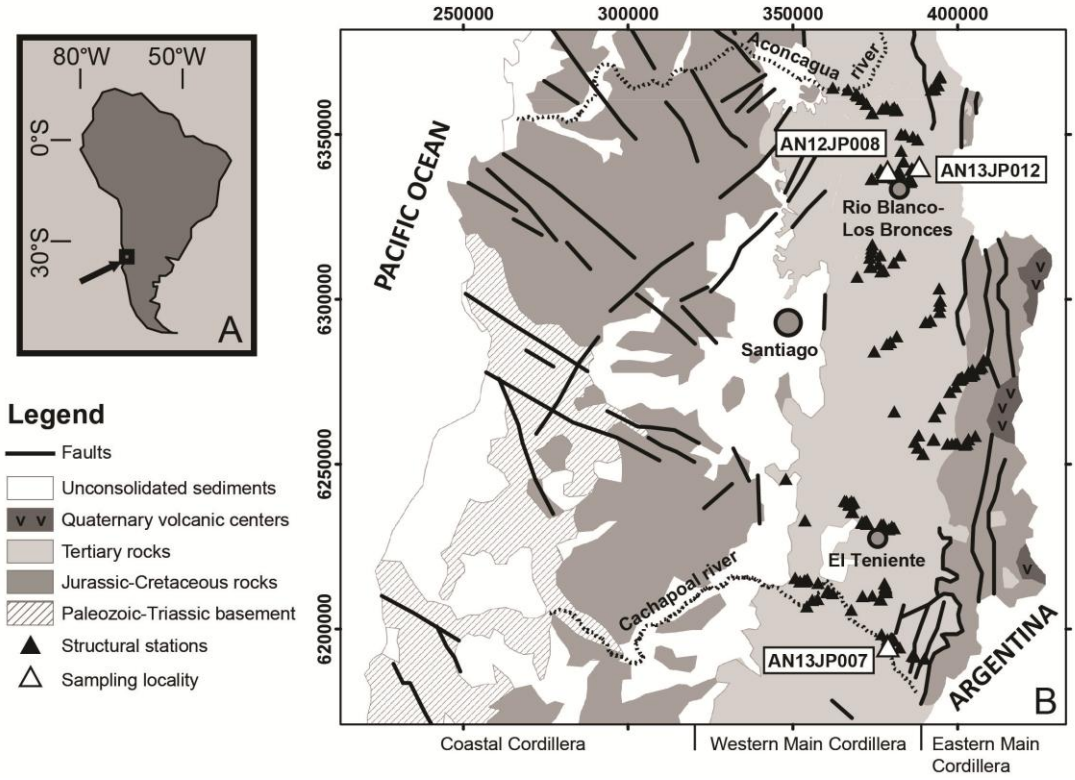

Figure 6.1. A. Location of the study area in South America. B. Main geological and morphological units of the Andes of central Chile. The location of structural stations and the sampling localities for $^{40}Ar/^{39}Ar$ geochronology are shown, as well as geographical features mentioned in the text.

6.2 Regional context: the Andes of central Chile

The geological history of central Chile is characterized by eastward migration of the magmatic arc in successive steps from the Jurassic to the Quaternary (Mpodozis and Ramos, 1989). The Coastal Cordillera, a N-trending mountain range parallel to the western coast of South America, marks the position of the Jurassic and Cretaceous magmatic arc, and consists mainly of Mesozoic volcanic, intrusive and sedimentary rocks. These Mesozoic rocks overlie late Palaeozoic to Triassic intrusive and metamorphic rocks, commonly termed the "basement" of the Andes. The Main Cordillera of central Chile is located to the east of the Coastal Cordillera, and can be

subdivided into western and eastern sections (Fig. 6.1B). The Western Main Cordillera, the focus of this work, was the position of the Tertiary magmatic arc and is dominated by Tertiary volcanic, intrusive and sedimentary rocks. The eastern Main Cordillera is characterized by Mesozoic, mainly sedimentary, units.

The mid-Tertiary magmatic arc of central Chile was characterized by extensional tectonics leading to the formation of the Abanico Basin, an intra-arc volcano-tectonic basin (Charrier et al., 2002). The basin was filled with up to 5 km of volcanic and volcano-sedimentary rocks (Chapter 3), which have been grouped into the late Eocene-early Miocene Abanico and Coya-Machali formations (Aguirre, 1960; Klohn, 1960). Basin-margin faults have been interpreted at some localities (Charrier et al., 2002; Fock et al., 2005; Farias et al., 2010; Piquer et al., 2010) as E- or W-dipping, high-angle, arc-parallel fault systems which were active as normal faults during the late Eocene-Oligocene. However, the basin-margin faults are discontinuous – they have not been mapped along the entire area (Fig. 6.1). The regional-scale internal structural architecture of the basin is dominated by NE- and NW-trending fault systems, oblique to the basin-margin faults and the magmatic arc (Chapter 4).

The basin was partially inverted in the Miocene-early Pliocene (Godoy et al., 1999; Charrier et al., 2002). The first pulses of compressional deformation occurred in the early Miocene (Charrier et al., 2002; Giambiagi et al., 2003b). Lavenu and Cembrano (1999), based on fault-slip data from central and southern Chile, identified two late Cenozoic deformation events. The first one is a compressional event of Pliocene age, associated with an E-W striking σ_1. The second event, which is of Quaternary age, is partitioned between two coeval stress states: compression in the present-day fore-arc, with N- to NNE-oriented σ_1, and transpression in the intra-arc zone with σ_1 striking NE. Tectonic inversion of the Abanico Basin under compressive regime was accompanied by a marked decrease in volcanic activity, growth of upper crustal magma chambers and, during the late Miocene-early Pliocene, the formation of giant porphyry Cu-Mo deposits (Mpodozis and Cornejo, 2012). Miocene volcanic rocks deposited during tectonic inversion are subdivided into the Farellones Formation (Klohn, 1960) and the slightly younger Teniente Volcanic Complex (Kay et al., 2005).

The last pulses of Tertiary magmatism in the Western Main Cordillera correspond to porphyries and diatremes emplaced in and around the mineral deposits during the early Pliocene (Maksaev et al., 2004; Deckart et al., 2005). Subsequently, magmatism migrated ~50 km to the east, to its current position in the Eastern Main Cordillera. The products of Pleistocene-Holocene volcanoes cover Mesozoic sedimentary rocks deposited in back-arc basins. These Mesozoic sequences underwent strong thin-skinned deformation during the Miocene, defining the Aconcagua fold and thrust belt, which is best exposed in the Argentinean flank of the Andes (Ramos, 1996). The volcanoes of the Eastern Main Cordillera of central Chile are the northernmost active volcanoes of the Southern Volcanic Zone of the Andes. To the north of the study area, the Chilean flat-slab segment underlies the Cordillera, which is reflected in a widening of the orogenic belt and in the absence of active volcanism (Kay et al., 1999).

6.3 Methodology

This study is based on the result of more than four months of field work, during which structural and stratigraphic information was collected in the Andes of central Chile. Efforts were made to achieve a good distribution of structural stations across the study area (Fig. 6.1), within the limitations imposed by the extreme topography. Transects were completed along major river valleys, and measurements were also collected around mining operations and ski resorts. At each structural station, the strike and dip of every fault plane was measured and information about the width of the fault and its damage zone was collected. When present, the pitch of fault plane striation and slickenfibres were measured. The sense of movement was established when possible, by using kinematic criteria for brittle faults (e.g., Petit, 1987). The type of kinematic indicator used was always recorded. Steps in slickenfibres were the most common indicator, followed by other criteria such as syn-tectonic minerals precipitated in strain fringes, dilational jogs filled by hydrothermal minerals or magma, displacement of markers and P-only surfaces (Petit, 1987). A total of 651 fault planes were measured, and 391 of them (60%) yielded reliable kinematic information. Additionally, three samples containing syn-tectonic hydrothermal minerals (Fig. 6.1) were analysed by the $^{40}Ar/^{39}Ar$ method to establish the age of fault activity. The samples were studied at the Argon Geochronology Laboratory of

the Oregon State University; analytical methods are described in Appendix IIA, and the complete analytical results are contained in Appendix IIB.

Predominant fault plane orientations were studied using the Stereonet™ software (Allmendinger et al., 2012). Kinematic and dynamic analyses were completed for 391 fault planes containing kinematic information. The fault-slip data was grouped according to different criteria to determine the spatial and temporal variations in the stress regime. For the kinematic analysis, the FaultKin™ software (Marrett and Allmendinger, 1990; Allmendinger et al., 2012) was used to calculate the orientation of the pressure and tension axes for each individual fault plane and the average kinematic axes (shortening, stretching and intermediate axes) for different fault populations.

For the dynamic analysis, the Multiple Inverse Method (Yamaji, 2000) was used to calculate the orientation of paleo-stress tensors from the inversion of fault-slip data. This method allows the identification of separate stress states from heterogeneous data sets. A stress state is defined by four parameters: the orientation of the three principal stresses and the stress ratio $\Phi = (\sigma_2-\sigma_3)/(\sigma_1-\sigma_3)$. To obtain the stress states, the program takes all the possible groups of k faults from the fault-slip database. The number k is referred to as the fault combination number, and is entered by the user; the software developers recommend k=5 for most datasets, or k=4 if the dataset is particularly large (more than 122 fault planes). A larger k value does not significantly change the results, while for $k<4$ the inversion solution is an under-determined problem. To calculate the optimal stress tensor for each of the groups of k fault planes, the software uses classical stress inversion methods based on the Wallace-Bott hypothesis (Wallace, 1951; Bott, 1959). It attempts to minimise the misfit angle, defined as the angle between the observed and theoretical slip direction on a fault plane (the latter obtained from an assumed stress state). If the software cannot find an optimal stress state for one of the groups of k faults, that group is said to be incompatible and discarded. An optimal stress state is defined as one with a misfit angle of less than 20° for each of the k fault planes contained in the group.

The program allows visualizing all the calculated optimal stress tensors for the different groups of k faults generating a paired stereoplot for σ_1 and σ_3. If all of the

calculated stress orientations for each of the groups of k faults plot in one single cluster, it means the fault-slip data are homogeneous and can be explained by a unique state of stress. If the data are heterogeneous, then it will form different clusters, each of them representing a different stress state.

6.4 Structural evolution of the Main Cordillera of Central Chile

Two discontinuous, arc-parallel, N-striking high-angle reverse fault systems bound the Tertiary belt of central Chile (Fig. 6.2). They juxtapose Tertiary rocks in the hanging wall with Mesozoic rocks in the footwall and consequently are interpreted as inverted basin-margin normal faults (Charrier et al., 2002; Chapter 3, Fig. 3.8).

Between the inverted basin-bounding faults, the Main Cordillera is dominated by arc-oblique, high-angle, NW- and NE-trending faults (Fig. 6.2). These oblique fault systems also preserve evidence of early normal movements, with syn-extensional deposition of volcanic rocks in the hanging walls. Figure 6.3 illustrates a sequence of Oligocene pyroclastic rocks of the Abanico Formation deposited syn-extensionally in the hanging wall of a NE-striking, NW-dipping fault. The pyroclastic rocks are absent in the footwall block. Their thickness increases to more than 800 meters towards the hinge of an incipient hanging wall syncline (Fig. 6.3). Kinematic indicators in fault planes, however, reflect strike-slip ± reverse movements (Fig. 6.4), suggesting that these structures, as for the basin-margin faults, were also reactivated during basin inversion.

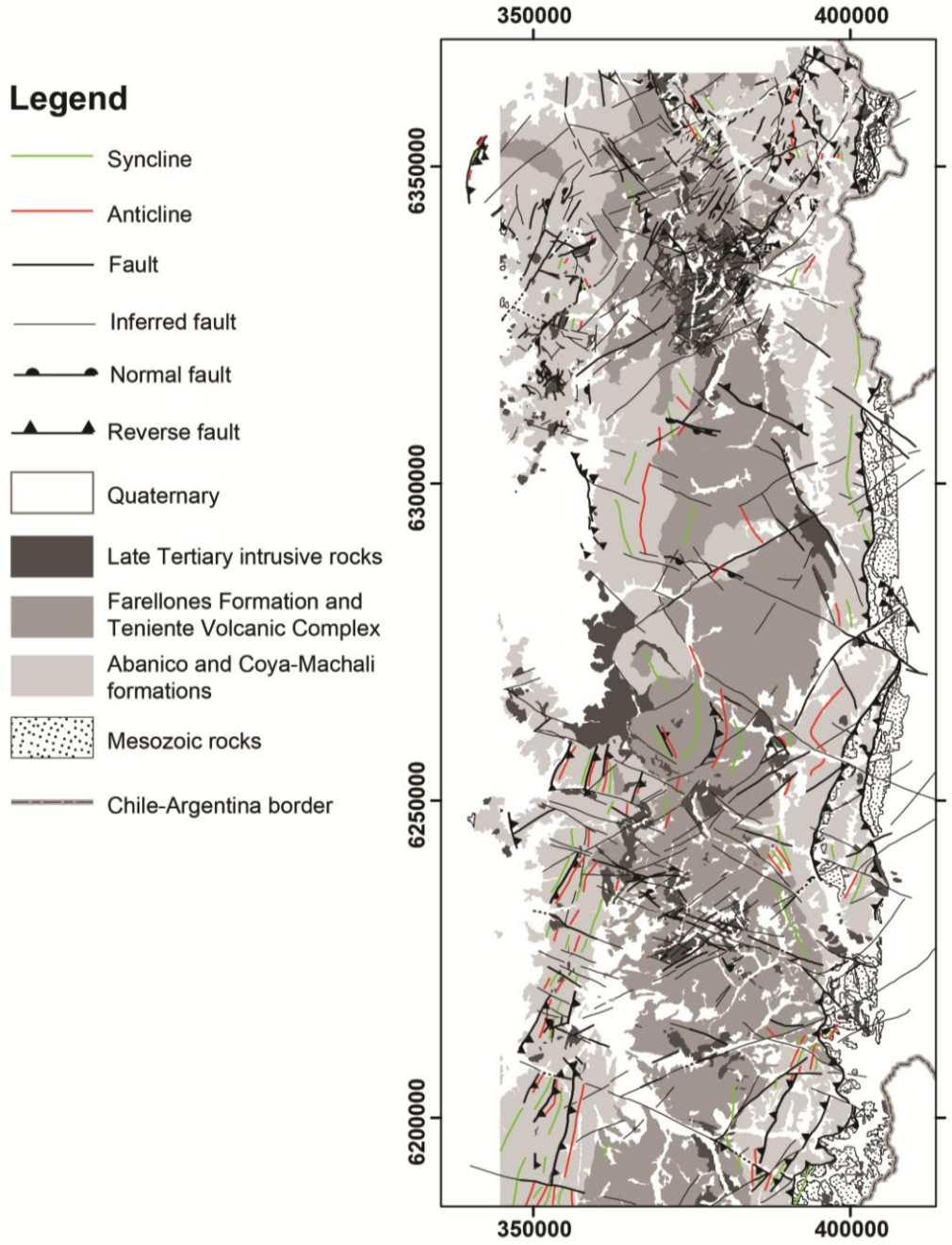

Figure 6.2. Simplified geological map of the Andes of central Chile, based on Rivera and Cembrano (2000), SERNAGEOMIN (2002), Fuentes et al. (2004), Fock et al. (2005) and this work.

6.4.1 Syn-tectonic hydrothermal and magmatic activity

Across the study area, fault surfaces are coated by a wide range of hydrothermal minerals that precipitated during fault slip (Fig. 6.4). This includes observations collected in the halo surrounding the porphyry Cu-Mo deposits of the area (Rio

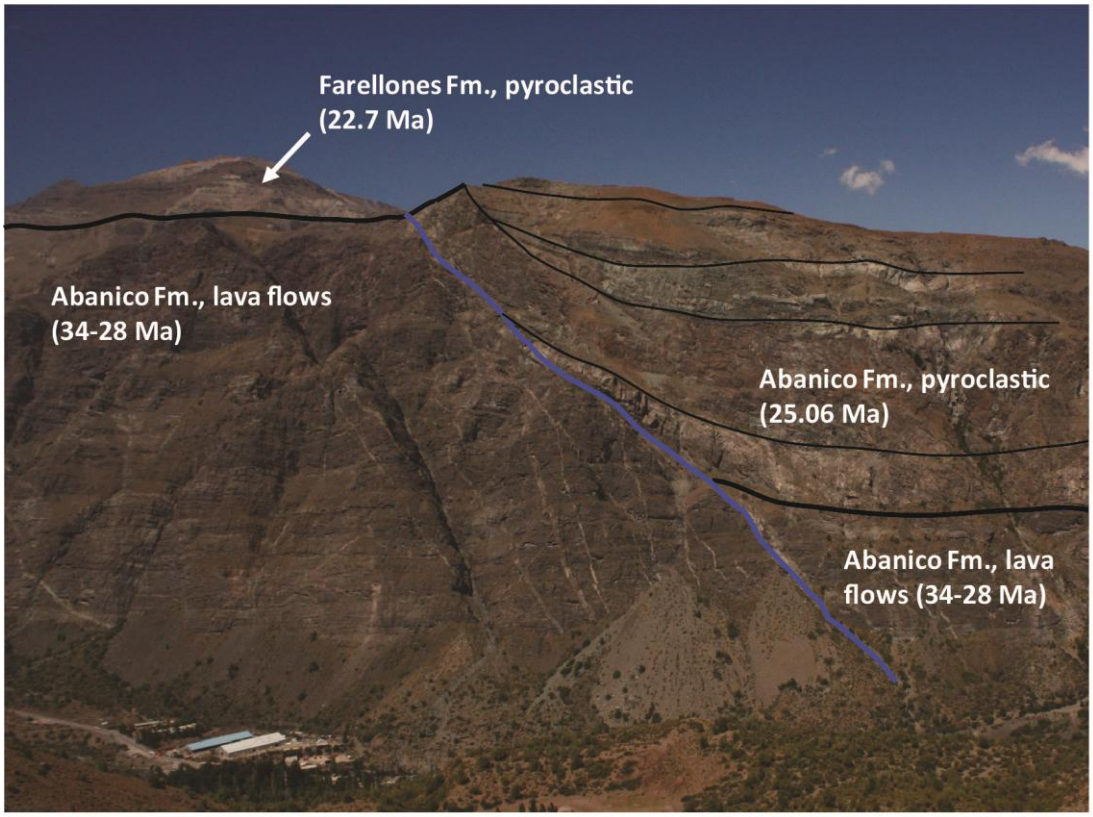

Figure 6.3. Syn-extensional sequence of Oligocene volcanic rocks. About 800 metres of pyroclastic deposits were accumulated in the hanging wall of a NE-striking, NW-dipping high-angle fault system (blue line). They are covered by early Miocene pyroclastic deposits, which are not affected by normal faulting. Black lines represent bedding. View SW from 381197mE, 6357471mN.

Blanco-Los Bronces and El Teniente; Fig. 6.1). Evidence for syn-tectonic precipitation of hydrothermal minerals was found in different generations of veins, from high-temperature biotite and actinolite veins associated with early stages of hydrothermal activity to lower temperature, later-stage veins composed of minerals such as tourmaline or muscovite, and more distal epidote, chlorite, calcite and/or barite veins (Fig. 6.4).

Arc-oblique fault systems exerted a strong spatial control on the location and geometry of Miocene-early Pliocene plutons (Fig. 6.2); the different intrusive facies are either strongly elongated following one of the oblique structural trends, or they have rhombic shapes with their margins being parallel to NE- and NW-trending fault systems. Evidence of syn-tectonic magmatism is given by magmas emplaced in

dilational jogs along arc-oblique strike-slip faults and in sets of en-echelon dilational lenses (Fig. 3.13).

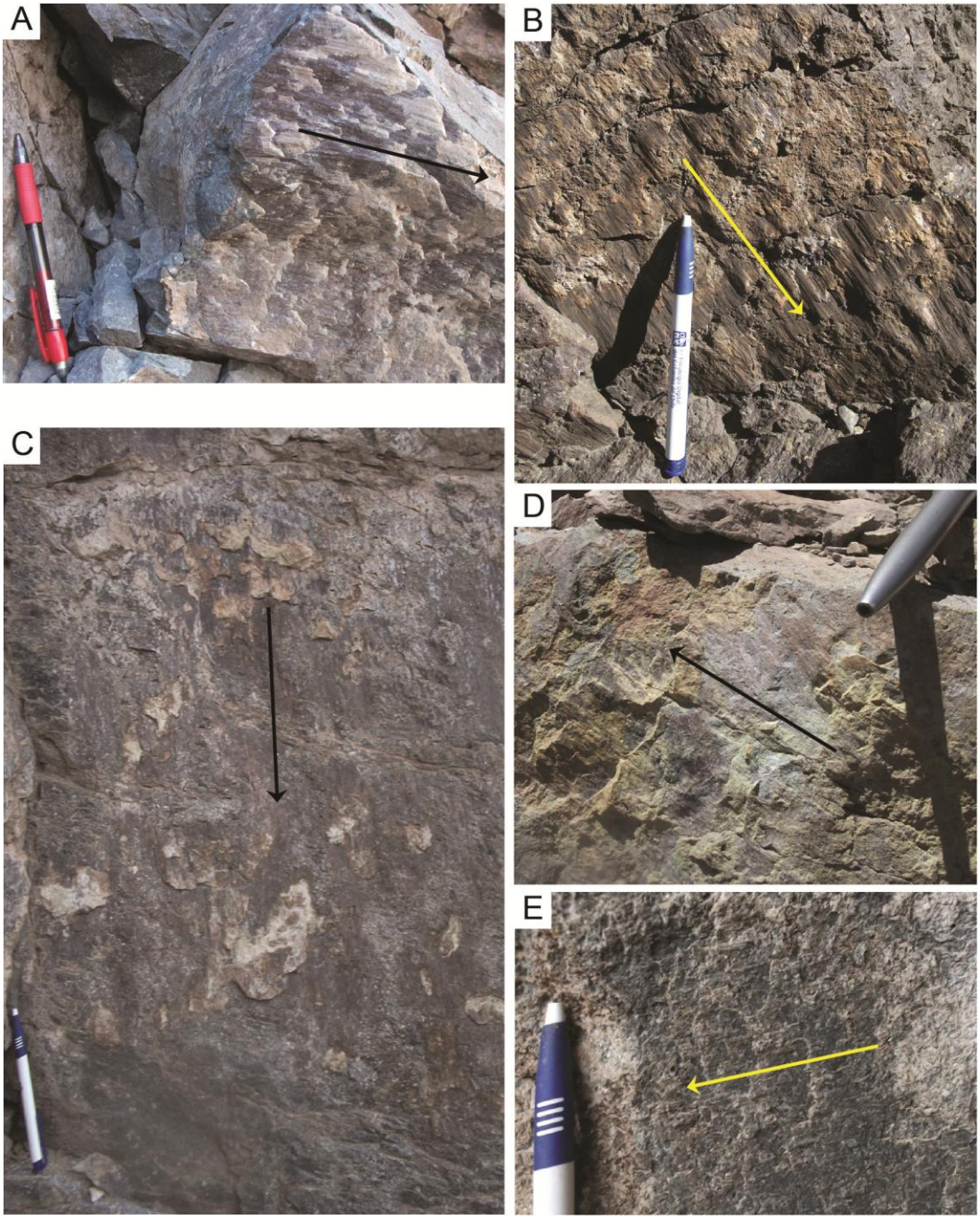

Figure 6.4. Examples of steps in syn-tectonic hydrothermal mineral fibres. Arrows indicate sense of movement of the missing block. A. Steps in calcite fibres; 394514mE, 6367346mN. B. Steps in quartz fibres; 389901mE, 6191043mN. C. Steps in calcite fibres; 393032mE, 6264509mN. D. Steps in epidote fibres; 381687mE, 6357528mN. E. Steps in tourmaline-quartz fibres; 387888mE, 6255000mN.

6.4.2 Chronological constrains on fault activity

The measured fault planes cut across rocks ranging in age from Late Jurassic to early Pliocene. As mentioned before, most of the kinematic indicators are associated with steps in slickenfibres, and in general, syn-tectonic hydrothermal minerals are ubiquitous (Fig. 6.4). The age range of hydrothermal activity within the segment considered in this study is constrained to the middle Miocene-early Pliocene (~14-4 Ma; Maksaev et al., 2004; Toro et al., 2012; Deckart et al., 2013), giving a first approximation to the age of fault activity.

Syn-tectonic biotite has been dated ($^{40}Ar/^{39}Ar$) in the Los Bronces sector of the Rio Blanco-Los Bronces cluster (Silva and Toro, 2009). Biotite crystals with textural evidence of syn-tectonic crystallization were collected from a NNW-striking shear zone of unknown sense of movement. All the calculated ages fall within the 7-6 Ma range.

To further constrain the age of fault movement, three samples (Fig. 6.1) were collected from fault planes containing syn-tectonic hydrothermal minerals. They were dated using the $^{40}Ar/^{39}Ar$ step heating method (Table 6.1, Fig. 6.5, Appendix IIA).

Sample AN12JP008 was collected on a fault plane striking at 75° and dipping 80°N, which contains syn-tectonic actinolite fibres. These slickenfibres define a slip vector with a pitch of 10°W, and a dextral sense of shear with a minor reverse component. A plateau age of 9.72 ± 0.09 Ma (late Miocene) was obtained from the analysis of actinolite crystals. The faulted rock corresponds to a granodioritic pluton with a U-Pb zircon age of 11.68 ± 0.26 Ma (Table 3.1, sample AN12JP008), about two million years older than the fault movement.

Sample AN13JP012 was also collected form a fault plane with actinolite syn-tectonic fibres. The strike of the fault plane is N65°W, and it dips 65°S. The slip vector has a pitch of 18°E, and steps in the slickenfibres indicate a sinistral strike-slip movement with a minor normal component. The calculated plateau age is 9.68 ± 0.24 Ma (Late Miocene), identical within error to the actiolite age calculated from sample AN12JP008, which was collected ~6 km to the WSW. The faulted rock in the

locality where sample AN13JP012 was collected corresponds to a Monzonite with a K-Ar age in magmatic biotite of 14.2 ± 0.5 Ma (Rivera and Navarro, 1996).

Sample AN13JP007 was collected in the southernmost part of the study area (Fig. 6.1), and it contains syn-tectonic muscovite crystals coating a fault plane striking N65°E and dipping 85°N. Striation has a pitch of 18°E, and the sense of movement is dextral with a reduced normal component. The step-heating process yielded a very good plateau age of 13.04 ± 0.07 (upper Late Miocene; Fig. 6.5). The volcanic rocks which are affected by the fault belong to the Coya-Machali Fm., which has a zircon U-Pb age range of 16-12 Ma (this work, Chapter 5.3.1).

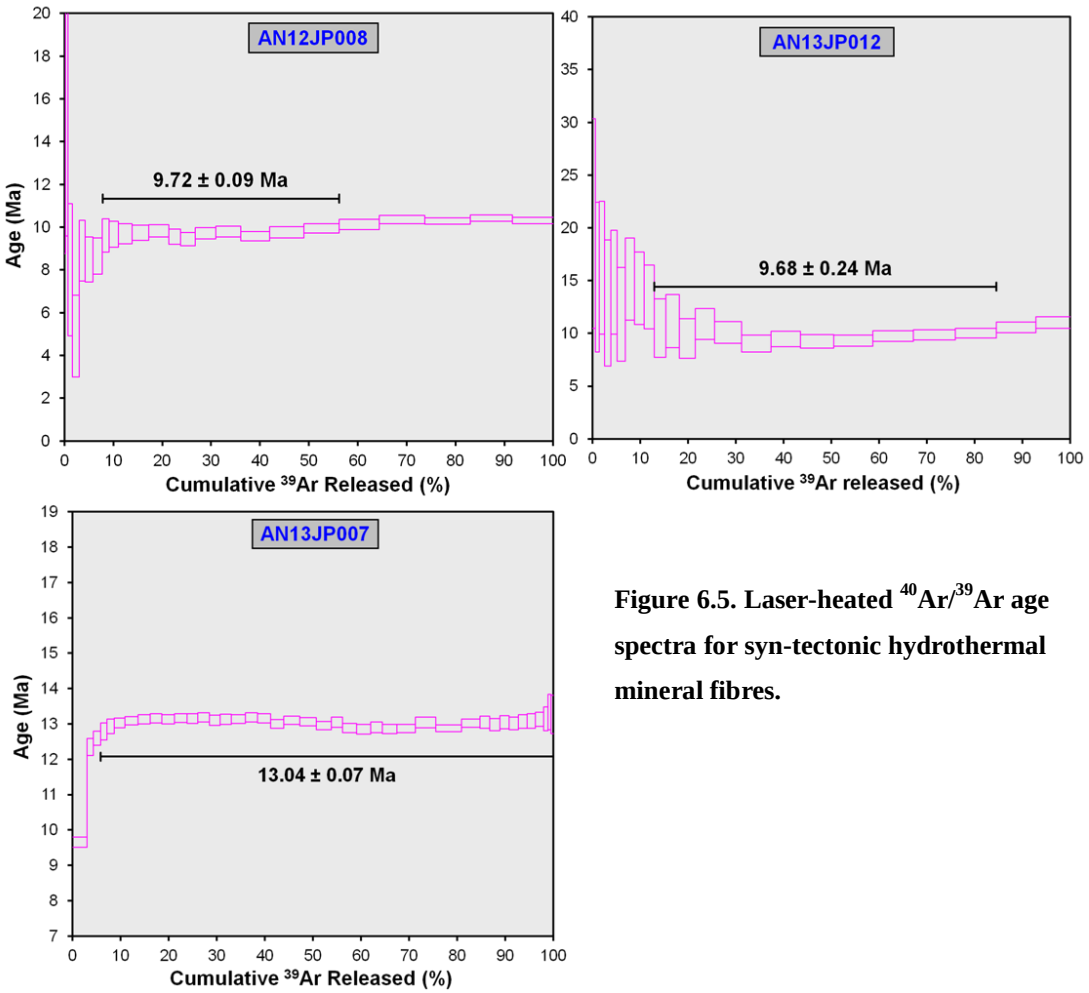

Figure 6.5. Laser-heated ^{40}Ar/^{39}Ar age spectra for syn-tectonic hydrothermal mineral fibres.

Table 6.1. Summary of $^{40}Ar/^{39}Ar$ results in syn-tectonic hydrothermal minerals

Sample	N (UTM)	E (UTM)	Elevation	Geological unit	Mineral	Age (Ma) (±2σ)
AN12JP008	6336679	380467	3248	Rio Blanco Granodiorite	Actinolite	9.72 ± 0.09
AN13JP007	6197015	379720	1288	Coya-Machali Fm.	Muscovite	13.04 ± 0.07
AN13JP012	6339690	386148	3108	Monzonite	Actinolite	9.68 ± 0.24

6.5 Analysis of fault plane data: results

The strikes of the 651 fault planes in our database are illustrated by the half-circle rose diagram in Figure 6.6A. Consistent with the regional-scale fault architecture illustrated in Figure 6.2, strong arc-oblique strikes dominate. N-striking, arc-parallel faults are subordinate and spatially restricted to the vicinity of the inverted basin margins. In general, the dominant ENE and WNW fault strikes evident in the rose diagram are slightly oblique to the NE and NW strikes of most of the regional-scale faults (Fig. 6.2). Kinematic evidence indicates slip on the ENE-striking fault planes commonly involves a dextral component, while slip on the WNW-striking faults is dominated by sinistral movement (Fig. 6.6B, C). Collectively, these kinematic and geometrical relations suggest that many of the measured fault planes correspond to R-type Riedel faults, developed in the damage zones of the main faults.

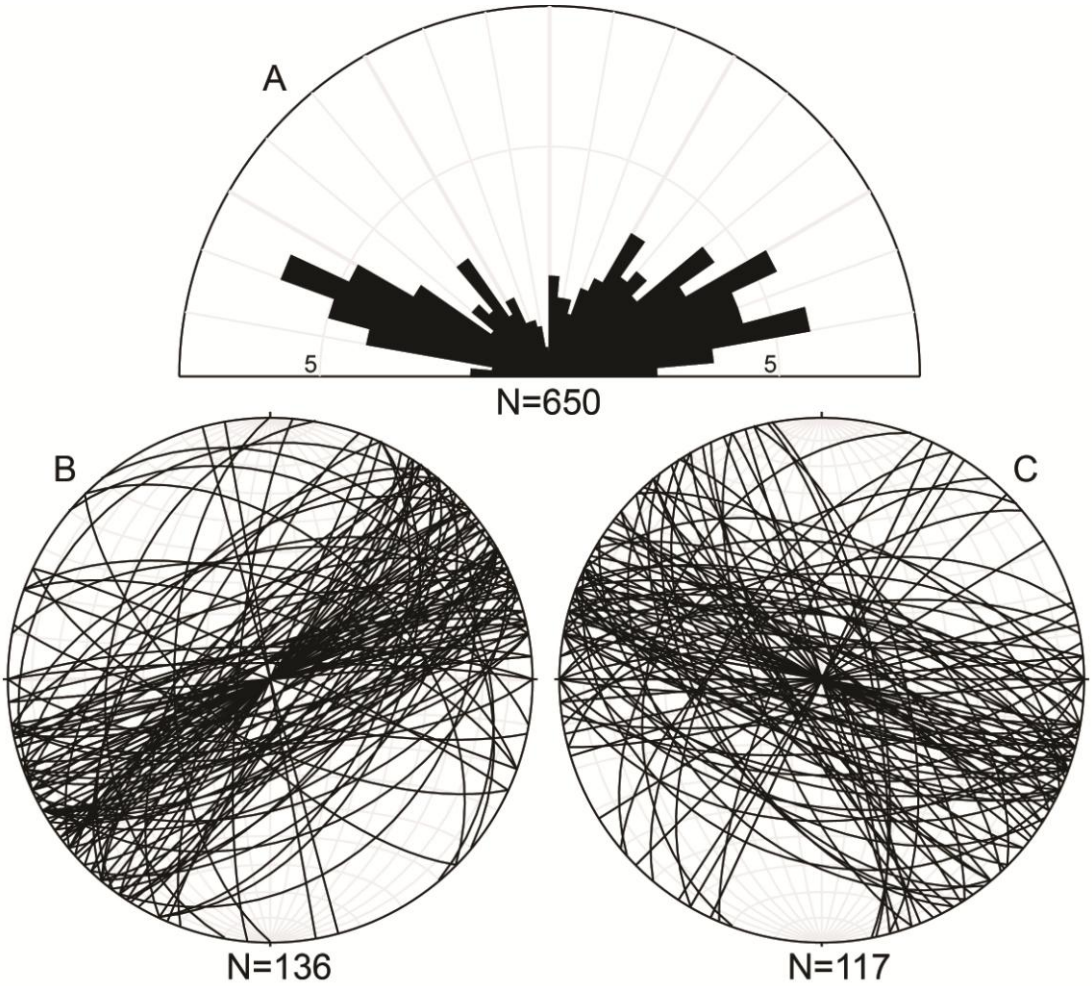

Figure 6.6. A. Half-circle rose diagram for the 650 fault planes measured in the Andes of central Chile. B. Lower hemisphere, equal-area projection of fault planes with a dextral strike-slip component and striations with pitch ≤ 45°. C. Same as in B but for fault planes with a sinistral slip.

6.5.1 Structural blocks

The study area was subdivided into structural blocks, defined here as geographically restricted areas with a well-defined lithotype and age range and a homogeneous deformation style. The structural blocks identified contain from 1 to 21 structural stations. Thirty one structural blocks were defined; their distribution is shown in Figure 6.7, and a summary of their lithological characteristics and age is provided in Table 6.1.

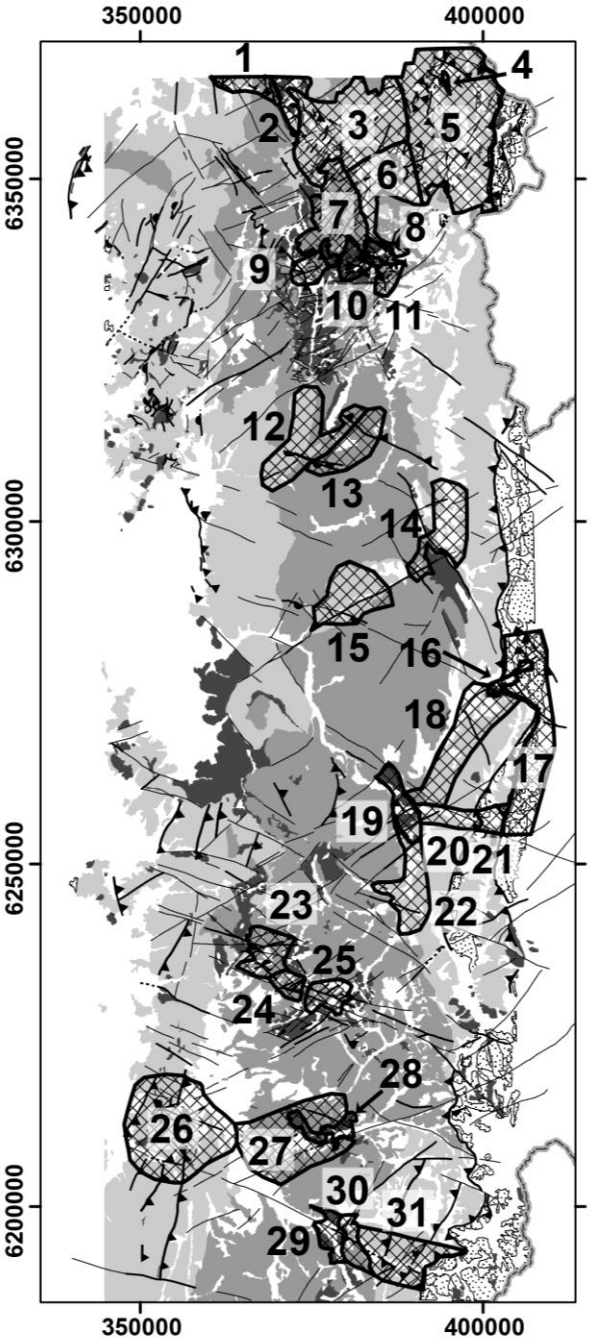

Figure 6.7. Location of the 31 structural blocks into which the study area was subdivided, shown over the geological map. Legend as in Fig. 6.2.

Figure 6.8 shows the result of the kinematic and dynamic analysis for each of the structural blocks. Four of them (2, 4, 15 and 29) contain less than four measured fault planes, and consequently were not used for the dynamic analysis. Structural blocks 19 and 28 contain four and five fault planes respectively, but all the possible subgroups of faults were found to be incompatible with any unique stress tensor. As a result of this, it was only possible to carry out dynamic analyses on 25 of the 31 structural blocks shown on Figure 6.7.

Table 6.2. Summary of the lithological units present in each of the 31 structural blocks defined in the study area. Age ranges from Gana and Wall (1997), Kurtz et al. (1997), Rivera and Falcon (1998), Baeza (1999), Aguirre et al. (2000), Charrier et al. (2002), Deckart et al. (2005, 2010), Muñoz et al. (2006), Montecinos et al. (2008) and this study.

Structural block	Geological unit	Lithology	Age range
1	Abanico Formation	Andesitic lava flows, pyroclastic intercalations	34-22 Ma
2	Rio Colorado batholith	Granodiorite	22-21 Ma
3	Abanico Formation	Andesitic lava flows, pyroclastic intercalations	34-25 Ma
4	Sills in Abanico Formation	Granodiorite	12-11 Ma
5	Abanico Formation	Andesitic lava flows, pyroclastic intercalations	34-25 Ma
6	Abanico Formation	Andesitic lava flows, pyroclastic intercalations	34-25 Ma
7	Farellones Formation	Andesitic lava flows and pyroclastic deposits	22-16 Ma
8	Estero Barriga Intrusive Complex	Quartz-monzonite	15-14 Ma
9	San Francisco batholith	Syenogranite	16-15 Ma
10	Rio Blanco Granodiorite	Granodiorite	12-11 Ma
11	Farellones Formation	Andesitic lava flows	17-16 Ma
12	Abanico Formation	Volcano-sedimentary deposits, pyroclastic intercalations	26-18 Ma
13	Farellones Formation	Andesitic lava flows, dacitic and rhyolitic intercalations	22-19 Ma
14	Abanico Formation	Andesitic lava flows, pyroclastic intercalations	31 Ma
15	Abanico Formation	Andesitic lava flows, pyroclastic and volcano-sedimentary deposits	31-19 Ma
16	Meson Alto pluton	Granodiorite	12-11 Ma
17	Rio Damas, Lo Valdes and Colimapu formations	Limestones, sandstones and conglomarates	Oxfordian-Albian
18	Abanico Formation	Andesitic lava flows, volcano-sedimentary intercalations	27-25 Ma
19	San Gabriel pluton	Granodiorite	12-11 Ma
20	Abanico Formation	Andesitic lava flows	34-21 Ma

21	Abanico Formation	Andesitic lava flows	34-25 Ma
22	Abanico Formation	Andesitic lava flows, volcano-sedimentary intercalations	34-21 Ma
23	Teniente Volcanic Complex	Pyroclastic deposits	13-12 Ma
24	Teniente Volcanic Complex	Andesitic lava flows	12-8 Ma
25	Teniente Volcanic Complex	Andesitic lava flows	12-8 Ma
26	Coya-Machali Formation	Volcano-sedimentary deposits, pyroclastic intercalations	23-13 Ma
27	Teniente Volcanic Complex	Andesitic lava flows	12-8 Ma
28	Pangal Intrusive Complex	Granodiorite	10-9 Ma
29	Cortaderal Intrusive Complex	Granodiorite	12-11 Ma
30	Teniente Volcanic Complex	Andesitic lava flows, pyroclastic intercalations	12-8 Ma
31	Coya-Machali Formation	Andesitic lava flows, volcano-sedimentary intercalations	16-12 Ma

Table 6.2. (Cont.)

Strong spatial patterns are evident from the analysis of structural blocks. In the structural blocks located close to the Rio Blanco-Los Bronces porphyry Cu-Mo cluster (structural blocks 7, 9, 10 and 11; Figs. 6.7, 6.8),fault-slip data is consistent with strike-slip regime under E-W compression (E-W trending, sub-horizontal shortening axis and σ_1; N-S oriented extension axis and σ_3; and sub-vertical intermediate kinematic axis and σ_2). No secondary clusters were recognized by the Multiple Inverse Method. Toward the east, structural block 6 shows a similar pattern of E-W compression and N-S extension, but a secondary cluster of sub-vertical σ_3 is evident using the Multiple Inverse Method. To the east of block 6, block 5 is composed of strongly deformed rocks of Abanico Formation, close to the eastern inverted basin-margin faults and the contact with the Mesozoic units (Fig. 6.7). Block 5 was also affected by E-W compression, but the stereographic projection for σ_3 shows two main steeply plunging clusters, while the average stretching kinematic axis is sub-vertical (Fig. 6.8). This indicates that in this area E-W shortening was mostly accommodated by reverse faulting. The rocks affected by faulting at blocks 5 and 6 belong to the same unit and age range (Table 6.1), and the same syn-tectonic hydrothermal minerals are found on the fault planes. This suggests that different stress regimes operated at the same time in different parts of the Abanico Basin during tectonic inversion. A similar situation can be observed around the El Teniente porphyry Cu-Mo deposit, at the transition between structural blocks 30 and 31 (Figs. 6.7, 6.8) which are both composed of late Tertiary volcanic rocks. In block 30, located in the central part of the inverted Abanico Basin, faulting is consistent with a strike-slip deformational regime, while at block 31, located immediately to the east and closer to the eastern basin margin, a dominant sub-vertical cluster for σ_3 indicates shortening was accommodated by reverse faulting.

Fault-slip data of most structural blocks is consistent with faulting under E- to ENE-directed compression. However there are several exceptions, particularly in the Maipo area. Some structural blocks (e.g., blocks 17, 18, 23 and 24) clearly show a cluster of sub-vertical σ_1 and pressure axes, indicating that faulting occurred in response to extensional deformation. Also, a unique characteristic of structural block 17 is the presence of a major cluster of almost N-S trending σ_1.

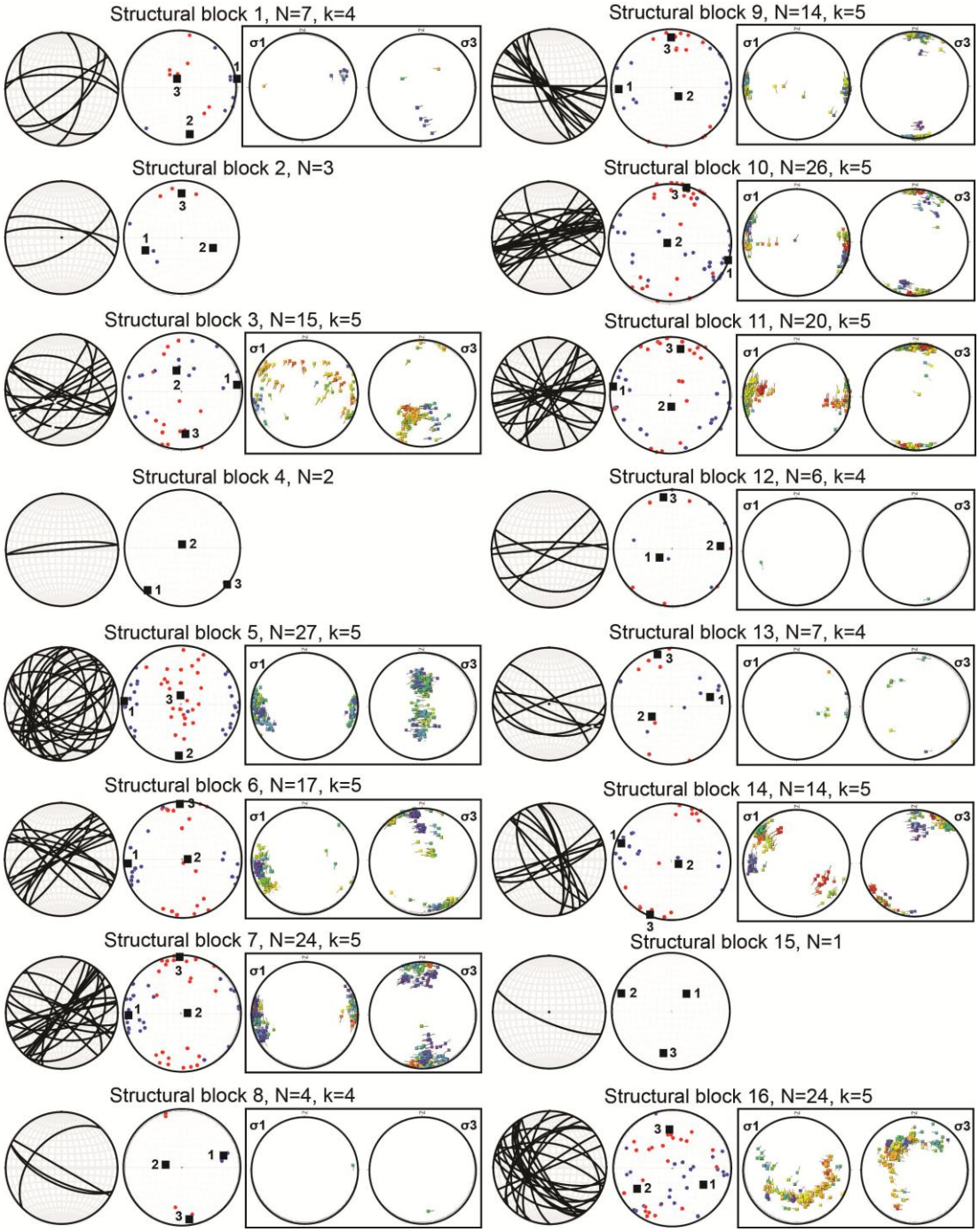

Figure 6.8. Results of the analysis of fault-slip data for the 31 structural blocks. All stereoplots are lower-hemisphere, equal-area projections. For each structural block, the first plot illustrates the fault planes. The second stereoplot shows the P and T axes for each fault plane as blue and red dots respectively, together with the average kinematic axes (1=shortening, 2=intermediate, 3=stretching). The third and fourth stereoplots show the calculated orientations of σ_1 and σ_3 for subgroups of fault-slip data using the Multiple Inverse Method.

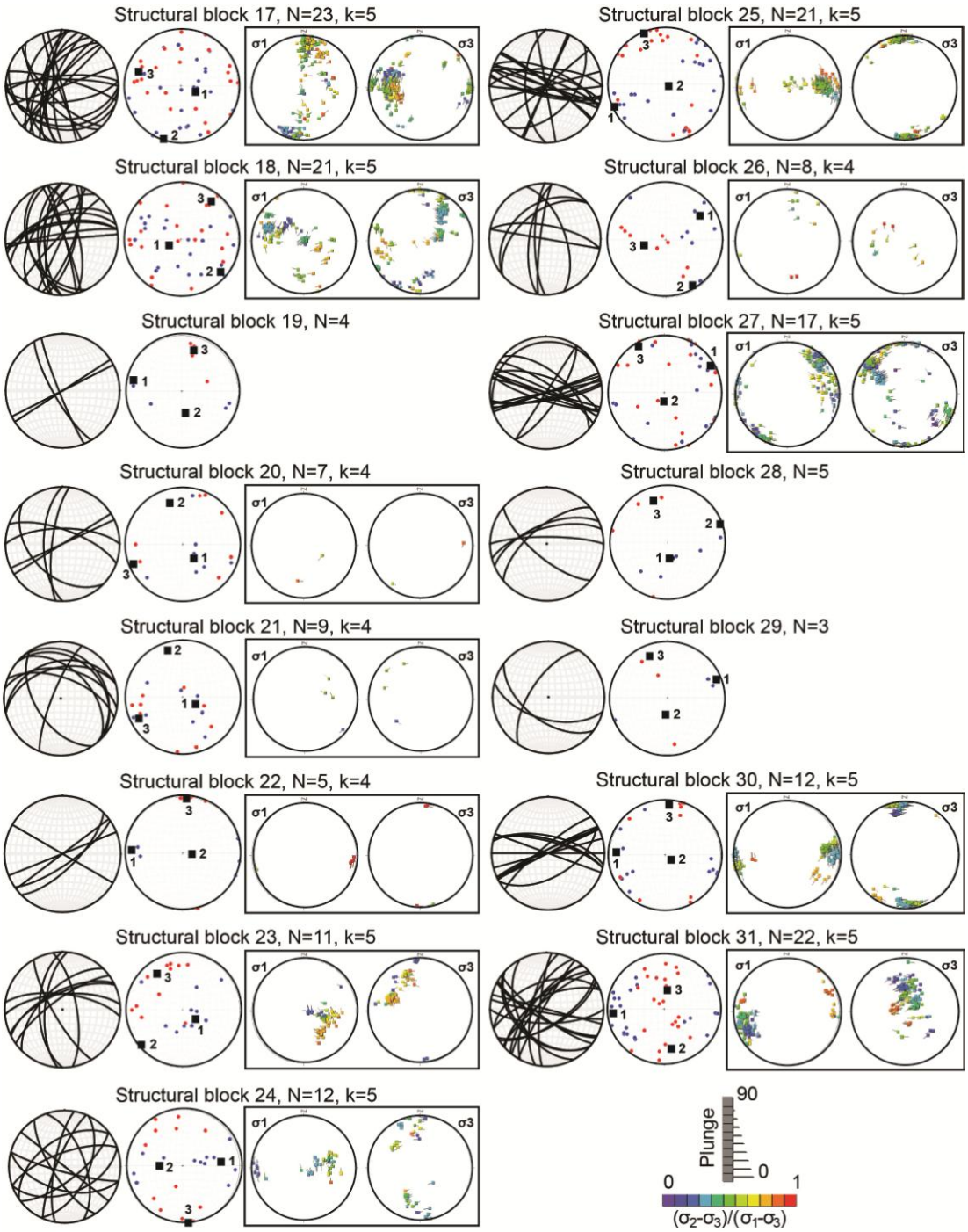

Figure 6.8. (Cont.)

6.5.2 Regional-scale segments

Structural patterns and variations at a larger scale were studied by grouping the structural blocks into three regional-scale segments: the Rio Blanco-Los Bronces and the El Teniente segments, around the porphyry Cu-Mo deposits of the same name, separated by the Maipo segment in the central part of the study area, which lacks any

known major mineral deposit (Fig. 6.9). There are 13 structural blocks located in the Rio Blanco-Los Bronces segment (structural blocks 1 to 13), 9 in the Maipo segment (14 to 22) and 9 in the El Teniente segment (23 to 31).

Fault plane kinematics in the Rio Blanco-Los Bronces and El Teniente segments are consistent with displacement during sub-horizontal, E- to ENE-directed compression (Fig. 6.9). Inversion of fault plane data using the Multiple Inverse Method does not show any secondary cluster of σ_1 (Fig. 6.9). Both the stretching kinematic axes (FaultKin software) and the main cluster of σ_3 (Multiple Inverse Method) are sub-horizontal and N-trending, indicating a predominantly strike-slip faulting regime. However, in both segments there is also a secondary cluster of sub-vertical σ_3, consistent with the analysis of structural blocks which showed that in the areas adjacent to the inverted basin margins compression was accommodated by reverse faulting. The homogeneity of the calculated stress tensors for these two segments is remarkable, particularly considering that they include a large number of structural stations from a wide area with large altitudinal variability and rock ages spanning the late Eocene to the early Pliocene. The main difference between the two segments in the calculated paleo-stress tensors and kinematic axes is a rotation of 10 degrees in the direction of compression: in the Rio Blanco-Los Bronces segment the shortening axis and the average σ_1 have an azimuth of 91° and 90° respectively, while in the El Teniente segment the azimuths are 77° and 83°.

The Maipo segment, between the Rio Blanco-Los Bronces and El Teniente segments, shows a completely different pattern of deformation (Fig. 6.9), in rocks of the same age range as the El Teniente and Rio Blanco-Los Bronces segments. Both the kinematic axes and stress tensors display high variabilities, with an overall large population of high-angle pressure axes and σ_1. In the plot for σ_1 in particular, it is possible to identify two main clusters: one is sub-vertical and the other shows E-directed compression. The main σ_3 cluster plunges gently to the NNE. This indicates that fault activity in this segment occurred in response to two contrasting stress regimes: one is extensional (vertical σ_1 and NNE-trending σ_3) and the other is characterized by strike-slip faulting in response to E-W shortening.

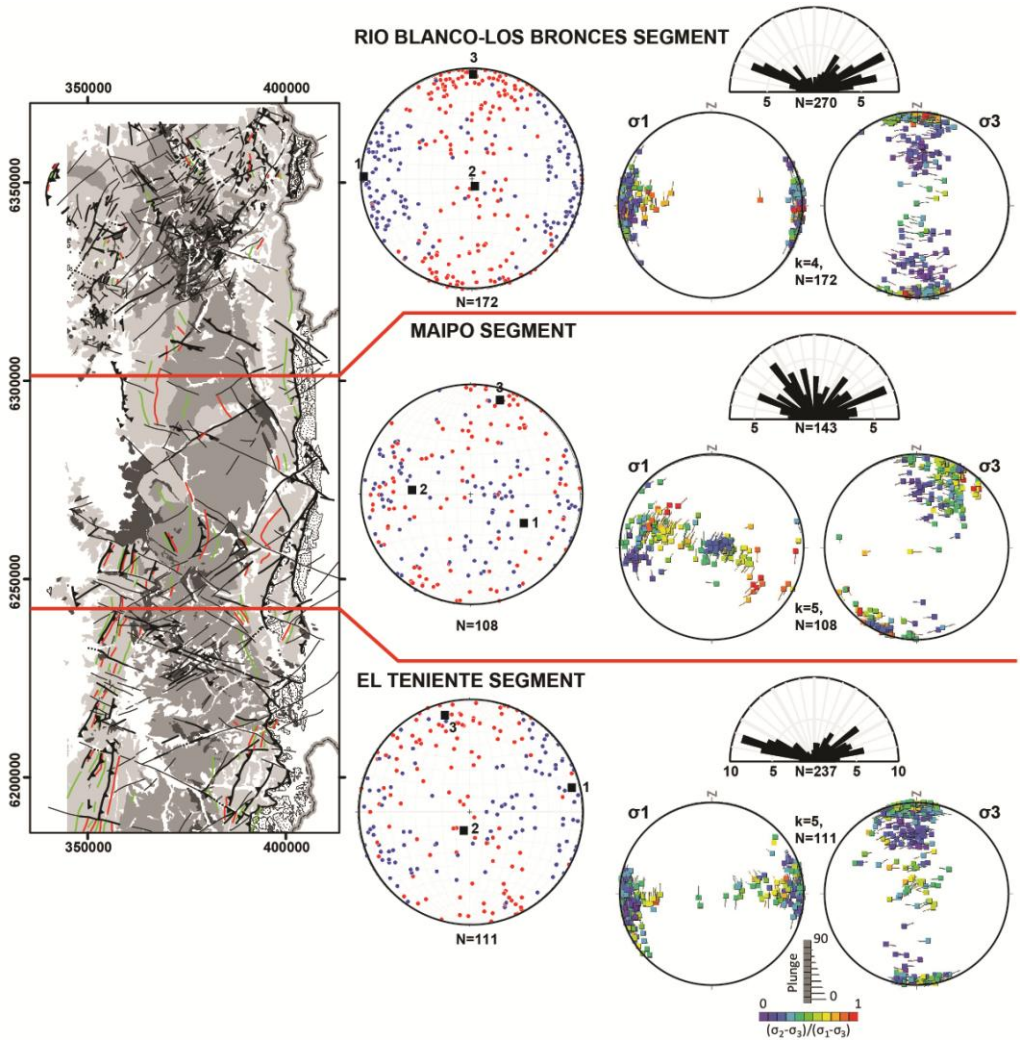

Figure 6.9. Results of the kinematic and dynamic analysis for the Rio Blanco-Los Bronces, Maipo and El Teniente segments. For each of the three segments, the upper plot corresponds to a half-circle rose diagram. The next three plots are all lower hemisphere, equal-area projections. The first one shows the P and T axes for each fault plane together with the average kinematic axes, while the second and third stereoplots show the calculated orientations of σ_1 and σ_3 for subgroups of fault-slip data using the Multiple Inverse Method. Colour legend in the stereoplots and numbering of the kinematic axes as in Fig. 6.8. Legend for the geological map as in Fig. 6.2.

6.6 Discussion

The results of the dynamic and kinematic analysis of fault plane data demonstrate that there have been strong spatial and temporal variations in the state of stress affecting the rocks of the inverted Abanico Basin. Most of the fault-slip data used in

the analysis is consistent with E- to ENE-directed shortening, parallel to the convergence direction between the Nazca and South American plates since the late Oligocene (Somoza and Ghidella, 2005). Fault activity under this compressive regime occurred during the middle Miocene-early Pliocene, constrained by the ages of the affected rocks and by new and available radiometric ages of syn-tectonic hydrothermal minerals. Field observations demonstrate that a large amount of middle Miocene-early Pliocene hydrothermal activity in central Chile was syn-kinematic (Fig. 6.4), including minerals precipitated within the halo of the Rio Blanco-Los Bronces and El Teniente porphyry Cu-Mo deposits. This period of syn-tectonic hydrothermal activity coincides with the interpreted age of tectonic inversion of the Abanico Basin from previous studies (e.g., Godoy et al., 1999; Charrier et al., 2002). However, our analysis demonstrates different segments of the basin accommodated E-W shortening in different ways; some by strike-slip faulting (vertical σ_2) and others by reverse faulting (vertical σ_3). In a few areas (e.g., structural blocks 17 or 23), there is no evidence of fault activity under E-directed compression. The thickness of the Tertiary volcanic deposits, the proportion of volcano-sedimentary intercalations and the fluctuations in fluid pressure related with magma and hydrothermal fluid flow are all factors which influenced the deformation style of each individual segment during tectonic inversion.

6.6.1 Segmentation of the Abanico Basin

The spatial pattern defined by the analysis of individual structural blocks (Figs. 6.7, 6.8) shows that reverse faulting was dominant at the margins of the inverted Abanico Basin (e.g., structural blocks 5, 26 and 31), whereas a strike-slip regime predominated in the central part of the former basin (e.g., structural blocks 7, 9, 10, 11, 25 or 30). This increase in the amount of vertical stress from the inverted basin margins towards the centre could be explained by changes in the Tertiary topography, stratigraphic thickness and volcanic facies. The axis of the Tertiary magmatic arc was located in the central part of the basin, and the stratovolcanoes associated with it were the most prominent topographic feature of the Central Chilean Cordillera, being the main source of sediments for the Argentinean foreland basins until the uplift of Mesozoic units in the Eastern Principal Cordillera in the middle Miocene and of basement blocks at the Frontal Cordillera in the late Miocene

(Giambiagi et al., 2003b). The Tertiary stratigraphic thickness increases from the basin margins to a maximum of 7 km towards the central part of the basin (Chapter 3). In the centre of the inverted basin, with a high topography and a thick rock column composed of proximal lava flows and pyroclastic deposits, the easiest escape direction is N-S and shortening was accommodated mostly by strike-slip faulting. Closer to the former basin margins, in contrast, pre-existing N-S faults, lower topography, a reduced thickness of the Tertiary units and a larger proportion of volcano-sedimentary intercalations allowed reverse faulting and more intense folding to occur in a thin-skinned deformation style.

It is clear from the kinematic and dynamic analysis that a subgroup of faults was active under extensional conditions. These faults occur predominantly in the Maipo segment (Fig. 6.9), away from any known major centre of magmatic and hydrothermal activity. One hypothesis is that in those areas faults were not reactivated during tectonic inversion, and fault kinematics reflects the extensional conditions dominant during the opening of the Abanico Basin. Pre-Miocene extensional deformation is supported by field evidence for large-scale normal faulting during the Oligocene (e.g., Fig. 6.3). This suggests that fault reactivation in strike-slip ± reverse mode during tectonic inversion after the early Miocene was favoured by high fluid pressures around magmatic-hydrothermal centres. In more distal positions, faults were not reactivated and the fault-slip data still reflects the previous, extensional tectonic regime.

Although this hypothesis may be correct for the volcanic rocks of the Maipo segment or the Mesozoic sedimentary rocks (structural blocks 17 and 18), there are also packages of younger rocks, which clearly post-date tectonic inversion, where normal faulting predominates. For example structural blocks 23 and 24 contain predominantly normal faults which affect flat-lying pyroclastic rocks of the middle to late Miocene Teniente Volcanic Complex. These local extensional regimes affecting rocks which clearly post-date the initiation of tectonic inversion may be explained by post-orogenic gravitational collapse and/or by caldera-forming volcanic events. In the particular case of block 34, the latter seems likely, as the area is characterised by a thick succession of coarse pyroclastic breccia not present elsewhere in the district, which could correspond to proximal, intra-caldera deposits. More detailed mapping

of the local volcanic facies and their spatial and temporal relationship to the faults is needed to test this hypothesis.

As mentioned previously, structural block 17 appears unique in showing a major cluster of NNE- to N-trending σ_1. Lavenu and Cembrano (1999, 2008) identified a Quaternary deformation event associated with N-S compression in Central Chile, with faulting affecting Tertiary rocks and also unconsolidated river terraces in the Maipo area. They explain this compression direction as the product of the northward motion of a fore-arc sliver detached from the continent by the dextral, arc-parallel Liquiñe-Ofqui fault system of southern Chile, producing N-S compression in the fore-arc of central Chile. Structural block 17 is composed exclusively of Mesozoic sedimentary rocks, and there are no other constraints on the age of the syn-tectonic hydrothermal minerals used as kinematic indicators in this area. In this block, mineral fibres are mainly calcite and gypsum, which can precipitate at very low temperatures and so could have been formed in the Quaternary. However, based on available data it is presently impossible to confidently assign an age to the N-S compression affecting block 17.

6.6.2 From fault plane data to trans-lithospheric fault systems

The Andean segment covered by this study is remarkable for the apparent absence of regional-scale, continuous fault systems. However, as Figure 6.2 illustrates, from the systematic measurement of individual fault planes it is possible to trace major fault systems across the entire orogenic belt. These discontinuous fault-systems are composed of networks of interconnected fault planes.

Figure 6.10 illustrates how the fault systems present in the Main Cordillera can be correlated with more evident, continuous structures which controlled the emplacement of Mesozoic plutons in the Coastal Cordillera, to the west of the study area.

Arc-oblique structures have been identified in several Andean segments (e.g., Salfity, 1985; Chernicoff et al., 2002; Acocella et al., 2011) and their activity can be traced back at least to the Triassic, when they were active as master and transfer faults of NW- to NNW-oriented rifts (Mpodozis and Ramos, 1989; Ramos, 1996; Giambiagi

et al., 2003a; Niemeyer et al., 2004; Sagripanti et al., 2014). Some authors (e.g., Ramos, 1994) have suggested that the geometry of the Triassic rifts, in turn, was controlled by NW-trending suture zones formed during the Proterozoic and Palaeozoic as a result of the accretion of continental blocks to the south-western margin of Gondwana.

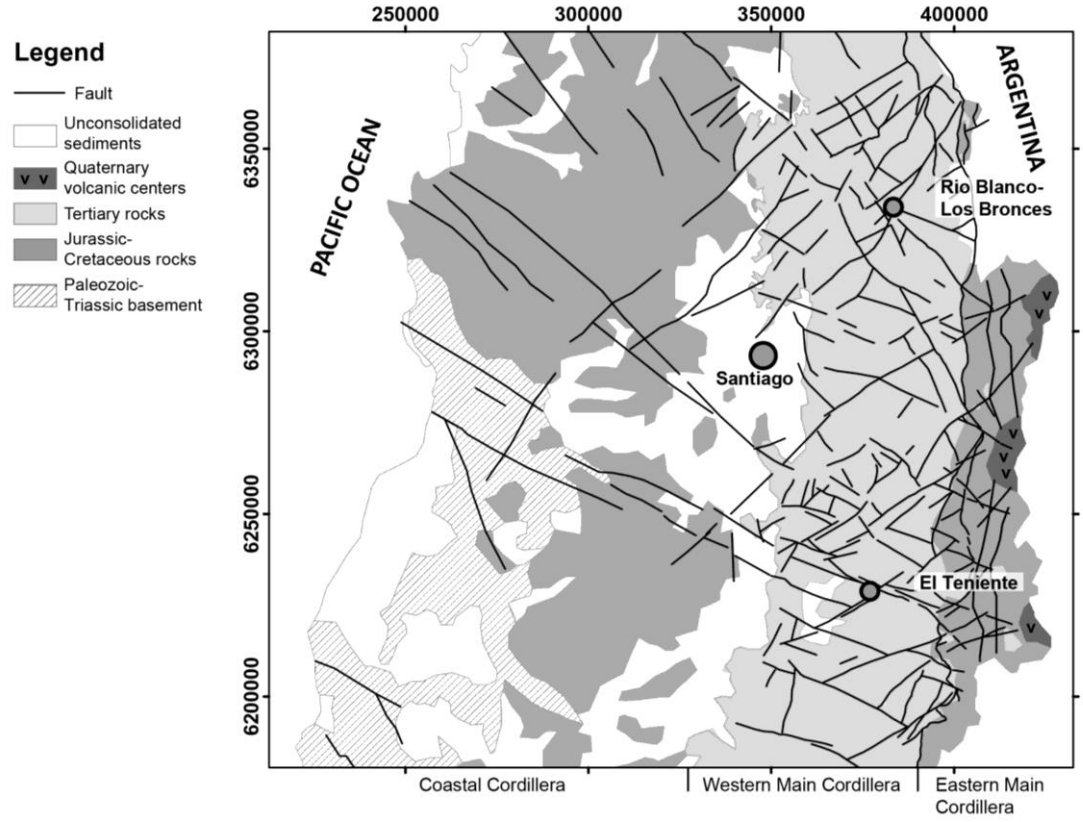

Figure 6.10. Main fault systems identified by this study in the Main Cordillera of central Chile (from Figure 6.2), and their correlation with similar oblique structures recognized by previous works in the Paleozoic and Mesozoic rocks of the Coastal Cordillera. Background geology simplified from SERNAGEOMIN (2002).

6.7 Conclusions

The internal architecture of the inverted Abanico Basin in the Main Cordillera of central Chile is dominated by NE- and NW-striking fault systems, oblique to the continental margin and to the axes of the Meso-Cenozoic magmatic arcs. The correlation of the fault systems recognized in this study with older structures present in the rocks of the Coastal Cordillera suggests that they reflect reactivation of long-lived basement structures, which penetrate deep into the lithosphere. Field evidence

shows some of them were active as normal faults in the late Eocene – Oligocene, during the deposition of the Abanico and Coya-Machali formations (Fig. 6.3). Fault plane kinematics demonstrates that most of these faults were reactivated as strike-slip ± reverse faults during tectonic inversion in the middle Miocene – early Pliocene (Fig. 6.4). Reactivation during tectonic inversion was associated with hydrothermal fluid flow, based on the widespread epidote, chlorite, tourmaline, quartz, calcite, actinolite and Cu-Fe sulfides precipitation on the fault planes (Fig. 6.4). The age of tectonic inversion was confirmed with three $^{40}Ar/^{39}Ar$ ages on syn-tectonic hydrothermal minerals.

The kinematic and dynamic analysis of fault-slip data shows that structural reactivation during tectonic inversion was concentrated around major plutons and porphyry Cu-Mo deposits (Figs. 6.8, 6.9). In these areas the fault-slip dataset is consistent with reactivation during E- to ENE-directed compression. This suggests feedback between magmatic and hydrothermal activity, fluid pressure, and the reactivation under compression of the structural architecture inherited from the extensional period. In the margins of the inverted Abanico Basin, compression was accommodated by reverse faulting (sub-vertical σ_3), while in the central part of the basin, where the rock column is considerably thicker and the topography higher, a strike-slip regime (sub-vertical σ_2) was predominant during Miocene-early Pliocene tectonic inversion.

Chapter 7 Discussion

"The valleys, by which the Cordillera are drained, follow the anticlinal or rarely synclinal troughs, which deviate most from the usual north and south course; or still more commonly those lines of faults or of unequal curvature (that is, lines with the strata on both hands dipping in the same direction, but at a somewhat different angle) which deviate most from a northerly course." (Darwin, 1846).

The results of this work show that the structural architecture and evolution of the Andes of central Chile is dominated by long-lived, arc-oblique fault systems inherited from the Andean basement which, as noted by Darwin (1846), deviate from the usual N-S trend of Andean structures in central Chile and Argentina. They interact with younger, arc-parallel faults formed during the Meso-Cenozoic. The Cenozoic geologic history is characterized by two main tectonic stages: stage one during which an extensional regime was dominant within the arc, and a second stage associated with tectonic inversion in a contractional to transpressional regime. Arc-oblique and arc-parallel structures were active during both tectonic episodes, with different kinematics controlled by their orientation and the prevailing stress field.

7.1 Intra-arc extension and the opening of the Abanico Basin

Different lines of evidence point towards a major extensional episode affecting the Andes of central Chile during the mid-Tertiary (e.g., widespread normal faulting, syn-extensional volcanic and sedimentary deposits, geochemistry of igneous rocks consistent with a thin continental crust). Extensional conditions prevailed in the Rio Blanco-Los Bronces and Maipo segments (Fig. 6.9) until the Oligocene-Miocene boundary, while extension was dominant until the middle Miocene in the El Teniente segment (Fig. 6.9).

7.1.1 Main sub-basins and stratigraphic definitions

The Abanico Basin contained several smaller-scale sub-basins or depocenters, each characterized by a specific array of volcanic and sedimentary facies and thicknesses (Figs. 4.2D, 6.3). At a larger scale, the Abanico Basin can be subdivided into two main sub-basins, each with different stratigraphic and tectonic histories (Fig. 5.8). In

the northern sub-basin (Rio Blanco-Los Bronces and Maipo segments) the Abanico Formation *sensu stricto* was accumulated from the late Eocene-late Oligocene (Fig. 5.8). The southern sub-basin (El Teniente segment) was the site of deposition of the Coya-Machali Formation from the late Oligocene-middle Miocene (Fig. 5.8). These two units were considered correlates by previous works (Charrier et al., 2002), and treated as a single diachronous volcanic and sedimentary unit, which gets younger towards the south (Charrier et al., 2005). The new mapping and geochronological data presented here indicates that there is almost no temporal overlap between the two units, and suggests the existence of a sharp boundary between two entirely different stratigraphic packages (Piuquencillo fault system; Fig. 5.8).

The Abanico Formation is composed mostly of lava flows of basaltic-andesitic composition (Appendix V). The lava flows are intercalated with volcanogenic sedimentary deposits, commonly medium-grained epiclastic sandstones, and with pyroclastic deposits, commonly ignimbrites and crystal-rich lithic tuffs of andesitic and dacitic composition (Appendix V). Because of the strong lateral variability across different sub-basins and volcanic centres, it is not possible to define regionally-consistent members within the Abanico Formation. However, it is clear that towards the upper part of the sequence, sedimentary and pyroclastic intercalations are more common (Fig. 3.6). The age of the lower part of the sequence, where basaltic-andesitic lava flows predominate, has been constrained to 34-26 Ma (Gana and Wall, 1997; Baeza, 1999; Vergara et al., 1999; Fuentes et al., 2002, 2004; this work, sample AN12JP005, Table 5.1). The pyroclastic and sedimentary deposits which characterize the upper part of the sequence were deposited within the age range 26-21 Ma (Fuentes et al., 2004; Muñoz, 2006; this work, samples AN12JP003 and AN12JP014, Tables 3.1, 5.1).

The Coya-Machali Formation also contains abundant andesitic-basaltic and andesitic lava flows (Appendix V), but intercalations of volcanogenic sedimentary rocks are much more common than in the Abanico Formation (Figs. 5.3, 7.1). The age range of this unit is 23-12 Ma (Charrier and Munizaga, 1979; Kay and Kurtz, 1995; Flynn et al., 1995; this work, samples AN12JP021, AN12JP024 and AN13JP006, Table 5.1).

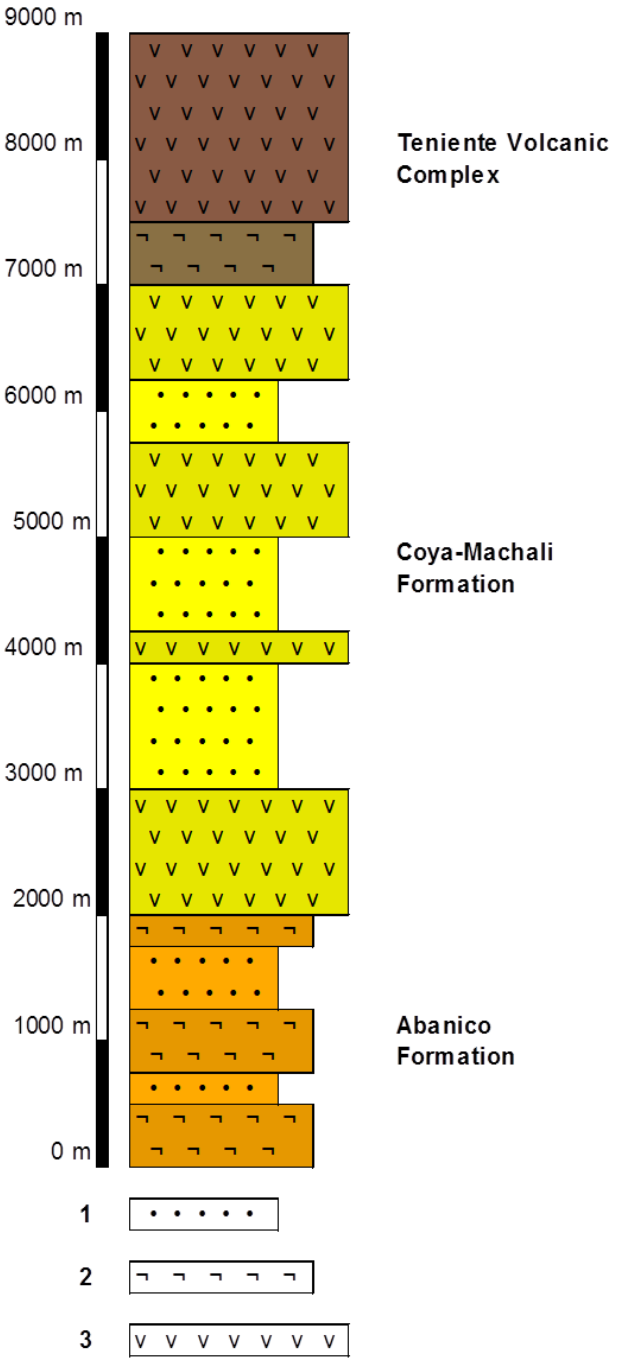

Figure 7.1. Generalized stratigraphic column of the southern segment of the inverted Abanico Basin (El Teniente segment). Thicknesses shown in the figure were estimated from cross-sections and correspond to maximum values. Key to rock types: 1 = volcaniclastic conglomerates and sandstones, 2 = pyroclastic deposits, 3 = andesitic and basaltic-andesitic lava flows.

The volcanic products of the Abanico and Coya-Machali formations have similar REE patterns (Fig. 5.5), with almost identical average La/Sm and Sm/Yb ratios (La/Sm=3.4 and 3.0; Sm/Yb=1.9 and 1.8 respectively) which indicate a moderate LREE enrichment and a flat HREE slope. This suggests that magmas were generated under a relatively thin continental crust (thickness of ~35 km estimated by Kay and Kurtz, 1995) with a pyroxene-dominated residual assemblage. This is consistent with the extensional tectonic regime implied by syn-depositional normal faulting (Fig.

6.3). Geochronological data for the Abanico and Coya-Machali formations implies that extensional conditions prevailed in the northern segment until ~22 Ma, while in the southern segment a similar tectonic setting persisted until ~13 Ma.

7.1.2 Reactivation of arc-oblique basement faults

Geological and geophysical evidence suggests that the main fault systems in the Andean basement of central Chile have predominant NW and NE trends (Figs. 2.1, 4.3, 6.10). These are oblique to the Andean magmatic arc and to the present-day continental margin. There are regional-scale fault systems that have been recognized in basement rocks to the west and east of the study area. To the west, the Coastal Cordillera of central Chile is dominated by NW- and NE-trending faults, which controlled the emplacement of Mesozoic plutons and bound blocks of late Paleozoic-Triassic basement (SERNAGEOMIN, 2002; Fig. 1.2B). To the east, the basement blocks in the Argentinean Andes are dominated by structures of identical orientations, which are associated with syn-extensional deposition of Triassic sedimentary sequences (Sagripanti et al., 2014) and which were partly reactivated during Andean, Mesozoic and Cenozoic deformation events (Giambiagi et al., 2003a). Geophysical evidence of deep structures with NW and NE trends below the Mesozoic and Cenozoic rocks of the Andes of central Chile includes the distribution of upper-crustal seismicity and linear trends in regional aeromagnetic surveys covering the study area (Fig. 4.3A, C). They suggest an array of deep structures oblique to the N-trending Andean orogen.

The NW- and NE-trending normal faults were active within the Abanico Basin during the Oligocene (Fig. 6.3) and early Miocene (Fig. 4.2D). They controlled the deposition of syn-extensional volcanic and sedimentary rocks. Given the geological and geophysical evidence outlined above, it is suggested that these arc-oblique normal faults were formed by reactivation of deep, long-lived, high-angle fault systems inherited from the Andean basement (Figs. 2.1, 6.10).

7.1.3 Arc-parallel high-angle faults

N-striking, arc-parallel normal faults were active during intra-arc extension. Some of them might correspond to reactivated Mesozoic faults, originated as high-angle

normal faults bounding different segments of the Jurassic-Early Cretaceous back-arc basins. The Pocuro fault (Figs. 1.2B, 3.2) in particular was active during the Cretaceous, as demonstrated by Jara and Charrier (2014). These structures, together with the reactivated arc-oblique basement faults, defined the geometry of the Abanico Basin and its segmentation into sub-basins during the late Eocene-Oligocene.

The eastern basin margin is defined by the El Fierro fault (Figs. 1.2B, 3.8B) and parallel structures. They have a broad N-S strike and dip to the west at moderate to high angles (Figs. 3.2, 3.8B, 5.3, 6.2), defining the contact between the Tertiary Abanico and Coya-Machali formations in the hanging wall block with Mesozoic units in the footwall. Evidence for syn-extensional deposition of the Tertiary volcanic rocks associated with normal movement of the El Fierro fault have been reported to the south of the study area (Charrier et al., 2002; Piquer et al., 2010). Similarly, the western basin margin is defined by N-striking, E-dipping faults (Fig. 6.2) which juxtaposes hanging wall rocks of the Abanico and Coya-Machali formations with footwall Mesozoic rocks. Individual faults defining the western margin of the basin include the Pocuro and Infiernillo faults in the Rio Blanco-Los Bronces segment (Fock, 2005; Farias et al., 2010; Figs. 1.2B, 3.2), the San Ramon fault in the Maipo segment (Armijo et al., 2010; Fig. 1.2B) and the high-angle, E-dipping faults at the Carretera del Cobre in the El Teniente segment (Fig. 5.3, 7.2).

Figure 7.2. Fault in the Carretera del Cobre area, striking N20°E and dipping 75-80°E. The affected rocks are pyroclastic deposits of the Coya-Machali Formation. The contact with the Mesozoic units lies immediately to the west of the picture location, covered by unconsolidated sediments. View S from 350473mE, 6215117mN.

7.2 Basin inversion

Beginning in the early Miocene, progressive unconformities were formed in the northern and central parts of the study area (Rio Blanco-Los Bronces and Maipo segments), associated with syn-tectonic deposits accumulated during folding of the older, syn-extensional units (Figs. 3.12). These unconformities mark the first pulse of compressional deformation affecting this Andean segment after Mid-Tertiary extension. Younger pulses of compression in the middle Miocene and late Miocene-early Pliocene affected the entire study area, including the El Teniente segment to the

south. They are responsible for younger generations of folds which affected the early and middle Miocene volcanic rocks, in addition to the older deposits (Figs. 3.5, 4.2B, 5.2).

7.2.1 Syn-tectonic deposits and unconformities

The transition between the Abanico and Coya-Machali formations and the younger, Neogene volcanic units is marked in several localities by progressive unconformities and syn-tectonic deposits (Fig. 3.12). In the Rio Blanco-Los Bronces and Maipo segments (Fig. 6.9), progressive unconformities were formed at 22-21 Ma, marking the transition between the syn-extension Abanico Formation and the syn-inversion Farellones Formation. The age at which this transition occurred is well constrained and consistent across these two segments. Two different pyroclastic flows deposited at the transition between the two formations at the Rio Blanco-Los Bronces district were dated at 22.7 ± 0.4 Ma (Piquer, 2010, U-Pb SHRIMP in zircons; sample 135376, Table 3.1) and 21.73 ± 0.27 (U-Pb LA-ICPMS in zircons, sample AN12JP010, Table 3.1). The first one covers a sequence of syn-inversion volcanogenic sedimentary deposits (Fig. 3.12). In the Maipo segment, another pyroclastic flow deposited in the transition between the Abanico and Farellones formations was dated at 21.41 ± 0.47 Ma (this work, U-Pb LA-ICPMS in zircons, sample AN12JP003, Table 5.1).

In the southern El Teniente segment (Fig. 6.9), the transition between syn-extensional and syn-compressional deposits occurred at a later time. The lava flows which host the El Teniente porphyry Cu-Mo deposit are underlain by pyroclastic flows dated at 12.73 ± 0.35 Ma (this work, U-Pb LA-ICPMS in zircons, sample AN12JP018, Table 5.1). The pyroclastic flows, in turn, cover strongly folded sedimentary and pyroclastic deposits of the Coya-Machali Formation (Fig. 7.3).

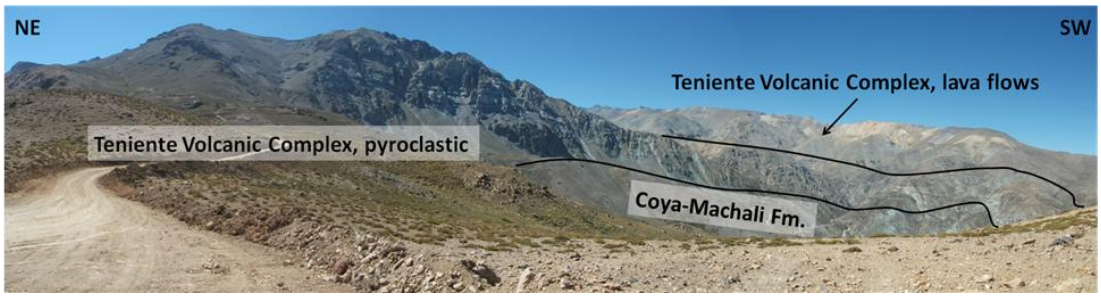

Figure 7.3. Basal pyroclastic flows of the Teniente Volcanic Complex covering strongly folded rocks of the Coya-Machali Formation. View SE from 367057mE, 6237375mN.

To the SE of the El Teniente segment, at the Las Leñas river valley (Fig. 5.1B), the transition between the Coya-Machali Formation and the Teniente Volcanic Complex is also exposed (Figs. 4.2A, B, 5.2A). In this area, the youngest lava flows affected by tight folds characteristic of the Coya-Machali Formation have been dated at 12.62 ± 0.36 Ma (this work, U-Pb LA-ICPMS in zircons, sample AN13JP006). They are covered to the west by flat-lying lava flows of the Teniente Volcanic Complex. This constrains the age of the transition between the Coya-Machali Formation and the Teniente Volcanic Complex to 13-12 Ma, and suggests that as with the transition between the Abanico and Farellones formations, there is no temporal hiatus between the two units.

7.2.2 Syn-inversion units and stratigraphic definitions

Neogene volcanic units that cover the Abanico and Coya-Machali formations crop out in the central part of the basin (Fig. 4.1A, 5.1A). The Farellones Formation overlies the Abanico Formation in the Rio Blanco-Los Bronces and Maipo segments, while the Teniente Volcanic Complex overlies the Coya-Machali Formation in the El Teniente segment.

The initial stage of the Farellones Formation volcanism was characterized by explosive events, the products of which can be grouped in a well-defined basal member composed of crystal- and lithic-rich pyroclastic flows and structurally-bounded massive pyroclastic breccias (Figs. 3.6, 5.9). The latter probably correspond to intra-caldera deposits, as suggested by the coarse grain size of the breccias, its massive character with up to 900 m of pyroclastic deposits with very poor internal bedding and the fact that the breccias are bounded by normal faults (Fig. 5.9). The

age range of this basal pyroclastic member is 23-18 Ma (Rivera and Navarro, 1996; this work). It is predominantly dacitic in composition (Appendix V). Pyroclastic rocks are covered by a thick sequence of up to 1500 m of lava flows intercalated with pyroclastic deposits towards the upper part of the sequence (Fig. 3.6). The lava flows are mainly andesitic to basaltic-andesitic in composition, and are intercalated with sporadic dacitic and rhyolitic lavas and domes. The age range of this stage of mainly effusive volcanism is constrained to 18-14 Ma (Deckart et al., 2005; this work, samples 135375, AN12JP007 and AN12JP012, Tables 3.1, 5.1).

The Teniente Volcanic Complex also contains massive pyroclastic deposits at the base of the sequence (Fig. 7.3), with thicknesses of up to 500 m (Fig. 7.1). The pyroclastic deposits were dated at 12.73 ± 0.35 Ma (this work, U-Pb LA-ICPMS in zircons, sample AN12JP018). The geographically-constrained distribution of the pyroclastic rocks and their association with normal faulting (Fig. 6.8, structural block 23) suggest that, as for the pyroclastic deposits of Farellones Formation, they are the product of caldera-forming events. The pyroclastic deposits are covered by a sequence of up to 2000 m of andesitic-basaltic lava flows (Fig. 4.2A, 7.3; Section 6228000N, Appendix VI) deposited from 12-6 Ma (Godoy, 1993; Rivera and Falcon, 1998).

Farellones Formation rocks have distinctive REE patterns compared with both the underlying Abanico Formation and with the Coya-Machali Formation to the south (Fig. 5.6). In particular, they have a strong LREE enrichment and moderate HREE fractionation (on average, La/Sm=4.5 and Sm/Yb=2.6; Fig. 5.6). Average La/Yb ratios are almost two times higher in the Farellones Formation (11.6) than in the Abanico (6.4) and Coya-Machali (5.6) formations. These patterns confirm the observations of Kay and Kurtz (1995) and support their conclusion that the volcanic products of Farellones Formation were erupted through a crust which had already been moderately thickened as a consequence of the first pulse of basin inversion and deformation in the early Miocene (22-21 Ma). Our data confirm that this event did not affect the southern El Teniente segment, where the first evidence of tectonic inversion occurs at 13-12 Ma. The Teniente Volcanic Complex, deposited on top of folded rocks of the Coya-Machali Formation, has a moderate LREE enrichment similar to the Abanico and Coya-Machali formations (average La/Sm=2.9), but it

also shows moderate HREE fractionation with Sm/Yb ratios more like the Farellones Formation (2.4 on average; Fig. 5.6). The average La/Yb ratio of 7.00 is slightly higher than in the Abanico and Coya-Machali formations but lower than in the Farellones Formation (Fig. 5.6).

7.2.3 Syn-inversion magmatic and hydrothermal activity

The U-Pb geochronological data reported here confirms that the emplacement of plutonic bodies in the upper crust was coeval with tectonic inversion of the Abanico Basin. Plutons were emplaced preferentially at the intersections of conjugate arc-oblique faults, or at the intersections of arc-oblique faults and the arc-parallel basin-margin faults (Fig. 7.4). Individual plutons are commonly elongated following the NW-trending faults, or they present rhombic shapes with the margins being defined by intersecting conjugate structures (Fig. 7.4). This suggests arc-oblique faults controlled the location and orientation of magmatic feeders.

The oldest Tertiary plutons were emplaced during the early Miocene, and occur only in the Rio Blanco-Los Bronces and Maipo segments (Fig. 6.9), to the north of the Piuquencillo fault system (Fig. 5.8). The Rio Colorado granodiorite, the La Obra granodiorite and the earliest facies of the Rio Blanco-San Francisco batholith (Fig. 7.4) were emplaced coevally with the formation of progressive unconformities between the Abanico and Farellones formations and with the deposition of the oldest pyroclastic flows of the basal member of Farellones Formation. The Rio Colorado pluton was emplaced at 21.8 ± 0.5 Ma (this work, U-Pb LA-ICPMS in zircons, sample AN12JP011, Table 3.1), the La Obra pluton was emplaced and cooled between and 21.6 and 16.2 Ma according to $^{40}Ar/^{39}Ar$ analyses in different minerals (Kurtz et al., 1997) and the earliest plutons of the Rio Blanco-San Francisco batholith were emplaced at 20.1 ± 2.0 Ma (K-Ar in hornblende, Warnaars et al., 1985). At the Rio Blanco-San Francisco batholith, the ~20 Ma plutons are cut by younger intrusions of diverse composition; the youngest intrusions of this suite of early Miocene plutons correspond to syenogranites emplaced at 16.4 ± 0.2 Ma (sample 153119, Table 3.1). Coeval with the emplacement of these major plutons, dioritic and gabbroic dikes were emplaced syn-tectonically in dilational jogs along a NW-trending, sinistral strike-slip fault (Fig. 3.13A). The dikes have been

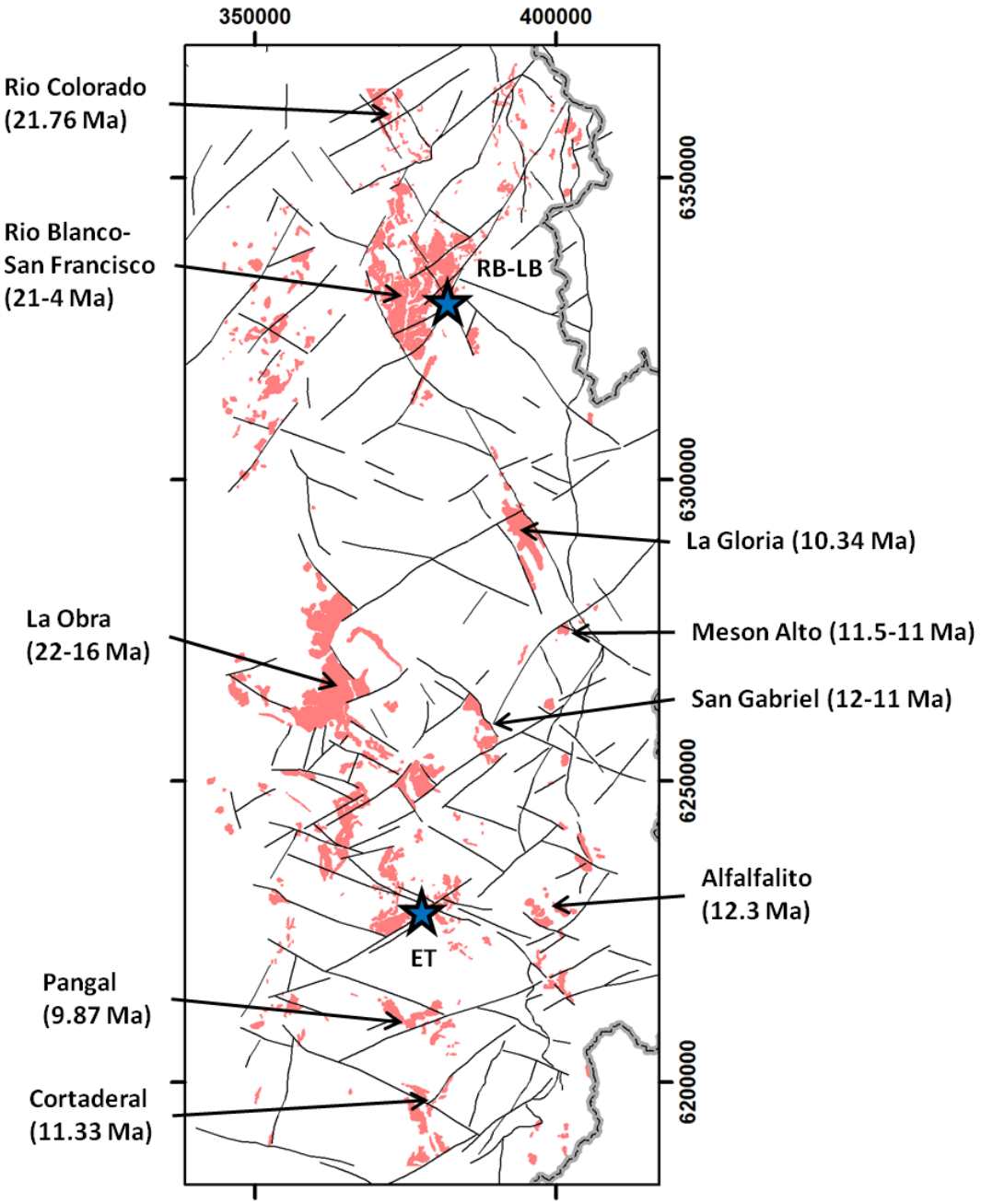

Figure 7.4: Main Miocene plutonic bodies and fault systems of the study area. Ages from Kurtz et al. (1997), Deckart et al. (2010) and this work.

dated at 22.2 ± 0.2 Ma (U-Pb in zircons, Montecinos et al., 2008), and the kinematics of the fault is consistent with emplacement under E-directed compression during the first pulse of basin inversion. Geochemically, these early Miocene intrusions are

characterized by LREE enrichment and HREE slopes slightly lower than the coeval Farellones Formation (Fig. 5.6; average La/Sm = 3.8 and Sm/Yb = 1.9).

Early Miocene plutons of the Rio Blanco and Maipo segments are cut by a set of middle Miocene, commonly medium-grained equigranular intrusions. They occur across the entire study area, and are the oldest plutonic units in the El Teniente segment (Fig. 6.9). Radiometric ages of middle Miocene plutons are strongly concentrated in the 13-10 Ma range, coeval with the transition between the Coya-Machali Formation and the Teniente Volcanic Complex in the El Teniente segment (Kurtz et al., 1997; Deckart et al., 2010; this work, samples AN12JP008, AN12JP013, AN13JP003, AN12MB029, AN12MB038, AN12MB041, AN12MB067 and AN12MB068, Tables 3.1 and 5.1). Major plutons of this age range include the Rio Blanco Granodiorite at the Rio Blanco-San Francisco Batholith, as well as the La Gloria, Meson Alto, San Gabriel, Alfalfalito, Pangal and Cortaderal plutons (Fig. 7.4). They commonly occur at the central part of the inverted Abanico Basin (Fig. 7.4). Middle Miocene plutons are cut by lower late Miocene andesitic and dacitic dikes and stocks of porphyritic texture, with ages between 11 and 9 Ma (Rivera and Navarro, 1996; Deckart et al., 2014; this work, samples AN12JP001 and AN13JP014, Tables 3.1 and 5.1).

Middle Miocene plutons emplaced in the Rio Blanco-Los Bronces and Maipo segments have a stronger LREE enrichment and HREE fractionation than any of the stratigraphic units (Fig. 5.6), with average La/Sm ratios of 5.8, Sm/Yb ratios of 3.5 and La/Yb ratios of 21.3. Those emplaced at the El Teniente segment, in contrast, show a REE chemistry similar to the Farellones Formation (average La/Sm = 3.9, Sm/Yb = 2.9 and La/Yb = 12.2; Fig. 5.6)

The youngest Tertiary rocks exposed in the Andes of central Chile correspond to late Miocene-early Pliocene porphyritic stocks and dikes, hydrothermal breccias and diatremes. They occur towards the central part of the inverted Abanico Basin in the Rio Blanco-Los Bronces and El Teniente segments. Rocks of this age range have not been documented in the Maipo segment. Some of these intrusions are temporally and genetically related with the Rio Blanco-Los Bronces and the El Teniente porphyry Cu-Mo deposits (Maksaev et al., 2004; Deckart et al., 2005). The age range of this

suite of porphyries and breccias is 7-4 Ma (Quirt et al., 1971; Warnaars et al., 1985; Maksaev et al., 2004; Deckart et al., 2005; this work, sample AN13JP013, Table 3.1). Late Miocene-early Pliocene rocks have a REE pattern similar to the middle Miocene plutons emplaced in the northern segments (Fig. 5.6): the average La/Sm ratio is 5.9, Sm/Yb ratio is 3.5 and La/Yb ratio is 21.0.

The oldest systems of hydrothermal alteration and mineralisation in the study area were developed during the middle Miocene at the Rio Blanco-Los Bronces segment, in the northern part of the study area. They produced the sub-economic Los Piches and El Plomo prospects (~13 Ma and ~10 Ma respectively, based on $^{40}Ar/^{39}Ar$ ages in sericite from tourmaline-cemented breccias, Toro et al., 2012) and the hydrothermal alteration and veins in samples AN12JP008 and AN13JP014 (Fig. 3.1, Table 3.1). These two samples were collected from pre- and post-mineral intrusions, and their zircon U-Pb LA-ICPMS ages constrain the age of hydrothermal activity in the area to the 11-9 Ma range. Actinolite mineral fibres collected from a NE-striking fault plane in sample AN12JP008 (Fig. 6.1) yielded an $^{40}Ar/^{39}Ar$ age of 9.72±0.09, consistent with the inferred age of hydrothermal activity in the area. The actinolite fibres form steps indicating dextral strike-slip movement, confirming that hydrothermal activity was syn-tectonic and, according to fault kinematics, associated with E-directed compression. Similar conclusions can be obtained from the other two samples in which late Miocene ages were obtained from syn-tectonic hydrothermal minerals (AN13JP007 and AN13JP012, Fig. 6.5, Table 6.1). These middle Miocene-lower late Miocene hydrothermal systems are coeval with the emplacement of the belt of middle Miocene plutons and with the transition from the Coya Machali Formation to the Teniente Volcanic Complex in the southern El Teniente segment.

The economically relevant hydrothermal systems of the study area were formed in the late Miocene-early Pliocene, between 7 and 4 Ma (Maksaev et al., 2004; Deckart et al., 2005, 2013, 2014), associated with the porphyritic stocks and hydrothermal breccias of the same age. The age of these hydrothermal systems overlaps with the most important period of uplift and exhumation affecting the Tertiary rocks of central Chile, according to existing zircon and apatite fission track data (Maksaev et al., 2009) and to nine new (U-Th)/He ages in zircons and apatites (this work, Table 5.2).

7.2.4 Reactivation of pre-existing high-angle faults

Kinematic indicators and the results of kinematic and dynamic analysis of fault-slip data show that most of the high-angle faults present in the area, which were active as normal faults during the deposition of the Abanico and Coya-Machali formations, were reactivated during basin inversion under E- to ENE-directed compression (Fig. 6.9). Fault reactivation was concentrated in the Rio Blanco-Los Bronces and El Teniente segments, around Miocene-early Pliocene hydrothermal centres and plutons (Fig. 6.9). Arc-oblique, NE- and NW-trending fault systems, were reactivated as strike-slip, dextral and sinistral faults respectively (Figs. 4.1C, 6.6). In some of these faults the sense of movement was oblique, and the strike-slip displacement is coupled with a reverse component. In those cases, faults are commonly associated with parallel trends of asymmetric folds affecting both the Abanico and the Farellones formations (Fig. 3.5). The basin-margin faults were reactivated in reverse mode, and are associated with tight, west-vergent folds at the western margin (Fig. 5.3B) and east-vergent folds at the eastern margin of the former Abanico Basin (Fig. 3.8). The pattern of predominantly strike-slip faulting in the central part of the basin and reverse faulting close to the basin margins is evident in both the Rio Blanco-Los Bronces and the El Teniente segments (Fig. 6.8). The inversion of high-angle normal faults, the presence of sub-horizontal dilational lenses (Fig. 3.13B) and the abundance of syn-tectonic hydrothermal minerals (Fig. 6.4) all suggest that fault reactivation occurred under high fluid pressures during fault-controlled hydrothermal fluid flow.

7.2.5 Newly-formed faults

Most of the deformation during inversion of the Abanico Basin was accommodated by the reactivation of the pre-existing extensional architecture. In contrast, at the Eastern Main Cordillera (Fig. 1.2B), where Mesozoic sedimentary rocks predominate, the weaker rheology and the presence of gypsum beds highly favourable as detachment surfaces caused rocks to deform in a thin-skinned style with large displacements on shallowly-dipping faults (Ramos, 1996; Giambiagi et al., 2003b). However, low-angle detachments and ramp-flat systems were also formed locally in the central part of the Abanico Basin during Miocene-early Pliocene

compression. The most favourable detachment was the contact between the basal pyroclastic flows and the overlying lava flows of the Farellones Formation. This plane was active as a W-vergent low angle detachment thrust in different localities at the western part of the Rio Blanco-Los Bronces segment (Fig. 3.9). Locally the detachment has propagated upward in a ramp which cuts through the sequence of lava flows (Fig. 3.9).

7.2.6 Chronology of basin inversion

The combination of structural, geochronological, thermochronological and geochemical data suggest that basin inversion did not occur at a constant rate during the Miocene-early Pliocene. Instead, it is possible to identify individual, short-lived stages of deformation, crustal thickening, uplift and exhumation.

- First stage, 23-21 Ma: evidence of this period of basin inversion is from the Rio Blanco-Los Bronces and Maipo segments (Fig. 6.9), to the north of the Piuquencillo fault zone (Fig. 5.8). Late Eocene-Oligocene volcanic rocks were deformed during this period, coeval with the deposition of syn-tectonic pyroclastic and sedimentary sequences which form progressive unconformities (Fig. 3.12). Syn-tectonic sequences are covered by the basal pyroclastic member of Farellones Formation (Fig. 3.12). The geochemistry of the Farellones Formation (Table 5.3) suggests that the crust beneath the Andes was moderately thickened as a result of this early Miocene deformation event (Fig. 5.6). As the crust thickened and tectonic regime changed from extensional to transpressional, the rates of volcanic output diminished and magmas began to pool in the upper crust, as reflected by the crystallization ages of the earliest Tertiary plutonic bodies. Kinematic indicators from syn-tectonic dikes emplaced in the early Miocene (Fig. 3.13A) show that by that time faults were already reactivated by E-directed compression.

- Second stage, 13-9 Ma: during this stage, the southern El Teniente segment (Figs. 5.8, 6.9) registered the occurrence of a sequence of events similar to the ones observed in the northern segments 10 m.y. before. The Coya-Machali Formation volcanic rocks were strongly folded, and they

were covered in the central part of the basin by the pyroclastic deposits and lava flows of the Teniente Volcanic Complex (TVC; Fig. 5.1A, 5.8). REE patterns of the TVC show a stronger HREE fractionation compared with the Coya-Machali and Abanico formations, similar to the Farellones Formation (Fig. 5.6). The earliest plutonic bodies of the El Teniente segment were emplaced during this time period. REE patterns of plutonic rocks, in particular La/Yb ratios (Fig. 5.6), suggest magmas were generated under a moderately thickened crust in the El Teniente segment, while very high La/Yb ratios in the Rio Blanco-Los Bronces and Maipo segments in plutonic rocks of the same age suggest magmas were generated and emplaced in an extremely thick crust, probably as a result of the cumulative effect of the two deformation stages that have affected those segments. The early Miocene Rio Colorado pluton in the Rio Blanco-Los Bronces district was exhumed during this stage, according to (U-Th)/He ages (Fig. 5.9). Faults were active with kinematics consistent with E- to ENE-directed compression, as shown by late Miocene syn-tectonic hydrothermal minerals (Figs. 6.4, 6.5). During this stage, the earliest porphyry-style centres of hydrothermal alteration and mineralisation were formed at the Rio Blanco-Los Bronces district, although so far none of these early centres has proved to be economically viable. To the north of the study area, however, this time period coincides with the emplacement of the giant Los Pelambres-El Pachon porphyry Cu-Mo cluster (Fig. 2.3).

- Third stage, 7-2 Ma: according to (U-Th)/He ages (Fig. 5.9), this was the main stage of uplift and exhumation affecting the rocks of the study area. Extremely high La/Yb ratios were achieved in the El Teniente segment during this period (Figs. 5.6, 5.7), with values similar to the ones observed in the northernmost segments after the second stage, suggesting migration of the locus of extreme crustal thickening to the El Teniente segment. Intrusive rocks emplaced during this stage correspond exclusively to local porphyritic stocks, dikes and hydrothermal breccias, which were fed by unexposed magma chambers and which cut through the exhumed early-middle Miocene plutons (e.g. Fig. 3.15). The giant

porphyry Cu-Mo deposits of the study area were formed during this period. After this stage, the axis of the magmatic arc, which had remained stationary since the Eocene, migrated to the east and a new magmatic arc was established at its present position in the eastern Main Cordillera (Fig. 1.2B).

7.3 Implications for mineral exploration

The Andes of central Chile have a long history of mining and mineral exploration. El Teniente was discovered and exploited by small scale operations since the times of the Spanish empire (17th and 18th centuries; Baros, 1995), while mineralisation at Rio Blanco-Los Bronces was discovered in 1864 by Agustin Nazario E., a worker from a nearby farm in the Santiago valley (Warnaars et al., 1985; Irarrázaval et al., 2010). Large scale operations at El Teniente and Los Bronces began in the early 20th century, and mineral exploration for porphyry-style deposits has been intense and uninterrupted since then. As a consequence of this, and coupled with the fact that this area lacks any appreciable post-mineral sedimentary cover or vegetation, it is commonly assumed that most of the outcropping mineralised systems or hydrothermal alteration zones have been identified and at least superficially explored. However, this is only partly true, because in areas of difficult access as a consequence of the extreme topography of the area, only the most evident colour anomalies have been reviewed. But more importantly, an enormous exploration potential remains for systems totally or partially "blind", which have not been eroded enough to expose mineralisation at the present-day surface. A good understanding of the district- and regional-scale structural controls on the emplacement of magmas and hydrothermal systems is critical for success in this new type of exploration.

As illustrated by Fig. 3.16, intersections of conjugate strike-slip faults are a favourable geometric location for the emplacement of magmatic bodies and hydrothermal breccias related with porphyry Cu-Mo systems. Both known porphyry Cu-Mo deposits (Rio Blanco-Los Bronces and El Teniente) and their satellites are located at the intersection of regional-scale, conjugate strike-slip fault systems (Figs. 3.2, 4.1C). It is possible then to define favourable areas for exploration based on the criteria that they must be located at the intersections of major conjugate fault systems

and that the area must present evidence of Miocene-early Pliocene multi-stage intrusive activity.

Figure 7.5 shows the results of this approach. Some of the detected areas have already been explored and drilled, although in many cases drill holes are relatively short (~300 m), not appropriate to recognize the potential of systems which have not been deeply eroded. Also, because of the size of the selected areas (~10 x 5 km), they may contain several individual prospects; the fact that one of them has been drilled and discarded does not imply that the area as a whole should be considered barren. In other cases, the areas have received little attention, mainly due to the difficult access and to the absence of evident colour anomalies. A detailed assessment of the exploration potential of each of these targets is beyond the scope of this work; however, the areas highlighted in Fig. 7.5 should rank high in any greenfields exploration program targeting new orebodies in the Andes of central Chile.

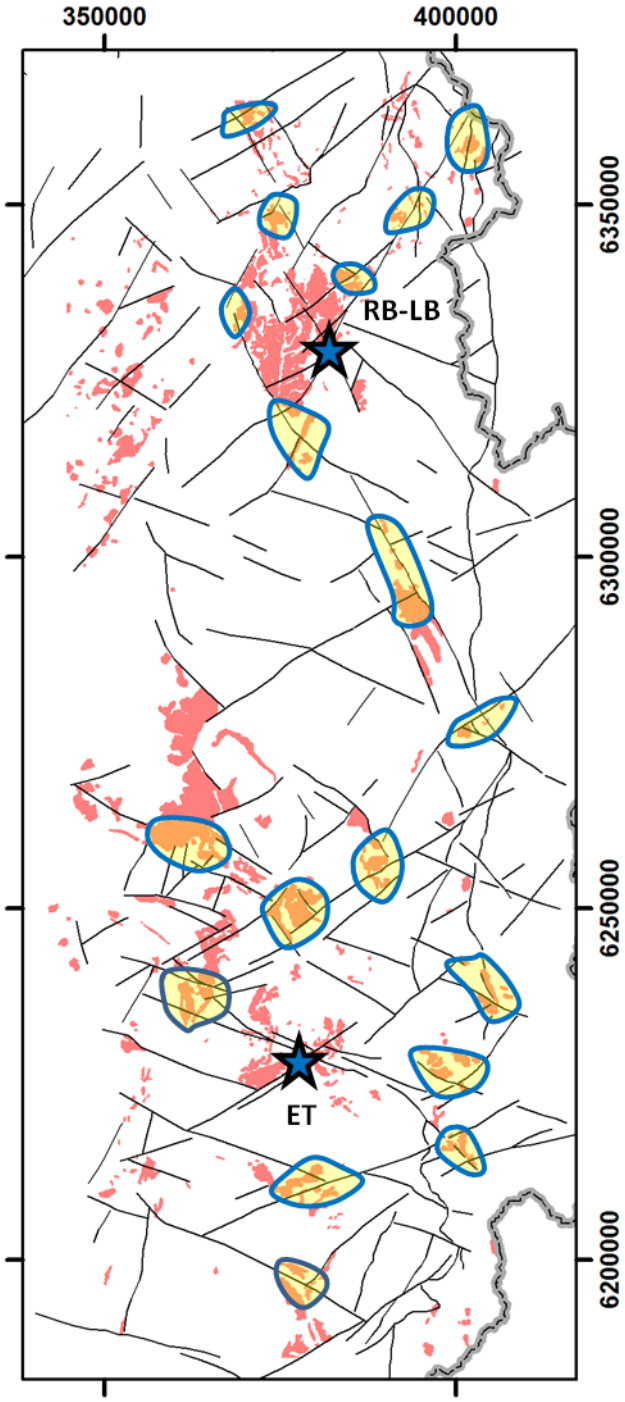

Figure 7.5. Selection of areas of interest (outlined in blue) based on the criteria that they must be located at the intersections of major fault systems and must contain evidences of Mio-Pliocene intrusive activity. RB-LB = Rio Blanco-Los Bronces, ET = El Teniente.

7.4 Additional applications

The new knowledge generated by this work about the structural architecture of the Main Cordillera of central Chile has applications which go beyond the realm of mineral exploration. The arc-oblique fault systems which controlled the flow of Tertiary magmas and hydrothermal fluids are still active today, as shown by the distribution of upper-crustal seismicity (Fig. 4.3A). The following sections discuss

the implications of the proposed structural architecture for the location of active hydrothermal systems (economically important as geothermal energy reservoirs), the position and alignment of active volcanic centres, and the geological hazards associated with active, upper-crustal faults.

7.4.1 Geothermal energy

Previous workers have demonstrated the strong control exerted by active faults in the circulation of hydrothermal fluids in active geothermal systems of southern Chile (e.g., Sanchez et al., 2013). However, there are no specific studies that address this issue in central Chile. Figure 7.6 show the distribution of thermal springs in central Chile over the structural architecture of the study area. Thermal springs located close to the eastern margin of the Abanico Basin or in the Eastern Main Cordillera are in some cases associated with fumaroles and show chemical characteristics typical of thermal waters discharge around active volcanoes. In contrast, those located in the western part of the Abanico Basin or in the Coastal Cordillera correspond to low-temperature waters whose chemistry indicate interaction with meteoric waters during transport along faults (Benavente et al., 2012).

The distribution of thermal springs (Fig. 7.6) suggests a strong correlation between fault architecture, fluid flow and the location of active hydrothermal cells. Most of the thermal occurrences are located over major arc-oblique fault systems, sometimes at their intersections with the basin-margin faults of the Abanico Basin. This concept can be applied to the exploration of geothermal energy resources in central Chile.

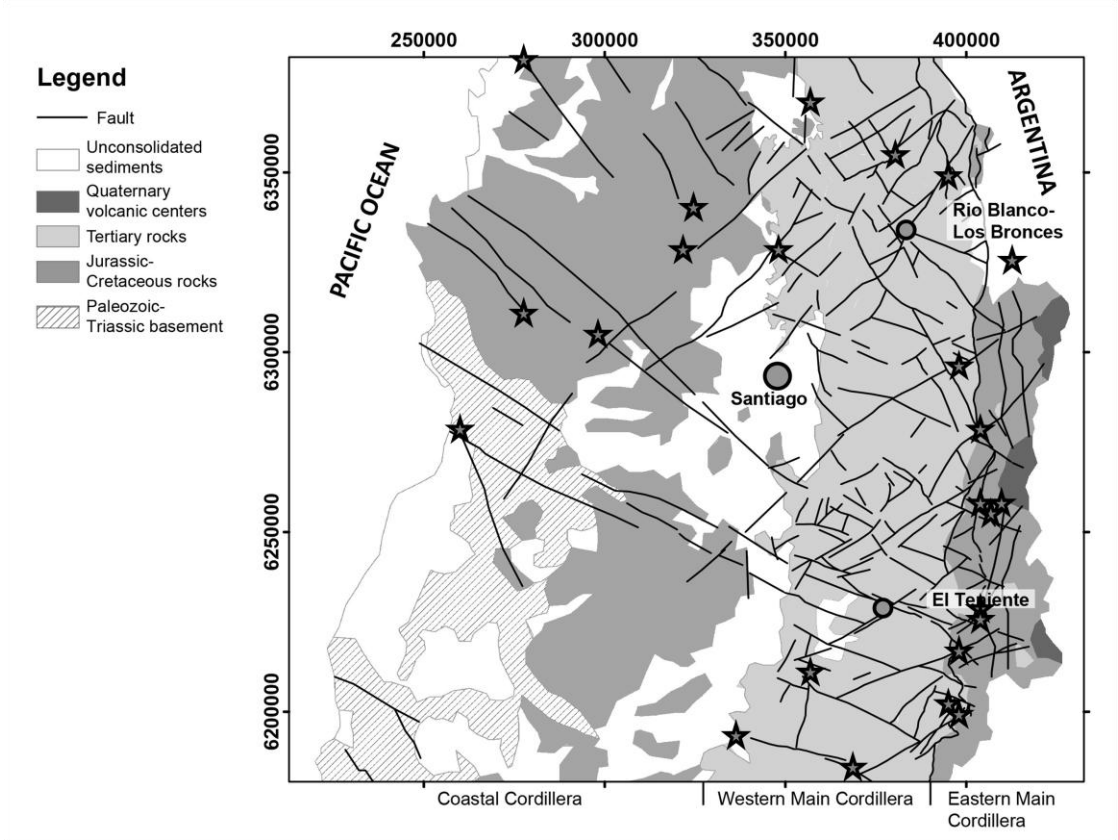

Figure 7.6. Distribution of thermal springs, represented by stars, shown over the geological map of Fig. 6.10. Thermal occurrences from the compilation of Benavente et al. (2012) and personal field observations.

7.4.2 Structural controls on active volcanism

Similar to the case of active geothermal systems, some work has been published about the link between crustal structures and volcanism in southern Chile (Cembrano and Lara, 2009) but no specific work exists about the structural control on active volcanism in central Chile. Figure 4.1C shows that Quaternary volcanoes of central Chile are located above major arc-oblique, NW- and NE-trending fault systems.

In particular, the trend of the regional-scale fault systems associated with each of the volcanic systems is parallel to the alignment of craters and volcanic centres. The Tupungato-Tupungatito complex is built over a major NE-striking, NW-dipping dextral strike-slip fault system, which show evidence of earlier normal movement (Fig. 4.2D). The alignment of the main volcanic centres follows this same NE trend (Fig. 7.7A). In the case of the San Jose volcanic complex, individual craters are aligned following NNW and NW trends (Fig. 7.7B), parallel to a major fault system

which can be followed from the volcano to the NNW and which is related to the emplacement of the La Gloria pluton, the Rio Blanco-San Francisco batholith, the Rio Colorado pluton and the Rio Blanco-Los Bronces porphyry Cu-Mo deposit (Fig. 4.1C). The Maipo volcano, in turn, has two main craters aligned along a WNW trend (Fig. 7.7C), parallel to a regional-scale fault system which can be followed across the entire Western Main Cordillera and which is related to the emplacement of the El Teniente porphyry Cu-Mo deposit (Fig. 4.1C).

This confirms the relevance of arc-oblique fault systems as pathways for the ascent of magmas in the Andes of central Chile.

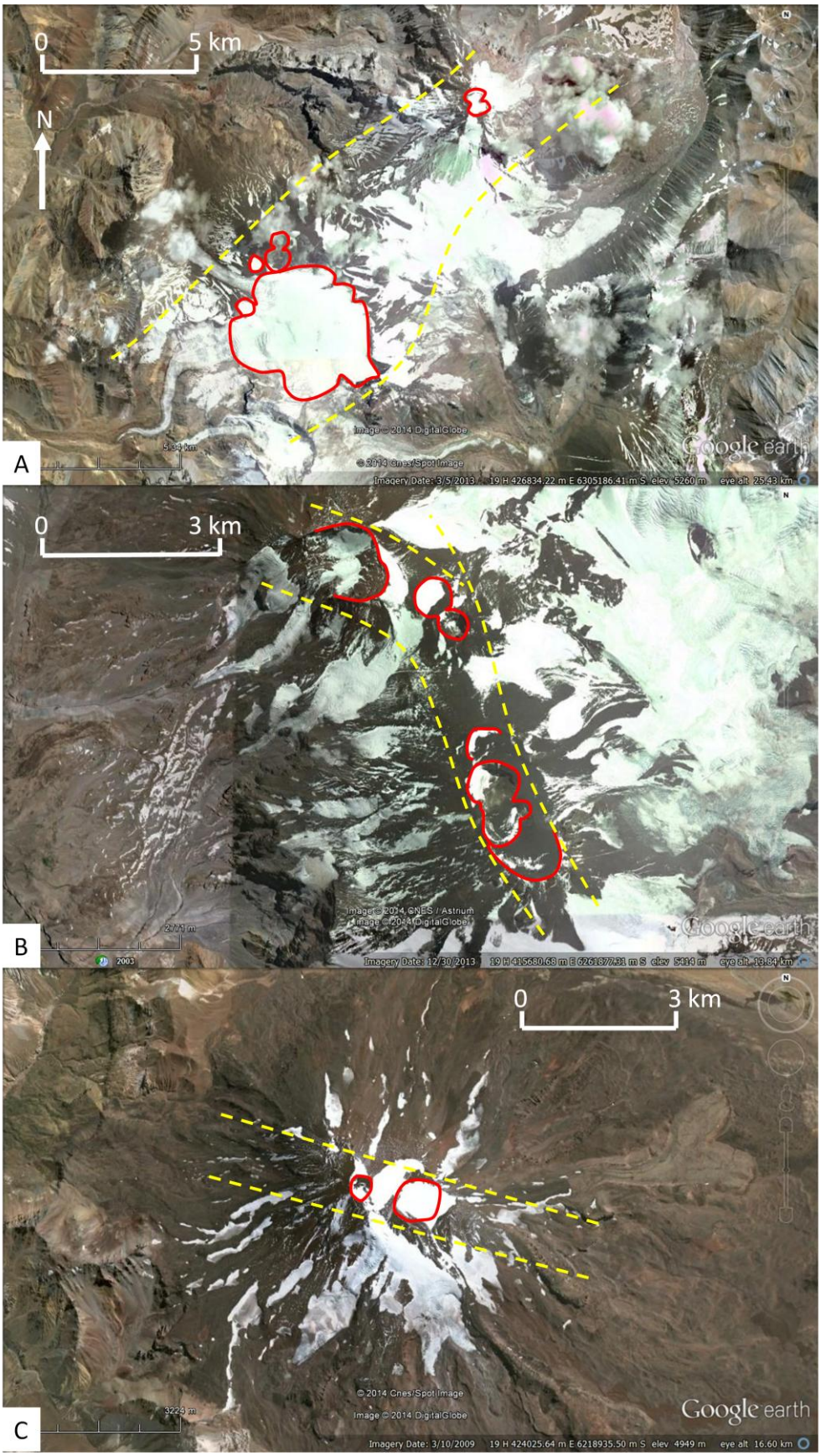
0
5 km
N
A
Image © 2014 DigitalGlobe
© 2014 Cnes/Spot Image
Google earth
Imagery Date: 3/5/2013
0
3 km
B
Image © 2014 CNES / Astrium
Image © 2014 DigitalGlobe
Google earth
Imagery Date: 12/30/2013
0
3 km
© 2014 Cnes/Spot Image
Image © 2014 DigitalGlobe
C
Google earth
Imagery Date: 3/10/2009

Figure 7.7. Alignment of individual craters in the three active volcanic centres of central Chile. A. Tupungato-Tupungatito volcanic complex. B. San Jose volcano. C. Maipo volcano.

7.4.3 Active faults and geologic hazards

Intra-plate seismicity in the upper crust of central Chile is being actively studied (e.g., Barrientos et al., 2004; Farias et al., 2006; Pardo et al., 2006). Both the western and the eastern margins of the Abanico Basin are seismically active, with focal solutions suggesting dextral strike-slip movements in the case of the fault systems along the eastern margin (Farias et al., 2006). Armijo et al. (2010) showed evidence of neotectonic activity at the inverted western margin of the basin and discussed the seismic hazard for the city of Santiago associated with active, west-vergent reverse faults.

Figure 4.3A shows the distribution of upper-crustal seismicity in central Chile, based on the most up to date seismic databases. It suggests that most of the fault ruptures occur at the eastern inverted margin of the basin, along the faults which separate the Western and the Eastern Main Cordillera. Little activity is observed at the inverted western basin margin. However, strong clusters of seismic activity are observed in the central part of the Abanico Basin, unrelated with the inverted basin margins. Their distribution show a strong correlation with the intersections of regional-scale, arc-oblique fault systems (Fig. 4.3A), suggesting that this type of structures are also active and accommodate part of the permanent deformation of the South American margin. Neotectonic activity of arc-oblique structures has been demonstrated by Lavenu and Cembrano (2008). They showed that Quaternary river terraces of the Maipo river have been faulted and folded by NE and WNW-striking reverse faults, parallel to the trend of regional-scale faults recognized by this study (Fig. 7.8). This is relevant for the seismic hazard for the city of Santiago, as some parts of the city are located over the projection towards the Central Depression of major potentially active arc-oblique fault systems. As illustrated in Figure 7.8, this is the case of the El Salto fault (Fig. 3.2) and the Piuquencillo fault (Fig. 5.8).

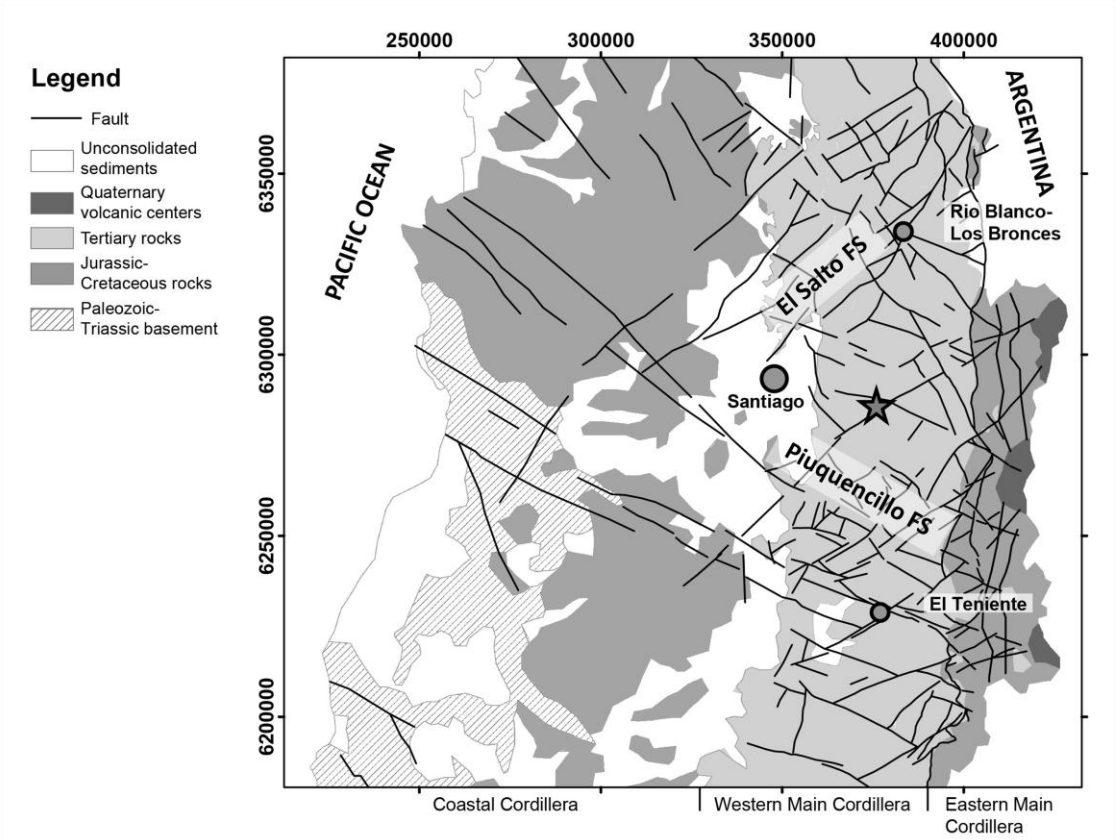

Figure 7.8. Position of the regional-scale Piuquencillo and El Salto fault systems in relation to the city of Santiago. The star marks the locality studied by Lavenu and Cembrano (2008) with Quaternary terraces affected by NE- and WNW-striking reverse faults.

7.5 Directions for future research

Several possible research avenues can be followed to increase our understanding of the structural geology of the Andes of central Chile and its relation with the transport of magmas and hydrothermal fluids. Some of them are:

- The results of this work suggest that the Piuquencillo fault is a major arc-oblique fault system, which bounds two different segments of the Abanico Basin with contrasting tectonic and stratigraphic histories. More detailed work along this fault system is needed to better understand the stratigraphic facies changes associated with it, in particular the transition between the Abanico and Farellones formation in the northern block to the Coya-Machali Formation and the Teniente Volcanic Complex in the south. Several Miocene plutonic bodies are emplaced along this fault; additional studies could be done to look for evidence of syn-tectonic

plutonic emplacement and to study the exploration potential of their associated hydrothermal systems.

- To the south of the Piuquencillo fault, most of the Tertiary rocks can be grouped in the Miocene Coya-Machali Formation and the Teniente Volcanic Complex. However, previous work has shown that at specific localities there are outcrops of late Eocene rocks coeval with the Abanico Formation. The contact relation between these older rocks and the Coya-Machali Formation *sensu stricto* remains unclear. Is there a temporal hiatus? What is the correct stratigraphic assignation of the older rocks? They could be considered as part of the Abanico Formation, as a lower member of the Coya-Machali Formation, or as an entirely different unit. Detailed stratigraphic mapping and radiometric dating is needed to solve this problem.

- The arc-oblique fault systems recognized by this study are commonly associated with syn-tectonic hydrothermal veins (e.g., Fig. 3.11). Some of them contain base and precious metal mineralisation and are exploited by small-scale operations. As most of the scientific studies in the area have focused on the giant porphyry Cu-Mo systems, these veins have received little attention. When were they formed? Under which conditions? Are they coeval with the porphyry Cu-Mo deposits? Are some of them related with "blind" porphyry Cu systems, or do they have no further exploration potential? All these questions remain unanswered.

- $^{40}Ar/^{39}Ar$ ages on volcanic rocks presented by this and previous studies suggest the possibility that in the Rio Blanco-Los Bronces and Maipo segments, Farellones Formation rocks were affected by the thin-skinned deformation at the eastern margin of the Abanico Basin. However, the reliability of the $^{40}Ar/^{39}Ar$ ages is questionable. Detailed structural and stratigraphic mapping and U-Pb zircon geochronology will be required to confirm or discard the presence of blocks of Farellones Formation rocks bounded by segments of the eastern basin-margin faults.

Chapter 8 Conclusions

Structural mapping and the study of regional geophysical datasets show that the Western Main Cordillera of central Chile is dominated by NE- and NW-striking fault systems, oblique to the continental margin and to the axes of the Meso-Cenozoic magmatic arcs (Fig. 4.1). Based on their correlation with older faults observed in the Coastal Cordillera to the west (Fig. 6.10) and in the Andean basement in Argentina to the east, it is proposed that these arc-oblique faults correspond to long-lived, reactivated basement structures. Some of them bound regional-scale gravimetric domains (Fig. 4.3B), suggesting that they define the deep architecture of the crust beneath the Andes of central Chile.

The orogen-oblique, NE- and NW-striking faults are associated with major changes in facies, thicknesses and age of the Tertiary volcanic deposits of the Western Main Cordillera (Figs. 3.11, 4.2), with stratigraphic correlations and syn-tectonic deposits indicating they were active as normal faults during the late Eocene-Early Miocene (Fig. 4.2, 6.3). During that period they bounded individual sub-basins within the intra-arc Abanico Basin. Fault plane kinematics and the geometry of fault-related folds, in turn, demonstrates that most arc-oblique faults were reactivated as strike-slip faults with varying degrees of reverse component during basin inversion in the middle Miocene – early Pliocene (Figs. 3.5A, 3.7, 6.4).

Orogen-oblique faults accommodated most of the internal deformation of the Abanico Basin during tectonic inversion, in combination with low-angle detachments and ramp-flat thrusts developed at different stratigraphic levels (Fig. 3.9). Intrusive contacts, dykes, hydrothermal breccias and veins show strong NE and NW preferred orientations (Figs. 3.2, 3.4B, 3.5B, 3.7, 7.4), indicating that hydrothermal fluids and magmas were channelled during tectonic inversion by the pre-existing NW- and NE-striking fault systems. Intersections of pairs of conjugate, arc-oblique strike-slip faults controlled the localization of the Rio Blanco-Los Bronces and El Teniente porphyry Cu-Mo deposits, and in general those intersections seem to have been highly favourable for the emplacement of Mio-Pliocene magmas and hydrothermal systems (Fig. 7.4).

The kinematic and dynamic analysis of fault-slip data shows that structural reactivation during tectonic inversion was concentrated around major plutons and porphyry Cu-Mo deposits, where there is widespread evidence of syn-tectonic precipitation of hydrothermal minerals on fault planes (Fig. 6.4). In these areas the fault-slip dataset is consistent with reactivation during E- to ENE-directed compression (Fig. 6.9). This suggests feedback between magmatic and hydrothermal activity, fluid pressure, and the reactivation under compression of the structural architecture inherited from the extensional period. In the margins of the inverted Abanico Basin, compression was accommodated by reverse faulting (sub-vertical σ_3), while in the central part of the basin, where the rock column is considerably thicker and the topography higher, a strike-slip regime (sub-vertical σ_2) was predominant during Miocene-early Pliocene tectonic inversion (Figs. 6.7, 6.8). The age of tectonic inversion was confirmed with three Late Miocene $^{40}Ar/^{39}Ar$ ages obtained on syn-tectonic hydrothermal minerals (Fig. 6.5, Table 6.1).

Based on a combination of U-Pb geochronology, (U-Th)/He thermochronology, whole rock geochemistry and structural data, it is proposed that the Abanico Basin in central Chile can be divided into two main segments (Fig. 5.8). The Rio Blanco-Los Bronces deposit is located in the northern segment, while El Teniente is in the southern one. The boundary between the two segments is controlled by the NW-striking Piuquencillo fault and probably by conjugate, NE-striking faults (Fig. 5.8). It is proposed that, while in the northern segment all the Tertiary volcanic and sedimentary rocks can be grouped in the Abanico and Farellones formations, this is not possible in the southern segment. The Abanico Formation may still be present, but it is overlain by the Coya-Machali Formation, which is equivalent in age to the Farellones Formation but it is strongly deformed and has a much larger volcano-sedimentary component. This unit is in turn covered by the Teniente Volcanic Complex, which is several m.y. younger than the youngest volcanic rocks of the northern segment (Table 5.1).

The Tertiary geologic evolution of both segments is characterized by the opening of an extensional basin and its subsequent inversion. However, they differ in their

exhumation history and geochemical variations over time. An early deformation event beginning at ~22 Ma affected only the northern segment, and is associated with the formation of progressive unconformities between the syn-extensional Abanico Formation and the syn-compression Farellones Formation (Fig. 3.12). This was the time of initiation of plutonic activity in this segment and coincided with the onset of crustal thickening as reflected in the geochemistry of the Farellones Formation (Fig. 5.6). A second crustal thickening and exhumation event began at ~12 Ma, reflected by a sharp increase of La/Yb ratios in the already thickened crust of the northern segment (Fig. 5.7). In the southern segment this event is characterized by a moderate increase of La/Yb ratios, the initiation of plutonic activity and the transition between the syn-extensional Coya-Machali Formation and the syn-compression Teniente Volcanic Complex (Fig. 5.7, 7.3). Finally, a third exhumation and crustal thickening event affected both segments at ~6 Ma. This was the main exhumation event affecting the Tertiary rocks of central Chile (Fig. 5.10), and is coeval with the formation of large hydrothermal breccia complexes associated with the porphyry Cu-Mo deposits. Geochemically, this event is reflected by a sharp increase in La/Yb ratios at the southern segment (Fig. 5.6, 5.7).

Seismic data show that arc-oblique fault systems control the distribution of upper-crustal hypocenters at the Western Main Cordillera of central Chile (Fig. 4.3A), showing that these faults are still active under the current stress regime. The distribution of thermal springs and active volcanoes in central Chile, in turn, shows a strong correlation between the arc-oblique fault systems identified by this study and the location of active hydrothermal cells and volcanic complexes (Figs. 4.1C, 7.6, 7.7).

Eighteen mineral exploration targets were defined at the intersections of major arc-oblique, conjugate fault systems (Fig. 7.5). This targets are particularly relevant for the exploration of totally or partially “blind” porphyry systems, which might have not been eroded enough to be exposed at the present-day surface.

A first-order role of arc-oblique fault systems in the geologic evolution of this Andean segment has never been suggested before, but there is compelling geological

and geophysical evidence to support this hypothesis. The presence of pre-existing, regional-scale arc-oblique fault systems such as the ones described in this study, might be the key to understand the structural controls on the emplacement of mineral deposits in other metallogenic belts, both in the Andes and in orogenic systems elsewhere. They can also lead to a better understanding of the structural controls on volcanism, geothermal activity and crustal seismicity.

References

Acocella, V., Gioncada, A., Omarini, R., Riller, U., Mazzuoli, R., and Vezzoli, L., 2011, Tectonomagmatic characteristics of the back-arc portion of the Calama-Olacapato-El Toro Fault Zone, Central Andes: Tectonics, v. 30, TC3005, doi:10.1029/2010TC002854.

Aguirre, L., 1960, Geologia de los Andes de Chile Central, Provincia de Aconcagua, 9, Instituto de Investigaciones Geologicas, 70 p.

Aguirre, L., Calderon, S., Vergara, M., Oliveros, V., Morata, D., and Belmar, M., 2009, Edades isotópicas de rocas de los valles Volcán y Tinguiririca, Chile central: XII Congreso Geologico Chileno, Santiago, 2009, Proceedings, S8.

Aguirre, L., Feraud, G., Vergara, M., Carrasco, J., and Morata, D., 2000, $^{40}Ar/^{39}Ar$ ages of basic flows from the Valle Nevado stratified sequence (Farellones Formation), Andes of central Chile: IX Congreso Geologico Chileno, Puerto Varas, 2000, Proceedings, p. 583-585.

Allmendinger, R. W., Cardozo, N., and Fisher, D. M., 2012, Structural Geology algorithms: vectors and tensors: New York, Cambridge University Press, 302 p.

Almandoz, G., Zulliguer, G., and Marquez-Zavalia, F., 2005, Altar: mineralizacion de alta sulfuracion vinculada a un sistema de porfido cuprifero, San Juan, Argentina: Congreso Geologico Argentino, La Plata, p. 369-376.

Alvarado, P., Barrientos, S., Saez, M., Astroza, M., and Beck, S., 2009, Source study and tectonic implications of the historic 1958 Las Melosas crustal earthquake, Chile, compared to earthquake damage: Physics of the Earth and Planetary Interiors, v. 175, p. 26-36.

Amilibia, A., Sabat, F., McClay, K. R., Munoz, J. A., Roca, E., and Chong, G., 2008, The role of inherited tectono-sedimentary architecture in the development of the central Andean mountain belt: Insights from the Cordillera de Domeyko: Journal of Structural Geology, v. 30, p. 1520-1539.

Arabasz, 1971, Geological and geophysical studies of the Atacama Fault Zone in Northern Chile: PhD thesis, Pasadena, Californian Institute of Technology.

Araneda, M., Avendaño, M., and Merlo, C., 2000, Modelo gravimetrico de la Cuenca de Santiago, etapa II final: IX Congreso Geologico Chileno, Puerto Varas, 2000, Proceedings, p. 404-408.

Armijo, R., Rauld, R., Thiele, R., Vargas, G., Campos, J., Lacassin, R., and Kausel, E., 2010, The West Andean Thrust, the San Ramon Fault, and the seismic hazard for Santiago, Chile: Tectonics, v. 29, TC2007, doi:10.1029/2008TC002427.

Aubouin, J., Borrello, A. V., Cecioni, G., Charrier, R., Chotin, P., Frutos, J., Thiele, R., and Vicente, J. C., 1973, Paleogeographic and structural sketch of the Southern Andes: Revue De Geographie Physique Et De Geologie Dynamique, v. 15, p. 207-216.

Baeza, O., 1999, Analisis de litofacies, evolucion depositacional y analisis estructural de la Formacion Abanico en el area comprendida entre los rios Yeso y Volcan, Region Metropolitana: Honours thesis, Santiago, Universidad de Chile, 119 p.

Baker, J., Peate, D., Waight, T., and Meyzen, C., 2004, Pb isotopic analysis of standards and samples using a Pb-207-Pb-204 double spike and thallium to correct for mass bias with a double-focusing MC-ICP-MS: Chemical Geology, v. 211, p. 275-303.

Baker, M., Cooke, D., and Hollings, P., 2011, LA-ICP-MS U-Pb zircon ages and Nd isotope data for the Teniente Plutonic Complex: implications for the evolution of the El Teniente Porphyry Cu-Mo Deposit: SGA Biennial Meeting, Antofagasta, 2011, Proceedings, p. 853-855.

Baros, M. C., 1995, El Teniente, los hombres del mineral: Santiago, Grafica Andes, 500 p.

Barrientos, S., Vera, E., Alvarado, P., and Monfret, T., 2004, Crustal seismicity in central Chile: Journal of South American Earth Sciences, v. 16, p. 759-768.

Benavente, O., Aguilera, F., Gutierrez, F., Tassi, F., Reich, M., and Vaselli, O., 2012, Los sistemas hidrotermales de Chile Central (33-36°S): XIII Congreso Geologico Chileno, Antofagasta, 2012, Proceedings, p. 559-561.

Bevins, R. E., Robinson, D., Aguirre, L., and Vergara, M., 2003, Episodic burial metamorphism in the Andes - A viable model?: Geology, v. 31, p. 705-708.

Black, L. P., and Gulson, B. L., 1978, The age of the Mud Tank Carbonatite, Strangways Range, Northern Territory: BMR Journal of Australian Geology and Geophysics, v. 3, p. 227-232.

Black, L. P., Kamo, S. L., Allen, C. M., Aleinikoff, J. N., Davis, D. W., Korsch, R. J., and Foudoulis, C., 2003, TEMORA 1: a new zircon standard for Phanerozoic U-Pb geochronology: Chemical Geology, v. 200, p. 155-170.

Boric, R., 1997, Nuevos antecedentes sobre el modelo geologico del yacimiento de cobre El Soldado, Chile Central: VIII Congreso Geologico Chileno, Antofagasta, 1997, Proceedings, p. 862-866.

Bott, M. H. P., 1959, The mechanics of oblique slip faulting: Geological Magazine, v. 96, p. 109-117.

Caceres, J., Comte, D., Charrier, R., Diaz, D., Pardo, M., Vera, E., Garcia, R., Parra, J. C., Piquer, J., and Yanez, G., 2006, En busqueda de un modelo conceptual para la genesis de porfidos gigantes en la Cordillera Principal de Chile Central, Proyecto Anillo: resultados preliminares en transectas geofisicas de Teno, Tinguiririca y Cachapoal: XI Congreso Geologico Chileno, Antofagasta, 2006, Proceedings, p. 167-170.

Camus, F., 2003, Geologia de los sistemas porfiricos en los Andes de Chile: Santiago, Servicio Nacional de Geologia y Mineria, 267 p.

Cannell, J., Cooke, D. R., Walshe, J. L., and Stein, H., 2005, Geology, mineralization, alteration and structural evolution of the El Teniente porphyry Cu-Mo deposit: Economic Geology, v. 100, p. 979-1003.

Cannell, J., Cooke, D. R., Walshe, J. L., and Stein, H., 2007, Geology, mineralization, alteration and structural evolution of El Teniente porphyry Cu-Mo deposit - A reply: Economic Geology, v. 102, p. 1171-1180.

Castelli, J. C., and Lara, L., 1999, Geología de exploración básica generativa entre Andina y Río Colorado, 1:50000, Unpublished report for Codelco.

Cembrano, J., and Lara, L., 2009, The link between volcanism and tectonics in the southern volcanic zone of the Chilean Andes: A review: Tectonophysics, v. 471, p. 96-113.

Cembrano, J., Herve, F., and Lavenu, A., 1996, The Liquine Ofqui fault zone: A long-lived intra-arc fault system in southern Chile: Tectonophysics, v. 259, p. 55-66.

Cembrano, J., Lavenu, A., Yanez, G., Riquelme, R., Garcia, M., Gonzalez, G., and Herail, G., 2007, Neotectonics, in Moreno, T., and Gibbons, W., eds., The Geology of Chile: London, The Geological Society, p. 231-261.

Charrier, R., and Munizaga, F., 1979, Edades K-Ar de vulcanitas cenozoicas del sector cordillerano del rio Cachapoal (34°15' de latitud Sur): Revista Geologica de Chile, v. 7, p. 41-51.

Charrier, R., and Vicente, J. C., 1972, Liminary and geosyncline Andes: major orogenic phases and synchronical evolutions of the central and Magellan sectors of the Argentine Chilean Andes: Solid Earth Problems Conference, Upper Mantle Project, Buenos Aires, 1972, p. 451-470.

Charrier, R., Wyss, A. R., Norell, M. A., Flynn, J. J., Novacek, M. J., McKenna, M. C., Swisher, C. C., Frassinetti, D., and Salinas, P., 1990, Hallazgo de mamíferos fósiles del Terciario Inferior en el sector de Termas del Flaco, Cordillera Principal, Chile Central: implicaciones paleontológicas, estratigráficas y tectónicas: II Simposio sobre el Terciario de Chile, 1990, p. 73-84.

Charrier, R., Wyss, A. R., Flynn, J. J., Swisher, C. C., Spichiger, S., and Zapatta, F., 1994, Nuevos antecedentes estratigráficos y estructurales para las Formaciones

Coya-Machalí y Abanico, entre 33º50' y 35ºS, Cordillera Principal Chilena: VII Congreso Geologico Chileno, 1994, p. 1316-1319.

Charrier, R., Wyss, A. R., Flynn, J. J., Swisher, C. C., Norell, M. A., Zapatta, F., McKenna, M. C., and Novacek, M. J., 1996, New evidence for late Mesozoic early Cenozoic evolution of the Chilean Andes in the Upper Tinguiririca Valley (35 degrees S), Central Chile: Journal of South American Earth Sciences, v. 9, p. 393-422.

Charrier, R., Baeza, O., Elgueta, S., Flynn, J. J., Gans, P., Kay, S. M., Munoz, N., Wyss, A. R., and Zurita, E., 2002, Evidence for Cenozoic extensional basin development and tectonic inversion south of the flat-slab segment, southern Central Andes, Chile (33°-36° SL): Journal of South American Earth Sciences, v. 15, p. 117-139.

Charrier, R., Bustamante, M., Comte, D., Elgueta, S., Flynn, J. J., Iturra, N., Munoz, N., Pardo, M., Thiele, R., and Wyss, A. R., 2005, The Abanico extensional basin: Regional extension, chronology of tectonic inversion and relation to shallow seismic activity and Andean uplift: Neues Jahrbuch Fur Geologie Und Palaontologie-Abhandlungen, v. 236, p. 43-77.

Charrier, R., Pinto, L., and Rodriguez, M. P., 2007, Andean Tectonostratigraphy, in Moreno, T., and Gibbons, W., eds., The Geology of Chile: London, The Geological Society, p. 21-114.

Chernicoff, C. J., Richards, J. P., and Zappettini, E. O., 2002, Crustal lineament control on magmatism and mineralization in northwestern Argentina: geological, geophysical, and remote sensing evidence: Ore Geology Reviews, v. 21, p. 127-155.

Corti, G., Van Wijk, J., Bonini, M., Sokoutis, D., Cloetingh, S., Innocenti, F., and Manetti, P., 2003, Transition from continental break-up to punctiform seafloor spreading: How fast, symmetric and magmatic: Geophysical Research Letters, v. 30, 1604, doi:10.1029/2003GL017374.

Darwin, C., 1846, Geological observations on South America, in The geology of the voyage of the Beagle: London, Smith Elder and Co.

Davidson, J., 1971, Contribución al estudio geológico de los Andes Meridionales Centrales: Geología del área de las Nacientes del Teno, Provincia de Curicó: Honours thesis, Universidad de Chile, 145 p.

Deckart, K., Clark, A. H., Aguilar, C., Vargas, R., Bertens, A., Mortensen, J. K., and Fanning, M., 2005, Magmatic and hydrothermal chronology of the giant Rio Blanco porphyry copper deposit, central Chile: Implications of an integrated U-Pb and Ar-40/Ar-39 database: Economic Geology, v. 100, p. 905-934.

Deckart, K., Godoy, E., Bertens, A., Jerez, D., and Saeed, A., 2010, Barren Miocene granitoids in the Central Andean metallogenic belt, Chile: Geochemistry and Nd-Hf and U-Pb isotope systematics: Andean Geology, v. 37, p. 1-31.

Deckart, K., Clark, A. H., Cuadra, P., and Fanning, M., 2013, Refinement of the time-space evolution of the giant Mio-Pliocene Rio Blanco-Los Bronces porphyry Cu-Mo cluster, Central Chile: new U-Pb (SHRIMP II) and Re-Os geochronology and Ar-40/Ar-39 thermochronology data: Mineralium Deposita, v. 48, p. 57-79.

Deckart, K., Silva, W., Sproehnle, C., and Vela, I., 2014, Timing and duration of hydrothermal activity at the Los Bronces porphyry cluster: an update: Mineralium Deposita, v. 49, p. 535-546.

Drake, R. E., Curtis, G., and Vergara, M., 1976, Potassium-Argon dating of igneous activity in Central Chilean Andes-Latitude 33 degrees: Journal of Volcanology and Geothermal Research, v. 1, p. 285-295.

Farias, M., Comte, D., and Charrier, R., 2006, Sismicidad superficial en Chile central: Implicancias para el estado cortical y crecimiento de los Andes Centrales australes: XI Congreso Geologico Chileno, Antofagasta, 2006, Proceedings, p. 403-406.

Farias, M., Charrier, R., Carretier, S., Martinod, J., Fock, A., Campbell, D., Caceres, J., and Comte, D., 2008, Late Miocene high and rapid surface uplift and its erosional response in the Andes of central Chile (33 degrees-35 degrees S): Tectonics, v. 27, TC1005, doi:10.1029/2006TC002046.

Farías, M., Comte, D., Charrier, R., Martinod, J., David, C., Tassara, A., Tapia, F., and Fock, A., 2010, Crustal-scale structural architecture in central Chile based on seismicity and surface geology: Implications for Andean mountain building: Tectonics, v. 29, TC3006, doi:10.1029/2009TC002480.

Farley, K. A., 2002, (U-Th)/He dating: Techniques, calibrations, and applications, in Porcelli, D., Ballentine, C. J., and Wieler, R., eds., Noble Gases in Geochemistry and Cosmochemistry, 47. Reviews in Mineralogy & Geochemistry, p. 819-844.

Farley, K. A., Wolf, R. A., and Silver, L. T., 1996, The effects of long alpha-stopping distances on (U-Th)/He ages: Geochimica Et Cosmochimica Acta, v. 60, p. 4223-4229.

Flynn, J. J., Wyss, A. R., Charrier, R., and Swisher, C. C., 1995, An early Miocene anthropoid skull from the Chilean Andes: Nature, v. 373, p. 603-607.

Flynn, J. J., Wyss, A. R., Croft, D. A., and Charrier, R., 2003, The Tinguiririca Fauna, Chile: Biochronology, Paleoecology, Biogeography, and a New Earliest Oligocene South American Land Mammal "Age": Palaeogeography, Palaeoclimatology, Palaeoecology, v. 195, p. 229-259.

Fock, A., 2005, Cronologia y tectonica de la exhumacion en el Neogeno de los Andes de Chile Central entre los 33 y los 34 grados S: M.Sc. thesis, Santiago, Universidad de Chile, 179 p.

Fock, A., Charrier, R., Farias, M., Maksaev, V., Fanning, M., and Alvarez, P. P., 2005, Deformation and uplift of the western Main Cordillera between 33º and 34ºS: International Symposium on Andean Geodynamics (ISAG), Barcelona, 2005, Proceedings, p. 273-276.

Fock, A., Charrier, R., Maksaev, V., and Farias, M., 2006, Neogene exhumation and uplift of the Andean Main Cordillera from apatite fission tracks between 33°30' and 34°00'S: Backbone of the Americas-Patagonia to Alaska, Mendoza, 2006, Proceedings, p. 102.

Frikken, P., 2004, Breccia-Hosted Copper-Molybdenum Mineralisation at Rio Blanco, Chile: Unpublished PhD thesis, Hobart, Australia, University of Tasmania, 290 p.

Frikken, P. H., Cooke, D. R., Walshe, J. L., Archibald, D., Skarmeta, J., Serrano, L., and Vargas, R., 2005, Mineralogical and isotopic zonation in the Sur-Sur tourmaline breccia, Rio Blanco-Los Bronces Cu-Mo deposit, Chile: Implications for ore genesis: Economic Geology, v. 100, p. 935-961.

Fuentes, F., Vergara, M., Aguirre, L., and Feraud, G., 2002, Contact relationships of Tertiary volcanic units from the Andes of central Chile (33° S): a reinterpretation based on $^{40}Ar/^{39}Ar$ dating: Revista Geologica de Chile, v. 29, p. 207-225.

Fuentes, F., Aguirre, L., Vergara, M., Valdebenito, L., and Fonseca, E., 2004, Miocene fossil hydrothermal system associated with a volcanic complex in the Andes of central Chile: Journal of Volcanology and Geothermal Research, v. 138, p. 139-161.

Gana, P., and Wall, R., 1997, $^{40}Ar/^{39}Ar$ and K-Ar geochronological evidences of an Upper Cretaceous Eocene hiatus in central Chile (33° - 33°30' S): Revista Geologica de Chile, v. 24, p. 145-163.

Garrido, I., 1995, Proyecto Geodinamico Mina El Teniente, Unpublished report for Codelco, 60 p.

Giambiagi, L. B., Alvarez, P. P., Godoy, E., and Ramos, V. A., 2003a, The control of pre-existing extensional structures on the evolution of the southern sector of the Aconcagua fold and thrust belt, southern Andes: Tectonophysics, v. 369, p. 1-19.

Giambiagi, L. B., Ramos, V. A., Godoy, E., Alvarez, P. P., and Orts, S., 2003b, Cenozoic deformation and tectonic style of the Andes, between 33 degrees and 34 degrees south latitude: Tectonics, v. 22, 1041, doi:10.1029/2001TC001354.

Giambiagi, L., Mescua, J., Bechis, F., Tassara, A., and Hoke, G., 2012, Thrust belts of the southern Central Andes: Along-strike variations in shortening, topography, crustal geometry, and denudation: Geological Society of America Bulletin, v. 124, p. 1339-1351.

Godoy, E., 1993, Geologia del area entre los rios Claro del Maipo y Cachapoal, Codelco-SERNAGEOMIN, 68 p.

Godoy, E., 1998, Intrusivos sintectónicos entre los ríos Aconcagua y Cachapoal, Andes de Chile Central: X Congreso Latinoamericano de Geología, Concepción, 1998, Proceedings, p. 149-154.

Godoy, E., 2012, Sobre el variable marco geotectónico de las formaciones Abanico y Farellones y sus equivalentes al sur de los 35°LS: Revista de la Asociación Geológica Argentina, v. 69, p. 570-577.

Godoy, E., Yanez, G., and Vera, E., 1999, Inversion of an Oligocene volcano-tectonic basin and uplifting of its superimposed Miocene magmatic arc in the Chilean Central Andes: first seismic and gravity evidences: Tectonophysics, v. 306, p. 217-236.

Gonzalez, O., 1963, Observaciones geologicas en el valle del rio Volcan: Revista Minerales, v. 17, p. 20-61.

Grocott, J., and Taylor, G. K., 2002, Magmatic arc fault systems, deformation partitioning and emplacement of granitic complexes in the Coastal Cordillera, north Chilean Andes (25° 30' S to 27° 00' S): Journal of the Geological Society, v. 159, p. 425-442.

Haschke, M., and Gunther, A., 2003, Balancing crustal thickening in arcs by tectonic vs. magmatic means: Geology, v. 31, p. 933-936.

Haschke, M., and Siebel, W., 2002, Repeated crustal thickening and recycling during the Andean orogeny in north Chile (21°-26°S): Journal of Geophysical Research, v. 107, p. ECV6-1-18.

Herve, M., 1976, Estudio geologico de la falla Liquiñe-Reloncavi en el area de Liquiñe: Antecedentes de un movimiento transcurrente (Provincia de Valdivia): I Congreso Geologico Chileno, Santiago, 1976, Proceedings, p. B39-B56.

Herve, F., 1994, The Southern Andes between 39° and 44°S Latitude: the geological signature of a transpressive tectonic regime related to a magmatic arc, in Reutter, K. J., Scheuber, E., and Wigger, P. J., eds., Tectonics of the Southern Central Andes: Berlin, Springer, p. 243-248.

Herve, F., Faundez, V., Calderon, M., Massonne, H. J., and Willner, A., 2007, Metamorphic and plutonic basement complexes, in Moreno, T., and Gibbons, W., eds., The Geology of Chile: London, The Geological Society, p. 5-19.

Hodgson, C. J., 1989, The structure of shear-related, vein-type gold deposits: A review: Ore Geology Reviews, v. 4, p. 231-273.

Hollings, P., Cooke, D., and Clark, A., 2005, Regional geochemistry of tertiary igneous rocks in central Chile: Implications for the geodynamic environment of giant porphyry copper and epithermal gold mineralization: Economic Geology, v. 100, p. 887-904.

Hourigan, J. K., Reiners, P. W., and Brandon, M. T., 2005, U-Th zonation-dependent alpha-ejection in (U-Th)/He chronometry: Geochimica Et Cosmochimica Acta, v. 69, p. 3349-3365.

House, M. A., Farley, K. A., and Stockli, D., 2000, Helium chronometry of apatite and titanite using Nd-YAG laser heating: Earth and Planetary Science Letters, v. 183, p. 365-368.

Infanta, J., Robles, W., Fincham, D., and Lermanda, E., 2006, Geologia y potencial de mineralizacion del sector Soldado Norte, posible proyeccion septentrional del

yacimiento El Soldado: XI Congreso Geologico Chileno, Antofagasta, 2006, Proceedings, p. 279-282.

Irarrazaval, V., Sillitoe, R. H., Wilson, A., Toro, J. C., Robles, W., and Lyall, G., 2010, Discovery history of a giant, high-grade, hypogene porphyry copper-molybdenum deposit at Los Sulfatos, Los Bronces-Rio Blanco district, central Chile: Society of Economic Geologists Special Publication 15, v. 15, p. 253-269.

Jackson, S. E., Pearson, N. J., Griffin, W. L., and Belousova, E. A., 2004, The application of laser ablation-inductively coupled plasma-mass spectrometry to in situ U-Pb zircon geochronology: Chemical Geology, v. 211, p. 47-69.

Jacques, J. M., 2003, A tectonostratigraphic synthesis of the Sub-Andean basins: inferences on the position of South American intraplate accommodation zones and their control on South Atlantic opening: Journal of the Geological Society, v. 160, p. 703-717.

Jara, P., and Charrier, R., 2014, New stratigraphical and geochronological constraints for the Mezo-Cenozoic deposits in the High Andes of central Chile between 32 degrees and 32 degrees 30 ' S: Structural and palaeogeographic implications: Andean Geology, v. 41, p. 174-209.

Jordan, T. E., Burns, W. M., Veiga, R., Pangaro, F., Copeland, P., Kelley, S., and Mpodozis, C., 2001, Extension and basin formation in the southern Andes caused by increased convergence rate: A mid-Cenozoic trigger for the Andes: Tectonics, v. 20, p. 308-324.

Kay, S. M., and Kurtz, A. C., 1995, Magmatic and tectonic characterization of the El Teniente region, Unpublished report for Codelco, 180 p.

Kay, S. M., and Mpodozis, C., 2002, Magmatism as a probe to the Neogene shallowing of the Nazca plate beneath the modern Chilean flat-slab: Journal of South American Earth Sciences, v. 15, p. 39-57.

Kay, S. M., Mpodozis, C., and Coira, B., 1999, Magmatism, tectonism and mineral deposits of the Central Andes (22°-33°S latitude) Society of Economic Geologists Special Publication 7, p. 27-59.

Kay, S. M., Godoy, E., and Kurtz, A., 2005, Episodic arc migration, crustal thickening, subduction erosion, and magmatism in the south-central Andes: Geological Society of America Bulletin, v. 117, p. 67-88.

Klohn, C., 1960, Geología de la Cordillera de los Andes de Chile Central: Santiago, Instituto de Investigaciones Geológicas, 95 p.

Koppers, A. A. P., 2002, ArArCALC - software for $^{40}Ar/^{39}Ar$ age calculations: Computers & Geosciences, v. 28, p. 605-619.

Koppers, A. A. P., Staudigel, H., and Wijbrans, J. R., 2000, Dating crystalline groundmass separates of altered Cretaceous seamount basalts by the $^{40}Ar/^{39}Ar$ incremental heating technique: Chemical Geology, v. 166, p. 139-158.

Kosler, J., 2001, Laser-ablation ICPMS study of metamorphic minerals and processes, in Sylvester, P. J., ed., Laser-ablation-ICPMS in the earth sciences; principles and applications, 29, Mineralogical Association of Canada Short Course Handbook, p. 185-202.

Kurtz, A. C., Kay, S. M., Tittler, A., Mpodozis, C., and Godoy, E., 1995, Neogene magmatism in the Andean Cordillera (26º to 34ºS): evidence for spatial and temporal changes in crustal thickness: Eos, v. 76, p. S272.

Kurtz, A. C., Kay, S. M., Charrier, R., and Farrar, E., 1997, Geochronology of Miocene plutons and exhumation history of the El Teniente region, Central Chile (34-35° S): Revista Geologica de Chile, v. 24, p. 75-90.

Lavenu, A., and Cembrano, J., 1999, Compressional- and transpressional-stress pattern for Pliocene and Quaternary brittle deformation in fore arc and intra-arc zones (Andes of Central and Southern Chile): Journal of Structural Geology, v. 21, p. 1669-1691.

Lavenu, A., and Cembrano, J., 2008, Quaternary compressional deformation in the Main Cordillera of Central Chile (Cajon del Maipo, east of Santiago): Revista Geologica de Chile, v. 35, p. 233-252.

Li, X.-H., Long, W.-G., Li, Q.-L., Liu, Y., Zheng, Y.-F., Yang, Y.-H., Chamberlain, K. R., Wan, D.-F., Guo, C.-H., Wang, X.-C., and Tao, H., 2010, Penglai Zircon Megacrysts: A Potential New Working Reference Material for Microbeam Determination of Hf-O Isotopes and U-Pb Age: Geostandards and Geoanalytical Research, v. 34, p. 117-134.

Maksaev, V., and Zentilli, M., 1988, Marco metalogenico regional de los megadepositos de tipo porfido cuprifero del Norte Grande de Chile: V Congreso Geologico Chileno, Santiago, 1988, Proceedings, p. B181-B212.

Maksaev, V., Munizaga, F., McWilliams, M., Fanning, M., Mathur, R., Ruiz, J., and Zentilli, M., 2004, New chronology for El Teniente, Chilean Andes, from U/Pb, $^{40}Ar/^{39}Ar$, Re/Os and fission-track dating: Implications for the evolution of a supergiant porphyry Cu-Mo deposit: Society of Economic Geologists Special Publication 11, p. 15-54.

Maksaev, V., Townley, B., Palacios, C., and Camus, F., 2007, Metallic Ore Deposits, in Moreno, T., and Gibbons, W., eds., The Geology of Chile: London, The Geological Society, p. 179-199.

Maksaev, V., Munizaga, F., Zentilli, M., and Charrier, R., 2009, Fission track thermochronology of Neogene plutons in the Principal Andean Cordillera of central Chile (33-35 degrees S): Implications for tectonic evolution and porphyry Cu-Mo mineralization: Andean Geology, v. 36, p. 153-171.

Marrett, R., and Allmendinger, R. W., 1990, Kinematic analysis of fault-slip data: Journal of Structural Geology, v. 12, p. 973-986.

Maydagan, L., Franchini, M., Chiaradia, M., Dilles, J. H., and Rey, R., 2014, The Altar Porphyry Cu-(Au-Mo) Deposit (Argentina): A Complex Magmatic-

Hydrothermal System with Evidence of Recharge Processes: Economic Geology, v. 109, p. 621-641.

McInnes, B. I. A., Evans, N. J., Fu, F. Q., Garwin, S., Belousova, E. A., Griffin, W. L., Bertens, A., Sukarna, J., Permanadewi, S., Andrew, R. L., and Deckart, K., 2005, Thermal history analysis of selected Chilean, Indonesian and Iranian porphyry Cu-Mo-Au deposits, in Porter, T. M., ed., Super porphyry copper and gold deposits: a global perspective: Adelaide, PGC Publishing, p. 27-42.

Meffre, S., Large, R. R., Scott, R., Woodhead, J., Chang, Z., Gilbert, S. E., Danyushevsky, L. V., Maslennikov, V., and Hergt, J. M., 2008, Age and pyrite Pb-isotopic composition of the giant Sukhoi Log sediment-hosted gold deposit, Russia: Geochimica Et Cosmochimica Acta, v. 72, p. 2377-2391.

Montecinos, P., Schaerer, U., Vergara, M., and Aguirre, L., 2008, Lithospheric origin of Oligocene-Miocene magmatism in central Chile: U-Pb ages and Sr-Pb-Hf isotope composition of minerals: Journal of Petrology, v. 49, p. 555-580.

Mpodozis, C., and Cornejo, P., 2012, Cenozoic Tectonics and Porphyry Copper Systems of the Chilean Andes: Society of Economic Geologists Special Publication 16, p. 329-360.

Mpodozis, C., and Ramos, V. A., 1989, The Andes of Chile and Argentina, in Ericksen, G. E., Pinochet, C., and Reinemud, J. A., eds., Geology of the Andes and its relation to Hydrocarbon and Mineral Resources. Earth Sciences Series: Houston, Circumpacific Council for Energy and Mineral Resources, p. 59-90.

Munizaga, F., and Vicente, J. C., 1982, Acerca de la zonación plutónica y del volcanismo miocénico en los Andes de Aconcagua (Lat. 32-33°S): datos radiométricos K-Ar: Revista Geológica de Chile, v. 16, p. 3-21.

Muñoz, M., Fuentes, F., Vergara, M., Aguirre, L., Nystrom, J. O., Feraud, G., and Demant, A., 2006, Abanico East Formation: petrology and geochemistry of volcanic rocks behind the Cenozoic arc front in the Andean Cordillera, central Chile (33 degrees 50 ' S): Revista Geologica de Chile, v. 33, p. 109-140.

Muñoz, M., Deckart, K., Charrier, R., and Fanning, M., 2009, New geochronological data on Neogene-Quaternary intrusive rocks from the high Andes of central Chile (33º15'-34º00'S): XII Congreso Geologico Chileno, Santiago, 2009, Proceedings, S11.

Muñoz, M., Farias, M., Charrier, R., Fanning, C. M., Polve, M., and Deckart, K., 2013, Isotopic shifts in the Cenozoic Andean arc of central Chile: Records of an evolving basement throughout cordilleran arc mountain building: Geology, v. 41, p. 931-934.

Nasdala, L., Reiners, P. W., Garver, J. I., Kennedy, A. K., Stern, R. A., Balan, E., and Wirth, R., 2004, Incomplete retention of radiation damage in zircon from Sri Lanka: American Mineralogist, v. 89, p. 219-231.

Niemeyer, H., Berrios, H., and Cruz, M. D. R., 2004, Temperatures of formation in triassic cataclasites of Cordillera Domeyko, Antofagasta, Chile: Revista Geologica de Chile, v. 31, p. 3-18.

Nystrom, J. O., Parada, M. A., and Vergara, M., 1993, Sr-Nd isotope compositions of Cretaceous to Miocene rocks in central Chile: a trend towards a MORB signature and a reversal with time: II International Symposium on Andean Geodynamics, Oxford, 1993, Proceedings, p. 21-23.

Nystrom, J. O., Vergara, M., Morata, D., and Levi, B., 2003, Tertiary volcanism during extension in the Andean foothills of central Chile (33 degrees 15 '-33 degrees 45 ' S): Geological Society of America Bulletin, v. 115, p. 1523-1537.

Pardo, M., Vera, E., Monfret, T., Yañez, G., and Eisenberg, A., 2006, Sismicidad cortical superficial bajo Santiago: implicaciones en la tectonica Andina y evaluacion del peligro sismico: XI Congreso Geologico Chileno, Antofagasta, 2006, Proceedings, p. 443-446.

Pardo, M., Vera, E., Monfret, T., and Yañez, G., 2008, Crustal seismicity and 3D seismic wave velocity models in the Andes cordillera of Central Chile (33°-34.5°S) from local earthquakes: ISAG, Nice, 2008, Proceedings, p. 377-380.

Perello, J., Sillitoe, R. H., Brockway, H., Posso, H., and Mpodozis, C., 2009, Contiguous porphyry Cu-Mo and Cu-Au mineralization at Los Pelambres, Central Chile: XII Congreso Geologico Chileno, Santiago, 2009, Proceedgins, S11.

Perello, J., Sillitoe, R. H., Mpodozis, C., Brockway, H., and Posso, H., 2012, Geologic Setting and Evolution of the Porphyry Copper-Molybdenum and Copper-Gold Deposits at Los Pelambres, Central Chile: Society of Economic Geologists Special Publication 16, p. 79-104.

Perez, D., and Ramos, V. A., 1996a, El basamento prejurasico, in Ramos, V. A., ed., Geología de la región del Aconcagua: Buenos Aires, Subsecretaría de Minería de la Nación, p. 27-58.

Perez, D., and Ramos, V. A., 1996b, Los depositos sinogogenicos, in Ramos, V. A., ed., Geología de la región del Aconcagua: Buenos Aires, Subsecretaría de Minería de la Nación, p. 317-341.

Petit, J. P., 1987, Criteria for the sense of movement on fault surfaces in brittle rocks Journal of Structural Geology, v. 9, p. 597-608.

Piquer, J., 2010, Geologia del Distrito Andina, escala 1:25000, Unpublished report for Codelco, 78 p.

Piquer, J., Rivera, O., and Yanez, G., 2009, Sistemas volcanicos asociados a la evacuacion de la Formacion Farellones en el rio Colorado del Aconcagua, V Region, Chile: XII Congreso Geologico Chileno, Santiago, 2009, Proceedings, S9.

Piquer, J., Castelli, J. C., Charrier, R., and Yanez, G., 2010, The Cenozoic of the upper Teno River, Cordillera Principal, Central Chile: stratigraphy, plutonism and their relation with deep structures: Andean Geology, v. 37, p. 32-53.

Proffett, J. M., 2009, High Cu grades in porphyry Cu deposits and their relationship to emplacement depth of magmatic sources: Geology, v. 37, p. 675-678.

Quirt, G. S., Clark, A., Farrar, E., and Sillitoe, R. H., 1971, Potassium-argon ages of porphyry copper deposits in northern and central Chile: Economic Geology, v. 67, p. 980-981.

Ramos, V. A., 1994, Terranes of Southern Gondwanaland and Their Control in the Andean Structure (30-33 SL), in Reutter, K. J., Scheuber, E., and Wigger, P. J., eds., Tectonics of the Southern Central Andes, Springer-Verlag, p. 249-262.

Ramos, V. A., 1996, Geologia de la region del Aconcagua: Buenos Aires, Subsecretaria de Mineria de la Nacion, 24, 510 p.

Ramos, V. A., Kay, S. M., and Perez, D., 1996, El volcanismo de la región del Aconcagua, in Ramos, V. A., ed., Geología de la región del Aconcagua: Buenos Aires, Subsecretaría de Minería de la Nación, p. 297-316.

Reutter, K. J., Scheuber, E., and Helmcke, D., 1991, Structural evidence of orogen-parallel strike slip displacements in the Precordillera of Northern Chile: Geologische Rundschau, v. 80, p. 135-153.

Reutter, K. J., Scheuber, E., and Chong, G., 1996, The Precordilleran fault system of Chuquicamata, Northern Chile: Evidence for reversals along arc-parallel strike-slip faults: Tectonophysics, v. 259, p. 213-228.

Richards, J. P., Boyce, A. J., and Pringle, M. S., 2001, Geologic evolution of the Escondida area, northern Chile: A model for spatial and temporal localization of porphyry Cu mineralization: Economic Geology, v. 96, p. 271-305.

Rivano, S., Espiñeira, D., Boric, R., and Sepúlveda, P., 1995, Hojas Quillota-Portillo. Regiones de Valparaíso y Coquimbo, 73. Carta geológica de Chile SERNAGEOMIN.

Rivera, O., and Cembrano, J., 2000, Modelo de formación de cuencas volcano-tectónicas en zonas de transferencia oblicuas a la cadena andina: el caso de las cuencas Oligo-Miocenas de Chile Central y su relación con estructuras NWW-NW

(33°00’-34°30’ LS): IX Congreso Geologico Chileno, Puerto Varas, 2000, Proceedings, p. 631-636.

Rivera, O., and Cerda, A., 2012, Los Pórfidos Cupríferos de Chile Central: Significado de Estructuras Translitosféricas y Anomalías Gravimétricas en la Metalogénesis Andina: XIII Congreso Geologico Chileno, Antofagasta, 2012, Proceedings, p. 2-4.

Rivera, O., and Falcon, M. F., 1998, Estudio geologico distrital de la division El Teniente de CODELCO-Chile, escala 1:25000, Unpublished report for Codelco.

Rivera, O., and Falcon, M. F., 2000, Secuencias de relleno de cuencas volcano-tectónicas transversales Oligo-Miocenas en los alrededores del yacimiento El Teniente (33°45’ - 34°30’ LS): IX Congreso Geologico Chileno, Puerto Varas, 2000, Proceedings, p. 819-823.

Rivera, O., and Navarro, M., 1996, Estudio geológico distrital de la División Andina, 2ª etapa, escala 1:25000, Unpublished report for Codelco.

Sack, P. J., Berry, R. F., Meffre, S., Falloon, T. J., Gemmell, J. B., and Friedman, R. M., 2011, In situ location and U-Pb dating of small zircon grains in igneous rocks using laser ablation-inductively coupled plasma-quadrupole mass spectrometry: Geochemistry Geophysics Geosystems, v. 12, 1525-2027, doi 10.1029/2010gc003405.

Sagripanti, L., Folguera, A., Giménez, M., Rojas Vera, E. A., Fabiano, J. J., Molnar, N., Fennell, L., and Ramos, V. A., 2014, Geometry of Middle to Late Triassic extensional deformation pattern in the Cordillera del Viento (Southern Central Andes): A combined field and geophysical study: Journal of Iberian Geology, v. 40, p. 349-366.

Salfity, J. A., 1985, Lineamientos transversales al rumbo andino en el noroeste argentino: IV Congreso Geologico Chileno, Antofagasta, Proceedings, p. 119-137.

Sánchez, P., Pérez-Flores, P., Arancibia, G., Cembrano, J., and Reich, M., 2013, Crustal deformation effects on the chemical evolution of geothermal systems: the intra-arc Liquiñe–Ofqui fault system, Southern Andes: International Geology Review, v. 55, p. 1384-1400.

Scheuber, E., and Andriessen, P. A. M., 1990, The kinematic and geodynamic significance of the Atacama Fault Zone, Northern Chile: Journal of Structural Geology, v. 12, p. 243-257.

Sepulveda, S. A., Astroza, M., Kausel, E., Campos, J., Casas, E. A., Rebolledo, S., and Verdugo, R., 2008, New findings on the 1958 Las Melosas earthquake sequence, central Chile: Implications for seismic hazard related to shallow crustal earthquakes in subduction zones: Journal of Earthquake Engineering, v. 12, p. 432-455.

SERNAGEOMIN, 2002, Mapa Geologico de Chile, scale 1:1,000,000: Santiago.

Serrano, L., Vargas, R., Stambuk, V., Aguilar, C., Galeb, M., Holgrem, C., Contreras, A., Godoy, S., Vela, I., Skewes, A., and Stern, C., 1996, The Late Miocene Río Blanco-Los Bronces copper deposit, central Chilean Andes: Society of Economic Geologists Special Publication 5, v. 5, p. 119-130.

Sibson, R. H., 1985, A note on fault reactivation: Journal of Structural Geology, v. 7, p. 751-754.

Sibson, R. H., 1986, Brecciation Processes in Fault Zones - Inferences from Earthquake Rupturing: Pure and Applied Geophysics, v. 124, p. 159-175.

Sibson, R. H., 2000, A brittle failure mode plot defining conditions for high-flux flow: Economic Geology and the Bulletin of the Society of Economic Geologists, v. 95, p. 41-47.

Sillitoe, R. H., 2003, Iron oxide-copper-gold deposits: an Andean view: Mineralium Deposita, v. 38, p. 787-812.

Sillitoe, R. H., 2010, Porphyry Copper Systems: Economic Geology, v. 105, p. 3-41.

Sillitoe, R. H., and Perello, J., 2005, Andean Copper Province: Tectonomagmatic settings, Deposit Types, Metallogeny, Exploration and Discovery: Economic Geology, v. 100, p. 845-890.

Silva, W., and Toro, J. C., 2009, Mineralización primaria sintectónica en el distrito minero Río Blanco-Los Bronces: XII Congreso Geologico Chileno, Santiago, 2009, Proceedings, S11.

Silver, P. G., Russo, R. M., and Lithgow-Bertelloni, C., 1998, Coupling of South American and African Plate motion and Plate deformation: Science, v. 279, p. 60-63.

Skarmeta, J., Martinez, M., and Ortiz, F., 2004, Modelo Estructural 3D del yacimiento Río Blanco, Unpublished report for Codelco, 85 p.

Skewes, A., Arevalo, A., Floody, R., Zúñiga, P., and Stern, C., 2002, The giant El Teniente breccia deposit: hypogene copper distribution and emplacement: Society of Economic Geologists Special Publication 9, v. 9, p. 299-332.

Skewes, M. A., and Stern, C. R., 2007, Geology, mineralization, alteration, and structural evolution of the El teniente porphyry Cu-Mo deposit - A discussion: Economic Geology, v. 102, p. 1165-1170.

Slama, J., Kosler, J., Condon, D. J., Crowley, J. L., Gerdes, A., Hanchar, J. M., Horstwood, M. S. A., Morris, G. A., Nasdala, L., Norberg, N., Schaltegger, U., Schoene, B., Tubrett, M. N., and Whitehouse, M. J., 2008, Plesovice zircon - A new natural reference material for U-Pb and Hf isotopic microanalysis: Chemical Geology, v. 249, p. 1-35.

Somoza, R., and Ghidella, M. E., 2005, Convergencia en el margen occidental de América del Sur durante el Cenozoico: subducción de las placas de Nazca, Farallón y Aluk: Revista de la Asociación Geológica Argentina, v. 60, p. 797-809.

Stern, C., 1989, Pliocene to present migration of the volcanic front, Andean Southern Volcanic Zone: Revista Geologica de Chile, v. 16, p. 145-162.

Stern, C., Amini, H., Charrier, R., Godoy, E., Herve, F., and Varela, J., 1984, Petrochemistry and age of rhyolitic pyroclastic flows which occur along the drainage valleys of the Rio Maipo and Rio Cachapoal (Chile) and the Rio Chaucha and Rio Papagayos (Argentina): Revista Geologica de Chile, v. 23, p. 39-52.

Stern, C., Moreno, H., Lopez-Escobar, L., Clavero, J., Lara, L., Naranjo, J., Parada, M. A., and Skewes, A., 2007, Chilean volcanoes, in Moreno, T., and Gibbons, W., eds., The Geology of Chile: London, The Geological Society, p. 147-178.

Thiele, R., 1978, Hoja Santiago, Region Metropolitana. Carta Geológica de Chile: Instituto de Investigaciones Geológicas, Santiago.

Thomas, H., 1953, Informe de la comision geologica Thomas-Junge sobre la alta cordillera entre el rio Aconcagua y el rio Colorado: CORFO, Santiago.

Thomas, H., 1958, Geologia de la Cordillera de la Costa entre el valle de La Ligua y la cuesta Barriga: Instituto de Investigaciones Geológicas, Santiago.

Tomlinson, A. J., Mpodozis, C., Cornejo, P., Ramirez, C. F., and Dumitru, T., 1994, El Sistema de Fallas Sierra Castillo-Agua Amarga: transpresion sinistral Eocena en la Precordillera de Potrerillos-El Salvador: VII Congreso Geologico Chileno, Concepcion, 1994, Proceedings, p. 1459-1493.

Toro, J. C., Ortuzar, J., Maksaev, V., Barra, F., and Zamorano, J., 2006, Cronologia de un nuevo cluster en la franja de porfidos cupriferos del Mioceno de Chile central: XI Congreso Geologico Chileno, Antofagasta, 2006, Proceedings, p. 367-370.

Toro, J. C., Ortuzar, J., Maksaev, V., and Barra, F., 2009, Nuevos antecedentes geocronologicos en la franja de porfidos de Cu-Mo del Mioceno-Plioceno, Chile central: implicancias metalogenicas: XII Congreso Geologico Chileno, Santiago, 2009, proceedings, S11.

Toro, J. C., Ortuzar, J., Zamorano, J., Cuadra, P., Hermosilla, J., and Sprohnle, C., 2012, Protracted Magmatic-Hydrothermal History of the Río Blanco-Los Bronces District, Central Chile: Development of World's Greatest Known Concentration of Copper: Society of Economic Geologists Special Publication 16, p. 105-126.

Van Dongen, M., Weinberg, R. F., and Tomkins, A. G., 2010, REE-Y, Ti, and P remobilization in magmatic rocks by hydrothermal alteration during Cu-Au deposit formation: Economic Geology, v. 105, p. 763-776.

Vargas, R., Gustafson, L., Vukasovic, M., Tidy, E., and Skewes, A., 1999, Ore Breccias in the Rio Blanco-Los Bronces Porphyry Copper Deposit, Chile: Society of Economic Geologists Special Publication 7, p. 281-298.

Vergara, M., Charrier, R., Munizaga, F., Rivano, S., Sepúlveda, P., Thiele, R., and Drake, R., 1988, Miocene volcanism in the central Chilean Andes: Journal of South American Earth Sciences, v. 1, p. 199-209.

Vergara, M., Morata, D., Villarroel, R., Nystrom, J. O., and Aguirre, L., 1999, $^{40}Ar/^{39}Ar$ ages, very low grade metamorphism and geochemistry of the volcanic rocks from Cerro El Abanico, Santiago, Andean Cordillera (338300S–708250W): International Symposium on Andean Geodynamics, Gottingen, 1999, Proceedings, p. 785-788.

Vergara, M., Lopez-Escobar, L., Palma, J. L., Hickey-Vargas, R., and Roeschmann, C., 2004, Late tertiary volcanic episodes in the area of the city of Santiago de Chile: new geochronological and geochemical data: Journal of South American Earth Sciences, v. 17, p. 227-238.

Vry, V. H., Wilkinson, J. J., Seguel, J., and Millan, J., 2010, Multistage Intrusion, Brecciation, and Veining at El Teniente, Evolution of a Nested Porphyry System: Economic Geology, v. 105, p. 119-153.

Wall, R., Selles, D., and Gana, P., 1999, Area Tiltil-Santiago, Region Metropolitana, scale 1:100,000: SERNAGEOMIN, Santiago.

Wallace, R. E., 1951, Geometry of shearing stress and relation of faulting: Journal of Geology, v. 59, p. 118-130.

Warnaars, F. W., Holmgren, C., and Barassi, S., 1985, Porphyry copper and tourmaline breccias at Los Bronces-Rio Blanco, Chile: Economic Geology, v. 80, p. 1544-1565.

Wiedenbeck, M., Alle, P., Corfu, F., Griffin, W. L., Meier, M., Oberli, F., Vonquadt, A., Roddick, J. C., and Speigel, W., 1995, 3 natural zircon standards for U-Th-Pb, Lu-Hf, trace element and REE analyses: Geostandards Newsletter, v. 19, p. 1-23.

Yamaji, A., 2000, The multiple inverse method: a new technique to separate stresses from heterogeneous fault-slip data: Journal of Structural Geology, v. 22, p. 441-452.

Yañez, G., and Rivera, O., 2009, Geophysical constraints of the Mapocho El Volcán block (MEV-b), and its geological significance: XII Congreso Geologico Chileno, Santiago, 2009, Proceedings, S9.

Yañez, G. A., Ranero, C. R., Von Huene, R., and Díaz, J., 2001, Magnetic anomaly interpretation across the southern central Andes (32°-34°S): The role of the Juan Fernández Ridge in the late Tertiary evolution of the margin: Journal of Geophysical Research B: Solid Earth, v. 106, p. 6325-6345.

Yañez, G., Cembrano, J., Pardo, M., Ranero, C., and Selles, D., 2002, The Challenger-Juan Fernandez-Maipo major tectonic transition of the Nazca-Andean subduction system at 33-34° S: geodynamic evidence and implications: Journal of South American Earth Sciences, v. 15, p. 23-38.

Yañez, G., Rivera, O., Comte, D., Pardo, M., Baeza, L., and Vera, E., 2008, Damage zones and the occurrence of world-class porphyry copper deposits in the active margin of Chile: Geophysical signatures and tectonomagmatic inferences: ISAG, Nice, 2008, Proceedings, p. 592-593.

Zurita, E., Munoz, N., Charrier, R., Harambour, S., and Elgueta, S., 2000, Madurez termal de la materia organica de la Formacion Abanico = Coya-Machali, Cordillera

Principal, Chile Central: resultados e interpretacion: IX Congreso Geologico Chileno, Puerto Varas, 2000, p. Proceedings, 726-730.

Appendix I Zircon U-Pb geochronology

Appendix IA Analytical procedures

For each sample, approximately 100 g of rock were repeatedly sieved and crushed in a Cr-steel ring mill to a grain size <400 micron. Non magnetic heavy minerals were then separated using a gold pan and a Fe-B-Nd hand magnet. The zircons were handpicked from the heavy mineral concentrate under the microscope in cross-polarised transmitted light. The selected crystals were placed on double sided sticky tape and epoxy glue was then poured into a 2.5 cm diameter mould on top of the zircons. The mount was dried for 12 hours and polished using clean sandpaper and a clean polishing lap. The samples were then washed in distilled water in an ultrasonic bath. The analyses in this study were performed on an Agilent 7500cs quadrupole ICPMS with a 193 nm Coherent Ar-F gas laser and the Resonetics S155 ablation cell at the University of Tasmania in Hobart. The downhole fractionation, instrument drift and mass bias correction factors for Pb/U ratios on zircons were calculated using two analyses on the primary (91500 standard of Wiedenbeck et al., 1995) and one analysis on each of the secondary standard zircons (Temora standard of Black et al., 2003 and JG1 of Jackson et al., 2004) analysed at the beginning of the session and every 15 unknown zircons (roughly every half hour) using the same spot size and conditions as used on the samples. Additional secondary standards (the Mud Tank Zircon of Black and Gulson, 1978, Penglai zircons of Li et al., 2010, and the Plesovice zircon of Slama et al., 2008) were also analysed. The correction factor for the $^{207}Pb/^{206}Pb$ ratio was calculated using large spots of NIST610 analyzed every 30 unknowns and corrected using the values recommended by Baker et al. (2004). Each analysis of the zircons began with a 30 second blank gas measurement followed by a further 30 seconds of analysis time when the laser was switched on. Zircons were sampled on 32 micron spots using the laser at 5 Hz and a density of approximately 2 J/cm2. A flow of He carrier gas at a rate of 0.35 litres/minute carried particles ablated by the laser out of the chamber to be mixed with Ar gas and carried to the plasma torch. Isotopes measured were ^{49}Ti, ^{56}Fe, ^{90}Zr, ^{178}Hf, ^{202}Hg, ^{204}Pb, ^{206}Pb, ^{207}Pb, ^{208}Pb,

^{232}Th and ^{238}U with each element being measured every 0.16 s with longer counting time on the Pb isotopes compared to the other elements. The data reduction used was based on the method outlined in detail in Meffre et al. (2008) and Sack et al. (2011). Element abundances on zircons were calculated using the method outlined by Kosler (2001) using Zr as the internal standard element, assuming stochiometric proportions and using the NIST610 to standard correct for mass bias and drift.

Appendix IB LA-ICPMS U-Pb zircon results

^{207} cor ^{206}Pb/^{238}U		^{206}Pb/^{238}U		^{208}Pb/^{232}Th		^{207}Pb/^{206}Pb		^{238}U/^{206}Pb		^{207}Pb/^{206}Pb		common Pb at
age	+/-1 ster	ratio	+/-1 RSE	ratio	+/-1 RSE	ratio	+/-1 RSE	ratio	+/-1 std err	ratio	+/-1 std err	age of zirc
						AN12JP001						
8.14	0.17	0.0013	2.1%	0.0005	3.1%	0.0554	4.0%	781.88	16.52	0.0554	0.0022	0.836
8.15	0.24	0.0016	2.7%	0.0015	3.2%	0.2106	3.2%	625.88	17.07	0.2106	0.0067	0.836
8.66	**0.13**	0.0013	1.5%	0.0004	2.8%	0.0455	3.9%	744.24	11.25	0.0455	0.0018	0.836
8.58	**0.11**	0.0014	1.3%	0.0010	4.2%	0.0615	2.8%	736.25	9.60	0.0615	0.0017	0.836
8.78	**0.15**	0.0014	1.7%	0.0004	2.0%	0.0517	4.3%	728.41	12.52	0.0517	0.0022	0.836
8.79	**0.12**	0.0014	1.4%	0.0004	1.9%	0.0437	3.6%	735.35	10.28	0.0437	0.0016	0.836
8.91	**0.17**	0.0014	1.9%	0.0006	3.5%	0.0644	5.9%	706.23	13.07	0.0644	0.0038	0.836
8.99	**0.13**	0.0015	1.4%	0.0007	2.8%	0.0832	3.1%	683.27	9.44	0.0832	0.0026	0.836
9.00	**0.20**	0.0014	2.2%	0.0004	4.3%	0.0495	6.6%	713.12	15.49	0.0495	0.0033	0.836
9.09	**0.19**	0.0014	2.0%	0.0005	2.8%	0.0633	5.6%	693.60	14.01	0.0633	0.0036	0.836
9.19	**0.20**	0.0014	2.1%	0.0005	3.9%	0.0471	6.1%	700.08	14.86	0.0471	0.0029	0.836
9.22	**0.25**	0.0014	2.6%	0.0005	4.3%	0.0507	8.2%	694.65	18.25	0.0507	0.0041	0.836
9.38	**0.28**	0.0014	3.0%	0.0004	4.9%	0.0429	11.3%	689.82	20.50	0.0429	0.0049	0.836
103	2	0.0162	1.7%	0.0054	1.8%	0.0508	2.5%	61.82	1.08	0.0508	0.0013	0.842

^{207} cor ^{206}Pb/^{238}U age	+/-1 ster	^{206}Pb/^{238}U ratio	+/-1 RSE	^{208}Pb/^{232}Th ratio	+/-1 RSE	^{207}Pb/^{206}Pb ratio	+/-1 RSE	^{238}U/^{206}Pb ratio	+/-1 std err	^{207}Pb/^{206}Pb ratio	+/-1 std err	common Pb at age of zirc
					AN12JP003							
21.0	**0.5**	0.0044	2.2%	0.0025	2.6%	0.2496	2.8%	228.03	5.01	0.2496	0.0070	0.837
21.1	**0.7**	0.0050	2.6%	0.0044	2.8%	0.3176	3.5%	200.83	5.17	0.3176	0.0110	0.838
21.5	**0.7**	0.0071	2.4%	0.0113	2.9%	0.4666	1.5%	140.55	3.34	0.4666	0.0072	0.839
21.7	**0.7**	0.0038	3.0%	0.0018	2.9%	0.1419	4.9%	260.25	7.74	0.1419	0.0070	0.837
21.6	**0.4**	0.0034	1.9%	0.0010	1.8%	0.0476	4.9%	296.83	5.65	0.0476	0.0024	0.837
21.4	**0.6**	0.0043	2.5%	0.0018	3.0%	0.2207	2.9%	234.62	5.78	0.2207	0.0063	0.837
23.5	*0.3*	0.0037	1.2%	0.0012	1.4%	0.0618	2.8%	268.98	3.32	0.0618	0.0017	0.837
23.5	*0.4*	0.0037	1.6%	0.0012	1.9%	0.0530	4.5%	271.41	4.22	0.0530	0.0024	0.837
23.8	*0.8*	0.0041	3.1%	0.0022	4.7%	0.1305	6.3%	241.60	7.60	0.1305	0.0083	0.837
24.0	*0.7*	0.0039	2.9%	0.0016	4.4%	0.0785	9.0%	256.94	7.33	0.0785	0.0071	0.837
24.8	*0.3*	0.0039	1.1%	0.0012	1.5%	0.0455	2.9%	259.64	2.94	0.0455	0.0013	0.837
25.0	*0.6*	0.0039	2.4%	0.0012	3.4%	0.0542	6.2%	254.46	6.22	0.0542	0.0034	0.837
178	5	0.0289	2.7%	0.0108	4.6%	0.0750	8.3%	34.60	0.92	0.0750	0.0062	0.848
451	4	0.0724	1.0%	0.0219	1.7%	0.0551	1.9%	13.81	0.14	0.0551	0.0011	0.866
1120	12	0.1893	1.1%	0.0538	1.9%	0.0745	1.4%	5.28	0.06	0.0745	0.0011	0.919
1161	13	0.1976	1.2%	0.0571	1.4%	0.0796	1.8%	5.06	0.06	0.0796	0.0014	0.922
1273	14	0.2280	1.1%	0.0946	2.2%	0.1194	0.7%	4.39	0.05	0.1194	0.0008	0.937
1277	72	1.0423	1.8%	52.8348	4.7%	0.8602	1.0%	0.96	0.02	0.8602	0.0085	1.067

^{207} cor ^{206}Pb/^{238}U age	+/-1 ster	^{206}Pb/^{238}U ratio	+/-1 RSE	^{208}Pb/^{232}Th ratio	+/-1 RSE	^{207}Pb/^{206}Pb ratio	+/-1 RSE	^{238}U/^{206}Pb ratio	+/-1 std err	^{207}Pb/^{206}Pb ratio	+/-1 std err	common Pb at age of zirc
					AN12JP003 (Cont.)							
2240	22	0.4182	0.9%	0.1150	1.7%	0.1468	0.9%	2.39	0.02	0.1468	0.0013	1.029
					AN12JP005							
30.9	**0.5**	0.0050	1.5%	0.0017	1.9%	0.0829	4.4%	198.58	3.05	0.0829	0.0036	0.838
31.2	**0.4**	0.0051	1.4%	0.0019	1.9%	0.0796	3.1%	197.75	2.75	0.0796	0.0024	0.838
31.7	**0.7**	0.0050	2.1%	0.0016	2.9%	0.0522	7.7%	201.63	4.14	0.0522	0.0040	0.838
31.7	**0.7**	0.0050	2.3%	0.0015	1.6%	0.0542	6.5%	200.95	4.56	0.0542	0.0035	0.838
32.3	**0.5**	0.0050	1.5%	0.0016	1.8%	0.0490	4.3%	198.44	3.02	0.0490	0.0021	0.838
32.4	**0.8**	0.0059	2.2%	0.0037	2.8%	0.1577	3.9%	170.66	3.75	0.1577	0.0062	0.838
33.1	0.5	0.0053	1.5%	0.0017	2.9%	0.0682	5.0%	188.94	2.87	0.0682	0.0034	0.838
1048	19	0.1784	1.9%	0.0480	1.7%	0.0830	1.9%	5.60	0.10	0.0830	0.0016	0.914
1263	21	0.2166	1.7%	0.0654	1.8%	0.0831	2.4%	4.62	0.08	0.0831	0.0020	0.931
1859	29	0.3678	1.6%	0.0644	2.2%	0.1950	1.3%	2.72	0.04	0.1950	0.0026	1.004
2052	21	0.3739	1.0%	0.1048	1.4%	0.1247	0.8%	2.67	0.03	0.1247	0.0009	1.007

^{207} cor ^{206}Pb/^{238}U		^{206}Pb/^{238}U		^{208}Pb/^{232}Th		^{207}Pb/^{206}Pb		^{238}U/^{206}Pb		^{207}Pb/^{206}Pb		common Pb at
age	+/-1 ster	ratio	+/-1 RSE	ratio	+/-1 RSE	ratio	+/-1 RSE	ratio	+/-1 std err	ratio	+/-1 std err	age of zirc
						AN12JP007						
17.0	**0.4**	0.0029	2.0%	0.0010	2.2%	0.1262	2.7%	341.46	6.88	0.1262	0.0034	0.837
17.0	**0.4**	0.0027	2.3%	0.0009	2.5%	0.0738	6.0%	365.79	8.49	0.0738	0.0044	0.837
17.3	**0.4**	0.0027	2.4%	0.0009	2.6%	0.0583	6.3%	365.51	8.91	0.0583	0.0037	0.837
17.4	**0.4**	0.0028	2.4%	0.0010	2.8%	0.0756	5.4%	355.32	8.63	0.0756	0.0041	0.837
17.8	**0.2**	0.0030	1.3%	0.0012	2.0%	0.0980	2.7%	338.53	4.34	0.0980	0.0027	0.837
18.1	**0.6**	0.0028	3.1%	0.0009	4.8%	0.0519	10.4%	353.38	11.11	0.0519	0.0054	0.837
18.1	**0.4**	0.0030	2.3%	0.0010	2.6%	0.0897	5.4%	336.35	7.72	0.0897	0.0049	0.837
18.4	**0.5**	0.0029	2.9%	0.0009	3.8%	0.0430	9.5%	350.76	10.13	0.0430	0.0041	0.837
18.6	**0.4**	0.0029	2.1%	0.0009	2.6%	0.0600	7.9%	340.95	7.27	0.0600	0.0047	0.837
18.6	**0.2**	0.0029	1.2%	0.0010	1.4%	0.0608	2.9%	340.13	3.95	0.0608	0.0018	0.837

^{207} cor ^{206}Pb/^{238}U		^{206}Pb/^{238}U		^{208}Pb/^{232}Th		^{207}Pb/^{206}Pb		^{238}U/^{206}Pb		^{207}Pb/^{206}Pb		common Pb at age of zirc
age	+/-1 ster	ratio	+/-1 RSE	ratio	+/-1 RSE	ratio	+/-1 RSE	ratio	+/-1 std err	ratio	+/-1 std err	
						AN12JP008						
11.2	**0.3**	0.0018	2.4%	0.0005	4.6%	0.0493	7.6%	571.06	13.86	0.0493	0.0038	0.836
11.3	**0.3**	0.0018	2.5%	0.0006	6.0%	0.0522	6.1%	567.64	14.13	0.0522	0.0032	0.836
11.3	**0.6**	0.0019	5.2%	0.0007	5.6%	0.0956	12.0%	533.80	27.69	0.0956	0.0115	0.836
11.4	**0.6**	0.0018	5.0%	0.0005	8.0%	0.0477	16.3%	566.24	28.18	0.0477	0.0078	0.836
11.4	**0.4**	0.0018	3.7%	0.0006	3.9%	0.0489	13.3%	564.88	20.62	0.0489	0.0065	0.836
11.5	**0.4**	0.0018	3.4%	0.0006	3.9%	0.0549	12.3%	551.61	18.81	0.0549	0.0068	0.836
11.6	**0.4**	0.0019	3.5%	0.0007	3.6%	0.0794	10.0%	533.93	18.51	0.0794	0.0079	0.836
11.6	**0.4**	0.0018	3.3%	0.0005	4.3%	0.0422	13.7%	559.84	18.69	0.0422	0.0058	0.836
11.6	**0.4**	0.0018	3.3%	0.0006	3.6%	0.0452	13.9%	556.60	18.09	0.0452	0.0063	0.836
11.7	**0.6**	0.0018	5.2%	0.0006	10.2%	0.0578	23.1%	541.61	28.29	0.0578	0.0133	0.836
11.7	**0.6**	0.0019	5.0%	0.0007	8.9%	0.0638	19.8%	537.13	27.09	0.0638	0.0126	0.836
12.1	**0.4**	0.0019	3.3%	0.0006	5.6%	0.0405	13.5%	536.82	17.89	0.0405	0.0055	0.836
12.1	**0.2**	0.0019	1.9%	0.0006	5.1%	0.0481	6.4%	530.51	10.17	0.0481	0.0031	0.836
12.2	**0.8**	0.0020	6.2%	0.0008	7.3%	0.0964	24.0%	493.05	30.60	0.0964	0.0232	0.836
13.1	**0.5**	0.0021	3.4%	0.0007	5.1%	0.0572	10.3%	486.58	16.69	0.0572	0.0059	0.836

^{207} cor ^{206}Pb/^{238}U		^{206}Pb/^{238}U		^{208}Pb/^{232}Th		^{207}Pb/^{206}Pb		^{238}U/^{206}Pb		^{207}Pb/^{206}Pb		common Pb at
age	+/-1 ster	ratio	+/-1 RSE	ratio	+/-1 RSE	ratio	+/-1 RSE	ratio	+/-1 std err	ratio	+/-1 std err	age of zirc
						AN12JP010						
21.0	**0.6**	0.0033	2.7%	0.0010	2.2%	0.0618	6.0%	300.77	8.13	0.0618	0.0037	0.837
20.9	**0.6**	0.0033	2.9%	0.0011	3.2%	0.0527	7.8%	305.27	8.91	0.0527	0.0041	0.837
21.0	**0.5**	0.0034	2.2%	0.0013	3.3%	0.0772	6.0%	294.35	6.39	0.0772	0.0046	0.837
21.1	**0.6**	0.0041	2.4%	0.0021	4.2%	0.1982	5.6%	246.56	5.84	0.1982	0.0111	0.837
21.4	**0.4**	0.0034	1.9%	0.0011	2.2%	0.0690	4.9%	292.82	5.46	0.0690	0.0034	0.837
21.4	**0.7**	0.0034	3.1%	0.0014	4.7%	0.0696	8.1%	291.46	8.93	0.0696	0.0056	0.837
21.8	**0.4**	0.0034	2.0%	0.0011	2.8%	0.0486	5.4%	295.00	5.87	0.0486	0.0026	0.837
21.9	**0.3**	0.0034	1.4%	0.0010	1.7%	0.0483	3.9%	293.55	4.19	0.0483	0.0019	0.837
21.3	**1.2**	0.0042	5.2%	0.0029	6.5%	0.2173	6.6%	237.19	12.42	0.2173	0.0143	0.837
21.9	**0.5**	0.0034	2.1%	0.0011	2.8%	0.0540	5.6%	291.07	6.18	0.0540	0.0030	0.837
22.1	**0.5**	0.0035	2.1%	0.0011	2.6%	0.0580	5.8%	286.52	5.98	0.0580	0.0034	0.837
22.7	**0.4**	0.0036	1.7%	0.0012	2.1%	0.0571	4.2%	279.74	4.72	0.0571	0.0024	0.837
23.2	**0.9**	0.0036	3.8%	0.0012	5.6%	0.0473	11.8%	277.66	10.54	0.0473	0.0056	0.837
1502	19	0.2801	1.3%	0.1270	1.7%	0.1485	1.4%	3.57	0.05	0.1485	0.0020	0.962
1726	16	0.3075	1.0%	0.0927	2.4%	0.1070	1.2%	3.25	0.03	0.1070	0.0012	0.975
1923	18	0.3477	0.9%	0.0989	1.4%	0.1179	1.0%	2.88	0.03	0.1179	0.0012	0.994

^{207} cor ^{206}Pb/^{238}U		^{206}Pb/^{238}U		^{208}Pb/^{232}Th		^{207}Pb/^{206}Pb		^{238}U/^{206}Pb		^{207}Pb/^{206}Pb		common Pb at
age	+/-1 ster	ratio	+/-1 RSE	ratio	+/-1 RSE	ratio	+/-1 RSE	ratio	+/-1 std err	ratio	+/-1 std err	age of zirc
						AN12JP011						
19.8	**1.5**	0.0031	7.6%	0.0010	12.9%	0.0636	20.4%	317.93	24.25	0.0636	0.0130	0.837
20.4	**0.9**	0.0035	4.1%	0.0017	6.9%	0.1236	10.2%	284.55	11.80	0.1236	0.0126	0.837
20.6	**0.9**	0.0032	4.1%	0.0011	6.8%	0.0529	14.6%	309.79	12.65	0.0529	0.0077	0.837
20.8	**0.6**	0.0033	2.7%	0.0010	2.7%	0.0710	6.0%	299.68	8.02	0.0710	0.0043	0.837
21.2	**0.9**	0.0034	4.1%	0.0012	5.7%	0.0658	13.4%	296.06	12.15	0.0658	0.0088	0.837
21.3	**1.2**	0.0036	4.8%	0.0020	7.3%	0.1159	15.4%	275.07	13.19	0.1159	0.0178	0.837
21.3	**1.2**	0.0033	5.3%	0.0012	8.2%	0.0506	28.0%	299.87	15.83	0.0506	0.0142	0.837
21.4	**0.9**	0.0034	4.2%	0.0013	5.9%	0.0712	12.8%	291.53	12.22	0.0712	0.0091	0.837
21.5	**1.0**	0.0035	4.4%	0.0014	5.7%	0.0738	13.4%	289.54	12.67	0.0738	0.0099	0.837
21.5	**0.7**	0.0034	3.0%	0.0011	5.0%	0.0560	9.2%	296.02	8.90	0.0560	0.0051	0.837
21.7	**0.7**	0.0036	3.1%	0.0012	3.9%	0.0904	7.6%	280.72	8.76	0.0904	0.0069	0.837
21.9	**1.1**	0.0033	5.0%	0.0010	10.6%	0.0258	52.8%	301.40	14.96	0.0258	0.0137	0.837
22.7	**0.9**	0.0051	3.3%	0.0055	3.4%	0.2931	4.2%	194.82	6.35	0.2931	0.0125	0.838
22.9	**1.3**	0.0035	5.5%	0.0013	10.7%	0.0452	27.5%	281.93	15.48	0.0452	0.0124	0.837
23.0	**0.4**	0.0037	1.7%	0.0016	3.2%	0.0729	4.2%	270.94	4.48	0.0729	0.0031	0.837

^{207} cor ^{206}Pb/^{238}U age	+/-1 ster	^{206}Pb/^{238}U ratio	+/-1 RSE	^{208}Pb/^{232}Th ratio	+/-1 RSE	^{207}Pb/^{206}Pb ratio	+/-1 RSE	^{238}U/^{206}Pb ratio	+/-1 std err	^{207}Pb/^{206}Pb ratio	+/-1 std err	common Pb at age of zirc
					AN12JP013							
10.9	**0.4**	0.0017	3.7%	0.0005	4.5%	0.0570	14.5%	582.45	21.84	0.0570	0.0083	0.836
11.0	**0.9**	0.0018	7.5%	0.0008	10.7%	0.0732	32.8%	568.11	42.46	0.0732	0.0240	0.836
11.0	**0.8**	0.0017	6.8%	0.0006	9.0%	0.0372	53.1%	594.70	40.22	0.0372	0.0198	0.836
11.0	**0.6**	0.0017	5.6%	0.0006	7.9%	0.0643	17.1%	573.86	32.03	0.0643	0.0110	0.836
11.1	**0.7**	0.0017	6.5%	0.0006	9.4%	0.0451	22.8%	582.01	37.68	0.0451	0.0103	0.836
11.1	**0.4**	0.0017	3.8%	0.0006	5.4%	0.0580	13.4%	571.87	21.80	0.0580	0.0078	0.836
11.1	**0.5**	0.0018	4.1%	0.0006	5.0%	0.0608	11.6%	569.39	23.39	0.0608	0.0071	0.836
11.3	**0.6**	0.0018	5.3%	0.0006	7.6%	0.0635	21.1%	559.12	29.49	0.0635	0.0134	0.836
11.3	**1.5**	0.0023	10.2%	0.0018	9.8%	0.2423	21.8%	428.23	43.60	0.2423	0.0529	0.837
11.4	**0.5**	0.0019	4.4%	0.0008	4.8%	0.1146	10.7%	515.88	22.77	0.1146	0.0123	0.836
11.5	**0.7**	0.0018	5.6%	0.0005	7.2%	0.0673	19.7%	545.78	30.33	0.0673	0.0133	0.836
11.5	**0.6**	0.0018	5.3%	0.0006	8.4%	0.0661	21.7%	544.19	28.73	0.0661	0.0144	0.836
11.5	**0.7**	0.0018	5.9%	0.0006	11.6%	0.0639	33.6%	545.61	32.02	0.0639	0.0215	0.836
11.6	**0.7**	0.0020	5.5%	0.0009	7.6%	0.1093	14.7%	510.22	28.13	0.1093	0.0160	0.836
17.1	13.0	0.0070	10.0%	0.0008	3.5%	0.5391	42.0%	142.41	14.18	0.5391	0.2266	0.839

^{207} cor ^{206}Pb/^{238}U		^{206}Pb/^{238}U		^{208}Pb/^{232}Th		^{207}Pb/^{206}Pb		^{238}U/^{206}Pb		^{207}Pb/^{206}Pb		common Pb at
age	+/-1 ster	ratio	+/-1 RSE	ratio	+/-1 RSE	ratio	+/-1 RSE	ratio	+/-1 std err	ratio	+/-1 std err	age of zirc
						AN12JP014						
24.6	**0.5**	0.0038	2.0%	0.0012	2.5%	0.0493	6.3%	260.60	5.14	0.0493	0.0031	0.837
24.8	**0.5**	0.0040	2.0%	0.0014	1.8%	0.0726	4.3%	251.07	4.90	0.0726	0.0031	0.837
24.9	**0.4**	0.0039	1.7%	0.0013	2.5%	0.0529	4.4%	256.64	4.35	0.0529	0.0023	0.837
25.0	**0.4**	0.0039	1.6%	0.0013	1.6%	0.0578	5.1%	253.75	4.00	0.0578	0.0029	0.837
25.2	**0.3**	0.0039	1.2%	0.0012	1.3%	0.0482	2.9%	255.25	3.08	0.0482	0.0014	0.837
25.4	**0.4**	0.0040	1.6%	0.0014	2.5%	0.0574	5.2%	249.64	3.95	0.0574	0.0030	0.837
25.5	**0.4**	0.0040	1.5%	0.0013	1.5%	0.0533	3.6%	250.02	3.83	0.0533	0.0019	0.837
25.5	**0.3**	0.0040	1.2%	0.0012	1.4%	0.0458	3.3%	252.20	3.12	0.0458	0.0015	0.837
24.6	**0.4**	0.0038	1.4%	0.0012	1.6%	0.0507	3.9%	260.45	3.67	0.0507	0.0020	0.837
24.6	**0.3**	0.0038	1.2%	0.0012	1.5%	0.0489	2.8%	260.33	3.03	0.0489	0.0014	0.837
24.8	**0.3**	0.0039	1.2%	0.0011	1.4%	0.0477	2.5%	259.34	2.99	0.0477	0.0012	0.837
24.8	**0.4**	0.0039	1.8%	0.0012	1.8%	0.0547	4.4%	256.72	4.54	0.0547	0.0024	0.837
24.8	**0.3**	0.0039	1.2%	0.0012	1.5%	0.0498	3.2%	257.93	3.08	0.0498	0.0016	0.837
25.5	**0.3**	0.0040	1.0%	0.0012	1.4%	0.0508	2.5%	250.97	2.59	0.0508	0.0013	0.837
25.8	**0.5**	0.0040	1.8%	0.0011	1.7%	0.0483	5.2%	249.16	4.46	0.0483	0.0025	0.837
88.6	1.6	0.0141	1.8%	0.0045	2.7%	0.0606	4.5%	71.13	1.25	0.0606	0.0027	0.841
94.2	1.9	0.0148	2.0%	0.0050	3.4%	0.0542	5.4%	67.36	1.34	0.0542	0.0029	0.842
97.3	2.0	0.0153	2.0%	0.0047	2.8%	0.0513	5.0%	65.50	1.32	0.0513	0.0025	0.842
373	5	0.0599	1.3%	0.0301	3.6%	0.0600	2.5%	16.68	0.21	0.0600	0.0015	0.861
1549	13	0.2778	0.8%	0.0831	2.4%	0.1155	0.8%	3.60	0.03	0.1155	0.0010	0.960
2093	21	0.3931	1.0%	0.1063	1.3%	0.1512	0.6%	2.54	0.03	0.1512	0.0009	1.016

^{207} cor ^{206}Pb/^{238}U		^{206}Pb/^{238}U		^{208}Pb/^{232}Th		^{207}Pb/^{206}Pb		^{238}U/^{206}Pb		^{207}Pb/^{206}Pb		common Pb at
age	+/-1 ster	ratio	+/-1 RSE	ratio	+/-1 RSE	ratio	+/-1 RSE	ratio	+/-1 std err	ratio	+/-1 std err	age of zirc
					AN12JP014 (Cont.)							
2796	26	0.5426	0.8%	0.1355	1.2%	0.1957	0.5%	1.84	0.01	0.1957	0.0010	1.087
					AN12JP018							
11.9	**0.7**	0.0024	4.7%	0.0017	9.2%	0.2394	7.5%	408.82	19.21	0.2394	0.0180	0.837
12.1	**1.0**	0.0019	7.2%	0.0006	11.6%	0.0397	71.7%	538.06	38.78	0.0397	0.0285	0.836
12.1	**0.7**	0.0021	5.4%	0.0011	6.5%	0.1434	13.4%	467.87	25.47	0.1434	0.0193	0.836
12.2	**0.7**	0.0020	5.1%	0.0009	7.5%	0.0823	19.5%	503.45	25.90	0.0823	0.0160	0.836
12.4	**0.5**	0.0019	4.0%	0.0006	5.7%	0.0518	15.2%	513.94	20.76	0.0518	0.0079	0.836
12.5	**0.4**	0.0019	3.4%	0.0006	4.1%	0.0463	11.1%	516.87	17.58	0.0463	0.0051	0.836
12.5	**0.5**	0.0026	3.7%	0.0017	6.9%	0.2374	5.7%	389.60	14.47	0.2374	0.0134	0.837
12.9	**0.8**	0.0019	6.0%	0.0006	10.7%	0.0238	60.9%	514.61	30.92	0.0238	0.0145	0.836
13.0	**1.0**	0.0025	6.1%	0.0023	6.6%	0.2068	14.8%	396.01	24.17	0.2068	0.0306	0.837
13.2	**0.8**	0.0021	6.1%	0.0009	9.4%	0.0546	26.7%	484.15	29.71	0.0546	0.0146	0.836
13.6	**0.9**	0.0021	6.0%	0.0006	9.7%	0.0281	54.6%	485.90	29.19	0.0281	0.0153	0.836
13.6	**0.6**	0.0026	4.1%	0.0016	5.3%	0.1831	8.3%	391.79	15.94	0.1831	0.0152	0.837
13.6	**0.6**	0.0021	4.5%	0.0007	9.3%	0.0324	30.4%	482.03	21.63	0.0324	0.0098	0.836
14.3	**1.0**	0.0023	6.2%	0.0006	11.2%	0.0599	31.2%	441.60	27.55	0.0599	0.0187	0.837

^{207} cor ^{206}Pb/^{238}U age	+/-1 ster	^{206}Pb/^{238}U ratio	+/-1 RSE	^{208}Pb/^{232}Th ratio	+/-1 RSE	^{207}Pb/^{206}Pb ratio	+/-1 RSE	^{238}U/^{206}Pb ratio	+/-1 std err	^{207}Pb/^{206}Pb ratio	+/-1 std err	common Pb at age of zirc
					AN12JP021							
14.7	**0.3**	0.0025	1.9%	0.0011	2.0%	0.1285	3.3%	392.44	7.59	0.1285	0.0042	0.837
15.4	**0.3**	0.0024	2.1%	0.0008	2.4%	0.0509	4.6%	415.53	8.54	0.0509	0.0023	0.837
15.7	**0.4**	0.0024	2.3%	0.0008	3.4%	0.0477	7.2%	409.39	9.25	0.0477	0.0034	0.837
15.8	**0.3**	0.0025	2.1%	0.0008	2.8%	0.0515	5.8%	406.04	8.61	0.0515	0.0030	0.837
15.8	**0.5**	0.0025	3.0%	0.0008	6.2%	0.0491	10.7%	407.07	12.19	0.0491	0.0053	0.837
16.0	**0.7**	0.0028	4.0%	0.0017	5.0%	0.1431	8.3%	353.80	14.09	0.1431	0.0119	0.837
16.0	**0.5**	0.0025	3.0%	0.0008	5.8%	0.0463	12.2%	401.28	12.09	0.0463	0.0056	0.837
16.4	**1.1**	0.0025	6.9%	0.0009	9.4%	0.0375	22.8%	396.88	27.40	0.0375	0.0085	0.837
139	2	0.0219	1.1%	0.0063	1.5%	0.0510	2.9%	45.72	0.50	0.0510	0.0015	0.845
1042	10	0.1755	1.0%	0.0501	1.4%	0.0741	1.4%	5.70	0.06	0.0741	0.0010	0.912
1053	16	0.1778	1.5%	0.0553	2.9%	0.0760	3.1%	5.62	0.09	0.0760	0.0024	0.913

^{207} cor ^{206}Pb/^{238}U		^{206}Pb/^{238}U		^{208}Pb/^{232}Th		^{207}Pb/^{206}Pb		^{238}U/^{206}Pb		^{207}Pb/^{206}Pb		common Pb at
age	+/-1 ster	ratio	+/-1 RSE	ratio	+/-1 RSE	ratio	+/-1 RSE	ratio	+/-1 std err	ratio	+/-1 std err	age of zirc
						AN12JP022						
12.1	**0.5**	0.0022	3.7%	0.0025	6.1%	0.1626	7.5%	455.30	17.01	0.1626	0.0122	0.837
12.1	**0.6**	0.0037	3.4%	0.0127	4.4%	0.4383	2.8%	267.70	9.17	0.4383	0.0124	0.837
12.4	**0.8**	0.0057	4.2%	0.0042	3.4%	0.5719	2.2%	174.36	7.32	0.5719	0.0124	0.838
13.0	**0.4**	0.0021	2.8%	0.0008	5.4%	0.0608	7.0%	486.50	13.66	0.0608	0.0042	0.836
13.0	**0.5**	0.0027	3.4%	0.0048	3.7%	0.2393	4.8%	374.00	12.72	0.2393	0.0115	0.837
13.1	**0.2**	0.0021	1.8%	0.0016	5.5%	0.0688	5.8%	476.99	8.41	0.0688	0.0040	0.836
13.6	**1.4**	0.0102	6.8%	0.0298	4.9%	0.6745	1.4%	98.50	6.66	0.6745	0.0095	0.840
14.2	0.6	0.0022	4.3%	0.0010	11.2%	0.0454	15.4%	454.44	19.39	0.0454	0.0070	0.837
15.0	1.1	0.0025	7.1%	0.0010	7.0%	0.0935	15.5%	402.61	28.40	0.0935	0.0145	0.837
16.9	1.3	0.0070	5.7%	0.0006	1.2%	0.5410	2.3%	143.15	8.20	0.5410	0.0126	0.838
178	3	0.0280	1.7%	0.0086	2.1%	0.0493	4.3%	35.74	0.60	0.0493	0.0021	0.847
313	3	0.0499	1.1%	0.0154	1.6%	0.0539	1.7%	20.05	0.21	0.0539	0.0009	0.857

^{207} cor ^{206}Pb/^{238}U		^{206}Pb/^{238}U		^{208}Pb/^{232}Th		^{207}Pb/^{206}Pb		^{238}U/^{206}Pb		^{207}Pb/^{206}Pb		common Pb at
age	+/-1 ster	ratio	+/-1 RSE	ratio	+/-1 RSE	ratio	+/-1 RSE	ratio	+/-1 std err	ratio	+/-1 std err	age of zirc
						AN13JP003						
11.0	**0.4**	0.0018	3.2%	0.0007	4.1%	0.0753	9.0%	564.78	17.89	0.0753	0.0068	0.836
11.1	**0.3**	0.0018	3.1%	0.0006	2.5%	0.0797	6.2%	555.18	16.98	0.0797	0.0050	0.836
11.2	**0.1**	0.0018	1.1%	0.0011	2.3%	0.0674	2.2%	561.09	6.07	0.0674	0.0015	0.836
11.3	**0.3**	0.0018	3.0%	0.0006	3.5%	0.0518	10.2%	568.02	17.24	0.0518	0.0053	0.836
11.3	**0.5**	0.0018	4.2%	0.0008	6.8%	0.0890	12.5%	540.75	22.81	0.0890	0.0111	0.836
11.3	**0.4**	0.0018	3.8%	0.0006	4.7%	0.0533	10.5%	563.24	21.57	0.0533	0.0056	0.836
11.4	**0.3**	0.0019	2.4%	0.0010	3.7%	0.1134	5.6%	518.13	12.36	0.1134	0.0064	0.836
11.4	**0.4**	0.0018	3.7%	0.0006	5.2%	0.0640	12.5%	550.71	20.54	0.0640	0.0080	0.836
11.5	**0.6**	0.0018	4.8%	0.0006	7.5%	0.0699	15.6%	545.28	26.40	0.0699	0.0109	0.836
11.6	**0.6**	0.0019	5.0%	0.0007	5.4%	0.0773	12.7%	533.55	26.73	0.0773	0.0098	0.836
11.7	**0.3**	0.0018	2.9%	0.0006	4.0%	0.0540	10.2%	546.02	15.78	0.0540	0.0055	0.836
11.7	**0.4**	0.0023	2.9%	0.0016	4.1%	0.2023	4.3%	442.06	12.96	0.2023	0.0088	0.837
11.8	**0.3**	0.0020	2.7%	0.0008	3.1%	0.0931	7.1%	512.63	13.73	0.0931	0.0066	0.836
11.8	**0.5**	0.0018	4.3%	0.0006	6.9%	0.0421	20.3%	543.62	23.49	0.0421	0.0086	0.836
12.2	**0.6**	0.0019	4.9%	0.0005	8.6%	0.0334	24.6%	527.62	25.60	0.0334	0.0082	0.836

^{207} cor ^{206}Pb/^{238}U		^{206}Pb/^{238}U		^{208}Pb/^{232}Th		^{207}Pb/^{206}Pb		^{238}U/^{206}Pb		^{207}Pb/^{206}Pb		common Pb at
age	+/-1 ster	ratio	+/-1 RSE	ratio	+/-1 RSE	ratio	+/-1 RSE	ratio	+/-1 std err	ratio	+/-1 std err	age of zirc
						AN13JP006						
10.3	**1.4**	0.0063	5.3%	0.0120	3.5%	0.6379	3.8%	158.11	8.30	0.6379	0.0243	0.838
11.7	**1.1**	0.0076	2.4%	0.0130	2.0%	0.6488	2.3%	132.32	3.17	0.6488	0.0149	0.839
12.0	**1.2**	0.0039	4.9%	0.0054	3.9%	0.4580	7.0%	257.15	12.69	0.4580	0.0321	0.837
12.4	**0.5**	0.0026	3.0%	0.0014	4.3%	0.2461	5.0%	387.20	11.46	0.2461	0.0122	0.837
12.5	**0.5**	0.0039	2.9%	0.0026	2.7%	0.4425	2.6%	256.53	7.48	0.4425	0.0115	0.837
12.6	**2.2**	0.0100	8.9%	0.0139	5.8%	0.6851	3.3%	99.82	8.92	0.6851	0.0225	0.840
12.7	**0.7**	0.0020	5.0%	0.0008	6.9%	0.0596	20.3%	500.37	24.92	0.0596	0.0121	0.836
12.7	**0.4**	0.0021	2.7%	0.0016	4.7%	0.1028	6.0%	469.88	12.50	0.1028	0.0062	0.836
12.8	**0.7**	0.0020	5.4%	0.0008	7.2%	0.0700	21.2%	489.87	26.42	0.0700	0.0148	0.836
12.9	**0.8**	0.0031	5.0%	0.0016	4.4%	0.3244	6.5%	324.09	16.35	0.3244	0.0212	0.837
12.9	**0.5**	0.0024	3.5%	0.0023	5.5%	0.1750	7.4%	418.23	14.66	0.1750	0.0129	0.837
13.3	**0.9**	0.0023	6.8%	0.0014	7.7%	0.1357	10.9%	429.55	29.24	0.1357	0.0148	0.837
14.2	**1.7**	0.0056	7.0%	0.0105	5.7%	0.5282	5.6%	177.32	12.47	0.5282	0.0297	0.838
38.1	0.7	0.0060	1.9%	0.0021	2.7%	0.0549	4.8%	167.09	3.14	0.0549	0.0026	0.838
133	2	0.0210	1.1%	0.0067	1.5%	0.0537	2.4%	47.57	0.54	0.0537	0.0013	0.844

^{207} cor ^{206}Pb/^{238}U		^{206}Pb/^{238}U		^{208}Pb/^{232}Th		^{207}Pb/^{206}Pb		^{238}U/^{206}Pb		^{207}Pb/^{206}Pb		common Pb at
age	+/-1 ster	ratio	+/-1 RSE	ratio	+/-1 RSE	ratio	+/-1 RSE	ratio	+/-1 std err	ratio	+/-1 std err	age of zirc
						AN13JP010						
18.6	**0.5**	0.0029	2.5%	0.0009	3.4%	0.0523	6.8%	344.35	8.53	0.0523	0.0035	0.837
18.6	**0.5**	0.0029	2.8%	0.0009	3.6%	0.0455	10.0%	345.32	9.74	0.0455	0.0045	0.837
18.6	**0.9**	0.0039	3.8%	0.0035	3.9%	0.2475	6.5%	257.41	9.66	0.2475	0.0162	0.837
18.8	**0.7**	0.0029	3.5%	0.0009	4.7%	0.0510	13.6%	340.54	12.01	0.0510	0.0069	0.837
18.9	**0.8**	0.0035	3.7%	0.0021	3.9%	0.1715	7.2%	286.60	10.49	0.1715	0.0123	0.837
19.1	**0.4**	0.0030	1.8%	0.0010	2.0%	0.0588	4.5%	332.00	6.11	0.0588	0.0027	0.837
19.2	**0.4**	0.0031	2.2%	0.0010	2.6%	0.0662	6.2%	326.40	7.20	0.0662	0.0041	0.837
19.3	**0.4**	0.0030	2.0%	0.0010	2.1%	0.0536	5.9%	331.26	6.68	0.0536	0.0032	0.837
19.3	**0.5**	0.0030	2.3%	0.0010	2.7%	0.0497	6.2%	331.46	7.71	0.0497	0.0031	0.837
19.4	**0.5**	0.0030	2.4%	0.0010	3.0%	0.0429	7.8%	331.76	8.02	0.0429	0.0034	0.837
19.5	**0.6**	0.0031	2.8%	0.0010	3.1%	0.0572	8.1%	326.38	9.14	0.0572	0.0046	0.837
19.6	**0.4**	0.0031	1.9%	0.0010	2.0%	0.0516	4.5%	327.00	6.07	0.0516	0.0023	0.837
19.8	**0.8**	0.0031	4.0%	0.0010	6.2%	0.0553	12.6%	321.59	12.97	0.0553	0.0070	0.837
19.9	**0.9**	0.0031	4.4%	0.0008	11.1%	0.0413	22.5%	323.67	14.33	0.0413	0.0093	0.837
20.7	**0.8**	0.0032	3.7%	0.0011	5.9%	0.0527	13.9%	307.92	11.25	0.0527	0.0073	0.837

^{207} cor ^{206}Pb/^{238}U		^{206}Pb/^{238}U		^{208}Pb/^{232}Th		^{207}Pb/^{206}Pb		^{238}U/^{206}Pb		^{207}Pb/^{206}Pb		common Pb at
age	+/-1 ster	ratio	+/-1 RSE	ratio	+/-1 RSE	ratio	+/-1 RSE	ratio	+/-1 std err	ratio	+/-1 std err	age of zirc
						AN13JP013						
4.3	**0.3**	0.0007	6.3%	0.0004	8.1%	0.1280	14.5%	1341.75	84.83	0.1280	0.0185	0.836
4.3	**0.3**	0.0007	6.1%	0.0004	8.0%	0.1046	17.1%	1373.95	83.76	0.1046	0.0179	0.836
4.4	**0.2**	0.0007	4.4%	0.0003	5.0%	0.0836	11.5%	1395.23	61.93	0.0836	0.0096	0.836
4.5	**0.7**	0.0011	8.5%	0.0014	7.2%	0.3383	18.4%	910.90	77.07	0.3383	0.0623	0.836
4.5	**0.4**	0.0007	7.5%	0.0002	12.3%	0.0538	34.9%	1426.90	107.73	0.0538	0.0188	0.836
4.6	**0.2**	0.0007	4.5%	0.0002	5.7%	0.0546	17.2%	1388.75	63.04	0.0546	0.0094	0.836
4.6	**0.3**	0.0008	6.4%	0.0005	6.8%	0.1500	13.5%	1216.40	77.97	0.1500	0.0203	0.836
4.6	**0.3**	0.0008	6.6%	0.0003	7.8%	0.1134	15.9%	1272.80	84.07	0.1134	0.0181	0.836
4.7	**0.4**	0.0008	7.3%	0.0003	17.4%	0.1107	18.2%	1256.18	91.53	0.1107	0.0202	0.836
4.8	**0.3**	0.0008	5.1%	0.0002	10.4%	0.0656	24.1%	1318.35	67.45	0.0656	0.0158	0.836
4.8	**0.3**	0.0008	6.3%	0.0002	15.8%	0.1241	18.3%	1202.78	75.56	0.1241	0.0227	0.836
5.1	**0.4**	0.0008	6.6%	0.0004	13.1%	0.0724	32.6%	1216.11	80.24	0.0724	0.0236	0.836
5.2	**0.3**	0.0008	5.3%	0.0003	8.0%	0.0614	21.3%	1210.20	63.77	0.0614	0.0131	0.836
5.7	**0.3**	0.0009	5.6%	0.0003	7.3%	0.0587	17.8%	1115.26	62.07	0.0587	0.0105	0.836
7.2	0.5	0.0011	6.2%	0.0003	11.3%	0.0648	29.8%	872.61	53.80	0.0648	0.0193	0.836

^{207} cor ^{206}Pb/^{238}U		^{206}Pb/^{238}U		^{208}Pb/^{232}Th		^{207}Pb/^{206}Pb		^{238}U/^{206}Pb		^{207}Pb/^{206}Pb		common Pb at
age	+/-1 ster	ratio	+/-1 RSE	ratio	+/-1 RSE	ratio	+/-1 RSE	ratio	+/-1 std err	ratio	+/-1 std err	age of zirc
						AN13JP014						
8.2	**0.6**	0.0018	5.7%	0.0015	4.9%	0.2612	9.4%	570.95	32.31	0.2612	0.0246	0.836
8.9	**0.3**	0.0014	3.4%	0.0011	8.4%	0.0817	9.0%	691.49	23.20	0.0817	0.0073	0.836
9.2	**0.2**	0.0015	1.7%	0.0005	3.0%	0.0722	5.8%	679.42	11.45	0.0722	0.0042	0.836
9.3	**0.5**	0.0015	5.0%	0.0005	8.1%	0.0784	13.8%	667.06	33.24	0.0784	0.0108	0.836
9.3	**1.0**	0.0022	6.1%	0.0027	5.7%	0.3121	15.0%	461.32	27.95	0.3121	0.0469	0.837
9.5	**0.2**	0.0016	2.0%	0.0007	3.2%	0.1249	3.8%	613.55	12.07	0.1249	0.0047	0.836
10.6	**0.7**	0.0022	5.6%	0.0013	4.5%	0.2497	9.3%	449.51	25.13	0.2497	0.0231	0.837
15.7	4.9	0.0031	11.1%	0.0053	8.3%	0.2162	84.8%	322.26	35.92	0.2162	0.1833	0.837

Appendix I Zircon U-Pb geochronology

Appendix II $^{40}Ar/^{39}Ar$ thermochronology

Appendix IIA Analytical procedures

For the $^{40}Ar/^{39}Ar$ analyses in groundmass, samples were crushed and sieved to typically a grain size of 200-300 µm (or alternatively 300-500 µm if the rock is relatively unaltered). The groundmass samples were then rinsed with distilled water several times until the water remains clear and these were dried in an oven at ~80 °C for several hours. For the analysis of individual minerals, mineral separation was done by hand-picking, magnetic separation, heavy-liquids or other means, followed by acid treatment. For all samples, a mild leach in an ultrasonic bath with ~5% HNO_3 for 20 minutes was employed, followed by an ultrasonic bath of DI water for 20 minutes. In between the samples were rinsed thoroughly with DI water for three times. Finally, the samples were dried in an oven that is no hotter than 80 °C. Additionally, groundmass samples were treated with an acid leaching procedure designed by Koppers et al. (2000). Samples were irradiated at the OSU Radiation Centre in the TRIGA experimental reactor, typically at 1 MW power for periods appropriate for the age and composition of sample unknowns. The neutron flux was monitored with a variety of standard samples (Mmhb-1 hornblende, FCT-3 biotite, TCR sanidine). There is also a Cd-shielded irradiation location which is designed to block slow (thermal) neutrons in preference to fast neutrons. The Thermo Scientific Model ARGUS VI multi-collector mass spectrometer has five fixed Faraday detectors (including amplifier circuits with 1012 Ohm resistors) and one ion-counting CuBe electron multiplier mounted next to the low mass 36 Faraday detector. The system is equipped with a 25 W Synrad CO_2 laser with industrial scan head for carrying out gas extractions. The ARGUS VI was operated in multi-collector mode to simultaneously collect all masses m/e = 36, 37, 38, 39 and 40 on the 1012 Ohm Faraday collector array. Even though the ARGUS VI has a fixed-position collector array, an electronic steering plate placed before every collector allows for nudging over the beams to fall exactly in the middle of all five collectors. The ARGUS VI is connected to an all-metal extraction system for $^{40}Ar/^{39}Ar$ age determinations. One SAES ST-101 Zr-Al getter (450 °C) and two SAES ST-172 Zr-V-Fe getters (21 °C and 250 °C) are used for cleaning up the reactive gasses. The

design of the CO_2 laser system uses an industrial Synrad XY scan head for steering the laser beam during sample heating. This allowed sample heating by setting up a beam raster pattern while keeping the sample housing stationary. Using this novel technique it is possible to produce a laser beam that can move continuously up and down at speeds up to 300 in/s and that results in an even heating of the entire sample being analyzed, a prerequisite for carrying out first-rate incremental heating experiments. All resulting ages were calculated using the ArArCALC v2.5.2 software package (Koppers, 2002).

Appendix IIB $^{40}Ar/^{39}Ar$ incremental heating results

Incremental Heating		36Ar(a) [fA]	37Ar(ca) [fA]	38Ar(cl) [fA]	39Ar(k) [fA]	40Ar(r) [fA]	Age (Ma)	± 2s	40Ar(r) (%)	39Ar(k) (%)	K/Ca	± 2s
					AN12JP008							
14D17368	1.80%	3.146943	2.1528	0.611061	1.42444	10.0056	22.43	± 13.66	1.06	0.26	0.285	± 0.103
14D17370	2.50%	2.470797	0.9693	0.681722	2.54216	12.6668	15.94	± 6.35	1.71	0.46	1.128	± 0.913
14D17371	3.20%	2.266927	1.9391	1.221828	4.87089	12.1597	8	± 3.09	1.78	0.87	1.08	± 0.438
14D17372	3.90%	2.237613	4.0581	1.685214	7.68842	11.7506	4.9	± 1.92	1.75	1.38	0.815	± 0.164
14D17374	4.60%	1.407801	2.0663	0.961517	7.18896	19.9702	8.9	± 1.43	4.58	1.29	1.496	± 0.574
14D17375	5.30%	1.161243	2.5326	0.774642	8.46211	22.4304	8.5	± 1.06	6.14	1.52	1.437	± 0.405
14D17377	6.00%	1.19654	3.8353	0.782052	11.09267	29.907	8.64	± 0.84	7.8	1.99	1.244	± 0.246
14D17378	**6.70%**	**0.583068**	**2.8081**	**0.25705**	**7.82943**	**23.4798**	**9.61**	**± 0.77**	**11.99**	**1.4**	**1.199**	**± 0.329**
14D17380	**7.30%**	**0.612398**	**3.7552**	**0.398323**	**10.45843**	**31.5615**	**9.67**	**± 0.60**	**14.85**	**1.88**	**1.198**	**± 0.251**
14D17381	**8.30%**	**0.78792**	**6.1242**	**0.600297**	**15.69131**	**47.4589**	**9.69**	**± 0.47**	**16.93**	**2.81**	**1.102**	**± 0.136**
14D17383	**9.30%**	**0.629979**	**7.0063**	**0.449467**	**18.7582**	**57.0119**	**9.74**	**± 0.35**	**23.44**	**3.36**	**1.151**	**± 0.125**
14D17384	**10.50%**	**0.662557**	**10.4301**	**0.534809**	**22.81976**	**70.0416**	**9.84**	**± 0.29**	**26.35**	**4.09**	**0.941**	**± 0.070**
14D17386	**10.50%**	**0.298843**	**6.1344**	**0.170238**	**13.51755**	**40.3027**	**9.55**	**± 0.36**	**31.33**	**2.42**	**0.948**	**± 0.125**
14D17387	**11.50%**	**0.382563**	**11.2142**	**0.318986**	**16.86607**	**49.7262**	**9.45**	**± 0.31**	**30.55**	**3.02**	**0.647**	**± 0.042**
14D17389	**12.70%**	**0.576203**	**38.3005**	**0.695899**	**23.62808**	**71.6023**	**9.71**	**± 0.26**	**29.6**	**4.24**	**0.265**	**± 0.006**
14D17390	**14.00%**	**0.781368**	**107.6759**	**1.700593**	**28.3518**	**86.7222**	**9.8**	**± 0.25**	**27.3**	**5.08**	**0.113**	**± 0.001**
14D17392	**15.50%**	**0.701773**	**173.472**	**2.335402**	**33.12969**	**99.0042**	**9.58**	**± 0.21**	**32.31**	**5.94**	**0.082**	**± 0.001**
14D17393	**17.10%**	**1.280128**	**226.3626**	**3.655485**	**38.86753**	**118.4393**	**9.76**	**± 0.26**	**23.84**	**6.97**	**0.074**	**± 0.001**

AN12JP008 (Cont.)

14D17395	**18.50%**	**1.070818**	**323.9388**	**4.48891**	**40.02256**	**124.2573**	**9.95**	**± 0.22**	**28.19**	**7.18**	**0.053**	**± 0.000**
14D17396	20.00%	1.389531	437.7655	6.474496	46.03894	145.4772	10.12	± 0.23	26.16	8.26	0.045	± 0.000
14D17398	21.50%	1.24116	553.8644	7.847896	51.77955	167.2004	10.35	± 0.19	31.31	9.29	0.04	± 0.000
14D17399	22.70%	0.769388	588.3379	7.624823	52.29427	167.7539	10.28	± 0.15	42.45	9.38	0.038	± 0.000
14D17401	23.80%	0.593541	502.3963	6.671596	47.53866	154.836	10.44	± 0.15	46.88	8.52	0.041	± 0.000
14D17402	24.80%	0.624896	497.2714	6.698532	46.78816	150.4966	10.31	± 0.15	44.9	8.39	0.04	± 0.000

Incremental Heating		36Ar(a) [fA]	37Ar(ca) [fA]	38Ar(cl) [fA]	39Ar(k) [fA]	40Ar(r) [fA]	Age (Ma)	± 2s	40Ar(r) (%)	39Ar(k) (%)	K/Ca	± 2s
					AN12JP012							
14D17254	1.50%	0.414222	3.87147	0.18576	7.53764	40.9813	16.82	± 0.58	25.08	0.88	0.84	± 0.16
14D17256	2.00%	0.426051	4.49285	0.355039	16.40465	110.1595	20.76	± 0.27	46.66	1.92	1.57	± 0.28
14D17257	2.60%	0.455769	7.60493	0.451878	30.67848	178.3398	17.98	± 0.15	56.97	3.58	1.73	± 0.18
14D17258	3.20%	0.373364	9.42608	0.302227	40.1006	188.1536	14.53	± 0.10	63.03	4.68	1.83	± 0.15
14D17260	3.60%	0.300648	9.41314	0.277057	42.71048	180.2152	13.07	± 0.09	66.97	4.99	1.95	± 0.16
14D17261	4.00%	0.3289	11.04116	0.331484	56.95373	248.666	13.52	± 0.07	71.89	6.65	2.22	± 0.15
14D17262	**4.40%**	**0.360078**	**11.85433**	**0.447022**	**69.57082**	**323.3426**	**14.39**	**± 0.06**	**75.23**	**8.13**	**2.52**	**± 0.16**
14D17264	**4.80%**	**0.344432**	**11.99778**	**0.443686**	**86.26857**	**405.1168**	**14.54**	**± 0.05**	**79.91**	**10.08**	**3.09**	**± 0.20**
14D17265	**5.20%**	**0.244816**	**10.35014**	**0.284624**	**84.06944**	**385.5941**	**14.2**	**± 0.05**	**84.19**	**9.82**	**3.49**	**± 0.27**
14D17266	**5.70%**	**0.213462**	**10.16112**	**0.239019**	**89.81792**	**410.6162**	**14.16**	**± 0.04**	**86.67**	**10.49**	**3.8**	**± 0.30**
14D17268	**6.20%**	**0.166966**	**8.10041**	**0.154312**	**71.2798**	**326.6268**	**14.19**	**± 0.05**	**86.86**	**8.33**	**3.78**	**± 0.38**
14D17269	**6.70%**	**0.184947**	**8.13336**	**0.201917**	**57.51631**	**268.1384**	**14.43**	**± 0.06**	**83.05**	**6.72**	**3.04**	**± 0.30**
14D17270	**7.20%**	**0.138596**	**8.32043**	**0.187462**	**42.15867**	**191.4156**	**14.06**	**± 0.08**	**82.36**	**4.92**	**2.18**	**± 0.21**
14D17272	**7.70%**	**0.112331**	**7.40719**	**0.199868**	**26.6134**	**122.404**	**14.24**	**± 0.11**	**78.65**	**3.11**	**1.54**	**± 0.16**
14D17273	8.20%	0.109173	7.38059	0.154873	17.43443	83.8327	14.89	± 0.17	72.2	2.04	1.02	± 0.11
14D17274	8.80%	0.157168	10.16587	0.240541	13.78784	77.0646	17.29	± 0.23	62.39	1.61	0.58	± 0.05
14D17276	9.40%	0.094153	8.51417	0.105191	9.41483	46.6295	15.33	± 0.30	62.62	1.1	0.48	± 0.04
14D17277	10.10%	0.155566	12.77588	0.203977	9.09116	53.6674	18.26	± 0.37	53.86	1.06	0.31	± 0.02
14D17278	10.90%	0.159925	15.55666	0.269145	8.23991	52.9918	19.88	± 0.39	52.86	0.96	0.23	± 0.01
14D17280	11.70%	0.135465	12.00834	0.25	5.7407	44.0933	23.72	± 0.59	52.41	0.67	0.21	± 0.01

AN12JP012 (Cont.)

14D17281	12.50%	0.17857	16.04386	0.329017	5.47795	59.6056	33.51	± 0.71	53.04	0.64	0.15	± 0.01
14D17282	13.50%	0.303348	20.80731	0.533438	6.00625	102.8345	52.46	± 0.90	53.43	0.7	0.12	± 0.01
14D17284	14.50%	0.446443	24.58021	0.906907	6.75676	163.8082	73.84	± 1.02	55.39	0.79	0.12	± 0.00
14D17285	15.50%	0.626458	26.75825	1.176589	7.09245	234.6252	100.02	± 1.26	55.9	0.83	0.11	± 0.00
14D17286	16.50%	0.662021	26.36802	1.269885	5.91239	236.5963	120.31	± 1.75	54.74	0.69	0.1	± 0.00
14D17288	17.50%	0.862202	31.61631	1.654901	6.54	297.7345	136.26	± 1.77	53.89	0.76	0.09	± 0.00
14D17289	19.00%	1.143243	52.08611	2.19395	7.60162	398.1641	155.91	± 1.78	54.1	0.89	0.06	± 0.00
14D17290	20.50%	1.225399	54.82814	2.345531	7.36612	405.9664	163.69	± 1.96	52.85	0.86	0.06	± 0.00
14D17292	22.00%	1.074059	45.86473	2.0161	5.92285	346.5328	173.31	± 2.44	52.19	0.69	0.06	± 0.00
14D17293	23.50%	1.260837	47.53328	2.465801	6.72653	406.0705	178.55	± 2.27	52.15	0.79	0.06	± 0.00
14D17295	24.50%	1.057128	31.63068	1.967023	5.37059	316.5404	174.52	± 2.62	50.33	0.63	0.07	± 0.00

Incremental Heating		36Ar(a) [fA]	37Ar(ca) [fA]	38Ar(cl) [fA]	39Ar(k) [fA]	40Ar(r) [fA]	Age (Ma)	± 2s	40Ar(r) (%)	39Ar(k) (%)	K/Ca	± 2s
					AN12JP024							
14D17211	1.5%	1.118858	7.0126	0.126692	21.5879	116.182	16.58	± 0.88	26	0.92	1.32	± 0.17
14D17213	2.0%	1.715103	17.546	0.097079	65.8778	386.145	18.05	± 0.43	43.24	2.81	1.61	± 0.08
14D17214	2.6%	2.133962	37.6416	0.155339	183.511	1175.484	19.71	± 0.19	65.08	7.83	2.1	± 0.05
14D17215	3.2%	1.499498	40.7205	0.058913	226.5523	1551.39	21.07	± 0.11	77.77	9.66	2.39	± 0.06
14D17217	3.6%	1.254009	44.7691	0.081375	272.3016	1937.067	21.88	± 0.08	83.93	11.61	2.62	± 0.06
14D17218	**4.0%**	**0.711872**	**32.1886**	**0.111984**	**210.9758**	**1521.465**	**22.18**	**± 0.07**	**87.84**	**9**	**2.82**	**± 0.08**
14D17219	**4.4%**	**0.538571**	**29.7578**	**0.019719**	**192.6216**	**1390.594**	**22.2**	**± 0.06**	**89.72**	**8.21**	**2.78**	**± 0.09**
14D17221	**4.8%**	**0.393842**	**24.8826**	**0.058539**	**158.5647**	**1139.279**	**22.1**	**± 0.06**	**90.72**	**6.76**	**2.74**	**± 0.10**
14D17222	5.2%	0.379121	26.3226	0.110926	143.2936	1023.194	21.96	± 0.06	90.12	6.11	2.34	± 0.09
14D17223	5.7%	0.231406	22.4893	0.042341	109.8381	776.354	21.74	± 0.06	91.89	4.68	2.1	± 0.09
14D17225	6.2%	0.285431	30.6807	0.129371	109.2439	765.421	21.55	± 0.06	90.06	4.66	1.53	± 0.04
14D17226	6.7%	0.11495	16.8028	0.121224	59.0538	411.29	21.42	± 0.07	92.36	2.52	1.51	± 0.08
14D17227	7.2%	0.109633	15.8089	0.121388	46.645	322.745	21.29	± 0.08	90.87	1.99	1.27	± 0.08
14D17229	7.7%	0.110587	15.2923	0.15956	38.0947	260.945	21.07	± 0.10	88.86	1.62	1.07	± 0.07
14D17230	8.2%	0.128078	16.8942	0.146518	35.1706	239.201	20.92	± 0.11	86.33	1.5	0.9	± 0.05
14D17231	8.8%	0.179354	23.1809	0.096763	34.8165	232.127	20.51	± 0.13	81.4	1.48	0.65	± 0.03
14D17233	9.4%	0.264502	30.7999	0.204958	34.3685	225.332	20.18	± 0.17	74.24	1.47	0.48	± 0.01
14D17234	10.1%	0.429068	43.7944	0.1602	35.9483	234.019	20.03	± 0.23	64.85	1.53	0.35	± 0.01
14D17235	10.9%	0.686605	62.9358	0.237836	39.2453	249.023	19.53	± 0.31	55.1	1.67	0.27	± 0.00
14D17237	11.7%	1.119726	83.8138	0.213632	46.7474	291.136	19.17	± 0.41	46.8	1.99	0.24	± 0.00
14D17238	12.5%	1.693855	91.4846	0.208971	53.2108	332.891	19.26	± 0.53	39.94	2.27	0.25	± 0.00
14D17239	13.5%	2.390132	99.5679	0.197237	57.5202	350.925	18.78	± 0.69	33.19	2.45	0.25	± 0.00

AN12JP024 (Cont.)

14D17241	14.5%	2.501879	85.1605	0.235949	47.6776	297.472	19.2	± 0.86	28.69	2.03	0.24	± 0.00
14D17242	15.5%	2.642978	75.9299	0.129042	37.2229	221.404	18.31	± 1.17	22.09	1.59	0.21	± 0.00
14D17243	16.5%	2.219677	58.2454	0.062247	24.9296	146.725	18.12	± 1.47	18.28	1.06	0.18	± 0.00
14D17245	17.5%	1.56338	35.7841	0.114951	13.8261	76.689	17.08	± 1.88	14.24	0.59	0.17	± 0.00
14D17246	19.0%	1.624527	41.2855	0.090649	13.1585	75.206	17.6	± 2.05	13.54	0.56	0.14	± 0.00
14D17247	20.5%	1.478795	35.997	0.093433	10.5365	59.016	17.25	± 2.34	11.9	0.45	0.13	± 0.00
14D17249	22.0%	1.290887	31.5036	0.044682	9.146	52.261	17.6	± 2.37	12.05	0.39	0.12	± 0.00
14D17250	23.5%	1.131422	25.7122	0.052105	6.9922	38.195	16.82	± 2.74	10.25	0.3	0.12	± 0.00
14D17252	24.5%	1.071299	24.3442	0.087008	6.1899	33.783	16.81	± 2.94	9.64	0.26	0.11	± 0.00

Appendix II $^{40}Ar/^{39}Ar$ thermochronology

Incremental Heating		36Ar(a) [fA]	37Ar(ca) [fA]	38Ar(cl) [fA]	39Ar(k) [fA]	40Ar(r) [fA]	Age (Ma)	± 2s	40Ar(r) (%)	39Ar(k) (%)	K/Ca	± 2s
					AN13JP007							
14D31208	1.8 %	0.4681778	0.500154	0.1532516	33.9879	109.2454	9.66	± 0.15	44.12	3.11	29.2	± 41.3
14D31210	2.0 %	0.0507290	0.365012	0.0688689	13.9157	57.2196	12.35	± 0.24	79.23	1.27	16.4	± 32.5
14D31211	2.2 %	0.0591953	0.058042	0.0000000	16.4575	69.0487	12.60	± 0.20	79.77	1.51	121.9	± 1485.3
14D31212	**2.4 %**	**0.0464712**	**0.550485**	**0.0450462**	**13.8252**	**58.8775**	**12.79**	**± 0.24**	**81.07**	**1.27**	**10.8**	**± 14.2**
14D31214	**2.7 %**	**0.0537671**	**0.208782**	**0.0629646**	**16.5696**	**71.3523**	**12.93**	**± 0.20**	**81.77**	**1.52**	**34.1**	**± 110.7**
14D31215	**3.0 %**	**0.0953577**	**0.119621**	**0.0000000**	**25.2350**	**109.5050**	**13.03**	**± 0.14**	**79.52**	**2.31**	**90.7**	**± 524.0**
14D31216	**3.3 %**	**0.1127269**	**1.742141**	**0.0467491**	**29.1473**	**127.0606**	**13.09**	**± 0.12**	**79.21**	**2.67**	**7.2**	**± 2.9**
14D31218	**3.6 %**	**0.1005165**	**0.305708**	**0.0150257**	**27.3896**	**119.7876**	**13.13**	**± 0.13**	**80.12**	**2.51**	**38.5**	**± 95.3**
14D31219	**3.7 %**	**0.1021596**	**0.145697**	**0.0365872**	**27.1433**	**119.0035**	**13.16**	**± 0.13**	**79.75**	**2.48**	**80.1**	**± 385.1**
14D31220	**3.9 %**	**0.1141456**	**0.050584**	**0.0000000**	**28.3990**	**124.1882**	**13.13**	**± 0.13**	**78.63**	**2.60**	**241.4**	**± 3520.9**
14D31222	**4.2 %**	**0.1156856**	**0.644242**	**0.0593108**	**28.4392**	**124.7489**	**13.17**	**± 0.13**	**78.48**	**2.60**	**19.0**	**± 20.6**
14D31223	**4.5 %**	**0.0936723**	**0.240347**	**0.0650891**	**24.0452**	**105.3365**	**13.15**	**± 0.14**	**79.18**	**2.20**	**43.0**	**± 126.1**
14D31224	**4.7 %**	**0.1210909**	**0.129581**	**0.0216836**	**27.2608**	**119.6882**	**13.18**	**± 0.13**	**76.97**	**2.49**	**90.5**	**± 501.7**
14D31226	**4.8 %**	**0.0996915**	**0.417149**	**0.0768068**	**23.5838**	**102.9148**	**13.10**	**± 0.14**	**77.73**	**2.16**	**24.3**	**± 42.8**
14D31227	**5.1 %**	**0.1190516**	**0.398021**	**0.0158756**	**25.8069**	**112.8820**	**13.13**	**± 0.14**	**76.23**	**2.36**	**27.9**	**± 49.4**
14D31228	**5.4 %**	**0.1696927**	**0.107834**	**0.0143643**	**31.5510**	**138.1068**	**13.14**	**± 0.12**	**73.35**	**2.89**	**125.8**	**± 829.2**
14D31230	**5.7 %**	**0.1491396**	**0.317872**	**0.0302244**	**28.1552**	**123.6884**	**13.19**	**± 0.13**	**73.72**	**2.58**	**38.1**	**± 85.9**
14D31231	**5.9 %**	**0.1634249**	**0.063644**	**0.0000000**	**29.7978**	**130.5852**	**13.16**	**± 0.13**	**72.99**	**2.73**	**201.3**	**± 2265.9**
14D31232	**6.1 %**	**0.1776557**	**0.260691**	**0.0168239**	**30.0363**	**130.0207**	**13.00**	**± 0.13**	**71.23**	**2.75**	**49.5**	**± 134.2**
14D31234	**6.5 %**	**0.2568364**	**0.403604**	**0.0616926**	**35.3416**	**154.2509**	**13.10**	**± 0.11**	**67.01**	**3.23**	**37.7**	**± 65.1**
14D31235	**6.9 %**	**0.2933748**	**0.326293**	**0.0356938**	**37.6959**	**163.9868**	**13.06**	**± 0.12**	**65.41**	**3.45**	**49.7**	**± 109.5**
14D31236	**7.1 %**	**0.2674692**	**0.642323**	**0.0125776**	**34.2161**	**147.5890**	**12.95**	**± 0.12**	**65.11**	**3.13**	**22.9**	**± 25.0**
14D31238	**7.3 %**	**0.1931348**	**0.203613**	**0.0075310**	**25.4292**	**110.5419**	**13.05**	**± 0.15**	**65.94**	**2.33**	**53.7**	**± 185.7**
14D31239	**7.8 %**	**0.3023447**	**0.260632**	**0.0218863**	**32.2138**	**138.1871**	**12.88**	**± 0.13**	**60.72**	**2.95**	**53.1**	**± 148.5**

AN13JP007 (Cont.)

14D31240	8.1 %	0.3094093	0.383056	0.0247206	31.4633	134.6845	12.85	± 0.14	59.56	2.88	35.3	± 69.2
14D31242	8.3 %	0.2597242	0.409283	0.0478755	27.0179	116.1107	12.90	± 0.15	60.20	2.47	28.4	± 51.2
14D31243	8.8 %	0.3388198	0.033437	0.0551063	33.0951	141.7226	12.86	± 0.13	58.59	3.03	425.6	± 9381.3
14D31244	9.3 %	0.4506447	0.176627	0.0000000	41.6771	178.6142	12.87	± 0.12	57.28	3.81	101.5	± 412.4
14D31246	9.9 %	0.4983406	0.274369	0.0343587	46.0093	199.8413	13.04	± 0.15	57.57	4.21	72.1	± 236.8
14D31248	10.5 %	0.6366138	0.014438	0.0420099	59.2291	253.9257	12.87	± 0.10	57.44	5.42	1763.9	± 87424.3
14D31249	11.2 %	0.4274792	0.080081	0.0670351	41.2251	178.8559	13.03	± 0.11	58.60	3.77	221.4	± 1995.4
14D31251	11.9 %	0.2199923	0.490770	0.0388804	22.6364	98.4030	13.05	± 0.17	60.21	2.07	19.8	± 29.2
14D31252	12.8 %	0.1960048	0.365001	0.0000000	23.3209	100.8002	12.98	± 0.17	63.50	2.13	27.5	± 53.7
14D31253	13.9 %	0.1762210	0.282026	0.0878187	20.4766	88.9951	13.05	± 0.18	63.08	1.87	31.2	± 78.7
14D31255	15.2 %	0.2048463	0.409586	0.0114410	21.6112	93.6936	13.02	± 0.18	60.74	1.98	22.7	± 40.8
14D31256	16.7 %	0.1826054	0.408610	0.0353713	19.6950	85.7563	13.07	± 0.19	61.37	1.80	20.7	± 37.0
14D31257	18.2 %	0.1506168	0.289271	0.0022895	18.1223	78.9679	13.08	± 0.20	63.94	1.66	26.9	± 64.9
14D31259	19.7 %	0.1413369	0.208203	0.0000000	18.8239	82.2972	13.13	± 0.20	66.33	1.72	38.9	± 133.4
14D31260	21.2 %	0.0860947	0.186859	0.0000000	9.9640	43.6380	13.15	± 0.34	63.16	0.91	22.9	± 88.0
14D31262	22.7 %	0.0544942	0.462435	0.0000000	6.5227	28.9738	13.34	± 0.51	64.27	0.60	6.1	± 9.6
14D31263	24.5 %	0.0513024	0.505835	0.0000000	6.1057	26.9898	13.27	± 0.54	64.02	0.56	5.2	± 7.4

Incremental Heating		36Ar(a) [fA]	37Ar(ca) [fA]	38Ar(cl) [fA]	39Ar(k) [fA]	40Ar(r) [fA]	Age (Ma)	± 2s	40Ar(r) (%)	39Ar(k) (%)	K/Ca	± 2s
					AN13JP012							
14D31141	1.8 %	2.866972	7.4053	0.319056	2.06085	14.0759	20.42	± 9.95	1.63	0.60	0.120	± 0.011
14D31143	2.5 %	2.973919	17.2014	0.414771	2.96419	15.1746	15.33	± 7.10	1.70	0.86	0.074	± 0.003
14D31144	3.2 %	3.403149	27.0467	0.501900	3.63401	19.7062	16.23	± 6.28	1.92	1.06	0.058	± 0.002
14D31145	3.9 %	4.236771	48.9939	0.550365	4.49476	19.3229	12.88	± 5.97	1.52	1.31	0.039	± 0.001
14D31147	4.6 %	3.488361	70.8933	0.578910	4.77075	23.6502	14.84	± 4.91	2.24	1.39	0.029	± 0.001
14D31148	5.3 %	3.995628	94.0115	0.702628	5.74178	22.6311	11.81	± 4.43	1.88	1.67	0.026	± 0.000
14D31150	6.0 %	3.909438	129.7149	0.743201	6.51622	32.9635	15.15	± 3.87	2.77	1.90	0.022	± 0.000
14D31151	6.7 %	3.656073	158.7551	0.658481	7.00946	33.4513	14.29	± 3.43	3.00	2.04	0.019	± 0.000
14D31153	7.3 %	3.107983	182.3198	0.549717	7.21003	32.3700	13.45	± 3.01	3.40	2.10	0.017	± 0.000
14D31154	**8.3 %**	**3.448339**	**198.3699**	**0.534556**	**8.47720**	**29.7387**	**10.52**	**± 2.77**	**2.84**	**2.47**	**0.018**	**± 0.000**
14D31156	**9.3 %**	**3.565497**	**147.7038**	**0.626824**	**9.56506**	**35.6471**	**11.17**	**± 2.52**	**3.27**	**2.79**	**0.028**	**± 0.000**
14D31157	**10.5 %**	**3.106883**	**104.1156**	**0.684029**	**11.47973**	**36.4112**	**9.51**	**± 1.88**	**3.81**	**3.35**	**0.047**	**± 0.001**
14D31158	**11.5 %**	**2.791650**	**75.4280**	**0.872213**	**13.86569**	**50.2978**	**10.87**	**± 1.47**	**5.75**	**4.04**	**0.079**	**± 0.001**
14D31160	**12.7 %**	**2.697803**	**76.9022**	**0.885865**	**19.29421**	**64.8613**	**10.08**	**± 1.03**	**7.52**	**5.62**	**0.108**	**± 0.001**
14D31161	**14.0 %**	**1.873071**	**83.2619**	**0.882245**	**21.10186**	**63.6880**	**9.05**	**± 0.80**	**10.32**	**6.15**	**0.109**	**± 0.001**
14D31162	**15.5 %**	**1.497826**	**110.2075**	**1.627994**	**21.31380**	**67.2365**	**9.46**	**± 0.74**	**13.19**	**6.21**	**0.083**	**± 0.001**
14D31164	**17.1 %**	**1.320951**	**104.8440**	**1.877674**	**23.90290**	**73.5801**	**9.23**	**± 0.64**	**15.86**	**6.97**	**0.098**	**± 0.001**
14D31165	**18.5 %**	**1.210240**	**104.1321**	**2.204096**	**27.87996**	**86.3878**	**9.29**	**± 0.52**	**19.45**	**8.12**	**0.115**	**± 0.001**
14D31166	**20.0 %**	**1.151847**	**89.4449**	**2.098326**	**29.17327**	**94.7853**	**9.74**	**± 0.50**	**21.78**	**8.50**	**0.140**	**± 0.001**
14D31168	**21.5 %**	**1.165955**	**80.0196**	**2.205225**	**30.09238**	**99.1259**	**9.88**	**± 0.48**	**22.34**	**8.77**	**0.162**	**± 0.002**
14D31169	**22.7 %**	**0.944152**	**63.8536**	**1.969583**	**29.47636**	**98.5710**	**10.03**	**± 0.47**	**26.10**	**8.59**	**0.198**	**± 0.003**
14D31170	23.8 %	0.879204	57.5342	1.923050	28.48051	100.4161	10.57	± 0.48	27.87	8.30	0.213	± 0.003
14D31172	24.8 %	0.731778	51.0652	1.722607	24.65186	90.6911	11.03	± 0.55	29.55	7.18	0.208	± 0.003

Appendix III (U-Th)/He zircon and apatite thermochronology

Appendix IIIA Analytical procedures

Selection of grains from mineral separates was undertaken with one Leica MZ16 stereozoom microscopes. Samples were examined, picked, and checked for inclusions under either cross-polarization with a rotating stage at 160x, or in plane-polarized darkfield illumination at 240x. Darkfield illumination at high power provides a much more robust screening for inclusions in apatite grains. Precise grain dimension measurements were made primarily in order to make precise alpha-ejection corrections. However, a second reason is that dimensions can be translated to grain volume and mass, permitting estimates of parent and daughter nuclide concentrations in the dated aliquot. Concentrations are not necessary for age determinations, as these are made by molar parent-daughter ratios. But concentrations can be useful for contextural and quality-control reasons (e.g., radiation damage, anomalous results, etc.). Grain dimensions were measured from digital photomicrographs taken in at least two different orientations, usually perpendicular to the c-axis. Imaging software that is manually calibrated and recorded using a stage micrometer at each operator sitting was used to measure several features of the grain. For zircon the approach outlined in Hourigan et al. (2005) was used, including the bipyramidal tip heights and two different c-axis parallel widths; for apatite a similar approach was used but assuming pinacoidal terminations (Farley et al., 1996; Farley, 2002). In both cases, fractures and other features are noted and, if appropriate, accounted for by decreasing the surface-area-to-volume ratio of the grain by a geometric factor. Alpha-ejection correction factors were calculated using surface-area-to-volume ratios and the approach of Farley (2002) for apatite and Hourigan et al. (2005) for zircon. Because direct lasing of minerals volatilizes parent nuclides, grains are wrapped in metallic foil microfurnaces for laser heating (House et al., 2000). Apatite was placed in 1-mm Pt tubing and the ends were pinched closed; zircon and other minerals requiring HF-HNO_3 -HCl dissolution were placed in 1-mm Nb foil envelopes. Approximately 30 crystal-bearing foil packets are placed in a Cu or SS planchet, under a KBr coverslip,

inside a ~7-cm laser cell pumped to <10 -9 torr. For Nd:YAG laser degassing a sapphire window is used; for CO_2 laser degassing a Cleartran ® (ZnS) window (and no coverslip) is used. Samples are heated for 3-15 minutes by a focused beam of a 1-2 W (Nd:YAG) or 5-15 W (CO_2) laser. Neither temperature nor wavelength of radiation emitted from the foils are quantified. However experiments with materials of known melting temperatures in Pt foils, with both qualitative visual correlation of these conditions with CRT images of incandescent foils and quantitative pyrometric measurements (albeit with a poorly constrained Pt emissivity parameter) constrain routine laser heating to temperatures of ~900-1000 °C for apatite and ~1000-1250 °C for zircon. Most importantly, routine reheating and analyses (re-extracts) were performed on most apatites and all zircons (sometimes multiple times), to confirm that ^{4}He has been quantitatively extracted (at least to below blank level) in apatite, and zircons yield less than 1-2% in subsequent re-extracts. Gas released from heated samples was then spiked with 0.1-0.2 pmol ^{3}He, and condensed onto activated charcoal the cold head of a cryogenic trap at 16 K. Helium was then released from the cold head at 37 K into a small volume (~50 cc) with an activated Zr-Ti alloy getter and the source of a Balzers quadrupole mass spectrometer (QMS) with a Channeltron electron multiplier. Peak-centered masses at approximately m/z of 1, 3, 4, and 5.2 are measured. Mass 5.2 establishes background, and mass 1 was used to correct mass 3 for HD and H_3+. Experiments relating masses 1, 2, and 3 with no He in the system generally showed better correlations between masses 1 and 3 (non-^{3}He-mass 3 = 0.005 ± 0.002 times mass 1, though this breaks down at higher gas pressures) than between masses 2 and 3, possibly because of other, multiply charged, species at mass 2. Corrected ratios of masses 4 to 3 were regressed through ten measurement cycles over ~15 s to derive an intercept value, which has an uncertainty of 0.05-0.5% over a 4/3 range of ~10^3 (approximately 10x the ratio of blank to typical Durango apatite standard ratios), and compared with the mean corrected ratio to check for significant anomalous changes in the ratio during analysis. Helium contents of unknown samples were calculated by first subtracting the average mass-1-corrected 4/3 measured on multiple procedural blanks analyzed by the same method, from the mass-1-corrected 4/3 measured on the unknown. This was then ratioed to the mass-1-corrected 4/3 measured on a shot of an online reference ^{4}He standard analyzed with the same procedure (minus the mass-1-corrected 4/3 measured on a ^{3}He-only spike shot analyzed using the same procedure as the

reference ^{4}He standard). The resulting ratio of measured 4/3's was then multiplied by the moles of ^{4}He delivered in the reference shot. This procedure assumes linearity between measured 4/3 and ^{4}He pressure, which has been confirmed over the vast majority of the range of ^{4}He contents by performing multiple replicate analyses of known-age standards with masses and therefore ^{4}He yields ranging over three orders of magnitude. This procedure also relies on the accuracy of the ^{4}He delivery from the reference standard and the precision of its measurement with the ^{3}He spiking procedure. The delivery and its depletion with time were calibrated by multiple capacitance manometry measurements of the volumes of the reference tank and pipette, and the final filling pressure of the tank. One of two He lines has a ^{4}He tank and pipette with volumes of 15920 ± 7.8 cc (0.05%, 1s) and 0.9439 ± 0.0016 cc (0.16%, 1s), respectively; uncertainties reported as standard errors on multiple (n=6) manometric volume determinations. The other He line has tank and pipette volumes of 3655 ± 8.2 cc (0.2%, 1s) and 0.09675 ± 0.0021 cc (2%, 1s). A similarly calibrated detachable portable tank can be moved between lines for cross-calibration. Between ~2-6 (depending on the number of unknowns) 4/3 measurements of spiked ^{4}He reference standards were made each measurement day. Although the long-term, day-to-day change in these measurements can be large due to drift of the QMS, in a single measurement day the corrected 4/3 measurements on reference standards vary by less than 0.5% (1s). This uncertainty can be reduced for reducing unknown data by monitoring intraday secular trends. Average measured 4/3 of lineblanks (^{3}He spike only) are nearly indistinguishable from that predicted by the purity of the ^{3}He spike (99.75% 3 He). Hotblanks, or procedural blanks measured by lasing/heating empty Pt or Nb foil packets are typically 0.05-0.1 fmol ^{4}He. Several routine standards for checking analytical procedures and calibrations were used. These include apatite from the Coast Mountains of British Columbia (House et al., 2000), one apatite sample from the Sierra Nevada, zircon from the Peach Springs Tuff, and gem-quality detrital samples from Sri Lanka (Nasdala et al., 2004). Two other commonly used standards are those of small (~20-200 um) fragments of much larger (~2-3 cm) gem-quality crystals of Durango apatite, and whole single crystals of Fish Canyon Tuff (FCT) zircon.

Appendix IIIB (U-Th)/He zircon and apatite results

Material	ppm eU (morph)	ppm U (morph)	d ppm U (morph)	ppm Th (morph)	d ppm Th (morph)	nmol 4He/g (morph)	d nmol 4He/g (morph)	**corr date (Ma)**	**1s ± date (Ma)**	1s ± date %	comment
						AN12JP001					
Apatite	21.25	13.73	0.20	31.98	0.46	0.21	0.01	**2.72**	**0.13**	4.80	
Apatite	40.38	30.73	0.45	41.09	0.61	0.23	0.02	**1.54**	**0.16**	10.12	high error; caution (v. low He)
Apatite	24.72	15.34	0.23	39.91	0.60	0.15	0.02	**1.73**	**0.29**	16.85	high error; caution (v. low He)
						AN12JP003					
Apatite	3.94	2.67	0.04	5.40	0.08	0.05	0.00	**3.23**	**0.17**	5.16	
Apatite	6.00	3.78	0.06	9.45	0.15	0.10	0.02	**4.78**	**0.80**	16.70	high error; caution (v. low He, low U)
Apatite	4.14	2.70	0.04	6.12	0.11	0.06	0.01	**3.33**	**0.32**	9.51	high error; caution (v. low He, low U)
						AN12JP005					
Apatite	7.24	3.94	0.06	14.05	0.20	0.07	0.00	**2.13**	**0.10**	4.72	
Apatite	6.71	3.75	0.06	12.62	0.19	0.04	0.00	**1.53**	**0.15**	9.93	high error; caution (v. low He, low U)
Apatite	6.84	3.89	0.06	12.54	0.18	0.06	0.01	**2.06**	**0.20**	9.53	high error; caution (v. low He, low U)

Material	ppm eU (morph)	ppm U (morph)	d ppm U (morph)	ppm Th (morph)	d ppm Th (morph)	nmol 4He/g (morph)	d nmol 4He/g (morph)	**corr date (Ma)**	**1s ± date (Ma)**	1s ± date %	comment
						AN12JP008					
Apatite	19.66	13.42	0.22	26.55	0.38	0.17	0.01	**2.76**	**0.23**	8.43	high error; caution (v. low He)
Apatite	18.05	11.52	0.18	27.76	0.41	0.06	0.02	**0.97**	**0.35**	36.48	very high error (very low He)
						AN12JP011					
Zircon	182.73	164.33	2.35	78.30	1.12	6.63	0.13	**9.71**	**0.23**	2.37	
Zircon	780.28	696.18	9.89	357.86	5.11	144.22	0.58	**47.84**	**0.62**	1.31	Unrealistic age, much older than U-Pb crystallization age
						AN12JP013					
Zircon	135.20	119.32	1.72	67.58	0.97	3.00	0.04	**5.17**	**0.09**	1.78	
Zircon	333.48	294.36	4.21	166.45	2.38	8.84	0.07	**6.01**	**0.09**	1.44	
Zircon	143.95	127.36	1.82	70.60	1.00	2.72	0.04	**4.44**	**0.08**	1.82	
Apatite	13.12	8.86	0.13	18.11	0.26	0.10	0.01	**2.11**	**0.20**	9.69	high error; caution (v. low He)
Apatite	24.48	16.31	0.24	34.73	0.50	0.07	0.01	**0.79**	**0.12**	14.66	high error; caution (v. low He)
Apatite	25.76	16.42	0.24	39.74	0.57	0.09	0.01	**1.00**	**0.15**	15.23	high error; caution (v. low He)

Material	ppm eU (morph)	ppm U (morph)	d ppm U (morph)	ppm Th (morph)	d ppm Th (morph)	nmol 4He/g (morph)	d nmol 4He/g (morph)	**corr date (Ma)**	**1s ± date (Ma)**	1s ± date %	comment
						AN12JP014					
Apatite	8.38	4.64	0.07	15.92	0.23	0.14	0.01	**4.04**	**0.27**	6.70	
Apatite	6.96	3.87	0.06	13.16	0.19	0.05	0.00	**1.68**	**0.18**	10.84	high error; caution (v. low He, low U)
						AN12JP018					
Apatite	13.77	7.33	0.11	27.41	0.85	0.23	0.01	**5.01**	**0.32**	6.41	
Apatite	14.25	8.71	0.14	23.58	0.34	0.16	0.02	**3.25**	**0.41**	12.47	high error; caution (v. low He)
Apatite	8.62	4.30	0.09	18.39	0.28	0.07	0.01	**2.44**	**0.48**	19.48	high error; caution (v. low He, low U)

Appendix IV Thin sections descriptions

AN12JP001 Pyroxene dacitic porphyry

Texture: porphyritic, microcrystalline groundmass

Phenocrysts (15%): plagioclase (10%, 1-2mm, subhedral, strongly replaced by sericite), pyroxene (3%, 0.5-1.5mm, subhedral, strongly replaced by clays, sericite and chlorite), biotite (2%, completely replaced by muscovite)

Groundmass (85%): quartz (50%, 0.05mm, anhedral), pyroxene (20%, 0.05-0.1mm, subhedral), sericite (10%, 0.05mm, probably after plagioclase), opaques (magnetite, 5%)

AN12JP002 Porphyritic andesite

Texture: porphyritic, microcrystalline groundmass

Phenocrysts (35%): plagioclase (35%, 1-5mm, sub to euhedral, partly replaced by sericite)

Groundmass (55%): plagioclase (40%, 0.1-0.4mm, no preferred orientation), opaques, fine-grained volcanic glass

Lithics (10%): porphyritic andesites

Celadonite in vesicles

AN12JP003 Lithic-rich welded ignimbrite

Texture: pyroclastic, subangular, low sphericity, moderately sorted, clast-supported.

Clasts (50%): porphiritic andesitic lava (25%, 1-6mm), flattened pumice recrystallised to fine-grained quartz (15%, 1-5mm), fragments of plagioclase crystals (10%, 0.5-2mm)

Matrix (50%): fine-grained ash (40%), plagioclase crystal fragments (5%, 0.05mm), glass shards (5%, 0.1mm)

Celadonite replacing matrix and lithic fragments

AN12JP004 Andesitic porphyry

Texture: porphyritic, trachytic microphaneritic groundmass

Phenocrysts (15%): plagioclase (13%, 1-2.5mm, sub to euhedral, partly replaced by muscovite), hornblende (2%, 0.2-1mm, subhedral, strongly replaced by biotite)

Groundmass (85%): plagioclase (70%, 0.15-0.2mm, sub to ehuedral, strong preferred orientation), pyroxene (5%, 0.1mm, subhedral), opaques (magnetite, 10%)

Chlorite and minor sericite in groundmass

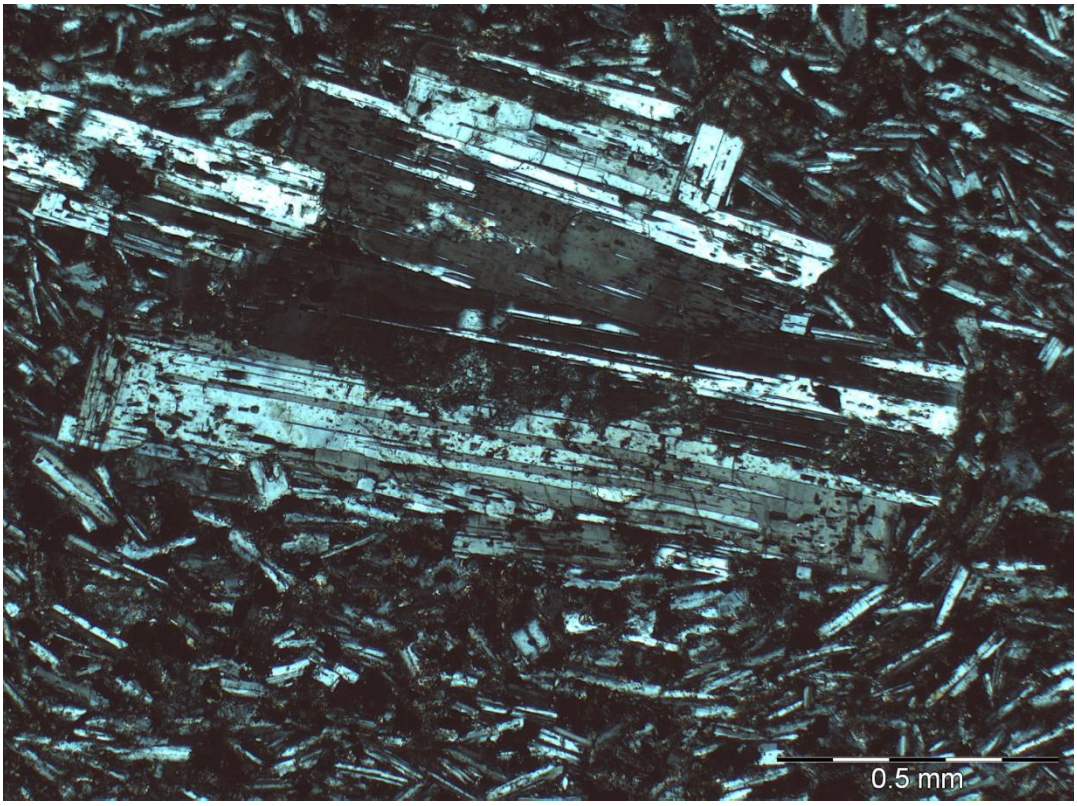

Figure IV.1. Sample AN12JP004, crossed polarisers. Plagioclase phenocryst in a groundmass composed of fine-grained plagioclase crystals oriented in the flow direction.

AN12JP005 Crystal- and lithic-rich welded ignimbrite

Texture: pyroclastic, subrounded, low sphericity, moderately sorted, matrix-supported.

Clasts (40%): fragments of plagioclase crystals (20%, 0.5-2mm, mostly fresh), porphiritic andesitic lava (15%, 1-12mm), flattened pumice partly recrystallised to fine-grained quartz (5%, 1-7mm)

Matrix (60%): fine-grained ash (40%), glass shards (15%, 0.1-0.2mm, partly devitrified), plagioclase crystal fragments (5%, 0.1-0.2mm)

AN12JP006 Crystal-rich welded ignimbrite

Texture: pyroclastic, subangular, low sphericity, moderately sorted, matrix-supported.

Clasts (30%): fragments of plagioclase crystals (15%, 0.5-1.5mm, mostly fresh), flattened pumice partly recrystallised to fine-grained quartz (10%, 2-5mm), porphiritic andesitic lava (5%, 1-2mm)

Matrix (70%): fine-grained ash (55%), plagioclase crystal fragments (13%, 0.1-0.2mm), glass shards (2%, 0.1mm, partly devitrified)

AN12JP007 Banded porphyritic rhyolite

Texture: banded, intercalations of bands of porphyritic rock with glassy groundmass and bands of fine-grained quartz.

Phenocrysts (2%): plagioclase (2%, 1mm, subhedral)

Groundmass (98%): fine-grained volcanic glass (65%), fine-grained quartz (20%, variable sizes, generally 0.05-0.1mm, anhedral), plagioclase (13%, 0.05-0.1mm, subhedral)

AN12JP008 Hornblende granodiorite

Texture: equigranular, phaneritic, medium grained.

Plagioclase (50%, 2-4mm, sub to euhedral, incipient sericitic alteration), quartz (25%, 0.4-1.5mm, anhedral), hornblende (13%, 1-2mm, subhedral), orthoclase (8%, 0.5-1.5 mm, anhedral), biotite (2%, 1mm, subhedral), opaques (magnetite, 2%)

AN12JP009 Porphyritic andesite

Texture: porphyritic, microcrystalline groundmass

Phenocrysts (20%): plagioclase (20%, 1-6mm, sub to euhedral, partly replaced by fine-grained biotite)

Groundmass (80%): plagioclase (55%, 0.05-0.15mm, no preferred orientation), fine-grained secondary biotite (15%, 0.02-0.03mm), opaques (10%, magnetite)

Minor chlorite after biotite

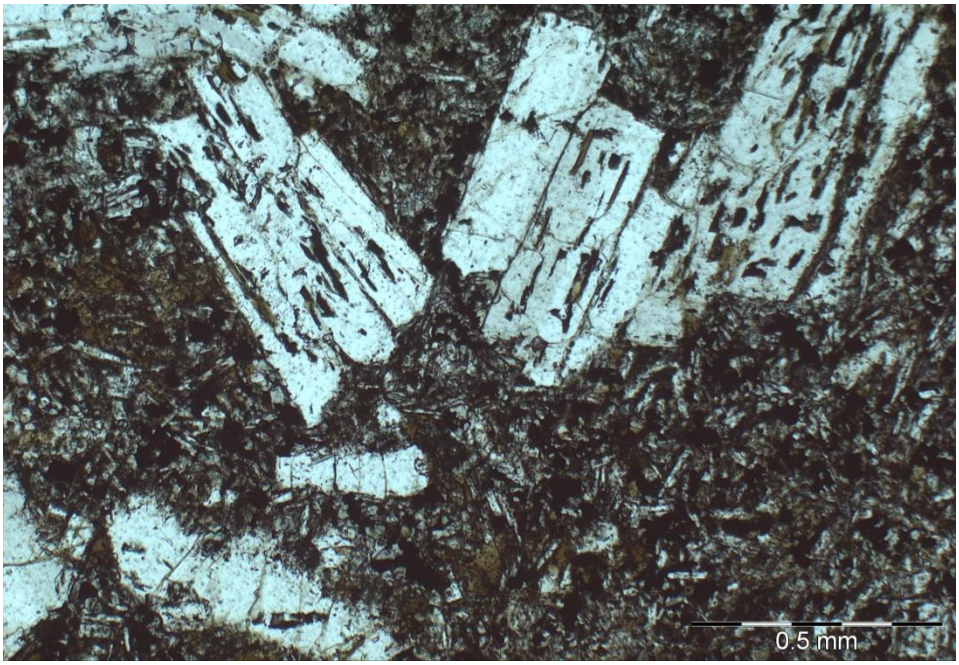

Figure IV.2. Sample AN12JP009, plane-polarized light. Plagioclase phenocrysts in a groundmass of fine-grained plagioclase, opaque minerals and secondary biotite (brown).

AN12JP010 Crystal-rich lapilli tuff

Texture: pyroclastic, subangular, low sphericity, poorly sorted, matrix-supported.

Clasts (40%): plagioclase crystals (70%, turbid, 1-3mm), andesitic lava (15%, 0.5-2mm), hornblende crystals (10%, 0.2-0.6mm, strongly altered to chlorite), diorite (5%, 1-20mm, irregular shape, possibly a spatter)

Matrix: fine-grained ash

AN12JP011 Hornblende monzogranite

Texture: equigranular, phaneritic, medium grained.

Plagioclase (35%, 1-4mm, sub to euhedral, incipient clay alteration), quartz (25%, 0.5-1.5mm, anhedral), orthoclase (20%, 0.5-1.5 mm, sub to anhedral, strong clay alteration, occasional perthitic texture), hornblende (10%, 0.5-1.5mm, subhedral, partly replaced by

chlorite), biotite (7%, 0.5-1mm, subhedral, partly replaced by chlorite), opaques (magnetite, 3%)

AN12JP012 Porphyritic andesite

Texture: porphyritic, microcrystalline groundmass

Phenocrysts (20%): plagioclase (20%, 0.5-2mm, sub to euhedral)

Groundmass (80%): plagioclase (70%, 0.1-0.2mm), opaques (magnetite, 10%)

Figure IV.3. Sample AN12JP012, crossed polarisers. Plagioclase phenocrysts in a groundmass composed of fine-grained plagioclase and opaque minerals (magnetite).

AN12JP013 Hornblende monzogranitic porphyry

Texture: porphyritic, microphaneritic groundmass

Phenocrysts (40%): plagioclase (30%, 0.5-2mm, subhedral, strongly replaced by sericite), hornblende (8%, 0.5-2mm, subhedral, strongly replaced by chlorite), biotite (2%, 0.5-1mm, subhedral, strongly replaced by chlorite)

Groundmass (60%): quartz (35%, 0.05-0.1mm, anhedral), orthoclase (25%, 0.05-0.2mm, anhedral, strong clay alteration), titanate (accessory), zircon (accessory)

AN12JP014 Sericite-altered crystal-rich ash tuff

Texture: pyroclastic, angular, matrix-supported.

Clasts (15%): plagioclase crystals (10%, 0.5-1mm, partly replaced by sericite), andesitic lava (5%, 0.5-1.5mm)

Matrix: completely replaced by sericite

AN12JP015 Pyroxene porphyritic andesite

Texture: porphyritic, microcrystalline groundmass

Phenocrysts (25%): plagioclase (22%, 0.5-5mm, sub to euhedral, weak preferred orientation), pyroxene (3%, 1-1.5mm, subhedral)

Groundmass (75%): plagioclase (60%, 0.1mm, weak preferred orientation), opaques (10%, magnetite), volcanic glass (5%)

Minor calcite and quartz in vesicles

AN12JP016 Hornblende andesitic porphyry

Texture: porphyritic, microphaneritic groundmass

Phenocrysts (10%): plagioclase (7%, 1-5mm, subhedral), hornblende (3%, 1-4mm, subhedral)

Groundmass (90%): plagioclase (75%, 0.05-0.5mm, subhedral), hornblende (5%, 0.05-0.2mm, subhedral), opaques (10%, magnetite)

AN12JP017 Quartz-sericite altered aphanitic lava

Texture: banded, aphanitic, strongly obliterated by sericite-clay alteration

Sericite and clays (40%), fine-grained quartz (40%), opaques (20%). Abundant goethite. One single 0.5mm plagioclase crystal, strongly replaced by sericite and quartz.

AN12JP018 Crystal-rich lapilli tuff

Texture: pyroclastic, angular, matrix-supported.

Clasts (30%): plagioclase crystals (25%, 0.2-5mm), pyroxene crystals (5%, 0.1-1mm)

Matrix: plagioclase crystal fragments and fine-grained ash

AN12JP019 Porphyritic hornblende andesite

Texture: porphyritic, microcrystalline groundmass

Phenocrysts (25%): plagioclase (23%, 1-5mm, sub to euhedral, incipient sericitic alteration), hornblende (2%, 1-2mm, subhedral)

Groundmass (75%): plagioclase (70%, 0.1-0.2mm), opaques (magnetite, 5%)

Vesicles filled with quartz (mostly on the rims), calcite, chlorite and celadonite

AN12JP020 Porphyritic pyroxene andesite

Texture: porphyritic, microcrystalline groundmass

Phenocrysts (20%): plagioclase (20%, 1.5-3mm, sub to euhedral)

Groundmass (80%): plagioclase (50%, 0.1-0.4mm), pyroxene (20%, 0.1-0.6mm), opaques (magnetite, 10%)

Vesicles filled with chlorite and calcite

AN12JP021 Andesitic porphyry

Texture: porphyritic, microphaneritic groundmass

Phenocrysts (5%): plagioclase (5%, 1.5-2mm, subhedral, partly replaced by sericite)

Groundmass (95%): plagioclase (70%, 0.4-0.8mm, sub to euhedral), opaques (25%, magnetite, goethite and possibly pyrite)

AN12JP022 Quartz-sericite altered, lithic-rich lapilli tuff

Texture: pyroclastic, clast-supported, strongly obliterated by quartz-sericitic alteration

Clasts (70%): andesitic lava flows and minor pyroclstic deposits (60%, 2-8mm, some with truncated quartz veins and strong quartz-sericitic alteration), pumice (10%, 10mm, completely replaced by sericite)

Matrix (30%): fine-grained ash, almost completely recrystallised to quartz and sericite

Leached veins, probably originally pyrite veins, with 0.4-0.6mm sericitic haloes

AN12JP023 Porhyritic andesite

Texture: porphyritic, microcrystalline groundmass

Phenocrysts (10%): plagioclase (10%, 1-2mm, sub to euhedral, partly replaced by sericite)

Groundmass (90%): plagioclase (80%, 0.05-0.4mm, partly replaced by sericite), opaques (10%, goethite, minor magnetite)

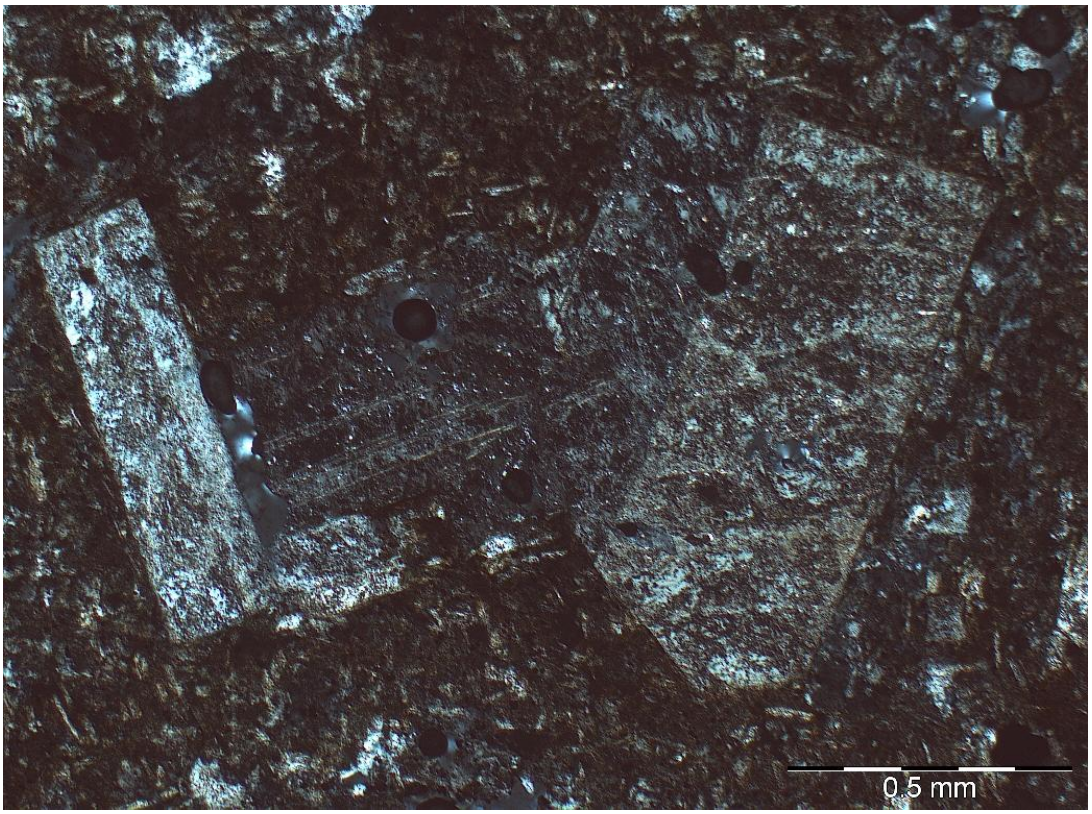

Figure IV.4. Sample AN12JP023, crossed polarisers. Plagioclase phenocrysts in a groundmass composed of fine-grained plagioclase and partially-oxidized magnetite.

AN12JP024 Porphyritic andesite

Texture: porphyritic, microcrystalline groundmass

Phenocrysts (10%): plagioclase (10%, 0.5-1mm, sub to euhedral, partly replaced by sericite)

Groundmass (90%): plagioclase (70%, 0.1-0.2mm), volcanic glass (10%), opaques (magnetite, 10%)

AN13JP001 Hornblende-pyroxene porphyritic andesite

Texture: porphyritic, microcrystalline groundmass

Phenocrysts (40%): plagioclase (30%, 0.5-1.5mm, sub to euhedral, mostly fresh), hornblende and possibly pyroxene (10%, 0.2-1mm, subhedral, almost completely replaced by goethite)

Groundmass (60%): plagioclase (40%, 0.1mm, no preferred orientation), pyroxene (10%), opaques (magnetite, 10%)

AN13JP003 Hornblende quartz-diorite

Texture: equigranular, phaneritic, medium grained.

Plagioclase (70%, 1-3mm, sub to euhedral, mostly fresh), hornblende (15%, 0.5-2mm, subhedral, strongly replaced by chlorite), quartz (10%, 0.5-1mm, anhedral), orthoclase (5%, 0.5-1.5 mm, sub to anhedral), titanite (accessory)

AN13JP005 Pyroxene porphyritic andesite

Texture: porphyritic, microcrystalline groundmass

Phenocrysts (30%): plagioclase (20%, 1-3mm, sub to euhedral, mostly fresh, minor sericite along fractures), pyroxene (10%, 0.5-1mm, subhedral, strongly replaced by chlorite)

Groundmass (70%): plagioclase microlites (50%, 0.1mm, no preferred orientation), pyroxene (10%), opaques (magnetite, 10%)

AN13JP006 Quartz-sericite altered biotite porphyritic andesite

Texture: porphyritic, microcrystalline groundmass

Phenocrysts (20%): plagioclase (15%, 1-3mm, subhedral, partially replaced by sericite), biotite (5%, 0.5-1.5mm, subhedral)

Groundmass (80%): plagioclase (55%, 0.1-0.2mm, subhedral, strongly replaced by sericite), quartz (25%, 0.1mm, anhedral)

AN13JP007 Quartz-sericite altered biotite porphyritic andesite

Texture: porphyritic, microcrystalline groundmass

Phenocrysts (25%): plagioclase (23%, 1-4mm, subhedral, partly replaced by sericite), biotite (2%, 0.5-1.5mm, subhedral, strongly replaced by muscovite and chlorite)

Groundmass (75%): plagioclase (30%, 0.1-0.2mm, subhedral, partly replaced by sericite), quartz (45%, 0.1-0.2mm, anhedral)

AN13JP008 Calcareous sedimentary breccia

Texture: clastic, subangular, low sphericity, poorly sorted, clast-supported. Weak preferred clast orientation.

Clasts (60%): micritic limestone (55%, 0.5-10mm), plagioclase crystals (5%, 0.5mm)

Matrix (10%): micritic limestone (0.1-0.2mm)

Cement (30%): calcite (27%), aragonite (3%)

AN13JP009 Aphanitic andesite

Texture: aphanitic

Groundmass: plagioclase (80%, 0.2-0.3mm, subhedral, no preferred orientation), pyroxene (10%, 0.1-0.2mm, subhedral), hornblende (5%, 0.2-0.6mm, subhedral, partly replaced by chlorite), opaques (magnetite, 5%)

Calcite in veins and vesicles. Chlorite and possible celadonite in vesicles.

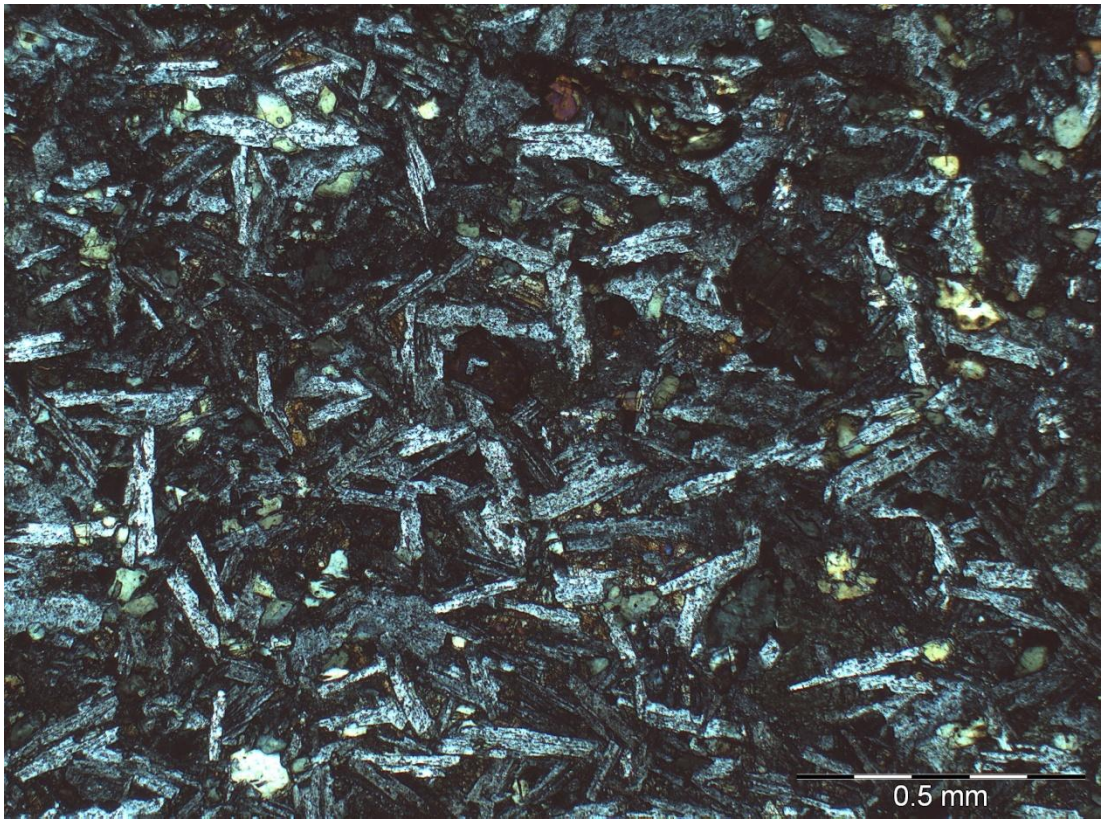

Figure IV.5. Sample AN13JP009, crossed polarisers. Aphanitic rock composed of fine-grained plagioclase, pyroxene and hornblende.

AN13JP010 Crystal-rich welded ignimbrite

Texture: pyroclastic, subangular, low sphericity, moderately sorted, matrix-supported.

Clasts (30%): plagioclase crystals (15%, 0.5-1mm, partly replaced by epidote), flattened and devitrified pumice (10%, 2-15mm), hornblende crystals (3%, 0.5-1mm, strongly replaced by epidote), andesitic lava (2%, 2mm)

Matrix (70%): fine-grained ash (45%), plagioclase crystal fragments (25%, 0.02-0.05mm)

AN13JP011 Lithic-rich lapilli tuff

Texture: pyroclastic, subangular, moderate sphericity, poorly sorted, clast-supported.

Clasts (50%): andesitic lava (80%, 0.5-5mm), plagioclase crystals (20%, 0.5-1mm)

Matrix: fine-grained ash

AN13JP012 Hornblende quartz-diorite

Texture: equigranular, phaneritic, medium grained.

Plagioclase (65%, 2-3mm, sub to euhedral, partly replaced by sericite in the halo of an epidote-actinolite vein), hornblende (13%, 1-2mm, subhedral, strongly replaced by actinolite and chlorite), quartz (10%, 0.5-1mm, anhedral), orthoclase (5%, 1-1.5 mm, sub to anhedral, pertitic and graphic textures observed), pyroxene (2%, 0.5mm, subhedral), opaques (magnetite, 5%), titanite (accessory)

AN13JP013 Quartz-sericite altered dacitic porphyry

Texture: porphyritic, strongly obliterated by hydrothermal alteration

Phenocrysts (5%): "phantoms" of possibly plagioclase and biotite, 1mm in size, completely replaced by fine-grained sericite (plagioclase) and coarse-grained muscovite (biotite).

Groundmass (95%): primary minerals completely replaced by an aggregate of quartz (60%, 0.1mm, anhedral) and sericite (35%, 0.1mm, subhedral)

AN13JP014 Hornblende andesitic porphyry

Texture: porphyritic, microcrystalline groundmass

Phenocrysts (20%): hornblende (15%, 0.5-2mm, sub to euhedral, completely replaced by biotite and subsequent chlorite), plagioclase (5%, 0.5-4mm, subhedral)

Groundmass (80%): plagioclase (60%, 0.05-0.1mm), hornblende (20%, 0.1-0.2mm)

AN13JP015 Hornblende monzo-granite

Texture: equigranular, phaneritic, medium grained.

Plagioclase (25%, 1-3mm, subhedral, completely replaced by sericite), quartz (30%, 1-1.5mm, anhedral), orthoclase (25%, 1-3 mm, sub to anhedral, partly replaced by clays and sericite), hornblende (12%, 1-3mm, subhedral, completely replaced by chlorite), biotite (3%, 0.5-1mm, subhedral, partly replaced by chlorite), opaques (magnetite, 5%, ilmenite, accessory), titanite (accessory)

Quartz>orthoclase vein, 1mm wide

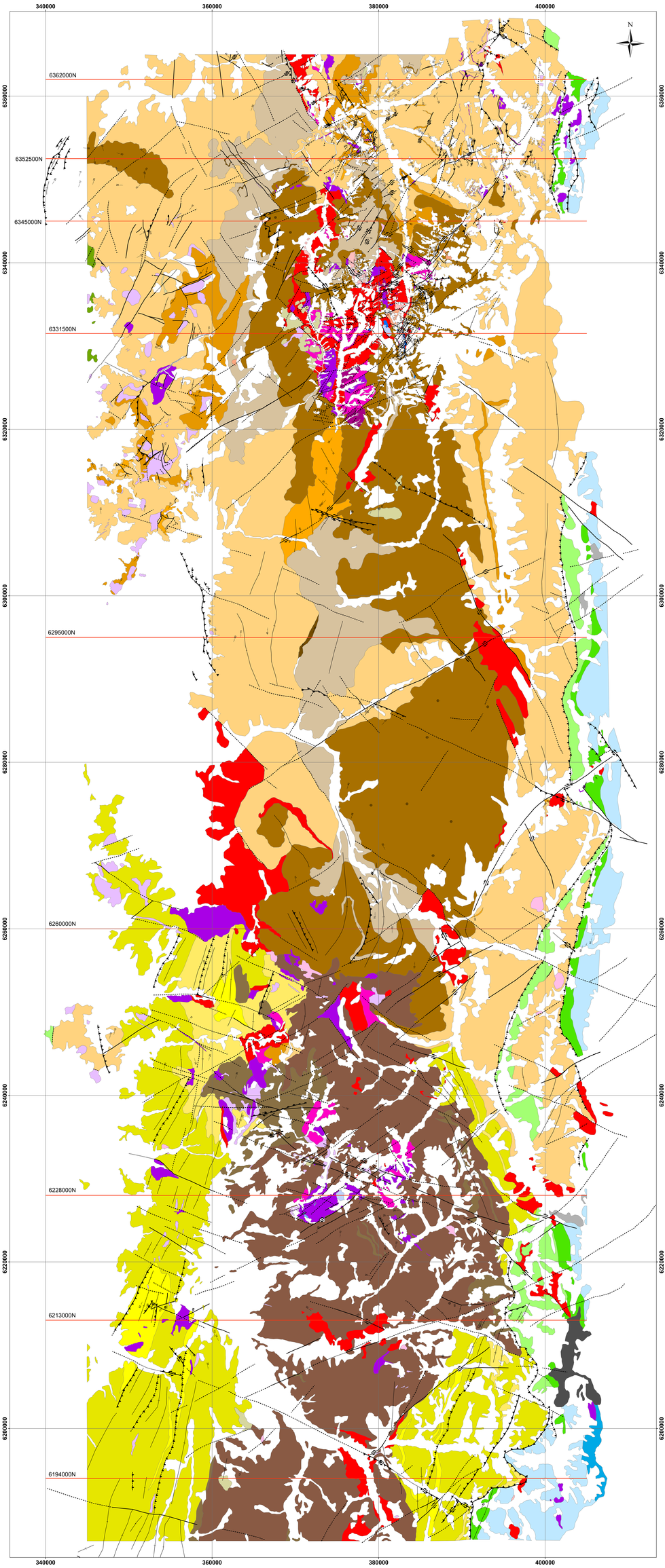

Geological map of the Andes of central Chile

Based on data from Wall et al. (1999), Rivera and Cembrano (2000), SERNAGEOMIN (2002), Fuentes et al. (2004), Fock (2005), Fock et al. (2005), Piquer (2010) and this work.

Legend

0 5 10 20 Kilometers

- Bedding
- Bedding (overturned)
- Horizontal bedding
- Vertical bedding
- Cross-sections

Structures

- Normal fault
- Fault
- Reverse fault
- Inferred fault
- Concealed fault
- Inferred reverse fault
- Syncline
- Anticline

Lithology

- Quaternary unconsolidated sediments
- Quaternary volcanic rocks

Intrusive rocks (Miocene-Early Pliocene)

- Rock-flour breccia
- Tourmaline breccia
- Other hydrothermal breccias
- Dacitic porphyry
- Andesitic porphyry
- Rhyolitic diatremes and domes
- Dacitic domes
- Granite
- Granodiorite
- Monzonite, quartz monzonite
- Monzodiorite, quartz monzodiorite
- Diorite, quartz diorite
- Gabbro

Teniente Volcanic Complex (Middle to Late Miocene)

- Lava flows
- Pyroclastic deposits

Farellones Formation (Early to Middle Miocene)

- Lava flows
- Pyroclastic deposits
- Volcano-sedimentary deposits

Coya-Machali Formation (Early to Middle Miocene)

- Lava flows
- Pyroclastic deposits
- Volcano-sedimentary deposits

Abanico Formation (Late Eocene-Oligocene)

- Lava flows
- Pyroclastic deposits
- Volcano-sedimentary deposits

Mesozoic units

- Lo Valle Formation (Late Cretaceous)
- Colimapu and Las Chilcas formations (Early Cretaceous)
- Gypsum beds and diapirs
- Lo Valdes and San Jose formations (Late Jurassic-Early Cretaceous)
- Río Damas Formation (Late Jurassic)
- Río Colina Formation (Middle Jurassic)

Cross-section 6194000N

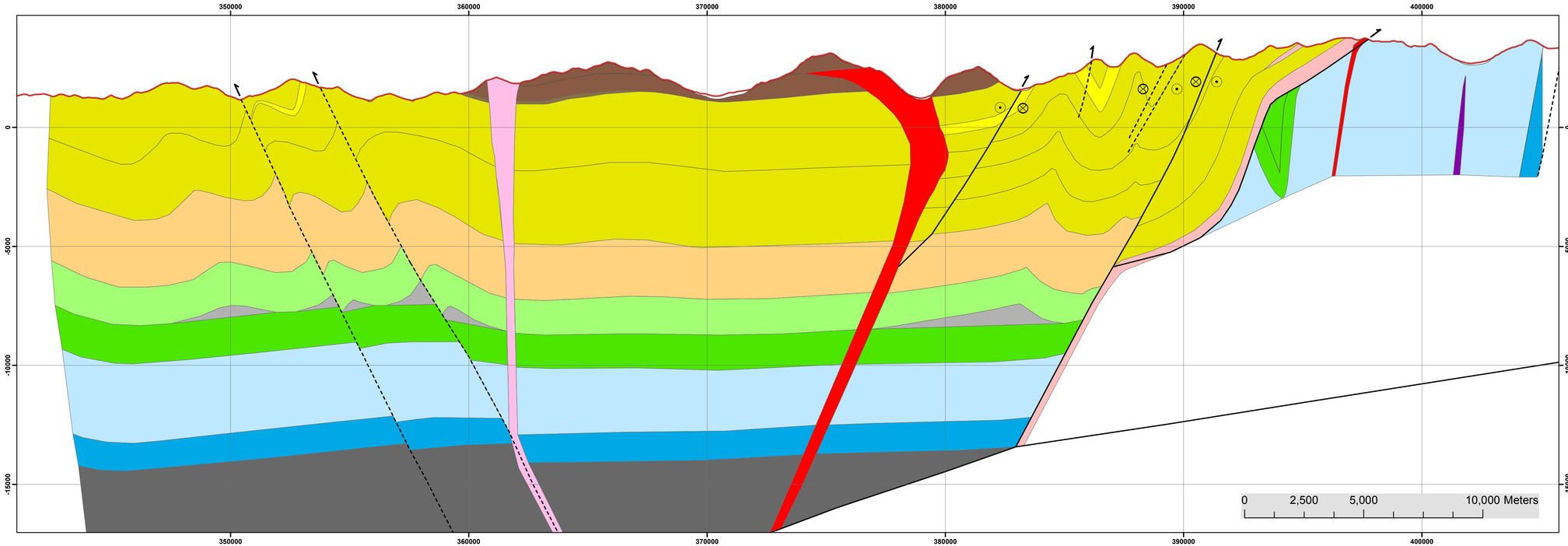

Legend

Structures

- Bedding
- Fault
- Inferred fault

Lithology

Intrusive rocks (Miocene)
- Dacitic porphyry
- Rhyolitic dikes and breccias
- Granodiorite, tonalite
- Diorite

Teniente Volcanic Complex (Middle-Late Miocene)
- Lava flows
- Pyroclastic deposits

Coya-Machali Formation (Early-Middle Miocene)
- Lava flows
- Volcano-sedimentary deposits

Abanico Formation (Late Eocene-Oligocene)
- Undiferentiated

Mesozoic units
- Gypsum beds and diapirs
- Colimapu and Las Chilcas formations (Early Cretaceous)
- Lo Valdes Formation (Late Jurassic-Early Cretaceous)
- Rio Damas Formation (Late Jurassic)
- Rio Colina Formation (Middle Jurassic)
- Basement (Paleozoic-Triassic)

Cross-section 6213000N

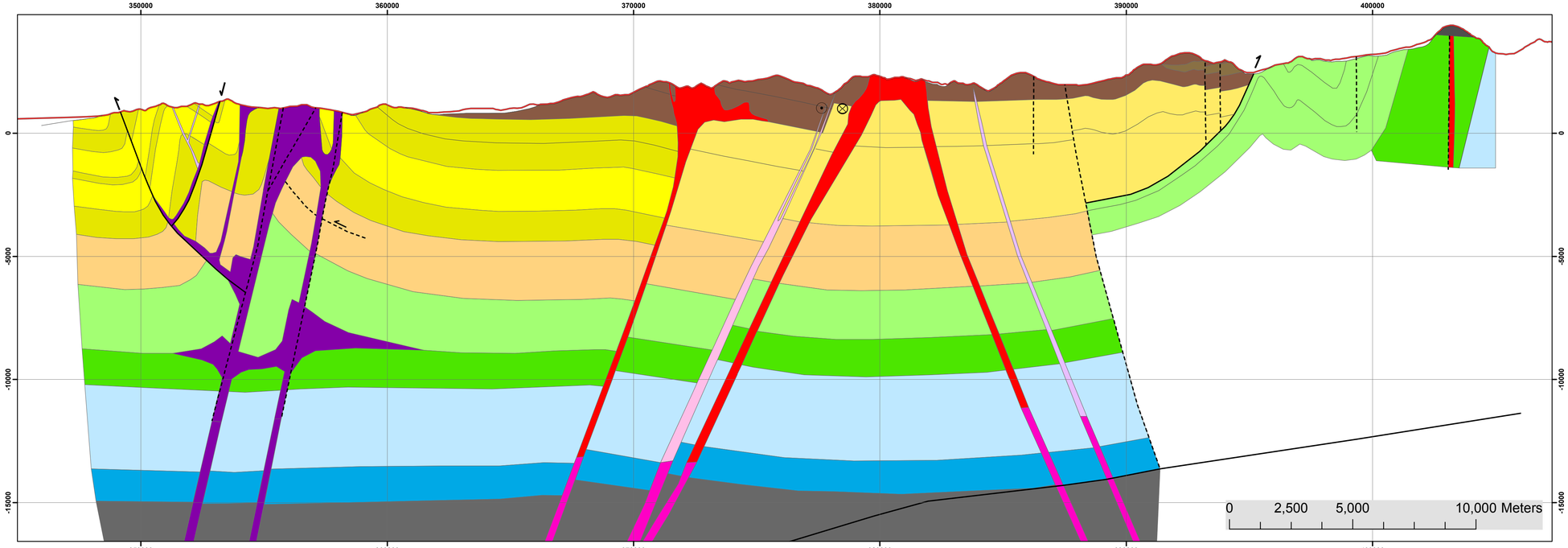

Legend

Structures

- Bedding
- Fault
- Inferred fault

Lithology

Intrusive rocks (Miocene)
- Dacitic porphyry
- Andesitic porphyry
- Granodiorite
- Diorite
- Undiferentiated

Teniente Volcanic Complex (Middle-Late Miocene)
- Lava flows
- Pyroclastic deposits

Coya-Machali Formation (Early-Middle Miocene)
- Volcano-sedimentary deposits
- Lava flows
- Undiferentiated

Abanico Formation (Late Eocene-Oligocene)
- Undiferentiated

Mesozoic units
- Colimapu and Las Chilcas formations (Early Cretaceous)
- Lo Valdes Formation (Late Jurassic-Early Cretaceous)
- Rio Damas Formation (Late Jurassic)
- Rio Colina Formation (Middle Jurassic)
- Basement (Paleozoic-Triassic)

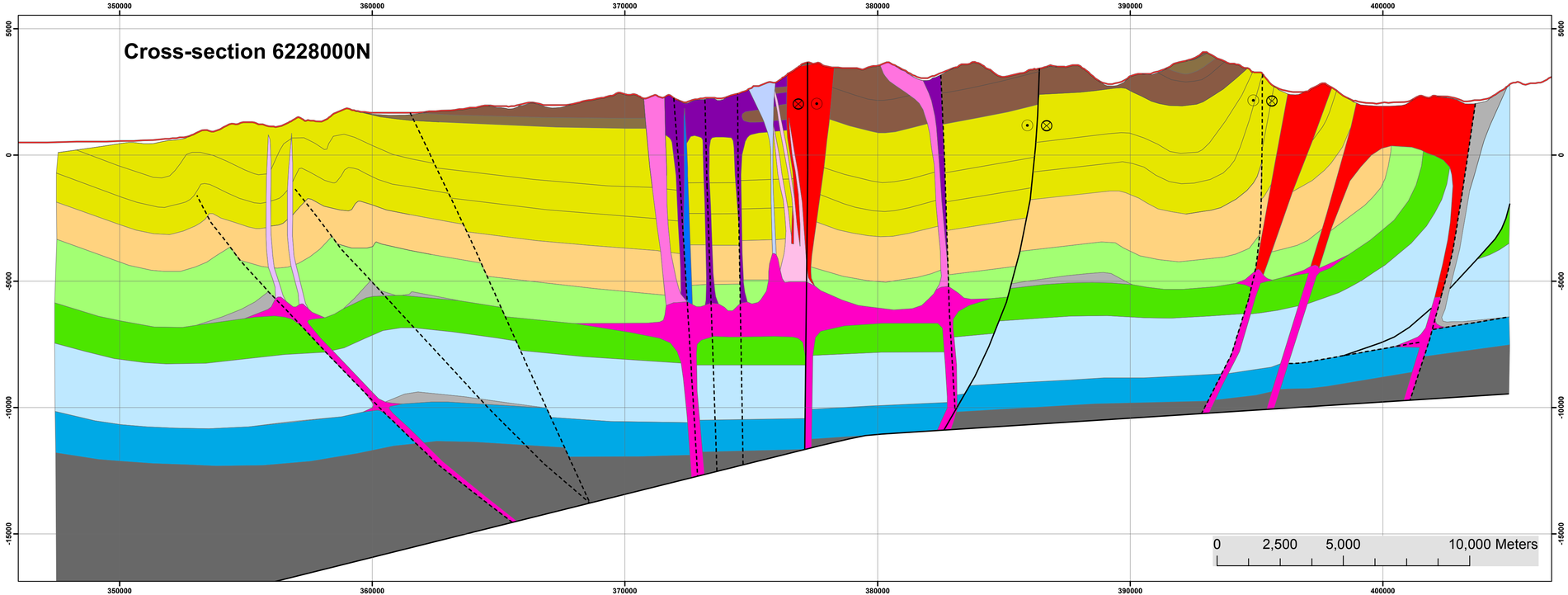

Legend

Structures

- Bedding
- Fault
- Inferred fault

Lithology

Intrusive rocks (Miocene-Early Pliocene)

- Braden breccia
- Hydrothermal breccia
- Dacitic porphyry
- Andesitic porphyry
- Granodiorite, tonalite
- Diorite porphyry
- Monzonite
- Undiferentiated intrusive rocks

Teniente Volcanic Complex (Middle-Late Miocene)

- Lava flows
- Pyroclastic deposits

Coya-Machali Formation (Early-Middle Miocene)

- Lava flows and volcano-sedimentary deposits

Abanico Formation (Late Eocene-Oligocene)

- Lava flows

Mesozoic units

- Gypsum beds and diapirs
- Colimapu and Las Chilcas formations (Early Cretaceous)
- Lo Valdes Formation (Late Jurassic-Early Cretaceous)
- Rio Damas Formation (Late Jurassic)
- Rio Colina Formation (Middle Jurassic)
- Basement (Paleozoic-Triassic)

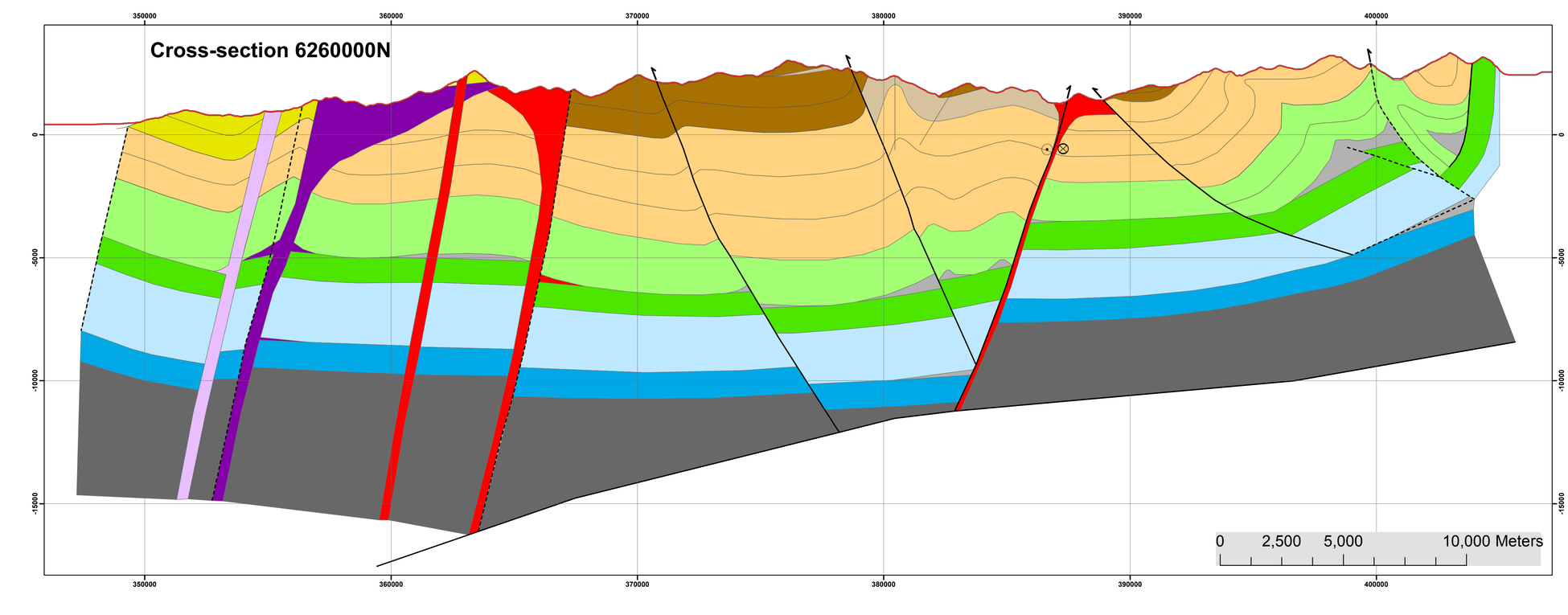

Legend

Structures

- Bedding
- Fault
- Inferred fault

Lithology

Intrusive rocks (Miocene)
- Andesitic porphyry
- Granodiorite
- Diorite

Farellones Formation (Early-Middle Miocene)
- Lava flows
- Pyroclastic deposits

Coya-Machali Formation (Early-Middle Miocene)
- Pyroclastic deposits
- Lava flows

Abanico Formation (Late Eocene-Oligocene)
- Lava flows

Mesozoic units
- Gypsum beds and diapirs
- Colimapu and Las Chilcas formations (Early Cretaceous)
- Lo Valdes Formation (Late Jurassic-Early Cretaceous)
- Rio Damas Formation (Late Jurassic)
- Rio Colina Formation (Middle Jurassic)
- Basement (Paleozoic-Triassic)

Cross-section 6295000N

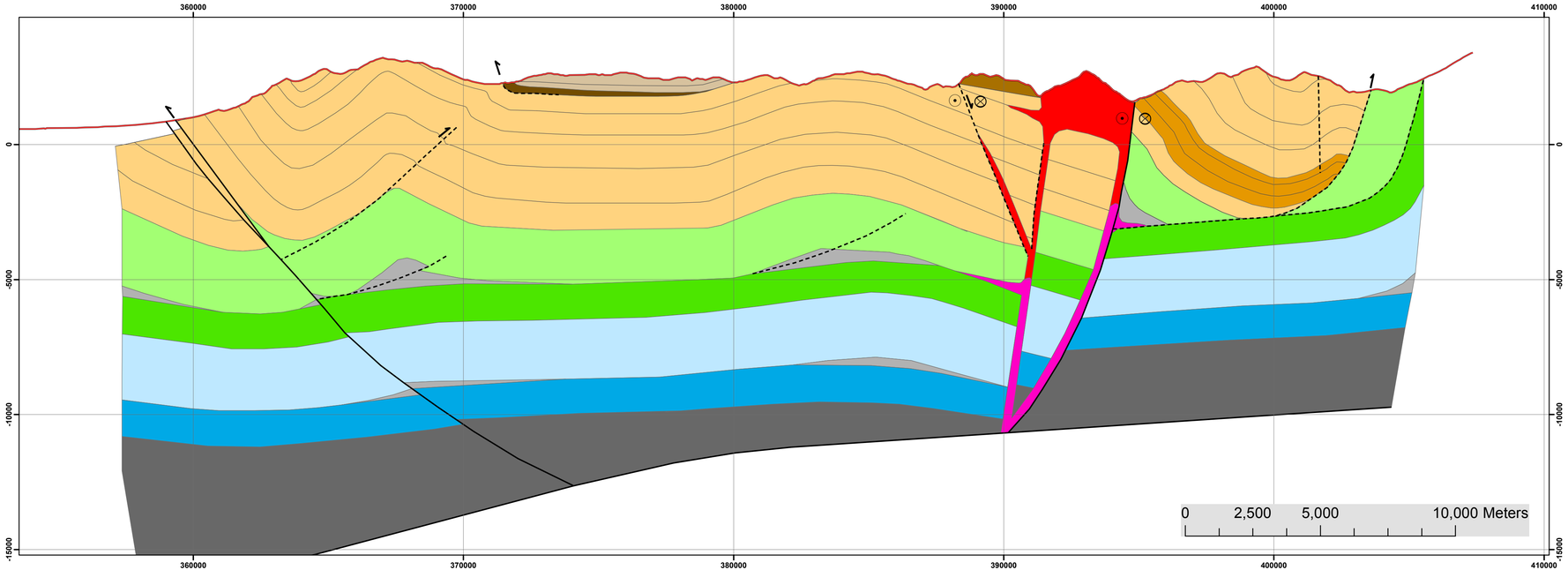

Legend

Structures

- Bedding
- Fault
- Inferred fault

Lithology

Intrusive rocks (Miocene)

- Granodiorite
- Undiferentiated intrusive rocks

Farellones Formation (Early-Middle Miocene)

- Lava flows
- Pyroclastic deposits
- Volcano-sedimentary deposits

Abanico Formation (Late Eocene-Oligocene)

- Lava flows
- Pyroclastic deposits

Mesozoic units

- Gypsum beds and diapirs
- Colimapu and Las Chilcas formations (Early Cretaceous)
- Lo Valdes Formation (Late Jurassic-Early Cretaceous)
- Rio Damas Formation (Late Jurassic)
- Rio Colina Formation (Middle Jurassic)
- Basement (Paleozoic-Triassic)

Cross-section 6331500N

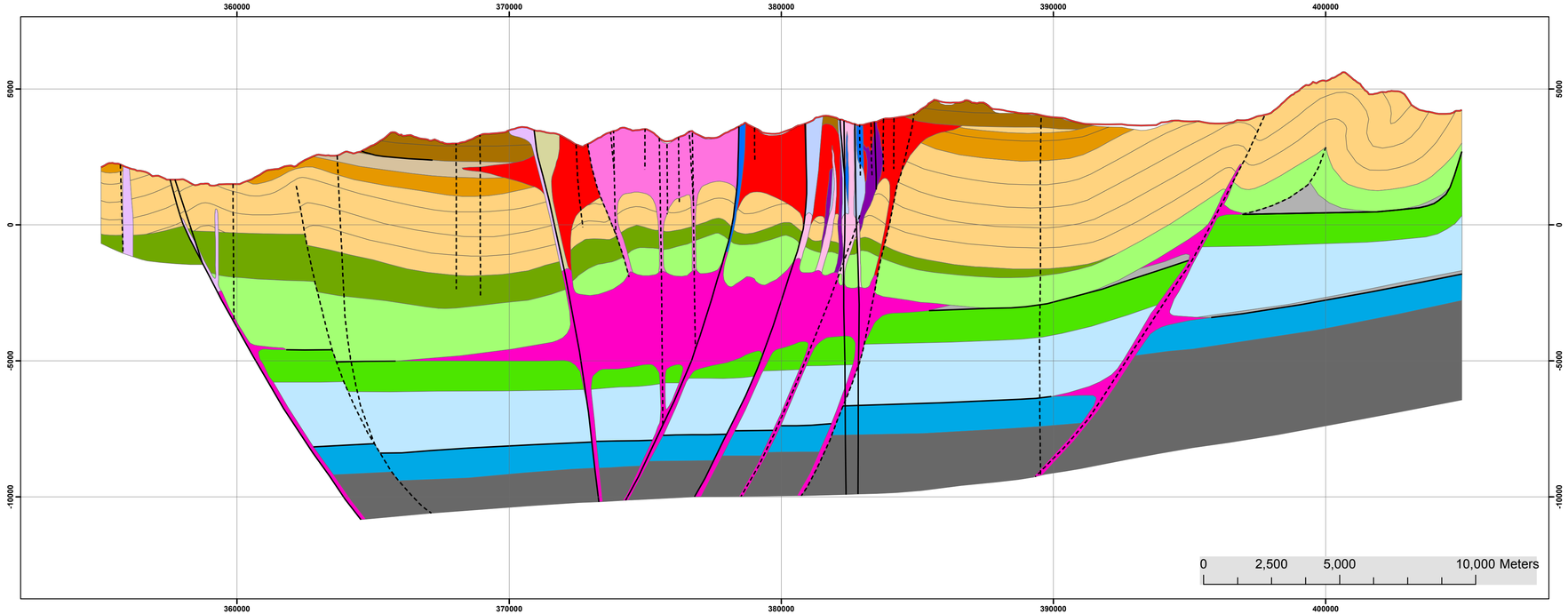

Legend

Structures

- Bedding
- Fault
- Inferred fault

Lithology

Intrusive rocks (Miocene-Early Pliocene)

- Rock-flour breccia
- Tourmaline breccia
- Dacitic porphyry
- Andesitic porphyry
- Dacitic domes
- Granodiorite, tonalite
- Monzonite
- Diorite
- Undiferentiated intrusive rocks

Farellones Formation (Early-Middle Miocene)

- Lava flows
- Pyroclastic deposits

Abanico Formation (Late Eocene-Oligocene)

- Lava flows
- Pyroclastic deposits

Mesozoic units

- Lo Valle Formation (Late Cretaceous)
- Gypsum beds and diapirs
- Colimapu and Las Chilcas formations (Early Cretaceous)
- Lo Valdes Formation (Late Jurassic-Early Cretaceous)
- Rio Damas Formation (Late Jurassic)
- Rio Colina Formation (Middle Jurassic)
- Basement (Paleozoic-Triassic)

Cross-section 6345000N

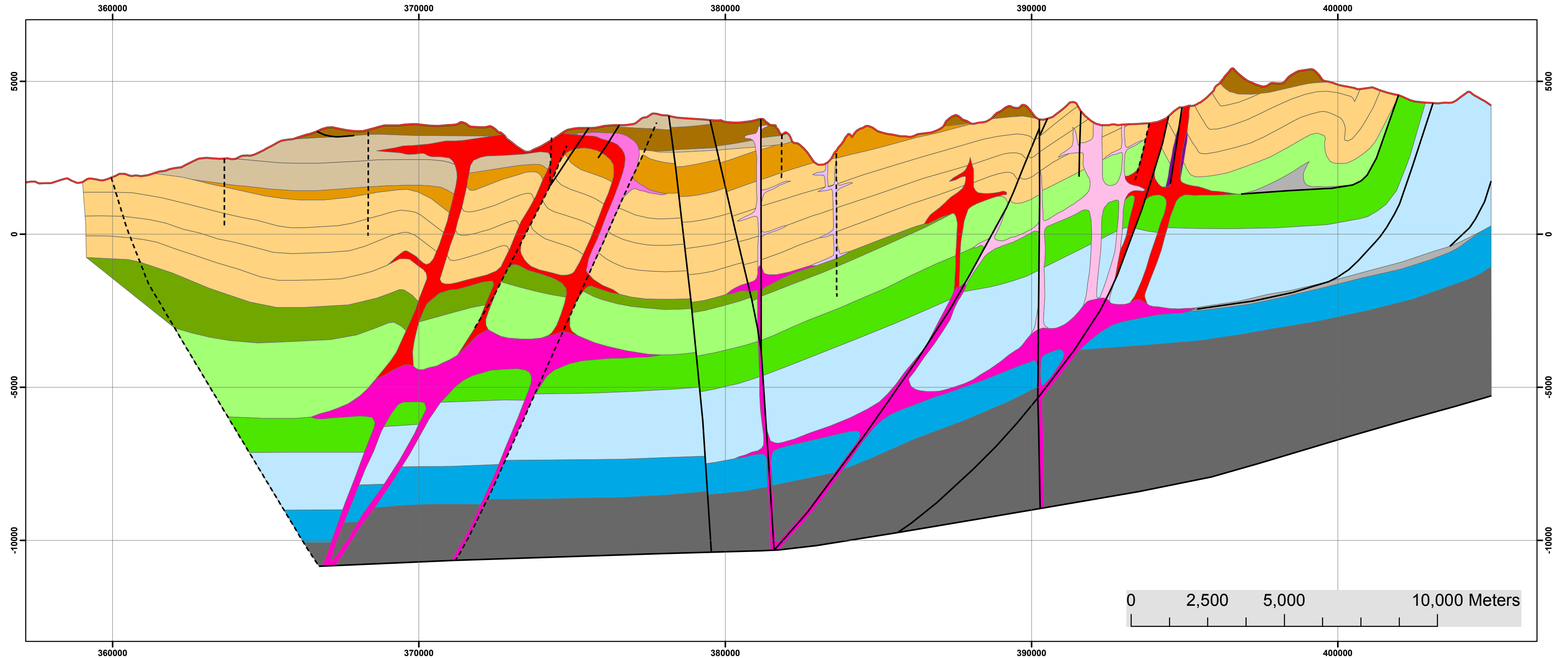

Legend

Structures

- Bedding
- Fault
- Inferred fault

Lithology

Intrusive rocks (Miocene)

- Dacitic porphyry
- Andesitic porphyry
- Granodiorite, tonalite
- Monzonite
- Diorite
- Undiferentiated intrusive rocks

Farellones Formation (Early-Middle Miocene)

- Lava flows
- Pyroclastic deposits

Abanico Formation (Late Eocene-Oligocene)

- Lava flows
- Pyroclastic deposits

Mesozoic units

- Lo Valle Formation (Late Cretaceous)
- Gypsum beds and diapirs
- Colimapu and Las Chilcas formations (Early Cretaceous)
- Lo Valdes Formation (Late Jurassic-Early Cretaceous)
- Rio Damas Formation (Late Jurassic)
- Rio Colina Formation (Middle Jurassic)
- Basement (Paleozoic-Triassic)

Cross-section 6352500N

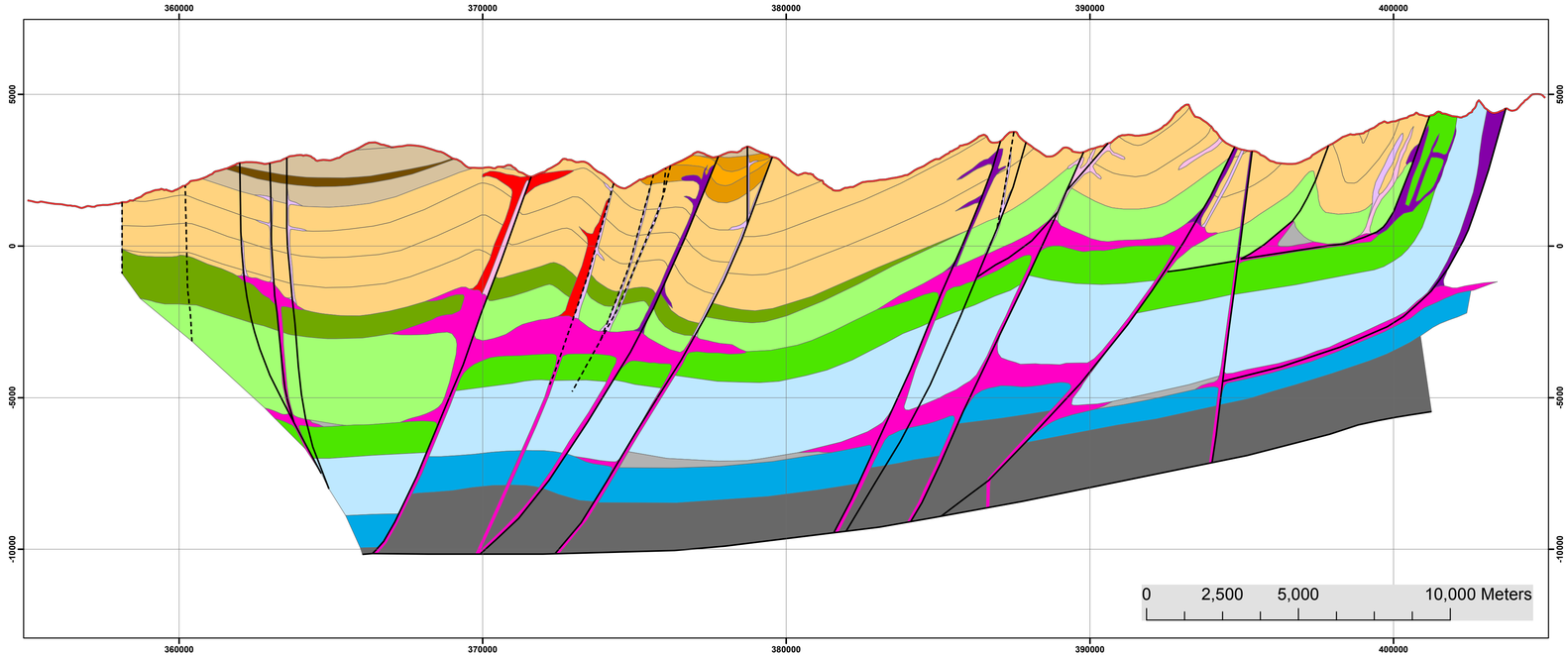

Legend

Structures

- Bedding
- Fault
- Inferred fault

Lithology

Intrusive rocks (Miocene)

- Dacitic porphyry
- Andesitic porphyry
- Granodiorite, tonalite
- Diorite
- Undiferentiated intrusive rocks

Farellones Formation (Early-Middle Miocene)

- Volcano-sedimentary deposits
- Pyroclastic deposits

Abanico Formation (Late Eocene-Oligocene)

- Lava flows
- Pyroclastic deposits
- Volcano-sedimentary deposits

Mesozoic units

- Lo Valle Formation (Late Cretaceous)
- Gypsum beds and diapirs
- Colimapu and Las Chilcas formations (Early Cretaceous)
- Lo Valdes Formation (Late Jurassic-Early Cretaceous)
- Rio Damas Formation (Late Jurassic)
- Rio Colina Formation (Middle Jurassic)
- Basement (Paleozoic-Triassic)

Cross-section 6362000N

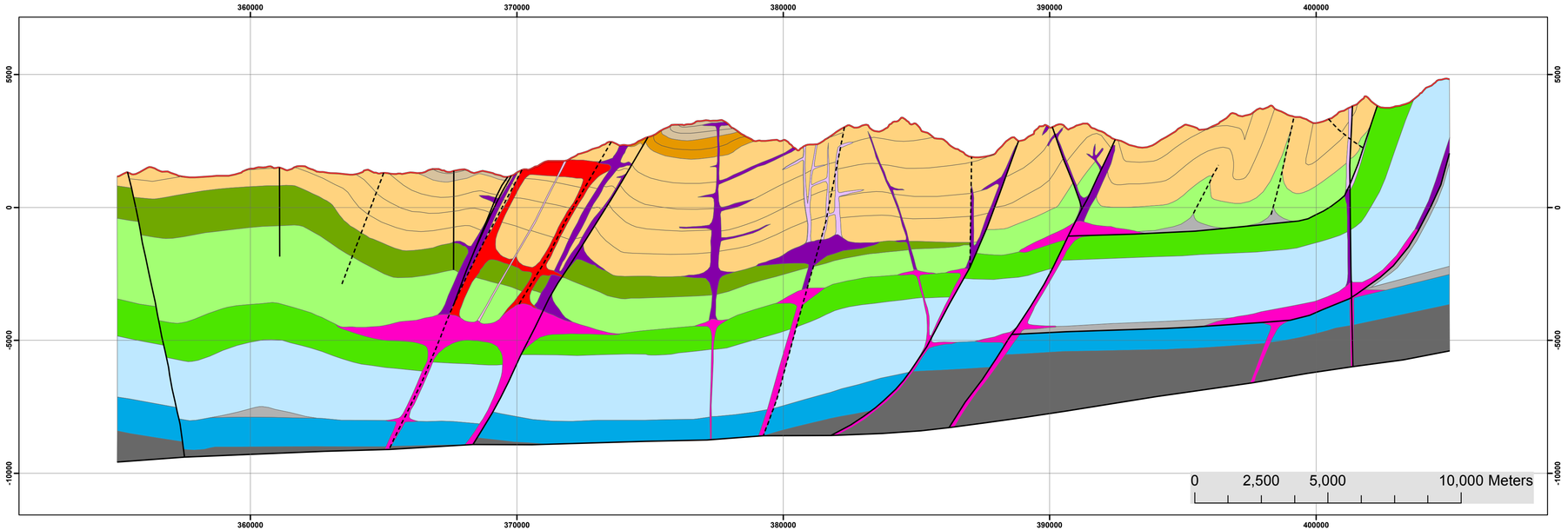

Legend

Structures

- Bedding
- Fault
- Inferred fault

Lithology

Intrusive rocks (Miocene)

- Dacitic porphyry
- Andesitic porphyry
- Granodiorite, tonalite
- Diorite
- Undiferentiated intrusive rocks

Farellones Formation (Early-Middle Miocene)

- Pyroclastic deposits

Abanico Formation (Late Eocene-Oligocene)

- Lava flows
- Pyroclastic deposits

Mesozoic units

- Lo Valle Formation (Late Cretaceous)
- Gypsum beds and diapirs
- Colimapu and Las Chilcas formations (Early Cretaceous)
- Lo Valdes Formation (Late Jurassic-Early Cretaceous)
- Rio Damas Formation (Late Jurassic)
- Rio Colina Formation (Middle Jurassic)
- Basement (Paleozoic-Triassic)